OAK RIDGE NATIONAL LABORATORY LIBRARIES

3 4456 0550913 4

ORNL-TM-5145

Cy 109

# Evaluation of the Structural Integrity of LMFBR Equipment Cell Liners—Results of Preliminary Investigations

W. J. McAfee
W. K. Sartory

OAK RIDGE NATIONAL LABORATORY
CENTRAL RESEARCH LIBRARY
DOCUMENT COLLECTION
LIBRARY LOAN COPY
DO NOT TRANSFER TO ANOTHER PERSON
If you wish someone else to see this document, send in name with document and the library will arrange a loan.

UCN-7969
(3 3-67)

OAK RIDGE NATIONAL LABORATORY
OPERATED BY UNION CARBIDE CORPORATION • FOR THE U.S. ATOMIC ENERGY COMMISSION

ORNL-TM-5145
NRC-7

Contract No. W-7405-eng-26

Reactor Division

# EVALUATION OF THE STRUCTURAL INTEGRITY OF LMFBR EQUIPMENT CELL LINERS – RESULTS OF PRELIMINARY INVESTIGATIONS

W. J. McAfee
W. K. Sartory

With Contributions from

Z. P. Bažant
Northwestern University

P. A. Stancampiano
Swanson Engineering Associates Corp.

JANUARY 1976

Work funded by Nuclear Regulatory Commission
under Interagency Agreement 40-495-75

OAK RIDGE NATIONAL LABORATORY
Oak Ridge, Tennessee 37830
operated by
UNION CARBIDE CORPORATION
for the
U.S. ENERGY RESEARCH AND DEVELOPMENT ADMINISTRATION

OAK RIDGE NATIONAL LABORATORY LIBRARIES
3 4456 0550913 4

CONTENTS

Page

PREFACE ..... v

ABSTRACT ..... 1

1. INTRODUCTION ..... 2

1.1 Background ..... 2

1.2 Work Scope and Objectives ..... 4

2. MECHANICAL AND PHYSICAL PROPERTIES OF LMFBR CELL AND LINER MATERIALS ..... 7

2.1 Materials Properties for Use in Inelastic Analysis ..... 7

2.1.1 Experimental Tensile Studies ..... 7

2.1.2 Summary of Mechanical and Physical Properties ..... 10

2.2 Review of Literature on High-Temperature Behavior of Concrete ..... 25

2.2.1 Physical and Chemical Changes ..... 26

2.2.2 Thermal Expansion and Shrinkage ..... 27

2.2.3 Pore Pressure ..... 27

2.2.4 Strength, Ductility, and Stress-Strain Diagrams ..... 28

2.2.5 Modulus of Elasticity and Poisson Ratio ..... 28

2.2.6 Creep ..... 29

2.2.7 Heat Capacity ..... 29

2.2.8 Thermal Conductivity and Diffusivity ..... 30

2.2.9 Moisture Conductivity and Diffusivity ..... 30

2.2.10 Explosive Thermal Spalling ..... 30

2.2.11 Reinforcing and Prestressing Steels ..... 31

3. BOUNDING-VALUE ASSESSMENT OF THE EFFECT OF THE SODIUM-CONCRETE REACTION ON LMFBR CELL LINER INTEGRITY ..... 32

3.1 Introduction ..... 32

3.2 Energy Release ..... 33

3.3 Temperature Buildup Due to Reaction ..... 34

3.4 Liner Plate Pressure Differential ..... 35

3.5 A Computer Model of the Reaction ..... 37

3.6 Summary ..... 44

Page

4. INELASTIC SCOPING ANALYSIS OF A REPRESENTATIVE LMFBR EQUIPMENT CELL LINER ..... 46

4.1 Introduction ..... 46

4.2 One-Dimensional Transient Thermal Analysis ..... 48

4.2.1 One-Dimensional Finite-Element Thermal Model ..... 49

4.2.2 One-Dimensional Analysis Results ..... 49

4.3 Three-Dimensional Thermal Analysis ..... 51

4.3.1 Three-Dimensional Finite-Element Thermal Model ..... 52

4.3.2 Three-Dimensional Thermal Analysis Results ..... 52

4.4 Three-Dimensional Plastic Structural Analysis ..... 56

4.4.1 Three-Dimensional Finite-Element Structural Model ..... 56

4.4.2 Three-Dimensional Structural Model Results ..... 57

5. CONCLUSIONS AND RECOMMENDATIONS ..... 63

REFERENCES ..... 67

APPENDIX I. REVIEW OF LITERATURE ON HIGH-TEMPERATURE BEHAVIOR OF CONCRETE ..... 69

APPENDIX II. THERMAL-STRUCTURAL ANALYSIS OF A REPRESENTATIVE LMFBR EQUIPMENT CELL LINER ..... 143

# PREFACE

These studies of liquid-metal-cooled fast breeder reactor (LMFBR) cell liner behavior under sodium spill conditions were performed at the request of the Oak Ridge National Laboratory (ORNL) Aerosol Release and Transport Program (189a No. B0121), which is supported by the Experimental Fast Reactor Safety Research Branch, Division of Reactor Safety Research, Nuclear Regulatory Commission. The studies were performed to investigate uncertainties related to the assessment of the consequences of a sodium spill onto an initially unflawed cell wall or a wall with an existing flaw.

The scope of the studies was limited by the time available, and no attempt was made to deal in depth with all the problems associated with an assessment of LMFBR cell liner integrity. Simple, but essential, characteristics of liner behavior were investigated to provide information to delineate the severity of the problem and to provide bases for recommendations for follow-up research, if needed. The results presented are thus preliminary in nature.

The authors would like to thank a number of people who contributed to this report. Dr. Zdeněk Bažant, Professor of Civil Engineering at Northwestern University, was retained as an ORNL consultant to conduct a literature review and bibliography on the behavior of concrete at high temperature. P. A. Stancampiano, Swanson Engineering Associates (SEA) Corp., performed essential thermal-inelastic structural analyses, with SEA Corp. serving as an ORNL subcontractor. R. H. Chapman, ORNL, contributed extensive literature files; J. M. Corum, ORNL, prepared initial program planning that was essential to the definition of the work scope; and D. D. Reiff, Experimental Fast Reactor Safety Research Branch, Nuclear Regulatory Commission, provided programmatic direction. Recognition is also due Myrtleen Sheldon of the ORNL Reactor Division Reports Office for her careful editing of this report. Finally, the authors wish to thank Dolores Eden and Linda Dockery for typing drafts of the report and Delores Weaver for typing the final report.

# EVALUATION OF THE STRUCTURAL INTEGRITY OF LMFBR EQUIPMENT CELL LINERS – RESULTS OF PRELIMINARY INVESTIGATIONS

W. J. McAfee W. K. Sartory

With Contributions from

Z. P. Bažant
Northwestern University

P. A. Stancampiano
Swanson Engineering Associates Corp.

## ABSTRACT

The behavior of a plane wall segment of a prototype liquid-metal-cooled fast breeder reactor (LMFBR) cell under conditions of a postulated massive sodium spill was studied. Sodium-concrete reaction calculations were performed assuming an initial flaw existed in the liner such that high-temperature sodium could penetrate to the concrete underneath. Based on existing sodium-concrete reaction rate data, bounding values were established for the maximum energy release per unit volume of concrete. The potential effect of this energy release on the deformation of the liner material was determined. The temperature buildup in the liner and the pressure differential across the flaw in the liner were also studied.

The transient thermal and structural responses of the steel liner and backup concrete were analyzed in detail using the inelastic computer code ANSYS. The conditions studied included a ramp temperature change of the liner surface inside the cell of 65.6°C (150°F) to 537.8°C (1000°F) in 1 sec, an isothermal steady-state period at 537.8°C (1000°F), and an isothermal cool-down back to 65.6°C (150°F). Stresses, strains, and displacements were calculated for each condition. A series of uniaxial tensile tests was run for ASTM type A212B carbon steel at selected temperatures from room temperature to 537.8°C (1000°F) to furnish the necessary stress-strain data as input to these structural analyses. Other mechanical and physical properties of carbon steel and concrete were determined from the literature.

The literature on the mechanical, physical, and general behavior properties of concrete at high temperature was reviewed. This review emphasized the structural behavior of concrete and did not cover the sodium-concrete reaction.

The results contained herein are preliminary and were intended primarily to delineate the scope of the problem. Additional follow-up studies are identified to resolve uncertainties involved in assessing cell liner behavior during a sodium spill.

Key words: cell liner, inelastic analysis, high-temperature design, high-temperature concrete, high-temperature carbon steel, sodium spill, sodium-concrete reaction.

# 1. INTRODUCTION

## 1.1 Background

The zoned-containment concept used in liquid-metal-cooled fast breeder reactor (LMFBR) buildings results in a rather complex structure consisting of many equipment cells and interconnecting pipe tunnels. These cells and tunnels are lined with thin steel membranes and are surrounded by a massive concrete structure. The steel liner is a containment barrier to maintain an inert-gas atmosphere surrounding the components within the cells and pipe tunnels in order to minimize chemical reactions between the sodium and air in the event of reactor coolant leaks. The surrounding concrete structure provides support for these thin steel liners.

A state-of-the-art review of technology related to the design of LMFBR equipment cell liners was performed by Chapman,[1] who reviewed the design of sodium-cooled reactors that have been built or are being planned in the United States and Europe. The specific design details of each reactor concept differ, but the functional requirements of cell liners held in common by each system are to:

1. provide a leak-tight (or low inleakage) containment for the inert-gas atmosphere during normal operation,
2. prevent (or minimize) release of fission products to the secondary containment under accident conditions,
3. prevent contact of the sodium coolant with the concrete structure in the event of accidental sodium spills,
4. facilitate cleanup operations following an accidental sodium spill.[1]

Obviously, the functioning of these liners is a key safety question in an assessment of the consequences of a sodium spill.

A spill of high-temperature sodium onto a liner surface could cause cracking or tearing of the liner or tearing of the liner away from the supporting concrete. The potential for loss of liner integrity is increased if a flaw already exists in the steel. If the liner ruptures, the high-temperature sodium will penetrate to and react with the concrete

underneath. Furthermore, if a cavity exists between the liner and the concrete, a quantity of high-temperature sodium can collect in a confined space and react with the concrete and with air or moisture trapped in the cavity. These reactions are exothermic and may result in high temperatures in the concrete and liner materials, high pressures between the liner and concrete, and the generation of hydrogen gas, which in turn will burn violently in contact with oxygen.

Most research related to the behavior of cell liners during sodium spills has been in connection with studies of sodium fire protection. Primary consideration has been given to methods of containing reaction products or of extinguishing the sodium-air or sodium-concrete reaction, and observations of structural behavior were only qualitative.

Tests have been run at Hanford Engineering Development Laboratory (HEDL) as proof tests of fire control measures designed into the Fast Flux Test Facility (FFTF). In one such test reported by Hilliard and Yatabe,[2] 318 kg (700 lb) of sodium at 582°C (1080°F) was spilled into a concrete catch pan with a 0.1-m-thick (4-in.) bottom. Damage to the concrete was major, most of the concrete reacted with the sodium, and maximum temperatures measured in the concrete exceeded 800°C (1472°F). In later tests by Hilliard and Muhlestein,[3,4] sodium at 593.3°C (1100°F) was spilled into steel catch pans supported by concrete. No sodium-concrete reaction occurred since the pans retained leak tightness, and the pans were essentially undamaged except for slight warping. However, these pans were not attached to the concrete as is common in LMFBRs and thus were not restrained as a liner would be. Hassberger et al.[5] studied the sodium-concrete reaction in a little more detail and, through simple models, investigated the leakage of sodium through a flawed liner. These were small-scale tests using conventional and magnetite* concretes. The concretes suffered extensive surface damage; very high temperatures were observed in both the concrete and sodium pool; and up to 80% of the total water content was driven out of each concrete specimen. In all cases, significant quantities of hydrogen were generated.

---

*Magnetite refers to a particular high-density concrete used in FFTF construction.

Through Chapman's review of design practice and tests such as those discussed above, a number of uncertainties have been identified in the ability to assess the performance of cell liners during massive sodium spills and/or sodium leaks in the form of sprays or jets. The work reported here was a limited follow-up effort to Chapman's interpretive report and was intended to further delineate the magnitude of the problem and help in defining possible required research or development activities.

## 1.2 Work Scope and Objectives

The primary criteria for liner performance are leak tightness and structural integrity, that is, the prevention of gross structural failure of the liner by tearing away from the concrete and developing major cracks or openings. The scope of the present work was limited to the structural behavior criterion; however, both criteria are intimately related, since structural failure of the liner could possibly lead to loss of leak tightness.

To accurately assess the consequences of a sodium spill requires, as a minimum, a reasonably accurate prediction of the structural response of the liner-concrete configuration to the sodium spill and a bounding-type estimate of the consequences of sodium penetrating the liner and reacting with the concrete.

The specific objectives of the present study were (1) to assess the predictability of the structural response of typical cell liner configurations to massive sodium spills, and (2) to establish bounding values for use in assessing the relationship between the cell liner system parameters (crack opening area, void space between the liner and concrete, etc.), the sodium-concrete reaction (energy release and pressure and temperature buildup), and the liner structural response.

The structural response of a simplified model of a cell-liner—concrete configuration was studied analytically. The thermal and structural behaviors of this model were determined for the conditions of a sudden sodium spill [surface of liner in contact with sodium goes from 65.6°C (150°F) to 537.8°C (1000°F) in 1 sec], a period of thermal equilibrium

for the liner, and an isothermal cooldown back to 65.6°C (150°F). A series of uniaxial tensile tests was run to provide the necessary stress-strain information for use in the analyses. In the tests, ASTM type A212B carbon steel specimens were tested at selected temperatures over the range room temperature to 537.8°C (1000°F). The other required mechanical and physical properties of carbon steel and of concrete were obtained from the literature.

The review made to collect the mechanical and physical properties of concrete indicated a great deal of variation in reported properties and actual gaps in the availability of data. A more in-depth review was thus conducted to survey the behavior of concrete with emphasis being given to conditions representative of a sodium spill (i.e., high temperature, thermal shock, etc.), and an extensive bibliography was prepared. The effects of sodium (i.e., the sodium-concrete reaction) were not considered.

The reaction of sodium and concrete was studied analytically to establish bounding values wherever possible. The maximum energy release available per unit volume of concrete was calculated as well as the maximum pressure and temperature buildups to be expected. In performing these reaction calculations, a structural configuration was used that has been identified as a potential model for the experimental scoping studies that are needed in conjunction with the type of analytical work discussed in this report. This configuration is discussed in detail in Chapter 3.

The remainder of this report presents the details of the work involved in meeting the above stated objectives. Chapter 2 covers the compilation of materials properties, including the tensile tests, required as input to the thermal-structural analyses and includes a summary of the review of high-temperature behavior of concrete. Chapter 3 discusses the sodium-concrete reaction calculations. Chapter 4 presents a summary of the thermal-structural analyses of a segment of a prototypic cell wall. Chapter 5 covers the conclusions and recommendations resulting from the work performed.

The report also contains two extensive appendices. Appendix I is the complete report prepared on the high-temperature properties of concrete. Appendix II is the complete report covering details of the thermal-structural analyses performed on a segment of a prototypic cell wall. These appendices are included for the reader who wants to study either the results of the literature review or the analyses in greater detail than is covered in the summary chapters.

# 2. MECHANICAL AND PHYSICAL PROPERTIES OF LMFBR CELL AND LINER MATERIALS

The investigation of material properties for LMFBR cell liners reported here is preliminary and was intended primarily to support the immediate needs of the study. These needs were data requirements for analyses and a general technology assessment for use in program planning.

## 2.1 Materials Properties for Use in Inelastic Analysis

The materials properties data needed to conduct the inelastic analysis of a typical LMFBR cell liner were defined in conjunction with Swanson Engineering Associates. These properties were required input to the ANSYS code to perform transient thermal analyses and detailed stress analyses. The data required were

1. stress-strain curves for the liner and stud steels at up to six temperatures between 65.6°C (150°F) and 537.8°C (1000°F);
2. specific heats, thermal conductivities, and mass densities of the liner, stud, and concrete wall materials;
3. elastic stress-strain data for the concrete wall material.

The properties compiled for use and their sources are the topics of the following subsections.

### 2.1.1 Experimental Tensile Studies

Both carbon steel and stainless steel are used as liner material, but for the purpose of this study type ASTM A516 carbon steel, grade 55 or 70, was chosen as the prototypic liner material.[1] An initial review indicated that a consistent set of stress-strain data on this material was not available either in the open literature or in-house. Previous tests have concentrated on material behavior from room temperature up to about 260°C (500°F), so that high-temperature stress-strain data are not readily available.

To provide a consistent set of stress-strain curves, tensile tests were run at specified temperatures between room temperature (RT) and

537.8°C (1000°F). Archive specimens of type ASTM A212B steel were available in the Metals and Ceramics Division of ORNL. This is a carbon steel that is very similar to ASTM A516 and should have very similar stress-strain behavior. The similarity in material composition is shown in Table 2.1, which gives the chemistry of the specimen material used in comparison to both ASME SA-516 and ASTM A516 steels.[6,7] The material available was a 4-in.-thick plate (plate 4, U.S. Steel heat A0456) that had been used as the reference material for extensive ASTM-code-related studies. The specimens were already prepared and had been taken from adjacent positions in the one-third (or two-thirds) thickness plane of the plate. The cutting plan is shown in Fig. 2.1, along with a sketch of the specimen geometry.

Eight specimens were tested: one each at RT, 65.6°C (150°F), 148.9°C (300°F), 260°C (500°F), 343.3°C (650°F), 426.7°C (800°F), 482.2°C (900°F),

Table 2.1. Chemical composition (wt %) of ASTM A212B and A516 carbon steel

| Element | Plate No. 4, heat A0456 (A212B)[a] | ASTM 516[b] | | ASME SA-516[c] | |
|---|---|---|---|---|---|
| | | Grade 55 | Grade 70 | Grade 55 | Grade 70 |
| C | 0.262 | 0.22 | 0.30 | 0.22 | 0.27 |
| Mn | 0.80 | 0.56/1.25 | | 0.56/1.25 | 0.89/1.25 |
| Si | 0.22 | 0.13/0.33 | 0.13/0.33 | 0.13/0.33 | 0.13/0.33 |
| Ni | 0.28 | NA | NA | NA | NA |
| Cr | 0.12 | NA | NA | NA | NA |
| Cu | 0.26 | NA | NA | NA | NA |
| P | 0.012 | 0.035[d] | 0.035[d] | 0.035[d] | 0.035[d] |
| S | 0.036 | 0.04[d] | 0.04[d] | 0.04[d] | 0.04[d] |

[a]Ref. 8.

[b]Ref. 7.

[c]Ref. 6.

[d]Indicates maximum.

ORNL-DWG 75-17368

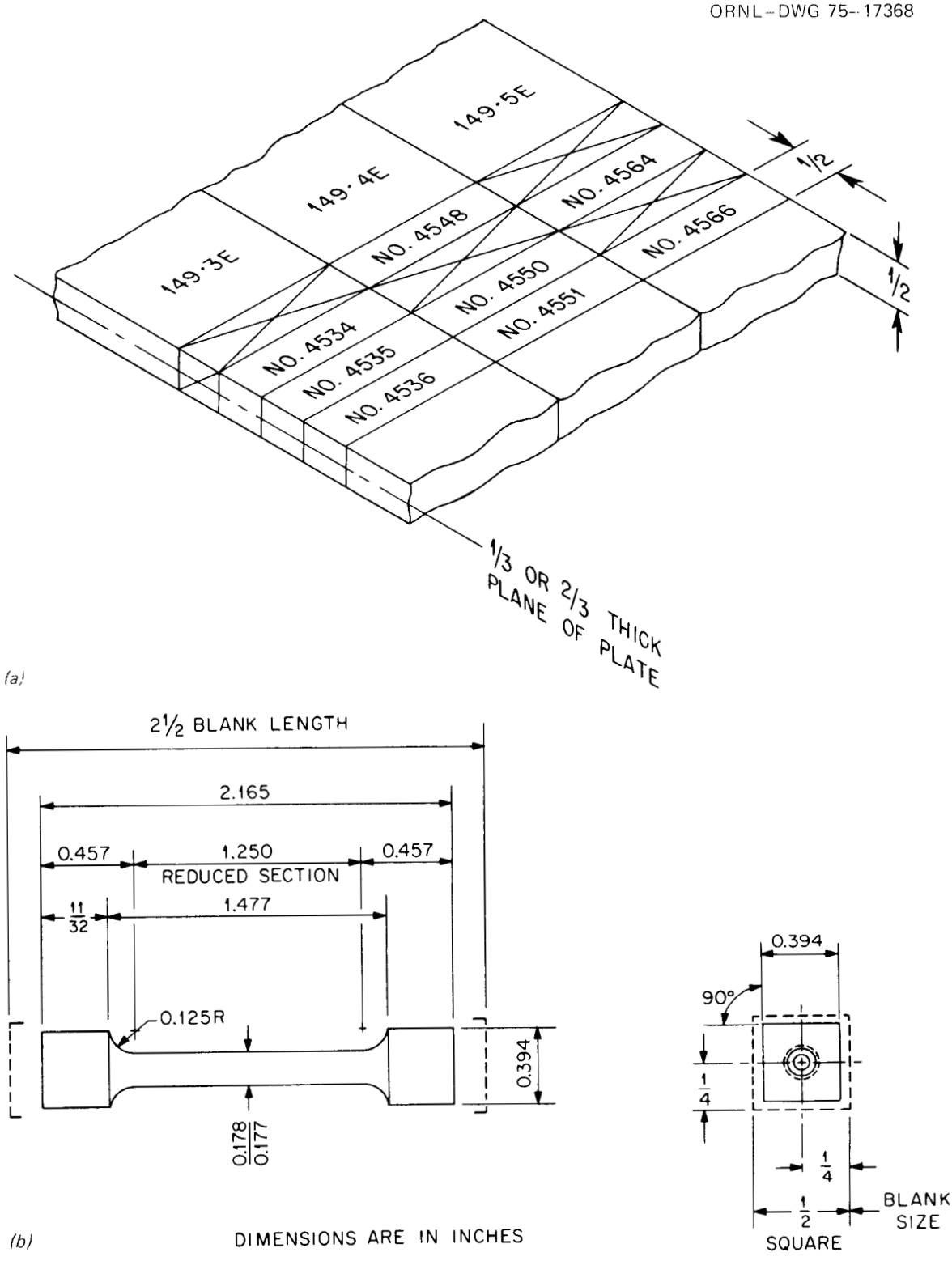


Fig. 2.1. (a) Cutting plan for test specimens. (b) Geometry of test specimen (1 in. = 25.4 mm).

and 537.8°C (1000°F). The particular temperatures picked were intended to maximize the data over a range where tensile properties were changing most rapidly with temperature. The strain rate used was 0.016/min, based on machine crosshead motion. Due to the high oxidation rate of carbon steel in air at elevated temperature, it was necessary to purge the specimens with an inert gas at temperatures exceeding 260°C (500°F). Strain measurements were made using an extensometer mounted on the shoulder of the specimen. The specimens as they appeared after testing are shown in Fig. 2.2, which also includes a standard untested specimen for comparison. The stress-strain results are included with other properties below.

### 2.1.2 Summary of Mechanical and Physical Properties

The required mechanical and physical properties of carbon steel and concrete were obtained from several sources, including the tests run at ORNL. The physical properties of ASTM A516 carbon steel at room temperature were taken from the ASM Materials Handbook,[9] and the temperature dependency of these properties as obtained from other sources was normalized to these room-temperature values. These reference room-temperature properties are given in Table 2.2.

For ferritic steels, density decreases approximately $1.9 \times 10^{-7}$ N/mm$^3$ (0.0007 lb/in.$^3$) per 62.5°C (100°F) increase in temperature.[10] This variation is shown numerically in Table 2.3 and graphically in Fig. 2.3.

Table 2.2. Room-temperature[a] physical properties of ASTM A516 carbon steel

| Property | Symbol | Value | |
|---|---|---|---|
| | | SI | English |
| Weight density | $\rho$ | $7.71 \times 10^4$ N/m$^3$ | 0.284 lb/in.$^3$ |
| Thermal conductivity | k | 46.73 W m$^{-1}$(°C)$^{-1}$ | 27 Btu hr$^{-1}$ft$^{-1}$(°F)$^{-1}$ |
| Coefficient of thermal expansion | $\alpha$ | $15.12 \times 10^{-6}$/°C | $8.4 \times 10^{-6}$/°F |
| Specific heat | c | 460 J kg$^{-1}$(°C)$^{-1}$ | 0.11 Btu lb$^{-1}$(°F)$^{-1}$ |

[a]RT = 21.1°C (70°F).

PHOTO 4367–75

Fig. 2.2. Posttest condition of tensile specimens used in generating required uniaxial, monotonic stress-strain curves.

The thermal expansion of carbon steel is essentially constant over the range of temperatures of interest;[9] therefore, the value as listed in Table 2.2 was used.

The thermal conductivity of ferritic steel (0.2 wt % carbon) is given graphically in Ref. 6 as being a linear function in temperature over the

Table 2.3. Temperature variation with weight density of ASTM A516 carbon steel

| Temperature [°C (°F)] | Density[a] (lb/in.$^3$) |
|---|---|
| 21.1 (70) | 0.2840 |
| 65.6 (150) | 0.2834 |
| 148.9 (300) | 0.2824 |
| 260.0 (500) | 0.2810 |
| 343.3 (650) | 0.2799 |
| 426.7 (800) | 0.2789 |
| 482.2 (900) | 0.2782 |
| 537.8 (1000) | 0.2775 |

[a]1 lb/in.$^3$ = $2.71 \times 10^{-4}$ N/mm$^3$.

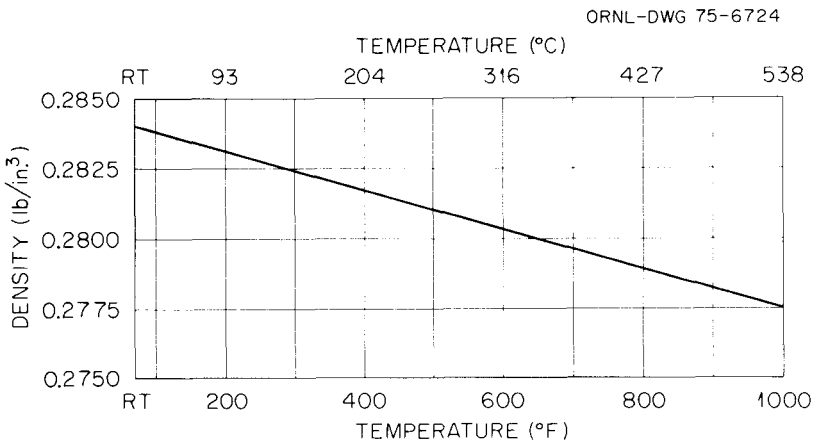


Fig. 2.3. Density vs temperature for carbon steel (nominal 0.2 wt % C).

range RT to 815.6°C (1500°F). This curve can be adequately described by

$$k = 351.119 - 0.08741T \text{ [Btu ft}^{-2}\text{in.}^{-1}\text{hr}^{-1}(°\text{F})^{-1}] ,$$

where T is temperature (°F). Normalizing this equation to the RT value of k in Table 2.2 yields

$$k = 27.5099 - 0.0073T \text{ [Btu ft}^{-2}\text{ft}^{-1}\text{hr}^{-1}(°\text{F})^{-1} \text{ or Btu ft}^{-1}\text{hr}^{-1}(°\text{F})^{-1}] .$$

This variation is shown graphically in Fig. 2.4.

The specific heat for the type of carbon steel being considered is given only at 21.1°C (70°F) in both Refs. 9 and 10. An alternate source is the Nuclear Systems Materials Handbook,[6] although values are given only to 426.7°C (800°F). A straight-line extrapolation was thus used to 537.8°C (1000°F), and the resulting curve was normalized to the value of specific heat given in Table 2.2. The results are shown in Fig. 2.5.

The elastic modulus of carbon steel was taken from Ref. 6 rather than from the tensile tests, because the sensitivity of the particular elongation transducer was not great enough to yield acceptable properties at very small (elastic) strains. The values used are given in Table 2.4 and shown graphically in Fig. 2.6. The experimental stress-strain curves were

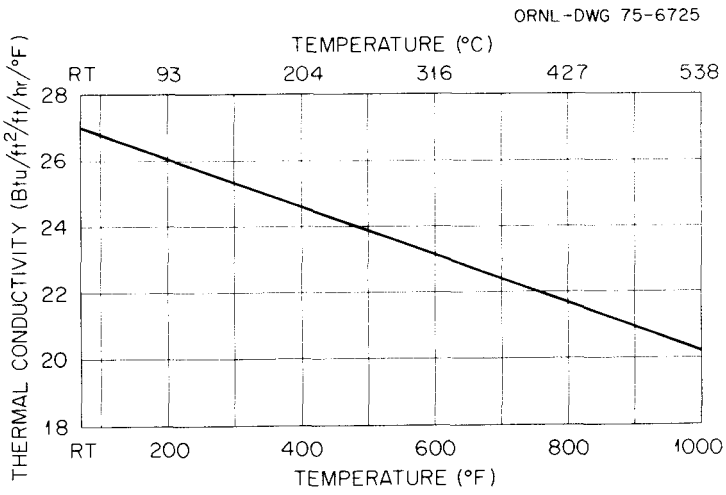


Fig. 2.4. Thermal conductivity vs temperature for carbon steel (nominal 0.2 wt % C). [1 Btu $ft^{-2}hr^{-1}ft^{-1}(°F)^{-1}$ = 1.73 W $m^{-1}(°C)^{-1}$.]

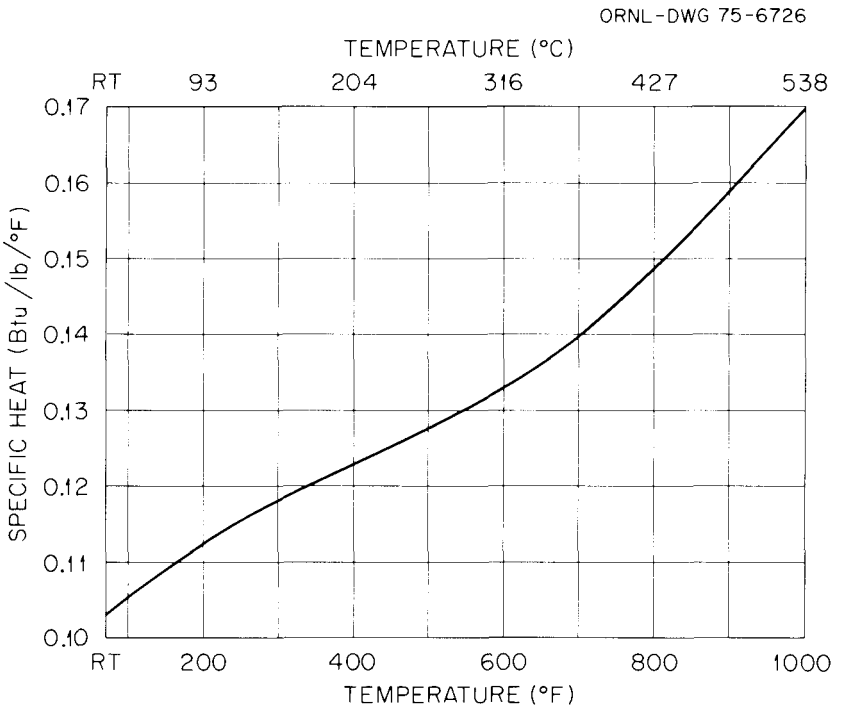


Fig. 2.5. Specific heat vs temperature for ASTM A516 carbon steel. [1 Btu $lb^{-1}(°F)^{-1} = 4.186 \times 10^3$ J $kg^{-1}(°C)^{-1}$.]

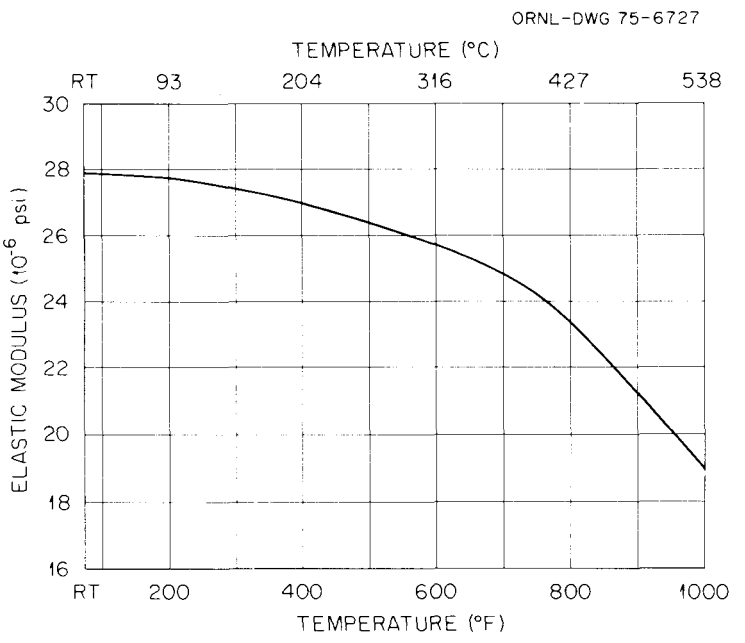


Fig. 2.6. Elastic modulus vs temperature for medium carbon steel. ($1 \times 10^{-6}$ psi = $0.6895 \times 10^{-4}$ MPa.)

Table 2.4. Modulus of elasticity for medium carbon steel

| Temperature | | Modulus | |
|---|---|---|---|
| °C | °F | MPa × $10^{-4}$ | psi × $10^{-6}$ |
| 21.1 | RT | 19.2 | 27.9 |
| 37.8 | 100 | 19.2 | 27.9 |
| 93.3 | 200 | 19.0 | 27.7 |
| 148.9 | 300 | 18.8 | 27.4 |
| 204.4 | 400 | 18.6 | 27.0 |
| 232.2 | 450 | 18.4 | 26.7 |
| 260.0 | 500 | 18.2 | 26.4 |
| 287.8 | 550 | 17.9 | 26.1 |
| 315.6 | 600 | 17.7 | 25.7 |
| 343.3 | 650 | 17.4 | 25.3 |
| 371.1 | 700 | 17.1 | 24.8 |
| 398.9 | 750 | 16.6 | 24.2 |
| 426.7 | 800 | 16.1 | 23.4 |
| 482.2 | 900 | 14.6 | 21.2 |
| 537.8 | 1000 | 12.7 | 18.5 |

modified to match these values of modulus by subtracting the experimentally determined elastic strain from the experimental curve and adding back an elastic strain component based on the reference moduli. The resulting stress-strain curves are shown in Figs. 2.7 to 2.14. Figure 2.15 is a composite of all the stress-strain curves for comparison. The curves were constructed out to 10% strain, since it was expected that this would be well beyond the maximum strains calculated in the inelastic analysis.

As can be observed, the curves are consistent with one another with respect to temperature behavior. The upper and lower yield points conventionally associated with carbon steel disappeared at temperatures in excess of 260°C (500°F). For use in the inelastic analysis, these curves

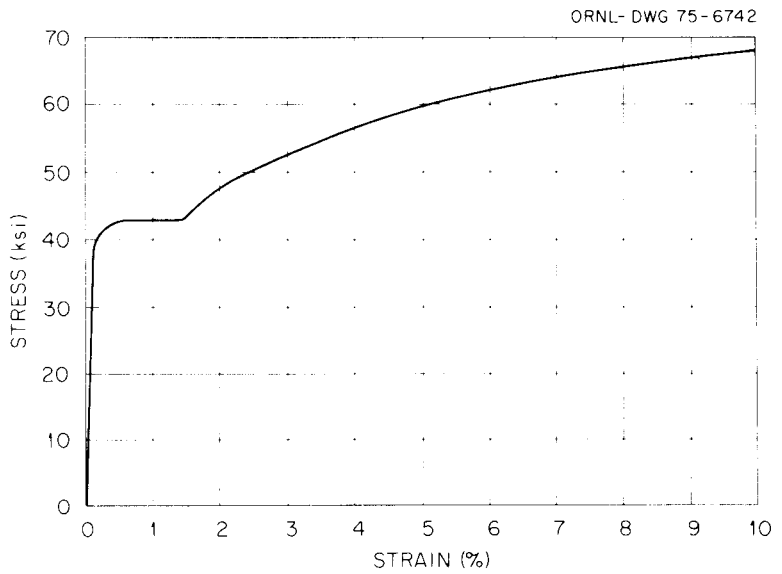


Fig. 2.7. Stress-strain curve for ASTM A212B carbon steel at room temperature. (1 ksi = 6.895 MPa.)

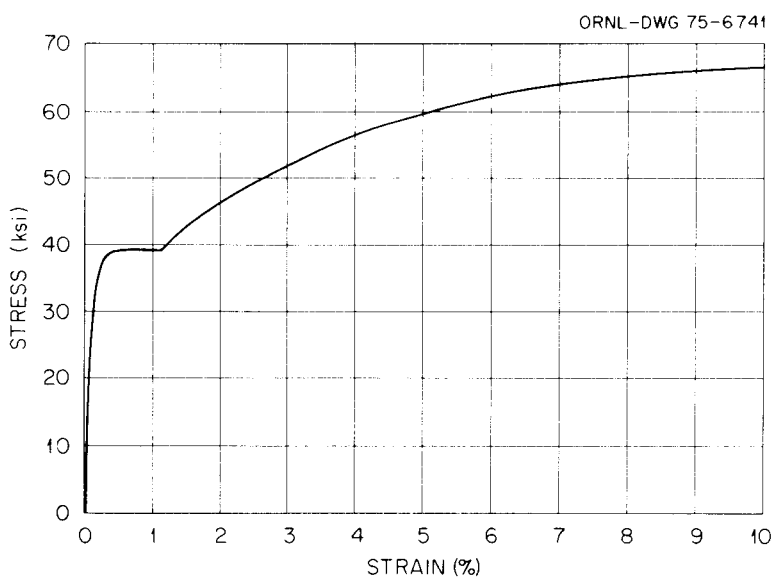


Fig. 2.8. Stress-strain curve for ASTM A212B carbon steel at 66°C (150°F). (1 ksi = 6.895 MPa.)

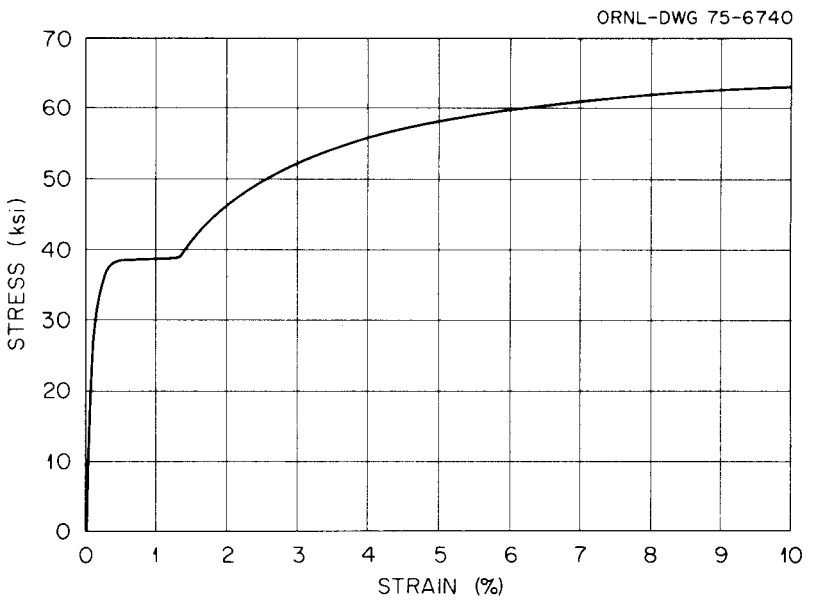


Fig. 2.9. Stress-strain curve for ASTM A212B carbon steel at 149°C (300°F). (1 ksi = 6.895 MPa.)

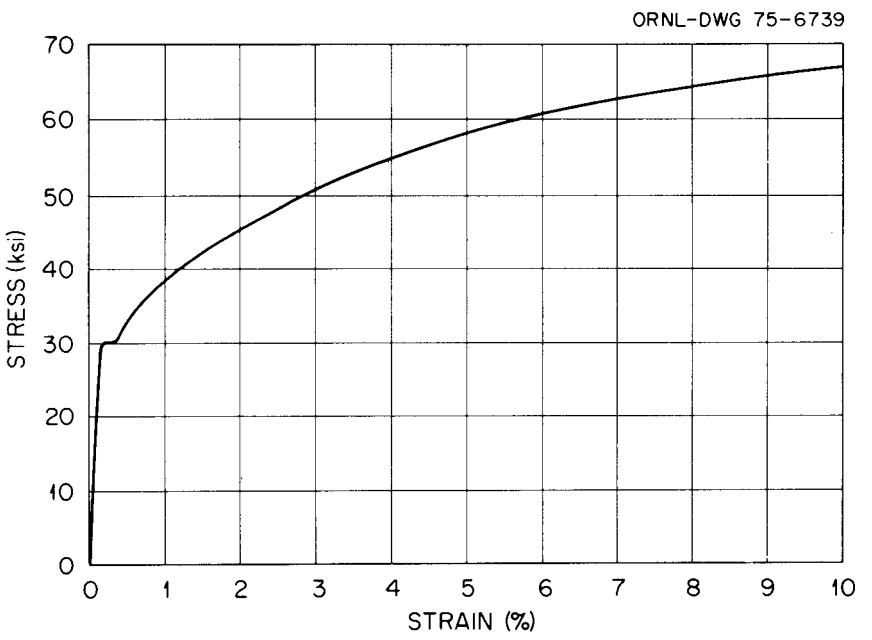


Fig. 2.10. Stress-strain curve for ASTM A212B carbon steel at 260°C (500°F). (1 ksi = 6.895 MPa.)

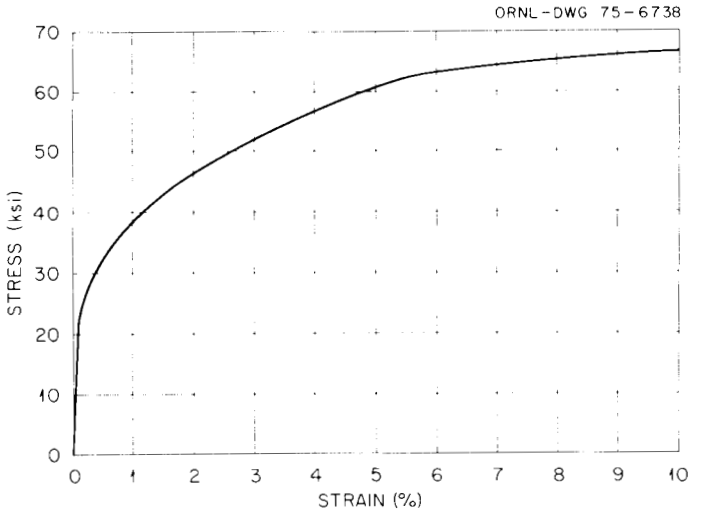


Fig. 2.11. Stress-strain curve for ASTM A212B carbon steel at 343°C (650°F). (1 ksi = 6.895 MPa.)

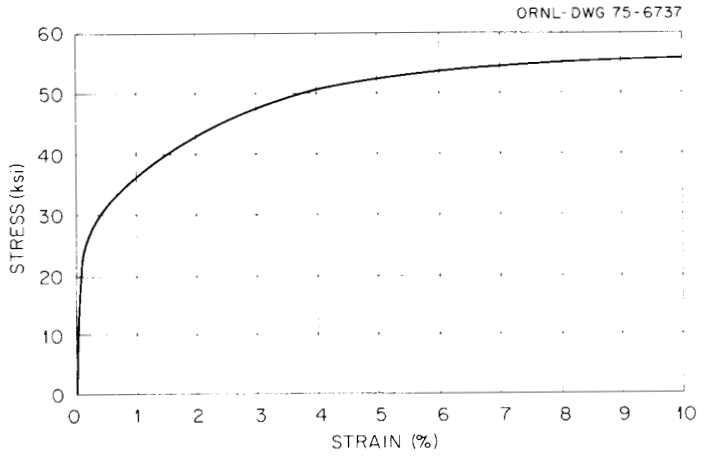


Fig. 2.12. Stress-strain curve for ASTM A212B carbon steel at 427°C (800°F). (1 ksi = 6.895 MPa.)

were represented by a bilinear fit out to approximately 1% strain. This bilinear fit is discussed in greater detail in Chapter 4.

A review of the literature indicated a wide variation in the properties of concrete, depending on temperature, moisture content, aggregate type, and age. Also, there does not seem to be a great deal of data on the mechanical and physical properties of a given concrete mix over the

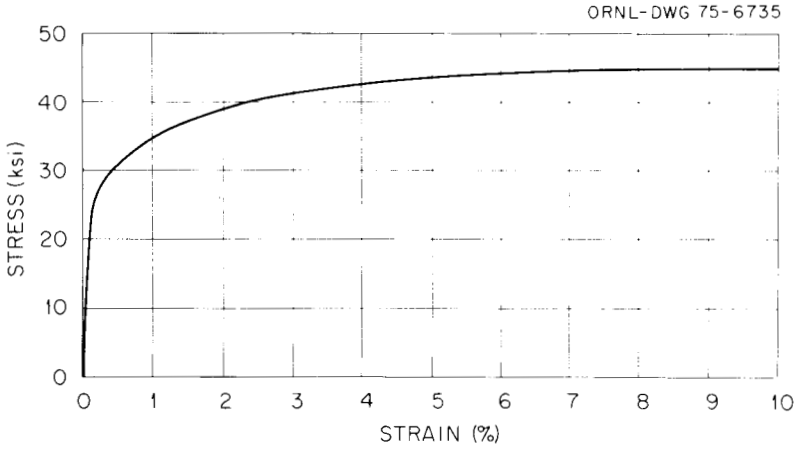


Fig. 2.13. Stress-strain curve for ASTM A212B carbon steel at 482°C (900°F). (1 ksi = 6.895 MPa.)

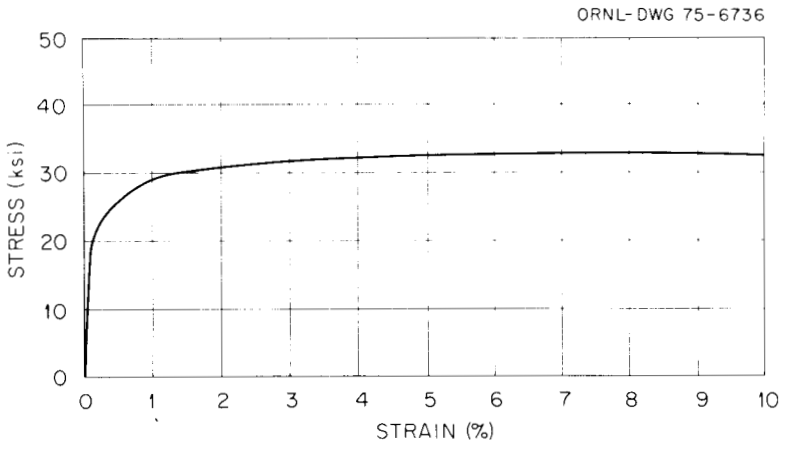


Fig. 2.14. Stress-strain curve for ASTM A212B carbon steel at 538°C (1000°F). (1 ksi = 6.895 MPa.)

temperature range of interest. Thus, it was necessary to "patch" together the work of different researchers to provide the set of data required.

The room-temperature mechanical properties of concrete were based on a particular mix that is being used at ORNL in the study of gas-cooled reactor containment vessels.[11] The RT density, also for the ORNL mix, was taken from Ref. 12. These properties are listed in Table 2.5. The modulus of elasticity vs temperature data were taken from a review paper by Benjamin[13] and were normalized to the RT value shown in Table 2.5. The results, elastic modulus vs temperature, are shown in Fig. 2.16.

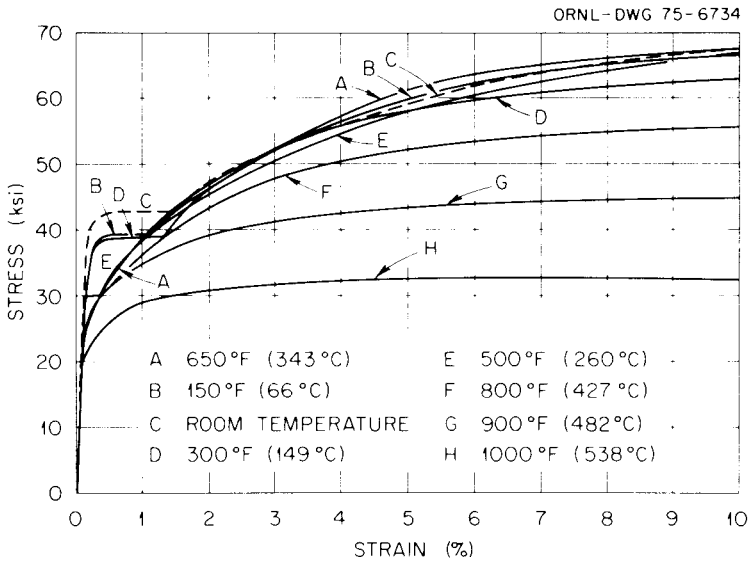


Fig. 2.15. Stress-strain curves for ASTM A212B carbon steel. (1 ksi = 6.895 MPa.)

Table 2.5. Room-temperature properties of concrete

| Property | Value | |
|---|---|---|
| | SI | English |
| Elastic modulus | $3.7 \times 10^4$ MPa | $5.4 \times 10^6$ lb/in.$^2$ |
| Poisson's ratio | 0.26 | 0.26 |
| Ultimate strength | 61.78 MPa | 8960 lb/in.$^2$ |
| Density | $2.641 \times 10^4$ N/m$^3$ | 168.1 lb/ft$^3$ |

No data were available on thermal expansion for the ORNL standard mix. Values of thermal expansion were found in Ref. 14 for a cement-limestone mixture similar in composition to the ORNL mix; these data are shown in Fig. 2.17.

Reference values of density vs temperature were not found in the sources used. Density was thus calculated based on the thermal expansion data. An approximate equation was used that neglected higher order terms.

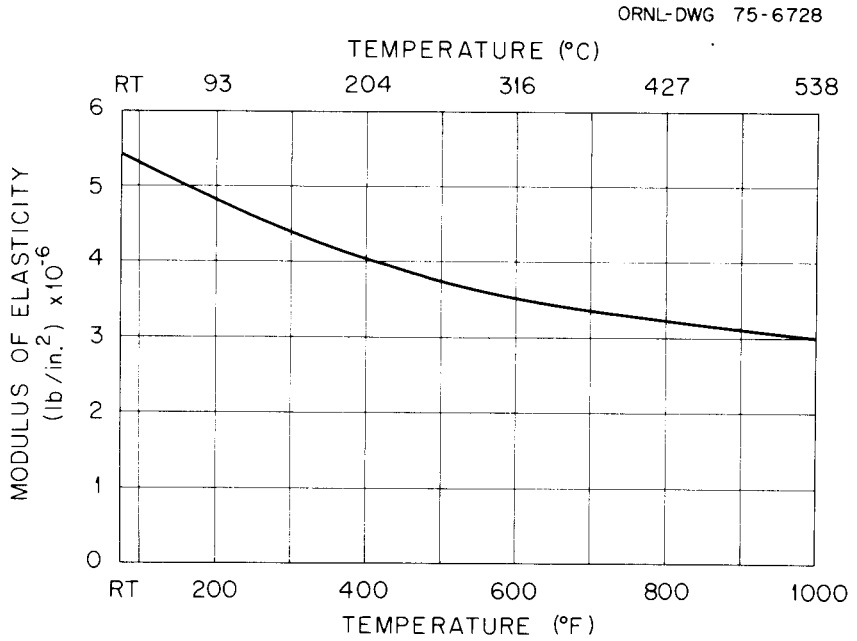


Fig. 2.16. Elastic modulus vs temperature for concrete. ($1 \times 10^{-6}$ psi = $0.6895 \times 10^{-4}$ MPa.)

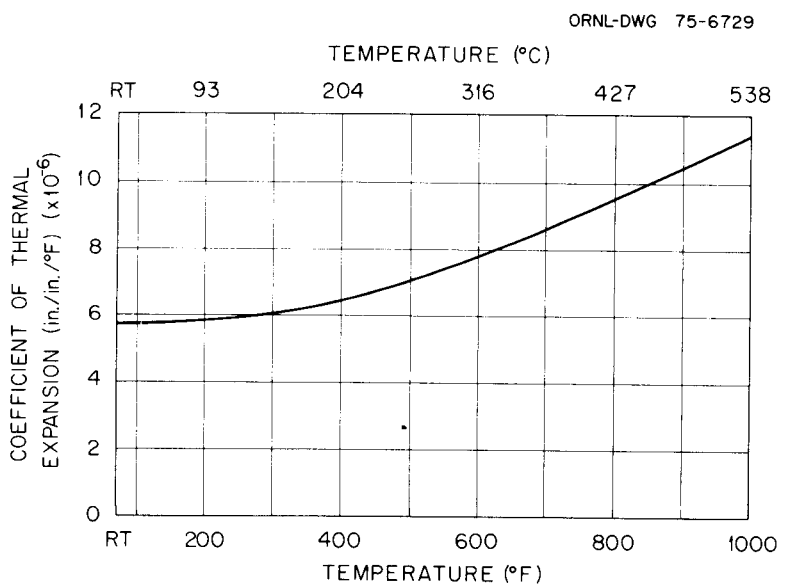


Fig. 2.17. Coefficient of thermal expansion vs temperature for concrete. [1 in. in.$^{-1}$(°F)$^{-1}$ = 1.8 mm$^{-1}$(°C)$^{-1}$.]

The equation, which is simply based on an expansion of volume increase–density relationship, is

$$\Delta\rho = -\rho_{RT} \frac{3\alpha\ \Delta T}{1 + 3\alpha\ \Delta T} ,$$

where

$\rho$ = density (RT is room-temperature reference),

$\alpha$ = coefficient of thermal expansion,

$\Delta T$ = temperature change (°F) from the reference temperature.

The change of density with increasing temperature is shown in Table 2.6 and in Fig. 2.18.

The values for thermal conductivity were taken from the work of Harada et al.[14] with a cross check from work by Crispino.[15] Harada presents thermal conductivity vs temperature up to 700°C (1292°F) for a number of concrete-aggregate type mixes, none of which include limestone. Crispino presents data for a limestone aggregate concrete but only up to 220°C (428°F). The Crispino results were used as a guide in choosing a thermal conductivity vs temperature curve from the Harada data that would represent the low-temperature behavior of a concrete-limestone mix. The results are shown in Fig. 2.19.

Table 2.6. Calculated change of density of concrete with temperature

| Temperature (°F) | Density | |
|---|---|---|
| | $N/m^3 \times 10^4$ | $lb/in.^3$ |
| RT | 2.641 | 0.0973 |
| 200 | 2.636 | 0.0971 |
| 400 | 2.625 | 0.0967 |
| 600 | 2.614 | 0.0963 |
| 800 | 2.600 | 0.0958 |
| 1000 | 2.584 | 0.0952 |

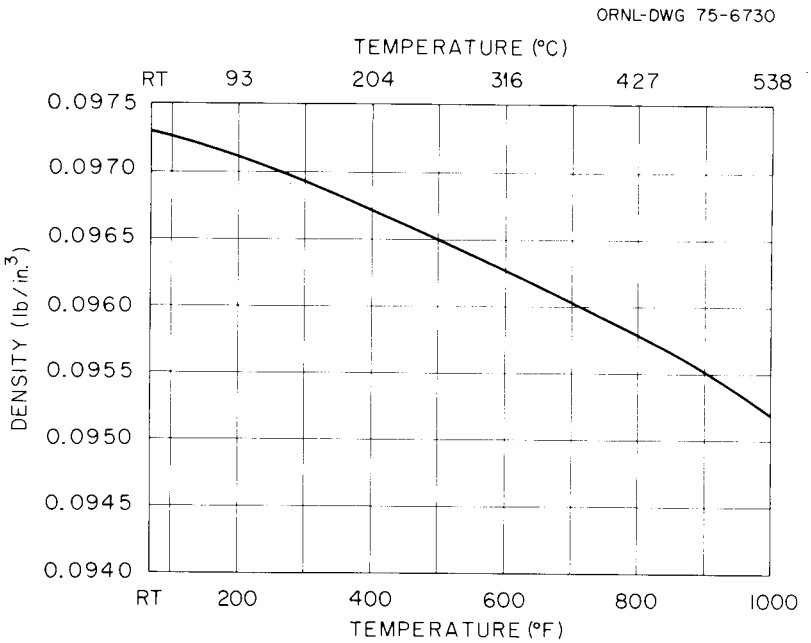


Fig. 2.18. Density vs temperature for concrete. [1 lb in.$^{-3}$ = $2.71 \times 10^{-4}$ N(mm)$^{-3}$.]

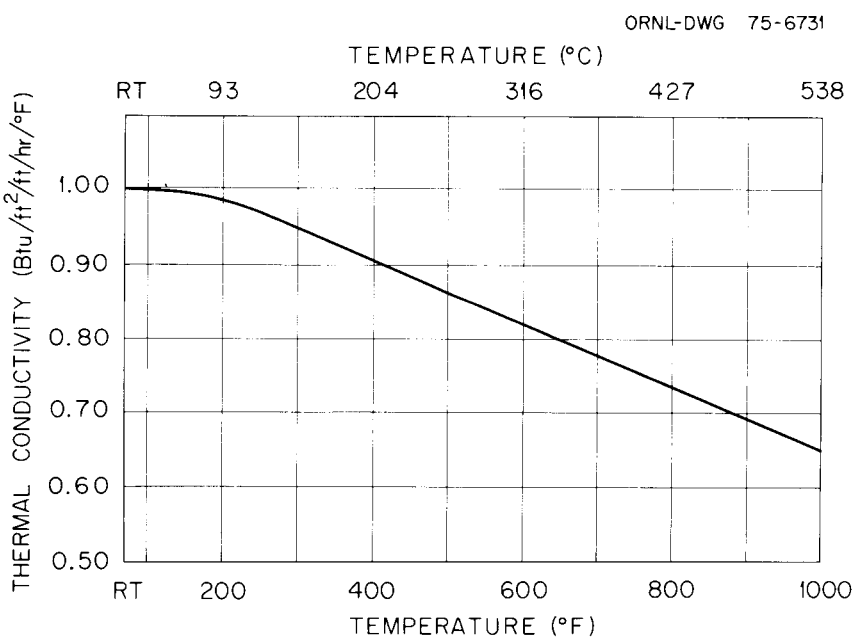


Fig. 2.19. Thermal conductivity vs temperature for concrete. [1 Btu ft$^{-2}$hr$^{-1}$ft$^{-1}$(°F)$^{-1}$ = 1.73 W m$^{-1}$(°C)$^{-1}$.]

Values of specific heat of concrete were not given in the references consulted. However, diffusivity values were given in Ref. 14, such that specific heat could be calculated:

$$a = \frac{k}{c\rho} ,$$

where

$a$ = diffusivity,

$k$ = thermal conductivity,

$c$ = specific heat,

$\rho$ = density.

Values of specific heat vs temperature were calculated by using the values of density and thermal conductivity in Figs. 2.18 and 2.19, respectively, with the diffusivity values from Ref. 10 (Fig. 2.20). These are tabulated in Table 2.7 and are shown graphically in Fig. 2.21.

The information on the mechanical and physical properties of carbon steel and concrete was supplied to Swanson Engineering Associates for use

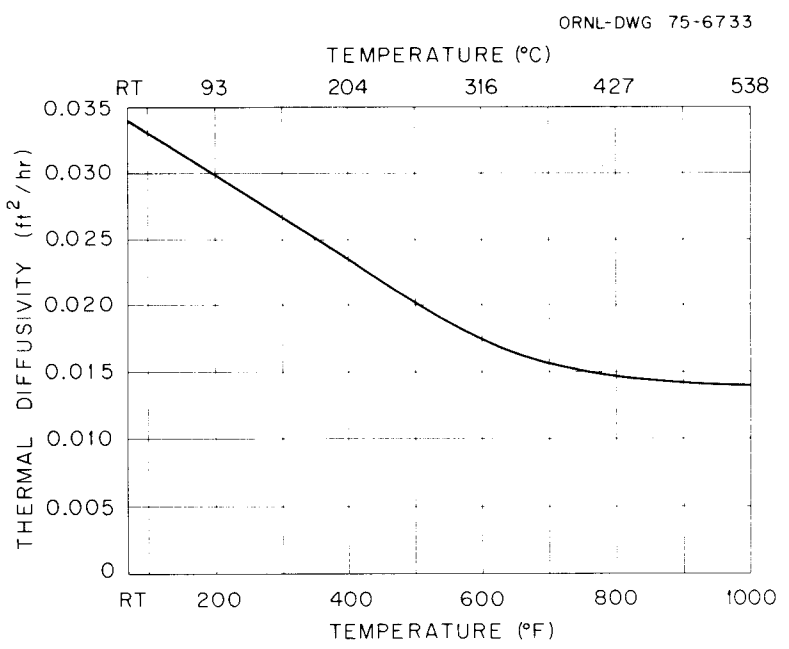


Fig. 2.20. Thermal diffusivity vs temperature for concrete. (1 $ft^2hr^{-1}$ = 0.0929 $m^2hr^{-1}$.)

Table 2.7. Summary of calculations for specific heat of concrete[a]

| Temperature [°C (°F)] | ρ (lb/in.$^3$) | k [Btu ft$^{-1}$hr$^{-1}$ft$^{-2}$(°F)$^{-1}$] | a (ft$^2$/hr) | c [Btu lb$^{-1}$(°F)$^{-1}$] |
|---|---|---|---|---|
| RT (RT) | 0.0973 | 1.000 | 0.0340 | 0.175 |
| 193.3 (200) | 0.0971 | 0.985 | 0.0298 | 0.197 |
| 204.4 (400) | 0.0967 | 0.905 | 0.0235 | 0.230 |
| 315.6 (600) | 0.0963 | 0.820 | 0.0175 | 0.282 |
| 426.7 (800) | 0.0958 | 0.735 | 0.0147 | 0.302 |
| 537.8 (1000) | 0.0952 | 0.650 | 0.0140 | 0.282 |

[a]1 lb/in.$^3$ = 2.71 × 10$^{-4}$ N/mm$^3$; 1 Btu ft$^{-1}$hr$^{-1}$ft$^{-2}$(°F)$^{-1}$ = 1.73 W m$^{-1}$(°C)$^{-1}$; 1 ft$^2$/hr = 0.0929 m$^2$/hr; 1 Btu lb$^{-1}$(°F)$^{-1}$ = 4.186 × 10$^3$ J kg$^{-1}$(°C)$^{-1}$.

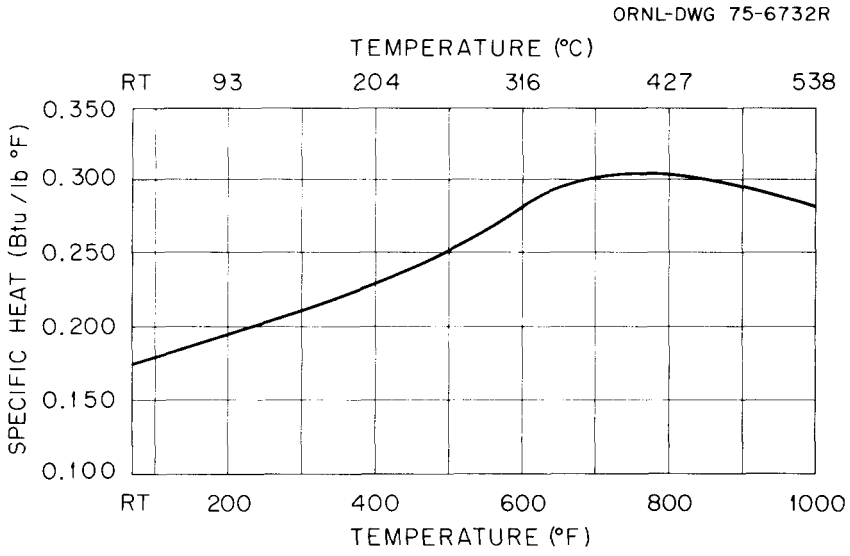


Fig. 2.21. Specific heat vs temperature for concrete. [1 Btu lb$^{-1}$(°F)$^{-1}$ = 4.186 × 10$^3$ J/kg-°C.]

in the thermal-inelastic analyses of a segment of an idealized LMFBR cell liner. The results of these analyses are discussed in Chapter 4.

## 2.2 Review of Literature on High-Temperature Behavior of Concrete

The compilation of material properties as discussed above indicated the wide variability in concrete behavior with changes in temperature,

moisture content, etc. Thus, it was concluded that a more extensive review of the high-temperature properties of concrete was warranted. The purposes of such a review would be to provide:

1. a more complete listing of references on the high-temperature properties of concrete,
2. a comparison of existing data on a consistent basis,
3. guidelines to be used in planning the essential elements of near-term and long-range programs to investigate LMFBR cell liner behavior.

This review was conducted by Dr. Zdeněk Bažant, Professor of Civil Engineering at Northwestern University. A summary of the section of his report devoted to the literature review follows. The interested reader is referred to Appendix I for the complete report, including an extensive bibliography.

### 2.2.1 Physical and Chemical Changes

A number of physical and chemical changes occur in concrete with increasing temperature. The most drastic of these is the complete structural disintegration of ordinary Portland Cement concrete at temperatures exceeding 1000°C (1832°F).

Loss of water, either evaporable (free) or chemically bound, is one of the most important mechanisms for changes in concrete. At room temperature, 50 vol % of saturated cement paste and 2 to 10 vol % of saturated structural concrete is evaporable water. Beyond 100°C (212°F), the loss of the free water is rapid and, given sufficient time, will become complete at temperatures beyond 105°C (221°F).

Additionally significant is the loss of chemically bound water through dehydration. This loss may be accompanied by chemical changes in the cement paste or aggregate that affect the physical or mechanical properties of the structural concrete. Dehydration begins at about 120°C (248°F) and may continue up to 850°C (1562°F), depending upon the constituent undergoing change. Due to the dehydration, porosity and microcracking grow with temperature and at 850°C (1562°F) may exceed by 40% that at 120°C (248°F). In addition, the mass density of the constituent grows, whereas

that of the gross structural concrete decreases. The average pore size also increases and is essentially preserved even after cooling.

One of the most important chemical changes occurring in aggregates is in quartz, which has a phase transformation between 500°C (932°F) and 650°C (1202°F) that is accompanied by a volume increase. Other irreversible changes, such as the release of $CO_2$ from carbonate rocks, can occur.

### 2.2.2 Thermal Expansion and Shrinkage

The thermal expansion characteristics of concrete are the result of the behavior of each of the individual mix constituents. Cement paste expands slowly up to 100°C (212°F), remains essentially stable in the range 100 to 300°C (212 to 572°F), and contracts rapidly beyond 300°C (572°F). The contraction is caused by dehydration, as discussed in Subsection 2.2.1. Aggregates always expand, although different aggregates behave differently. Quartz and siliceous rock generally display the largest expansion, whereas artificial aggregates expand very little and generally display the largest degree of stability (chemical changes, change in weight, etc.). This difference in thermal expansion between the paste and aggregate undoubtedly causes internal stresses that contribute to the decrease in strength with increasing temperature.

The thermal expansion of concrete is not fully reversible on cooling, owing to chemical changes, microstructural changes, free water loss, etc. Thermal expansion without moisture loss is of greatest significance to concrete nuclear reactor structures, since the concrete walls are so thick that no significant amount of moisture can be lost to the environment in a reasonable time.

### 2.2.3 Pore Pressure

Heating of concrete can produce very large pore pressures within the material, as evidenced by explosive spalling of heated concrete in specimens that have not had time to adequately dry. Presently, there is no method of predicting pore pressures and very little experimental data, particularly at temperatures beyond 100°C (212°F), to permit an assessment

of this phenomenon. This is a very complex problem and should be investigated further under conditions more reflective of a sodium spill.

### 2.2.4 Strength, Ductility, and Stress-Strain Diagrams

The strength properties of concrete are well documented, but the data are generally on material for which the moisture content has been reduced to the equilibrium value for a given temperature at atmospheric pressure. Such data are not necessarily representative of a large concrete reactor structure with massive sections. The strength of concrete decreases with increasing temperature, with tensile strength being reduced more drastically than compressive strength. This loss of strength is marked above 450°C (842°F), with the strength at 850°F (1562°F) being 10 to 20% of the cold value. In conjunction with a strength reduction, there is a moderate increase in ductility and a decrease in tangent modulus.

The reduction in strength is partly due to the incompatibility of thermal expansions of the aggregates and cement paste. The increase in porosity with increasing temperature also contributes to strength loss, as evidenced by the fact that the strength of dried concrete is greater than that of wet if the drying rate was slow enough to prevent microcracking. On cooling from a higher temperature, the residual strength is generally lower than at the higher temperature due to cracking on cooling.

The duration of exposure to temperature has no appreciable effect on strength, although the heating rate in reaching this temperature may. The heating rate effect is very complicated; for a more extensive discussion, the reader is referred to Appendix I.

It is noted that the loss of concrete strength at high temperature is much smaller when the concrete is restrained from freely expanding. Such restraint prevents microcracking. The large thicknesses of reactor structures could provide such restraint.

### 2.2.5 Modulus of Elasticity and Poisson Ratio

The elastic modulus E and the shear modulus G decrease with increasing temperature, primarily due to breaking of bonds in the microstructure of the cement paste. The modulus is dependent on the drying rate since, as has been discussed previously, fast rates of drying cause proportionally

more damage to the microstructure than slow rates. In addition, the rate of heating causes variation in E due to difference in thermal stresses, pore pressure, stresses due to shrinkage, etc.

The type of aggregate used in the mix also influences the value of elastic modulus. Aggregates such as limestone, which are more compatible and more chemically stable, cause a smaller drop in modulus with increasing temperature. Observations of Poisson's ratio $\nu$ indicate a decrease with increasing temperature, probably due to microcracks developed during heating.

### 2.2.6 Creep

Creep in concrete is present at all temperatures and seems to be a diffusion process. An increase in temperature accelerates the diffusion of solid components and water in the cement paste along gaps between particles. Such a process should obey an activation energy model. For a more in-depth discussion of modeling of creep behavior of concrete, the reader is referred to Section 6.2 of Appendix I.

Temperature, temperature changes, moisture migration, and moisture content all affect the creep behavior of concrete. Higher temperature, as well as changes in temperature, cause an acceleration of creep. Higher moisture content provides the environment for increased diffusion and thus increased creep rate. Creep is also higher when moisture movement is present, and the migration of moisture will be different in massive concrete structures than in test specimens. This implies different behavior under load and temperature, but the procedure for testing meaningful specimens is as yet unclear.

### 2.2.7 Heat Capacity

The specific heat $c_p$ of bulk concrete is a complex phenomenon that depends on chemical and structural changes in the material, changes in the binding energy of water, phase changes of water, and changes in moisture content. The apparent specific heat of cement paste rises with temperature to 500°C (932°F) and then declines to 1000°C (1832°F). However, for bulk concrete, specific heat seems to be dominated by the characteristics of the aggregate. The specific heat of most aggregates increases

smoothly up to about 900°C (1652°F). Thus, bulk concrete will show a trend similar to the specific aggregate used.

### 2.2.8 Thermal Conductivity and Diffusivity

The thermal conductivity of bulk concrete is a rather complex combination of the thermal conductivities of its individual constituents. Thermal conductivities for aggregates vary. That of crystalline rocks decreases with temperature up to 1000°C (1832°F); that of amorphous rocks is much lower and remains essentially constant. The thermal conductivity of cement paste, as well as that of bulk concrete, generally decreases with temperature. The presence of moisture increases thermal conductivity such that conductivity decreases as concrete dries.

Thermal diffusivity displays temperature dependency similar to that of conductivity. Thermal diffusivity can be determined as the product of specific heat and thermal conductivity, although it can be measured experimentally with reasonable ease.

### 2.2.9 Moisture Conductivity and Diffusivity

The transfer of moisture in cement paste and uncracked concrete is very slow at moderate temperatures. This transfer increases with increasing temperature, and, above 100°C (212°F), drying times become an order of magnitude shorter. This large increase in drying rate is probably due to migration of moisture in the vaporized state. However, little data are available above 100°C (212°F) to permit an assessment of the mechanisms involved or prediction of moisture conductivity and diffusivity.

A temperature gradient, in addition to an elevation in temperature, causes moisture migration. However, this phenomenon has received only limited study.

### 2.2.10 Explosive Thermal Spalling

Explosive thermal spalling is a phenomenon that may result from the rapid application of a high temperature to a localized area of the surface of a concrete structure that was initially at a lower temperature. It is

characterized by the rather violent rupture of the surface and the material directly beneath the surface. Two different explanations have been advanced as to the cause of explosive spalling.

1. Localized sudden heating of a wall may cause thermal expansion, large thermal stresses due to the restraint of the surrounding cooler structure, and failure by crushing.

2. Very high steam pressure due to the localized heating is produced just under the surface of the concrete. There is no resisting compressive thermal stress normal to the surface so that material is literally blown out of the surface.

While it is unclear which hypothesis is correct, it has been observed that high restraint promotes spalling (supports item 1) and higher moisture content promotes spalling (supports item 2). Probably both mechanisms contribute.

It is uncertain whether or not explosive spalling will be a problem for concrete reactor structures. Experiments indicate that spalling is less likely to occur in thick structures, yet the high heating rates that would be encountered in a sodium spill should promote spalling. Obviously, this is an area needing further clarification.

### 2.2.11 Reinforcing and Prestressing Steels

This subsection is included primarily as a flag. Consideration should be given to the consequences of exposure of the prestressing or reinforcing steel to high temperature for prolonged periods of time. Such steels normally have a sharp drop in yield strength at the temperatures of concern. Additionally, for prolonged load durations, creep could be significant. The behavior of these steels should be considered in analyzing the structural behavior during a sodium spill.

# 3. BOUNDING-VALUE ASSESSMENT OF THE EFFECT OF THE SODIUM-CONCRETE REACTION ON LMFBR CELL LINER INTEGRITY

## 3.1 Introduction

A spill of high-temperature sodium on an initially flawed or cracked LMFBR cell liner or on a liner that develops a crack as a result of the spill could precipitate a sodium-concrete reaction that would generate high temperatures and pressures. These events could, in turn, lead to gross structural failure of the liner.

The purpose of the work described here was to establish bounding values regarding the energy release and the temperature and pressure buildup resulting from the sodium-concrete reaction, and to assess, in a gross way, the maximum resultant effect on the structural behavior of the liner.

LMFBR equipment cell liners might take a variety of geometric forms. For some parts of the present study, it was convenient to have some specific geometry in mind. Figure 3.1 shows the model geometry used in this study. This geometry was chosen, since it represents a simplified form of a structural test that has been proposed to study sodium spill conditions. (This was discussed briefly in Chapter 1.) In this test, the air

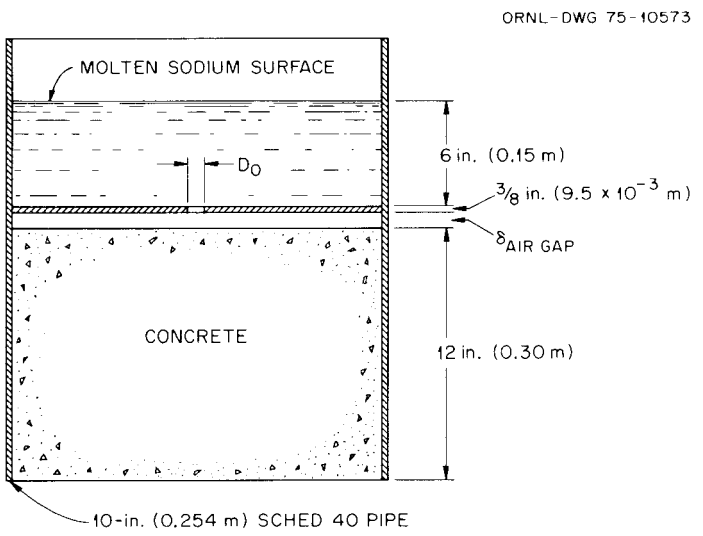


Fig. 3.1. Simplified geometry of segment of cell liner wall used in sodium-concrete reaction calculations.

gap and the orifice diameter can be varied to study the effect of these parameters on both the structural behavior of the specimen and the characteristics of the sodium-concrete reaction when high-temperature sodium is spilled into the upper chamber of the container.

## 3.2 Energy Release

The first topic considered in the present investigation is the magnitude of the energy released by the sodium-concrete reaction and the maximum possible effect of that energy if it were all converted into structural deformation. The energy release due to the reaction of sodium with concrete is very uncertain and varies with the type of concrete, moisture content, etc. The heat release for ordinary concrete is estimated by Ref. 16 to be $1.128 \times 10^6$ J/kg (485 Btu/lb) of concrete. On this basis, the energy release per cubic yard of concrete is $2.2 \times 10^6$ Btu or $2.3 \times 10^9$ J. If this amount of energy were released slowly it would be equivalent to 183 lb of burning coal; if it were released instantly it would be equivalent to 1100 lb of TNT.* These comparisons are intended only to give a gross intuitive feel for the range of structural damage that might result from the sodium-concrete reaction.

If we consider a test assembly containing a 0.305-m (1-ft) depth of concrete in a 0.25-m-diam (10-in.) sched-40 pipe (Fig. 3.1), the energy release would be 44,500 Btu, $4.7 \times 10^7$ J, or 22 lb of TNT. Further indication of the maximum structural damage possible in the test assembly can be obtained by calculating the deflection and stress in a 0.25-m-diam (10-in.) by 0.95-cm-thick (3/8-in.) steel liner plate clamped at the edge and subjected to a uniform pressure load. If the entire energy release of $4.7 \times 10^7$ J ($4.5 \times 10^4$ Btu) were converted to mechanical energy and applied to the plate, a small deflection elastic calculation gives a center deflection of 1.5 m (59 in.) and a maximum stress of 496,000 MPa ($72 \times 10^6$ psi). While a simple elastic calculation is obviously not valid at such a large deflection and stress, it does indicate that the elastic limit of the plate is exceeded by a large margin; therefore, gross inelastic deformation of the plate would occur.

---

*Based on an energy content of 12,000 Btu/lb for coal and 1,990 Btu/lb for TNT.

Thus, we conclude that sufficient energy is released by the sodium-concrete reaction to cause gross deformation of the liner. It remains to be determined whether any mechanism exists for conversion of thermal energy of reaction into mechanical energy of liner deformation.

### 3.3 Temperature Buildup Due to Reaction

This section considers the maximum temperature buildup which could occur as a result of the reaction between sodium and concrete in order to determine whether this temperature buildup is sufficient to significantly weaken the liner or to cause significant thermal stress (besides the thermal stress caused by direct heating of the liner by the hot sodium).

The liner plate may be heated from the outside by the heat of reaction of the sodium-concrete reaction. At the same time, the plate is in contact with sodium on the inside, which should tend to limit its temperature rise.

The maximum heat flux due to the sodium-concrete reaction is estimated in Ref. 5 to be $3.15 \times 10^4$ W/m$^2$ ($10^4$ Btu hr$^{-1}$ft$^{-2}$) for magnetite concrete. Since no corresponding estimate is given for ordinary concrete, the value for magnetite concrete will be used here.

For natural convection heat transfer between two plates with a fluid between them, Globe and Dropkin[17] give the equation

$$Nu = 0.069\ Ra^{1/3}\ Pr^{0.074}\ ,$$

where Nu is the Nusselt number, Ra is the Rayleigh number, and Pr is the Prandtl number of the fluid. For heat transfer between a single plate and a bulk fluid, we then take the Nusselt number to be twice as high:

$$Nu = 0.138\ Ra^{1/3}\ Pr^{0.074}\ .$$

Assuming that all the heat of reaction flows across the plate and into the sodium pool, we find a heat transfer coefficient of 17,500 W m$^{-2}$(°K)$^{-1}$ [3100 Btu hr$^{-1}$ft$^{-2}$(°F)$^{-1}$] and a maximum temperature differential of 1.8°C (3.2°F) between the liner and the pool.

Thus, for the conditions considered, the maximum possible temperature rise of the plate above that of the sodium pool is very limited and, within itself, is not sufficient to cause significant degradation of the strength of the plate. However, it is noted that these calculations have assumed the sodium pool to be a constant-temperature heat sink. The rationale for this was that the calculations depicted the proposed experimental setup as shown in Fig. 3.1 in which the temperature of the sodium pool is to be controlled at 538°C (1000°F).

In an actual LMFBR cell, however, if no facilities for cooling of the sodium pool are provided, it would also be necessary to consider the temperature rise of the sodium. This would depend on the cell geometry. For example, if we consider a cell in the form of a cube measuring 3 m (9.84 ft) on a side and if we assume as the worst case that heat is evolved at a maximum rate of $3.15 \times 10^4$ W/m$^2$ ($10^4$ Btu hr$^{-1}$ft$^{-2}$) on all six sides, all of which flows into the sodium (no loss into concrete), then the rate of temperature rise of the pool is 218°C/hr (393°F/hr). Thus, this bounding estimate indicates that difficulty could be encountered due to long-term heating of the sodium in the event of a massive sodium leak through the liner. Calculations of the type required to pursue the study of this behavior were considered beyond the scope of the present work. (The direct effect of the thermal stress caused by bringing the liner in contact with hot sodium is considered in Chapter 4.)

## 3.4 Liner Plate Pressure Differential

If there is a small defect in the liner (either caused by the thermal shock of the sodium or present beforehand), sodium might leak into any gap between the liner plate and concrete and react with the concrete, causing an evolution of gas (hydrogen). This section is concerned with the problem of whether such a hydrogen evolution can build up sufficient pressure in the test assembly (Fig. 3.1) to cause gross structural deformation of the liner plate.

Based on the maximum measured concentration of hydrogen in the purge gas of test S1 of Ref. 5, the peak rate of hydrogen evolution adjusted for an area of reaction equivalent to the internal cross-sectional area

of a 10-in.-diam (0.25-m) sched-40 pipe (Fig. 3.1) is estimated to be $1.8 \times 10^{-5}$ kg/sec ($4 \times 10^{-5}$ $lb_m$/sec). In order to develop a pressure drop sufficient to severely deform a 10-in.-diam by 3/8-in.-thick plate, it is necessary to reach sonic flow in a defect orifice. Lapple[18] has developed equations and graphs describing compressible flow through a contraction followed by a length of pipe. Based on his results, Fig. 3.2 shows the estimated pressure drop across the liner plate for a hydrogen flow of $1.8 \times 10^{-5}$ kg/sec ($4 \times 10^{-5}$ $lb_m$/sec) through a circular defect orifice of various diameters.

For reference, it should be noted that the yield strength of the plate (131 MPa or 19,000 psi) at 538°C (1000°F) is reached when the pressure differential reaches 1.5 MPa (220 psi). Thus, at the maximum hydrogen evolution rate, a defect orifice diameter less than about 0.25 mm (0.010 in.) is required to produce plastic deformation of the liner plate in the model used.

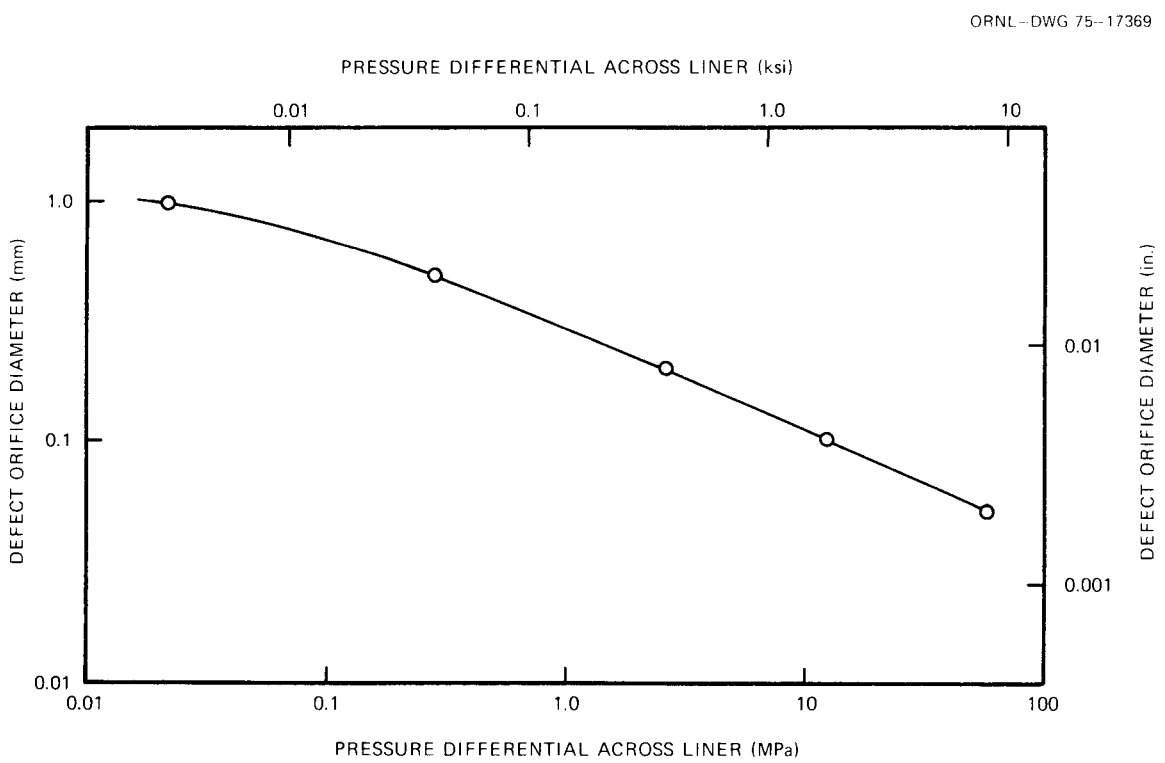


Fig. 3.2. Pressure differential across liner due to hydrogen discharge.

## 3.5 A Computer Model of the Reaction

It was concluded in the preceding section that liner defects equivalent to circular orifices greater than 0.25 mm (0.010 in.) diameter would be able to vent any hydrogen gas evolved fast enough to prevent gross deformation of the liner. It is a somewhat paradoxical result of the preceding section that very small defects are the most dangerous (in the sense that they are most likely to result in gross liner deformation). The reason for this paradox is that it was assumed in the preceding section that the maximum hydrogen evolution rate would be reached, regardless of the size of the defect. We might expect that smaller defects would limit the sodium leakage and thus limit the rate of the sodium-concrete reaction and hydrogen evolution. In order to study this possibility, a detailed computer model of the test assembly was constructed.

The computer model involves:

1. A one-dimensional thermal transient conduction calculation across the concrete. Heat is considered to be added to the upper concrete surface due to radiation and conduction of heat across the gap between the liner and the concrete, by leakage of hot sodium from the pool onto the concrete, and by chemical reaction between the sodium and the concrete. Heat leaves the lower surface of the concrete, due to radiation and natural convection to the ambient temperature of 55°C (131°F). A finite-difference calculation with 100 nodes was used for the transient conduction in the concrete.

2. Sodium leaks through the liner defect countercurrent to the upward flow of hydrogen. It was anticipated that in the very early stages of the process when the concrete surface was relatively cool and the reaction rate low, sodium inflow would predominate, whereas after the concrete heated, hydrogen outflow would predominate and would cut off the sodium leakage. Although some data were found in the literature on countercurrent two-phase flow through an orifice, the data were not sufficient to construct a complete model needed for the present calculations. Therefore, a model developed for countercurrent two-phase flooded flow in a pipe was used.[19]

3. The pressure drop for hydrogen flow through the defect was calculated from the work of Lapple[18] on compressible flow through a contraction and a length of pipe. This calculation ignores the effect of the liquid phase in determining the pressure drop of the gas phase. Only hydrogen flow (no steam) through the defect was considered.

4. The temperature dependence of the sodium-concrete reaction rate was obtained by constructing an Arrhenius plot of log (rate) vs 1/T (°K). There are three possible quantities which might be used to measure the reaction rate – the rate of penetration of sodium into the concrete, the rate of hydrogen evolution, and the rate of heat evolution. It was found that a sufficient range of data was available only for the depth of penetration. Therefore, all three rates were assumed to be proportional to one another, and the rate-of-penetration data were used to establish the temperature dependence of all three rates. A plot of the rate-of-penetration data from Refs. 5 and 20 is presented in Fig. 3.3.

5. The rate of reaction was considered to depend on the amount of sodium present relative to the amount of reaction products present. This assumption was based on an analogy with the drying theory.[21] When a porous solid or a layer of granular material having a high moisture content dries, the drying rate is a maximum determined by the rate of surface drying. When the moisture content falls below some critical value, moisture is no longer able to migrate to the surface fast enough to maintain the maximum drying rate. The drying rate is then determined by the rate at which moisture can migrate by capillary flow to the surface. For the sodium-concrete reaction, we consider a porous or granular mass of concrete reaction products with sodium absorbed in the pores. When the ratio of unreacted sodium volume to reaction product volume exceeds some critical value, the sodium-concrete reaction is considered to proceed at its maximum rate, determined by the temperature as given above. Below the critical sodium content, the reaction rate was considered to be proportional to the volumetric percentage sodium content. The critical sodium content was taken arbitrarily to be 0.1 volume fraction, based on a wide range of results obtained for the drying of various porous materials.[19]

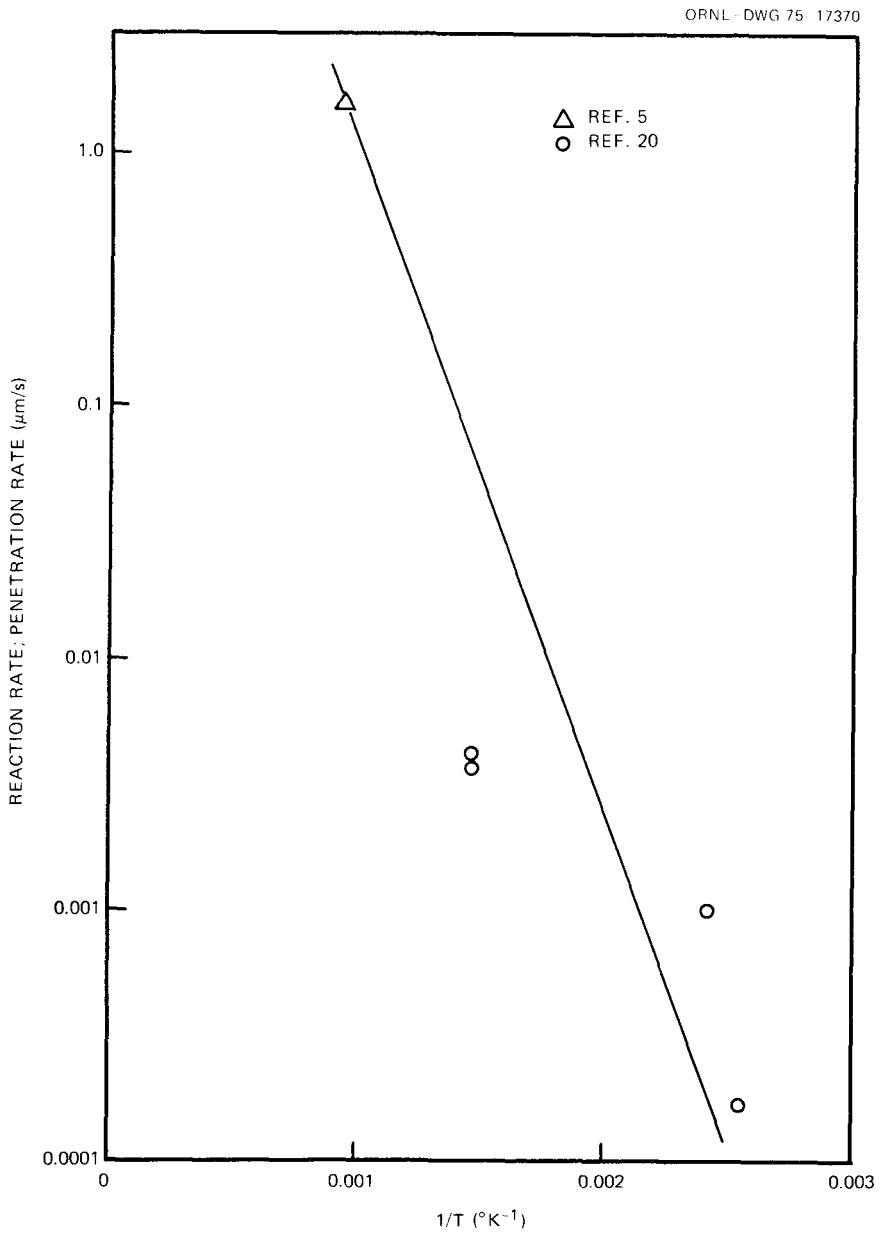


Fig. 3.3. Reaction rate vs temperature.

6. When the ratio of sodium volume to reaction product volume exceeded 0.38, the sodium was considered to spread out on the concrete surface until a depth of 0.1 mm (0.004 in.) was reached. When the ratio was less than 0.38, the sodium was considered to remain absorbed in the pores of the reaction products and not to spread further. (The volume fraction of 0.38 used here is arbitrary but is based on the fact that a bed of

randomly packed spherical particles has an open pore volume of about 38% of the bed volume.) The reaction rate was considered to be proportional to the area of wetted concrete.

It should be evident from the above discussion that the computer model assumptions as to the reaction rate are highly speculative and much more experimental data in this area are needed.

The computer integration of the equations describing the above mechanisms was continued for 1000 integration time steps of 1 sec each. Six different defect orifice sizes from 0.05 mm (0.002 in.) to 2 mm (0.079 in.) were considered. The gap between the liner plate and the concrete surface was taken to be 1 mm (0.040 in.), 3 mm (0.118 in.), or 6.35 mm (0.25 in.).

Figures 3.4 to 3.6 show the history of the pressure differential across the plate during the course of the calculation. It will be noted that no structurally damaging pressure differentials developed for any orifice size considered.

The most dramatic feature of the pressure curves is the sharp break in slope occurring at about 200 sec in Fig. 3.4, about 350 sec in Fig. 3.5, and about 500 sec in Fig. 3.6. This break is caused by the reaction using up the accumulated unreacted sodium in the gap. Early in the test, the concrete surface temperature is low, causing low hydrogen evolution and rapid accumulation of unreacted sodium in the gap. Later, after the concrete surface heats, the reaction proceeds faster and uses up unreacted sodium faster than it can enter through the defect orifice. According to the reaction model used here, the reaction rate continues unabated as the unreacted sodium is used up until the volume fraction of unreacted sodium to reaction products falls below a critical fraction of 0.1. This critical fraction, which is reached in about 200 sec in Fig. 3.4, accounts for the break in slope.

However, it should be noted that if the reaction rate had been considered entirely independent of the unreacted sodium content, the reaction rate would have continued unabated until <u>all</u> the unreacted sodium in the gap had been used up. Then, an abrupt shift to a new rate, at which sodium reacts at about the same rate that it enters, would have to occur.

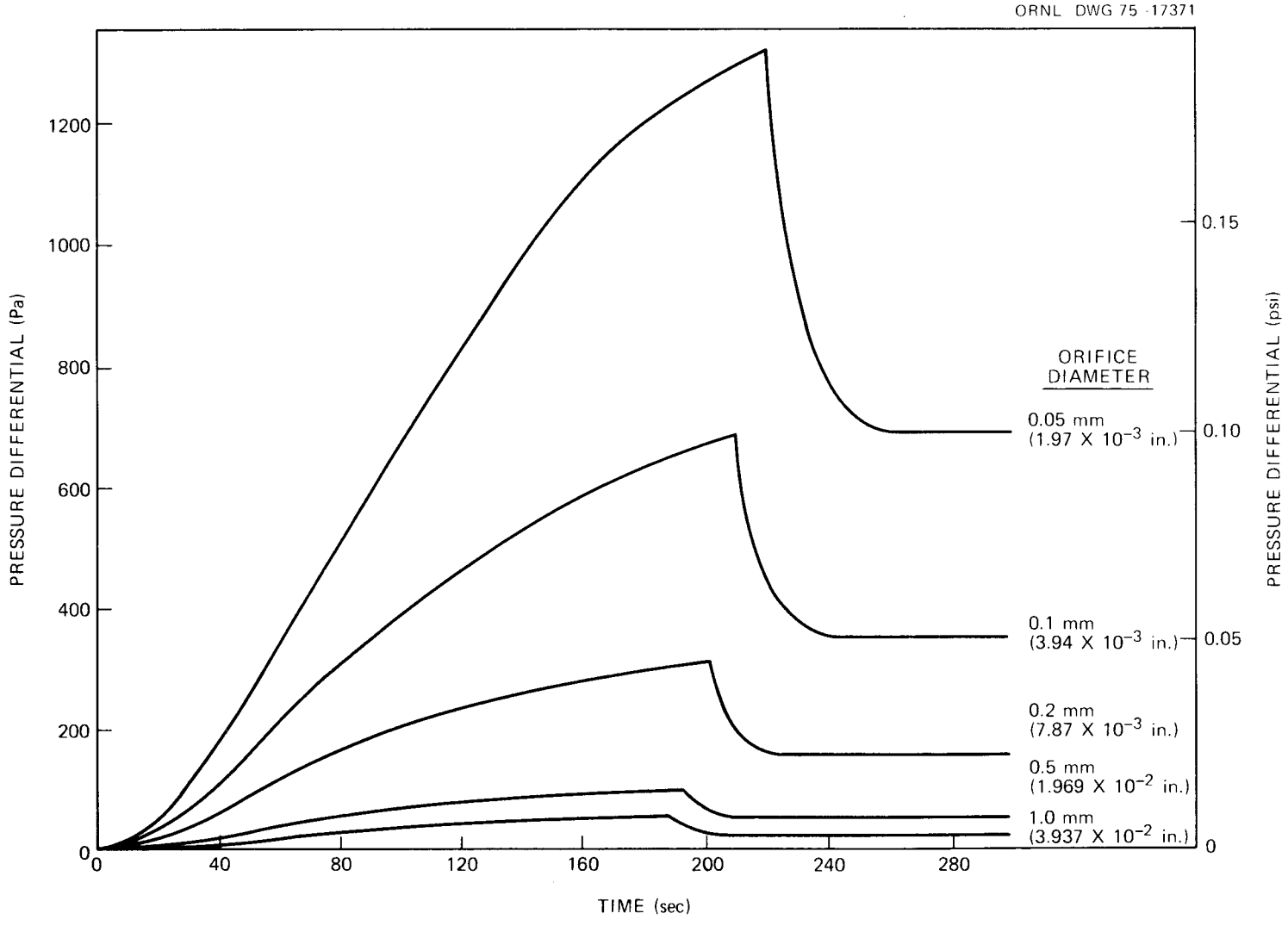


Fig. 3.4. Pressure differential vs time for 1.0-mm (0.039-in.) gap.

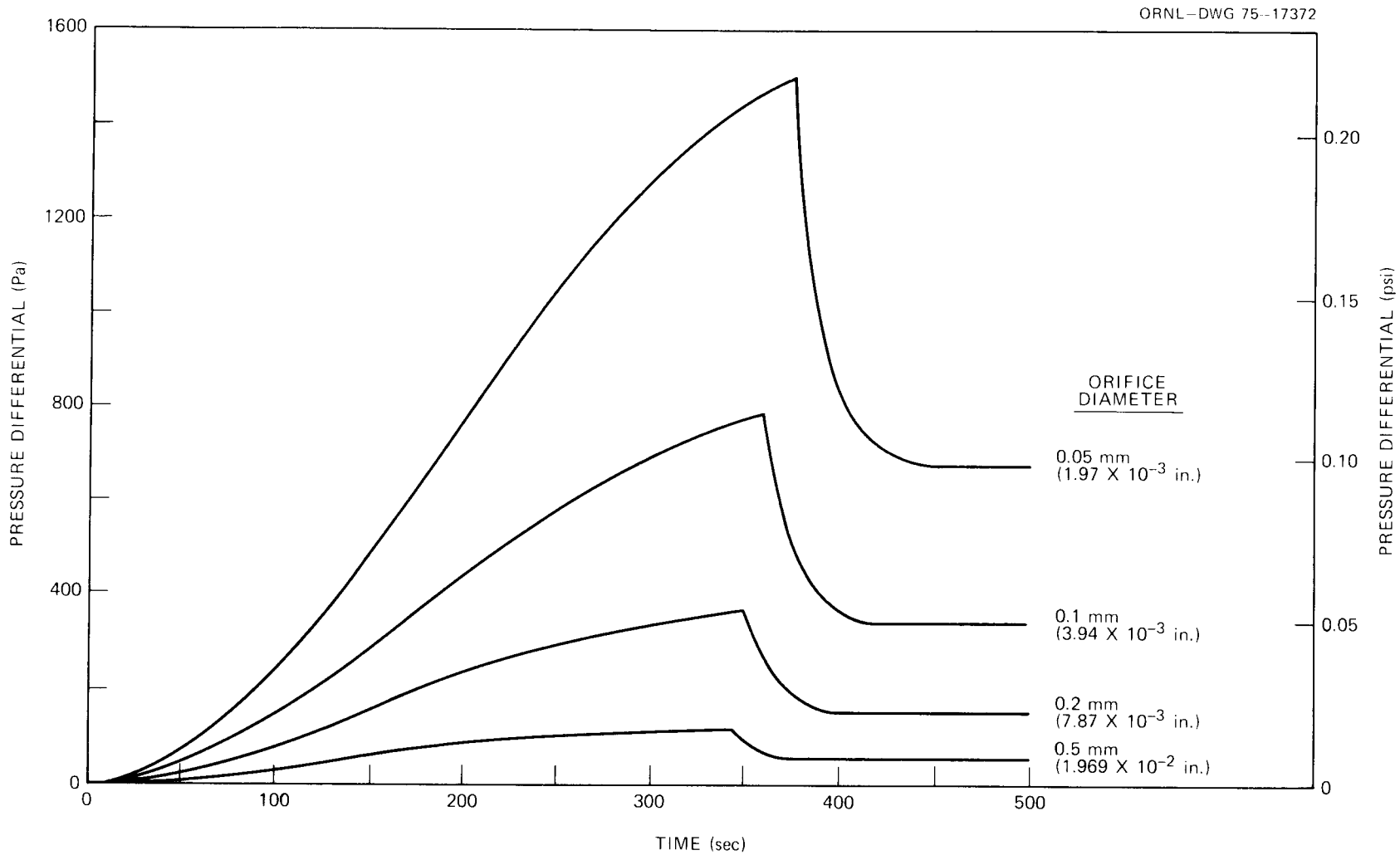


Fig. 3.5. Pressure differential vs time for 3.0-mm (0.118-in.) gap.

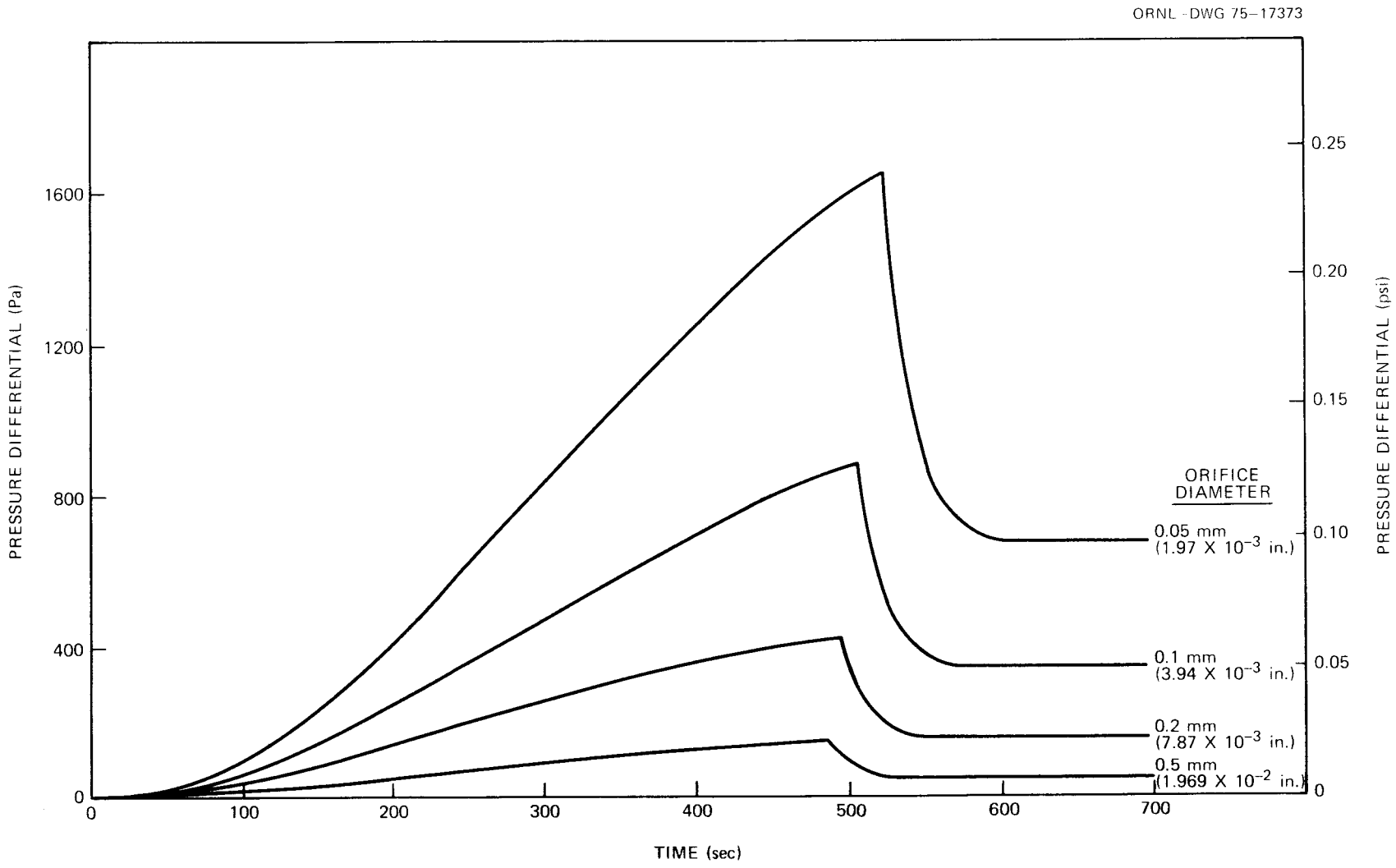


Fig. 3.6. Pressure differential vs time for 6.35-mm (0.25-in.) gap.

Thus, the model used here, linking the reaction rate to the volume fraction of unreacted sodium to reaction products, is responsible for the detailed shape of the pressure curves in the neighborhood of the break; but a similar phenomenon would occur for other reaction models.

It might also be worth noting that the temperature of the concrete surface at the gap never rose above the temperature of the sodium in the pool; that is, the generation of heat by the sodium-concrete reaction occurred so slowly that the heat was carried off by conduction into the concrete and did not build up the temperature in the gap above the temperature in the pool.

One of the most serious limitations of the above computer model of the sodium-concrete reaction is that it assumes that the only gas discharged through the defect orifice is hydrogen resulting from the sodium-concrete reaction. Actually, the presence of steam driven off from the concrete by the heating is likely to be important also. For cases involving very small defect orifice sizes, where the sodium leakage was very limited, steam would have been generated faster than it could react with sodium, and the discharge from the orifice could have been principally steam. The pressure differential across the liner could then be much larger than calculated for small defect orifice sizes. In particular, in the limiting case of no defect orifice at all, a sufficient structural deformation would have to occur in some way to release the steam.

Although the importance of steam generation was recognized in the present study, the time available did not permit its inclusion in the calculations. It was felt that the limited time available could be best spent by confining the study to direct effects of the sodium-concrete reaction.

## 3.6 Summary

The following conclusions can be drawn from the present study.

1. Enough energy could be released by the sodium-concrete reaction to produce gross liner deformation, provided all the reaction energy could be converted into deformation energy.

2. The reaction cannot heat the liner plate very far above the sodium pool temperature, but it could cause a long-term excessive temperature rise in both the pool and the liner in the case of a major sodium leak.

3. Hydrogen pressure due to the reaction can cause inelastic plate deformation only for small defect orifices.

4. The rather speculative computer model indicates that neither the hydrogen pressure nor the heat generation rate is excessive.

One example of a rather unlikely mechanism not studied which could produce gross deformation is the presence of a large defect in the liner which becomes completely blocked (by reaction products or in some other way) after the gap between the liner and the concrete becomes filled with sodium. All the evolved hydrogen would then be trapped in the gap until sufficient deformation occurred to provide an escape path.

A mechanism of possible liner failure not directly related to the sodium-concrete reaction and not studied here is the direct evolution of steam by the heated concrete. Future analytical work should consider this possibility.

# 4. INELASTIC SCOPING ANALYSIS OF A REPRESENTATIVE LMFBR EQUIPMENT CELL LINER

## 4.1 Introduction

A comprehensive state-of-the-art review of LMFBR cell liner design performed by Chapman[1] indicates that most liners are firmly anchored to the backup concrete structure. Such an arrangement introduces the potential for the accumulation of large thermal strains in the liner due to a sodium spill.

The purpose of the work summarized in this chapter was to perform an inelastic scoping analysis of a hypothetical cell wall with a fixed steel liner. The objective of the analysis was not to examine specific design details, but rather to delineate the relative importance and significance of the various behavioral features that could ultimately influence structural integrity during a massive sodium spill. The results of the analysis are to be used as one element in the preparation of a program plan for additional, needed work.

The structural model selected, a simplified segment of an LMFBR cell liner wall, is depicted in Fig. 4.1. The liner is 9.53-mm-thick (3/8-in.) ASTM type A516 carbon steel plate and is anchored to the concrete wall by 203.2-mm-long (8-in.), 12.7-mm-diam (1/2-in.) steel studs, which are assumed to be of the same material as the liner plate for this analysis. The studs are rigidly attached to the liner plate, although the method of attachment is unspecified (i.e., parent material properties are used throughout). In practice, these studs would be welded to the liner. The plan view in Fig. 4.1 shows the stud arrangement to be symmetric on a 381-mm-square (15-in.) pitch. Chapman's review[1] indicated many different stud arrangements (staggered, square, etc.) and spacings [6 to 24 in. (15.24 to 60.96 cm), with 30.48 cm (12 in.) to 45.72 cm (18 in.) being typical].

The concrete was assumed to be 0.91-m-thick (36-in.) ordinary Portland Cement concrete. This thickness was a compromise between ensuring the structural rigidity of a massive concrete structure and the limiting requirements of the computer program. While it is not shown explicitly

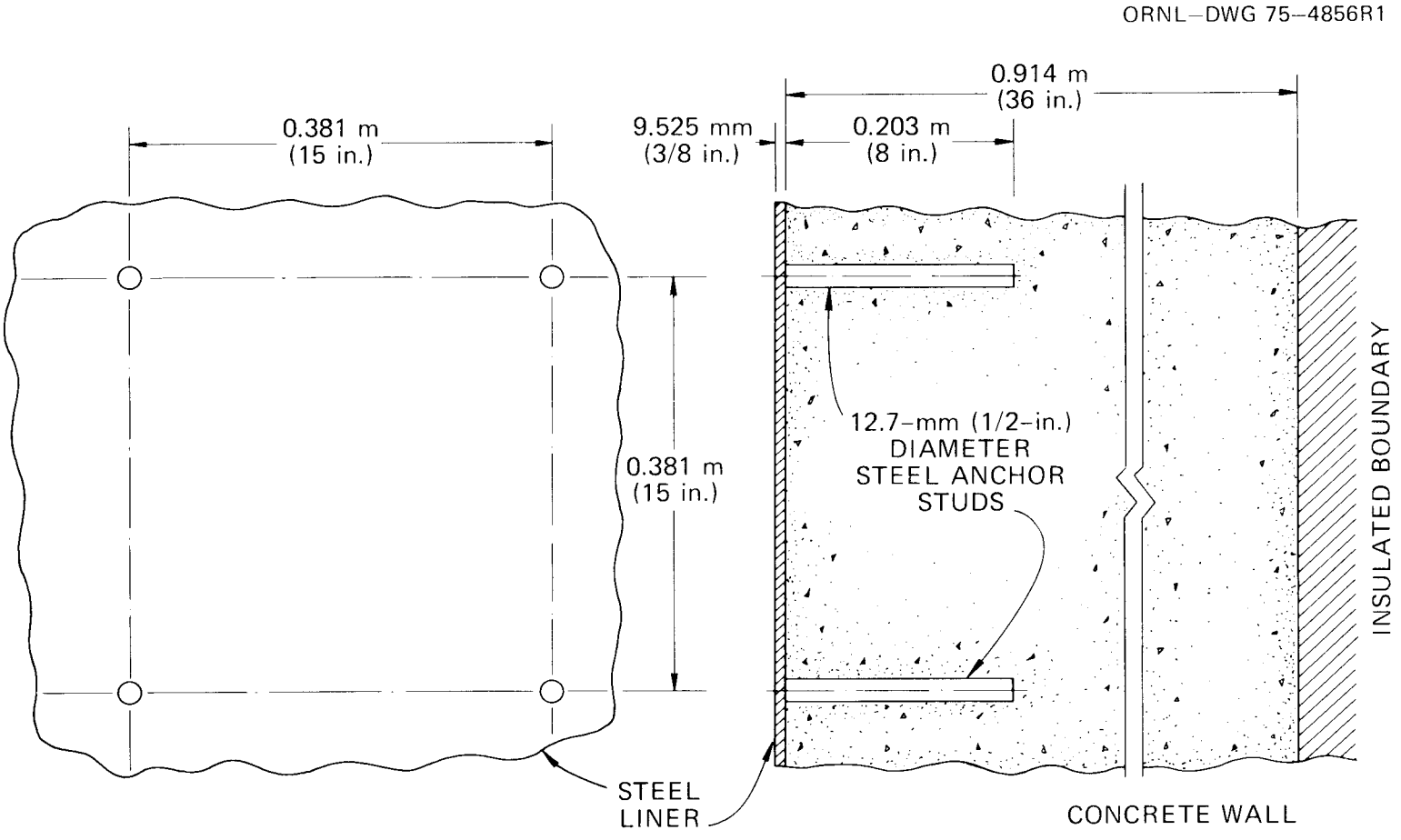


Fig. 4.1. Simplified representation of LMFBR equipment cell wall used as model for inelastic structural analysis.

in Fig. 4.1, the presence of an air gap between the liner and concrete is possible. The effects of such a gap were investigated and are described in Subsection 4.2.

The postulated loading condition was a sudden sodium spill accident in which the outer surface of the steel liner heats from 65.6°C (150°F) to 537.8°C (1000°F) in 1 sec. In addition, in performing the inelastic analysis, an isothermal steady state at 537.8°C (1000°F) followed by an isothermal cooldown to 65.6°C (150°F) to unload the plate was considered.

The problem was analyzed in three steps. First, a simplified one-dimensional transient thermal model of the cell liner was used to parametrically study the effects of the stagnant air gap size between the liner and concrete wall. Second, a three-dimensional transient heat transfer analysis was conducted guided by the results of the one-dimensional analysis. Finally, the transient temperatures calculated from the three-dimensional thermal analysis were used as input to model the elastic-plastic structural behavior of the steel liner plate and coupled concrete structure. These three analysis steps are discussed in Sections 4.2, 4.3, and 4.4.

This work was performed by Swanson Engineering Associates Corporation using the ANSYS computer program. This chapter presents only a summary; the interested reader is referred to Appendix II for a thorough discussion of the details of the analysis.

## 4.2 One-Dimensional Transient Thermal Analysis

The mechanisms of heat flow in the liner and concrete are (1) radiation between the back face of the steel liner and front face of the concrete, (2) conduction through the air gap between the liner and concrete assuming stagnant air, and (3) conduction along the steel anchor studs, which act like fins. Neglecting air circulation in the air gap, heat conduction is primarily dependent on the gap size, which in turn is dependent on the thermal structural deformation of the liner relative to the concrete. The heat flow is three dimensional due to conduction to and through the studs. However, since the net heat flow is essentially one dimensional, a simplified one-dimensional analysis was used to assess the importance of the stagnant air gap.

### 4.2.1 One-Dimensional Finite-Element Thermal Model

The one-dimensional model simulates a prism with 0.381-m-square (15-in.) bases where the anchor stud is at the center of the base. The plate, stud, and concrete wall materials were modeled with conducting bar elements of the same type. Both conduction and radiation were simulated across the air gap.

The length of the air gap was studied parametrically. Gap dimensions of 0.254 mm (0.01 in.), 6.60 mm (0.26 in.), and 12.95 mm (0.51 in.) were used for respective calculations. Since a one-dimensional analysis was employed, the steel and concrete material was coupled such that, over the anchor stud length, the temperatures calculated were weighted averages of both materials.

The thermal properties of the steel and concrete used are listed in Chapter 2. Also, as a first approximation, the temperature dependence of materials properties was neglected. The analysis was performed using a mid-range temperature of 260°C (500°F). In modeling radiation, the temperature dependence of the emissivities of the back face of the liner and the front face of the concrete was neglected, the radiant absorptivity of the air was neglected, and a form factor of 1 for infinite parallel surfaces was assumed.

### 4.2.2 One-Dimensional Analysis Results

Four cases were run with the one-dimensional model. In three cases the air gap length was varied; in the fourth case one air gap length [(6.60 mm)(0.26 in.)] was repeated, but the times between integration points were doubled. The purpose was to check the convergence of the transient solution, particularly the performance of the radiation link element used. The cases and number of time steps used are shown in Table 4.1.

In each case the steel liner comes to a "quasi-steady-state" temperature about 20 sec after the spill. At this point, the entire plate is above 510°C (950°F) and continues to heat slowly. The smaller air gap results in more rapid heating of the concrete face, although little difference in behavior was observed between cases 1 and 2. The concrete wall

Table 4.1. Summary of one-dimensional thermal analysis cases investigated

| Case No. | Size of air gap [(mm)(in.)] | Number of time integration points |
|---|---|---|
| 1 | [(6.60)(0.26)] | 113 |
| 2 | [(12.95)(0.51)] | 113 |
| 3 | [(0.254)(0.01)] | 113 |
| 4 | [(6.60)(0.26)] | 57 |

surface responds very slowly, and the bulk concrete 101.6 mm (4 in.) and greater into the wall displays little or no response for the duration of the analysis. This is shown in Fig. 4.2. The locations of the different nodal points are as follows:

| Node | Location |
|---|---|
| 1 | Front surface of liner plate |
| 2 | Middle surface of liner plate |
| 3 | Back surface of liner plate |
| 4 | Front surface of concrete wall |
| 9 | 101.6 mm (4 in.) into concrete wall |
| 63 | 559 mm (22 in.) into concrete wall |

The results shown in Fig. 4.2 were chosen for summary, since, based on the one-dimensional analyses, this particular air gap was used for the three-dimensional thermal analysis and the inelastic analysis.

For more detailed presentation and discussion of results, see Chapter 3 of Appendix II.

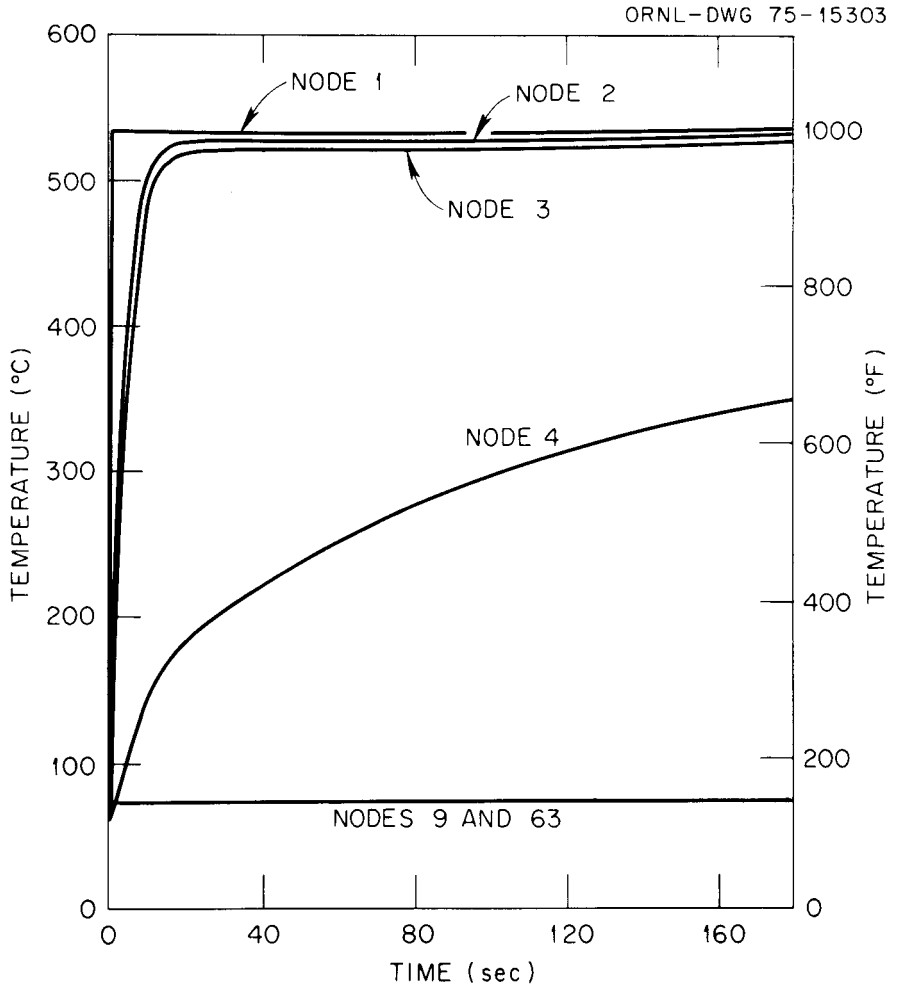


Fig. 4.2. Temperature vs time for nodes 1, 2, 3, 4, 9, and 63 of one-dimensional finite-element model; case 1, 6.6-mm (0.26-in.) stagnant air gap.

## 4.3 Three-Dimensional Thermal Analysis

A three-dimensional transient thermal analysis was done of the cell liner geometry shown in Fig. 4.1. The results of the one-dimensional analysis (Section 4.2) was used to set up this problem. The heat transfer mechanisms considered for the one-dimensional case were considered here also.

### 4.3.1 Three-Dimensional Finite-Element Thermal Model

Exposure of the outside surface of the liner to 537.8°C (1000°F) sodium caused the liner to deform away from the concrete wall. Thus, any size initial air gap will be increased by this deformation. It was observed from the one-dimensional analysis that the heat transfer was essentially unaffected by air gaps greater than 6.60 mm (0.26 in.). Thus, for the three-dimensional thermal analysis, a constant-length air gap of 6.35 mm (0.25 in.) was assumed. This effectively decoupled the thermal analysis from structural deformation.

In addition, the one-dimensional analysis indicated that the bulk of the concrete wall had not responded to the transient in the first 180 sec. The concrete was thus modeled to a depth of 254 mm (10 in.), and the remainder of the concrete was neglected in the three-dimensional model.

Due to symmetry, it was necessary to consider only one-eighth of the liner segment as is shown in Fig. 4.3. Note also the location and shape of the elements in each plane. The plate was modeled with five equally spaced layers, each having 15 three-dimensional isoparametric thermal-conducting solid elements. The stagnant air gap was modeled with one layer of elements, the anchor stud was modeled with nine, and the concrete was modeled with ten. Conduction and radiation were considered across the air gap. Essentially the same assumptions and approximations were made here as in the one-dimensional case.

### 4.3.2 Three-Dimensional Thermal Analysis Results

The transient three-dimensional analysis was conducted for the following load steps:

1. The first load step was a steady-state solution to initialize all node temperatures at 65.6°C (150°F).

2. In the second load step, the outer surface of the steel liner plate was ramped from 65.6°C (150°F) to 537.8°C (1000°F) in 1 sec with five substeps (i.e., $\Delta t = 0.2$ sec between solutions).

3. In the third load step, the outer surface of the liner was held at 537.8°C (1000°F) for 19 sec from $t = 1$ to $t = 20$ sec with 19 integration points or substeps of 1.0 sec each.

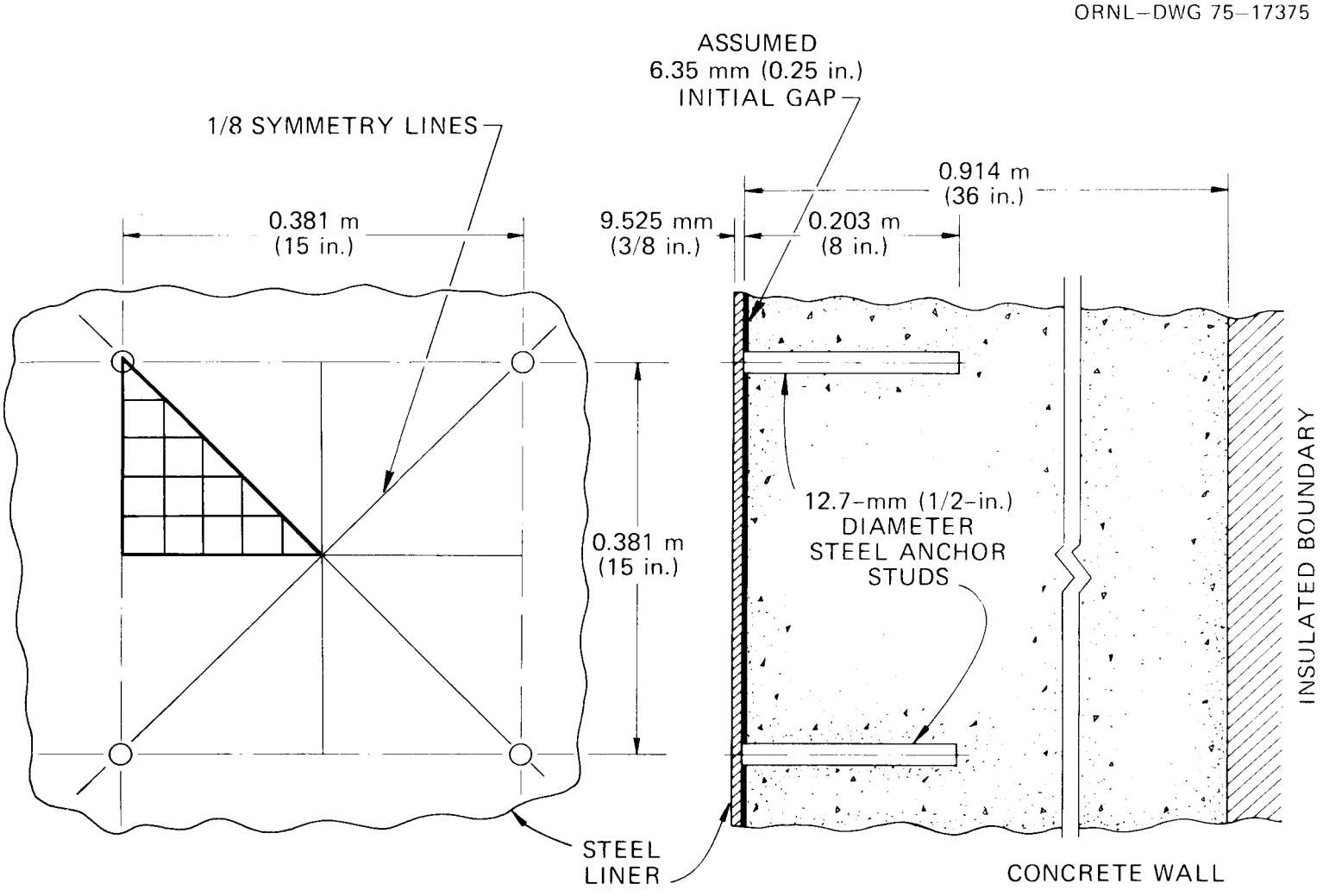


Fig. 4.3. Schematic of representative anchored LMFBR cell liner arrangement showing 1/8 symmetry lines and assumed 6.35-mm (0.25-in.) initial air gap.

4. The fourth load step consisted of 32 integration points or substeps of 5.0 sec each and extended the solution to t = 180 sec. Again, the outer surface of the steel liner was held at 537.8°C (1000°F).

As would be expected, the plate responds very rapidly to the loading, and, at the center of the plate away from the anchor, the temperature exceeds 510°C (950°F) at all points through the thickness within 20 sec after loading. This is shown graphically in Fig. 4.4. The plate response at the anchor stud location was somewhat slower due to more rapid heat

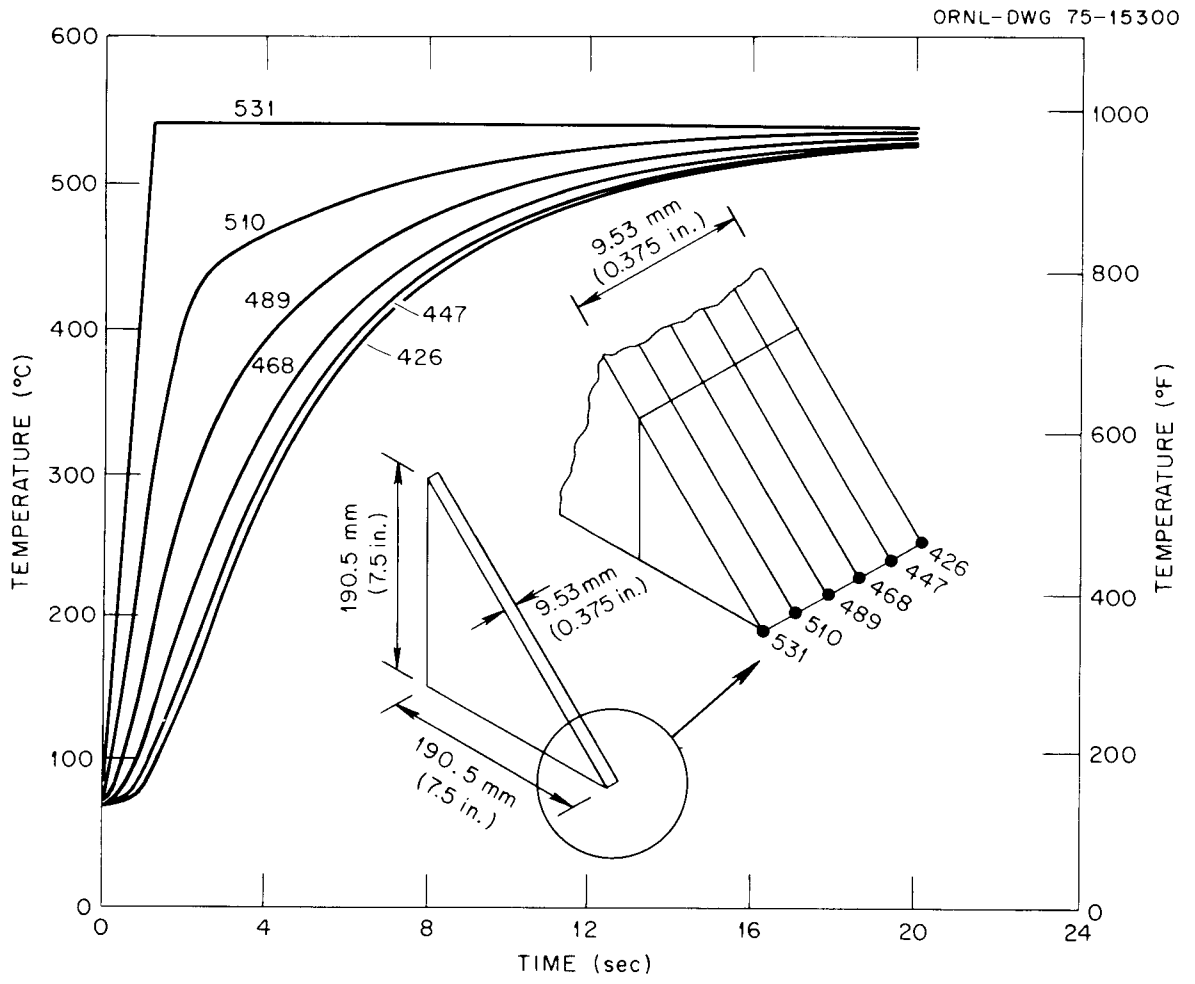


Fig. 4.4. Calculated liner plate transient temperatures at nodes through the thickness at center of model – 537.8°C (1000°F) sodium spill accident.

conduction through the anchor into the concrete. This slower response causes a higher thermal gradient, which is of significance in calculating the thermal stresses.

The temperature response across the air gap, which in turn drives the concrete response, is rather slow as is indicated in Fig. 4.5. The front face of the concrete responds slowly, as is shown in Fig. 4.6, and has begun to heat to a depth of only 1 in. in about 3 min after the transient. The analysis was not carried further (in time), but one could assume that a significant amount of time would be required to bring a major portion of the concrete wall to elevated temperature.

The results of the three-dimensional thermal analysis were used in the inelastic structural analysis.

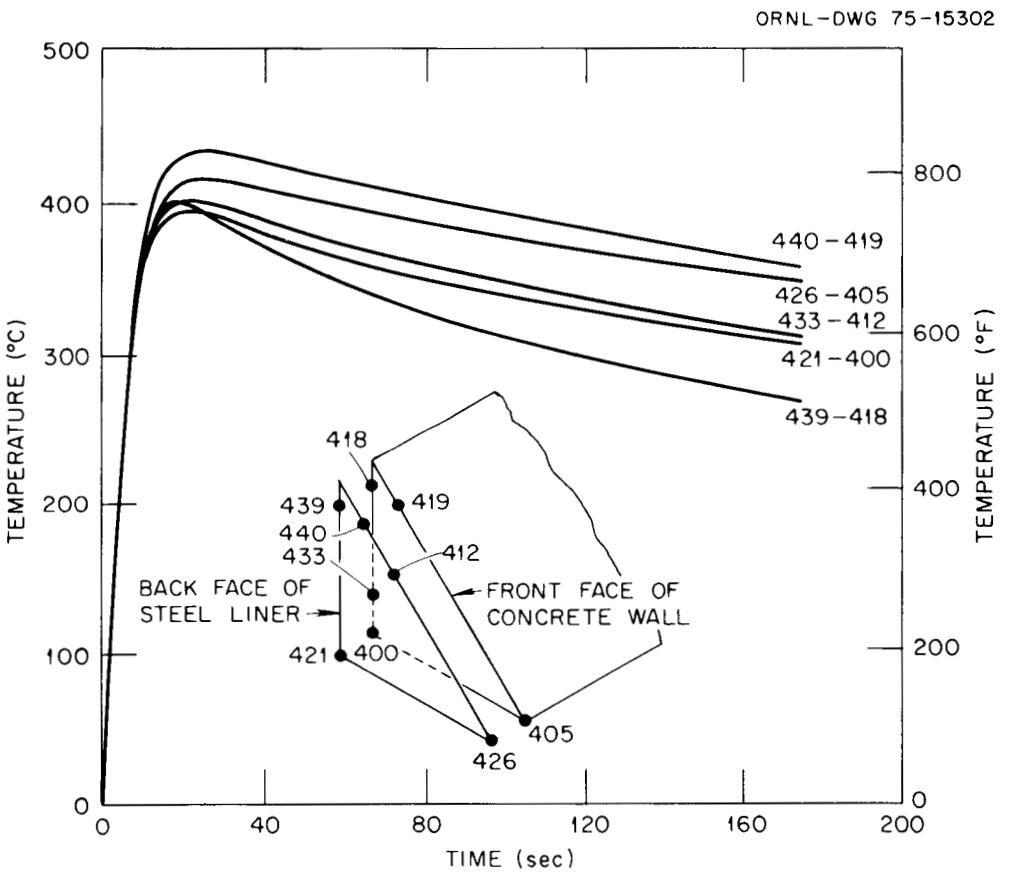


Fig. 4.5. Calculated transient temperature drops across the air gap between the steel liner and concrete wall – 537.8°C (1000°F) sodium spill accident.

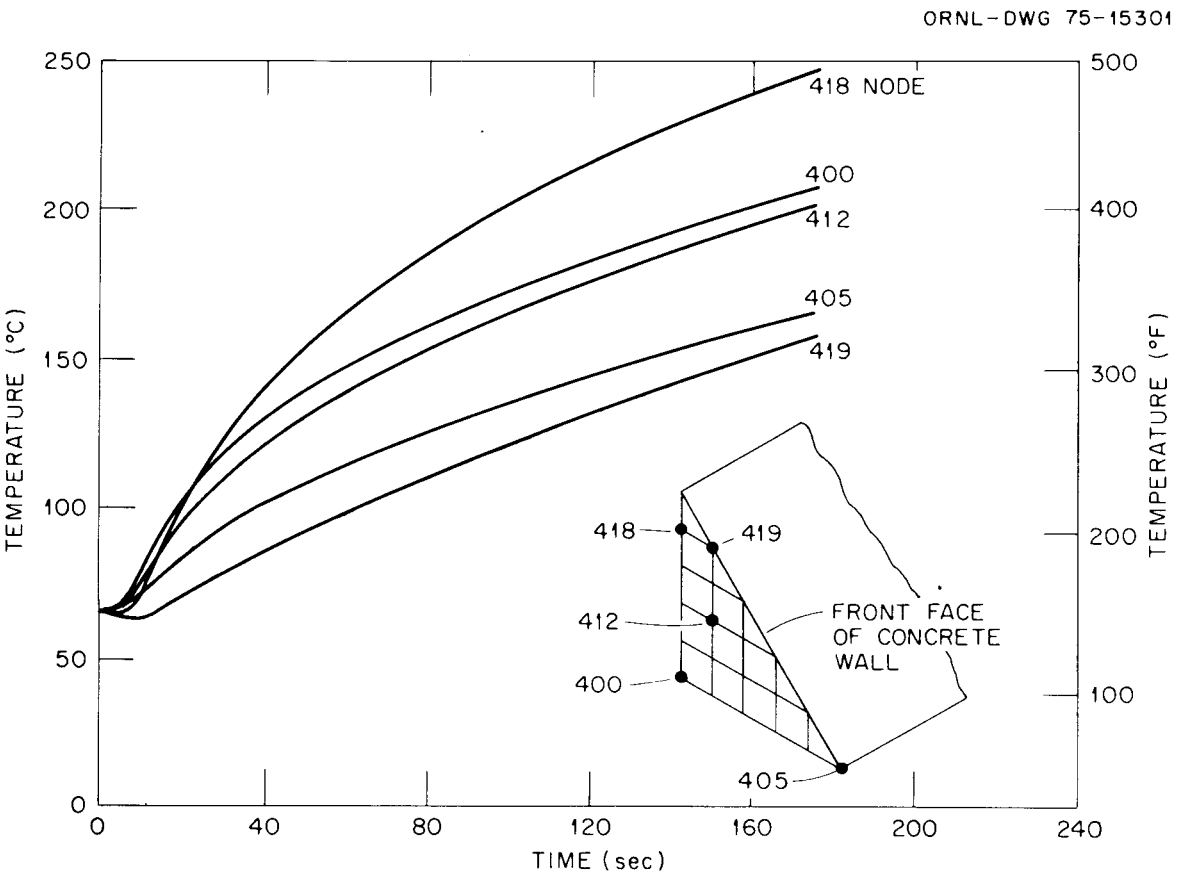


Fig. 4.6. Calculated transient temperatures of front face of concrete wall – 537.8°C (1000°F) sodium spill accident.

## 4.4 Three-Dimensional Plastic Structural Analysis

For the elastic-plastic structural analysis, as with the three-dimensional thermal analysis, symmetry required consideration of only a one-eighth section of the liner segment. The structural analysis also considered an isothermal cooldown back to 65.6°C (150°F), the initial temperature.

### 4.4.1 Three-Dimensional Finite-Element Structural Model

The three-dimensional thermal analysis results indicated that while the steel plate heats rapidly to a quasi-steady state, the concrete wall

responds very slowly to the transient. Therefore, the conservative assumption was made that the concrete wall remains rigidly at the initial temperature (65.6°C), which was reasonable since the intent was to study the plate performance.

The stud was not explicitly treated in the structural analysis. Due to the assumed symmetry, there is little or no structural interaction with the stud. Also, the three-dimensional mesh was not fine enough to pick up the stud-concrete interaction in detail. Additionally, the slow thermal response of the anchor stud and concrete and the abrupt shear gradient between the anchor and the concrete would require consideration of creep effects. This was beyond the scope of the present work.

The liner plate was modeled with plastic, flat, three-dimensional triangular shell elements as shown in Fig. 4.7. The 21 in-plane nodes were the same number and initial location as in the three-dimensional thermal analysis. Five temperatures were specified through the thickness of the liner; these were at the outer surface; at the 1/4, 1/2, and 3/4 thicknesses; and at the inside surface and were the output of the three-dimensional thermal analysis.

Nonlinear effects such as large displacements and plasticity were included through options of the ANSYS code. For the cooldown, reversed loading was simulated by a bilinear kinematic hardening model. The complete stress-strain curves generated as a function of temperature (see Section 2.1) were used to develop the required bilinear curves to 1% strain. The method and the essential model parameters are shown in Table 4.2.

### 4.4.2 Three-Dimensional Structural Model Results

The incremental elastic-plastic structural analyses were conducted for the same time span as the thermal analysis, approximately the first 3 min of the transient. In addition, an isothermal steady state at 537.8°C (1000°F) followed by an isothermal cooldown to 65.6°C (150°F) to unload the plate was considered.

The plate rapidly bulged out at the center and had reached what was essentially the maximum deformation 40 sec after the transient (Fig. 4.8).

ORNL-DWG 75-15296

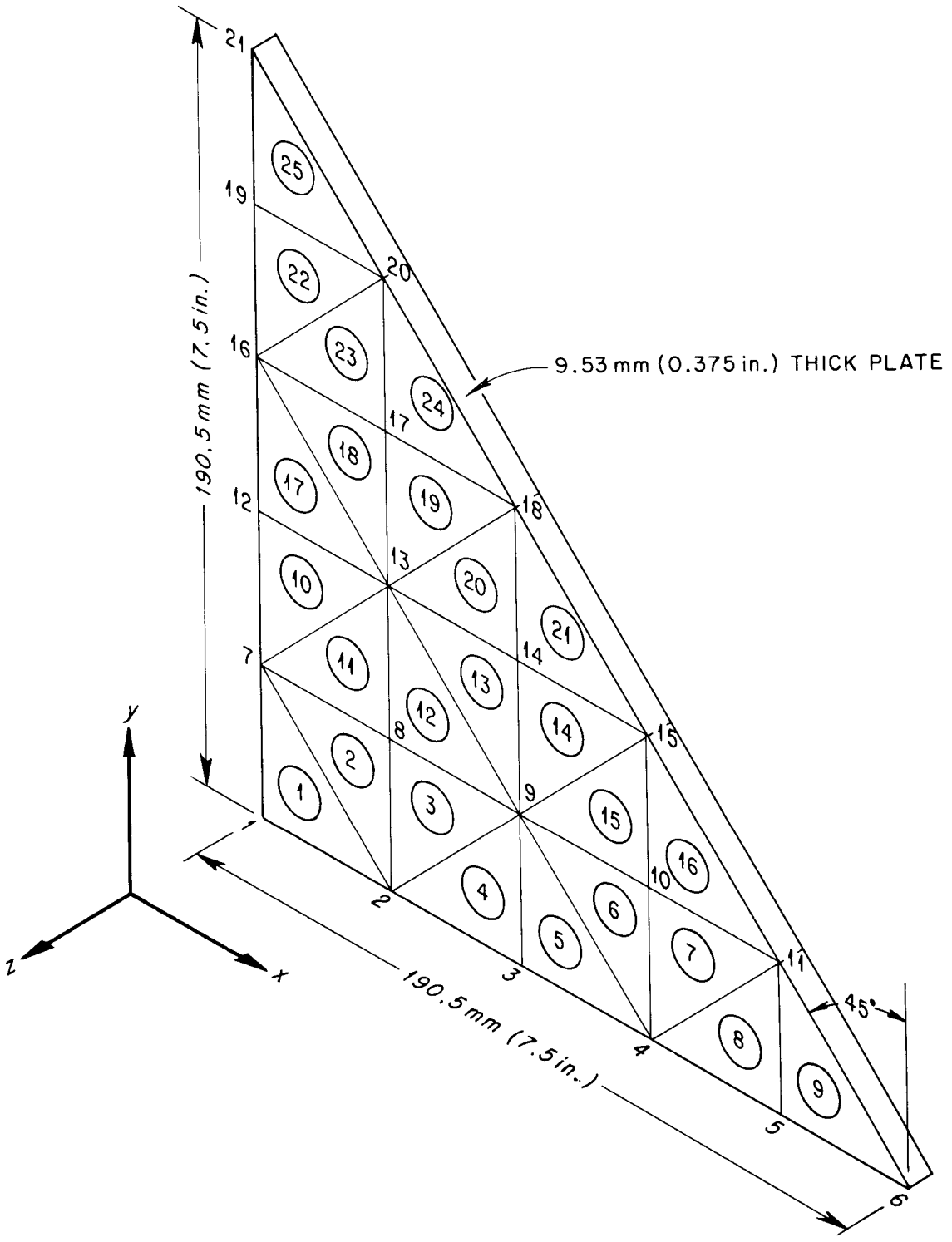


Fig. 4.7. Schematic of the 1/8 symmetry three-dimensional elastic-plastic finite-element shell model of the LMFBR cell liner plate.

Table 4.2. Stress-strain data vs temperature assumed in structural model of LMFBR steel cell liner

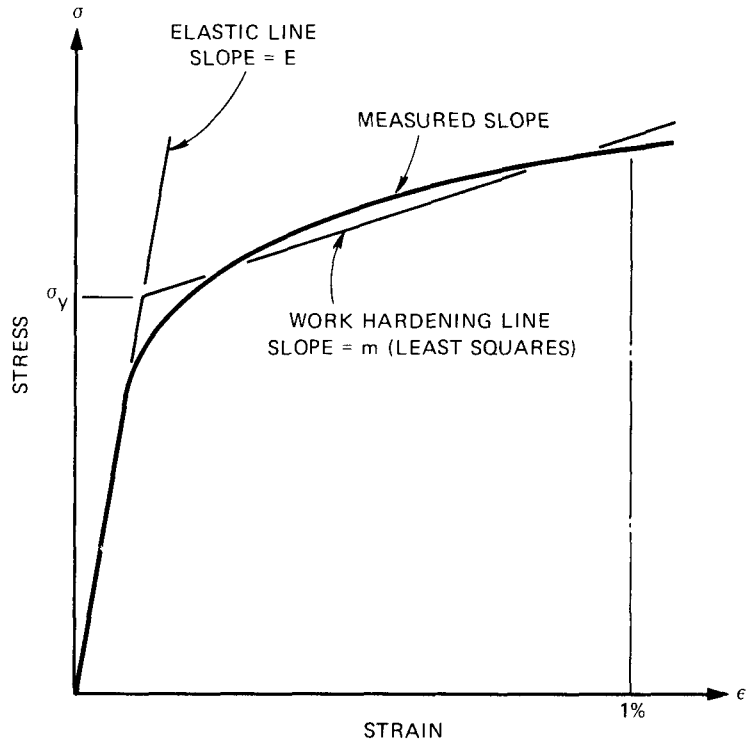


| Temperature [°C (°F)] | Elastic modulus E [$10^3$ MPa ($10^6$ psi)] | Poisson's ratio $\nu$ | Coefficient of thermal expansion $\alpha$ [$10^{-6}$°C$^{-1}$ ($10^{-6}$°F$^{-1}$)] | Yield stress $\sigma_y$ [MPa (ksi)] | Work hardening m/E |
|---|---|---|---|---|---|
| 65.6 (150) | 191.7 (27.8) | 0.3 | 15.12 (8.4) | 268.9 (39.0) | 0.004[a] |
| 260.0 (500) | 182.0 (26.4) | 0.3 | 15.12 (8.4) | 195.1 (28.3) | 0.0436 |
| 343.3 (650) | 174.4 (25.3) | 0.3 | 15.12 (8.4) | 175.8 (25.5) | 0.0613 |
| 426.7 (800) | 161.3 (23.4) | 0.3 | 15.12 (8.4) | 174.4 (25.3) | 0.0543 |
| 482.2 (900) | 146.2 (21.2) | 0.3 | 15.12 (8.4) | 183.4 (26.6) | 0.0467 |
| 537.8 (1000) | 127.6 (18.5) | 0.3 | 15.12 (8.4) | 147.6 (21.4) | 0.0503 |

[a]Measured curve at 65.6°C (150°F) was flat to 1% strain; therefore, a value of 0.004 was assumed.

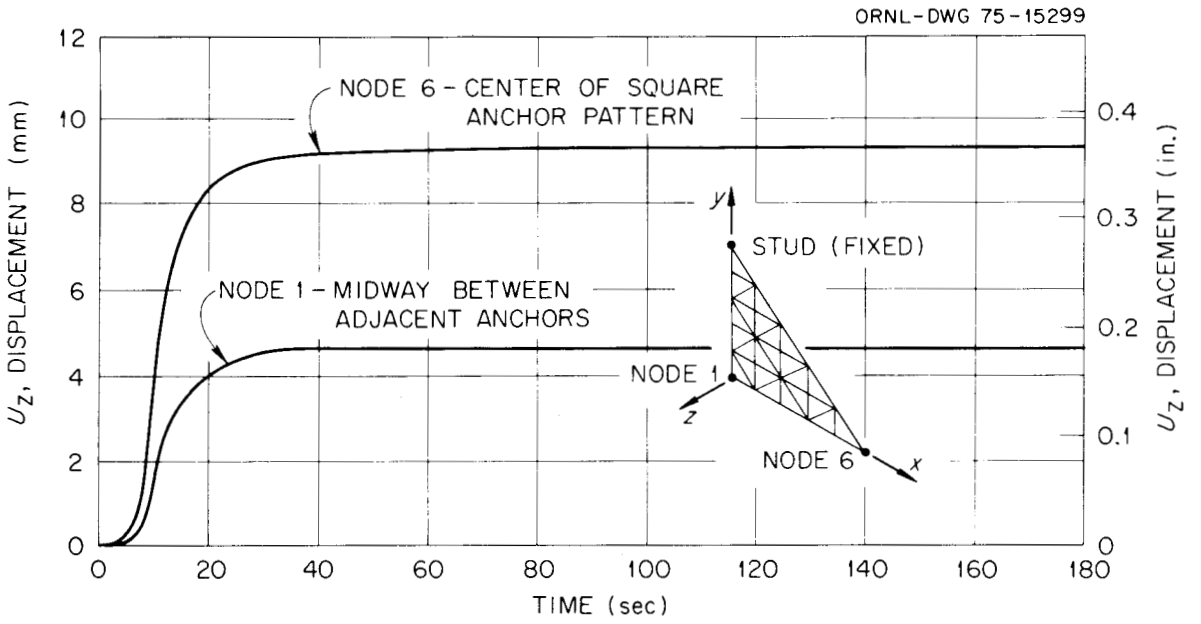


Fig. 4.8. Calculated transient out-of-plane displacements ($U_z$) of nodes 1 and 6 – 537.8°C (1000°F) sodium spill accident.

The steady-state configuration is shown in Fig. 4.9. The maximum generalized plastic membrane plus bending strain for the configuration, 1.7%, occurred at the back face of the plate at the anchor attachment. The development of this strain with time is shown in Fig. 4.10. The generalized plastic strain in this case is the von Mises effective plastic strain. The cooldown relieves the deformation such that the subsequent equilibrium deformation state at 65.6°C (150°F) is very small (i.e., an essentially flat plate). However, the plate undergoes tensile yielding during unloading such that there is a residual biaxial membrane tension in the plate of about 293 MPa (42.5 ksi).

Two observations are made concerning the inelastic analysis. First, the maximum strain occurs at a location where the potential for failure is the greatest (i.e., at the juncture of the anchor and plate, where a weld will more than likely be used). Second, the deformation of the liner is in the direction to increase the free volume available for sodium to fill in case of liner tearing. As indicated in Chapter 3, the continuing sodium-concrete reaction will depend on the unreacted sodium available in proximity to the surface of the concrete.

ORNL-DWG 75-15297

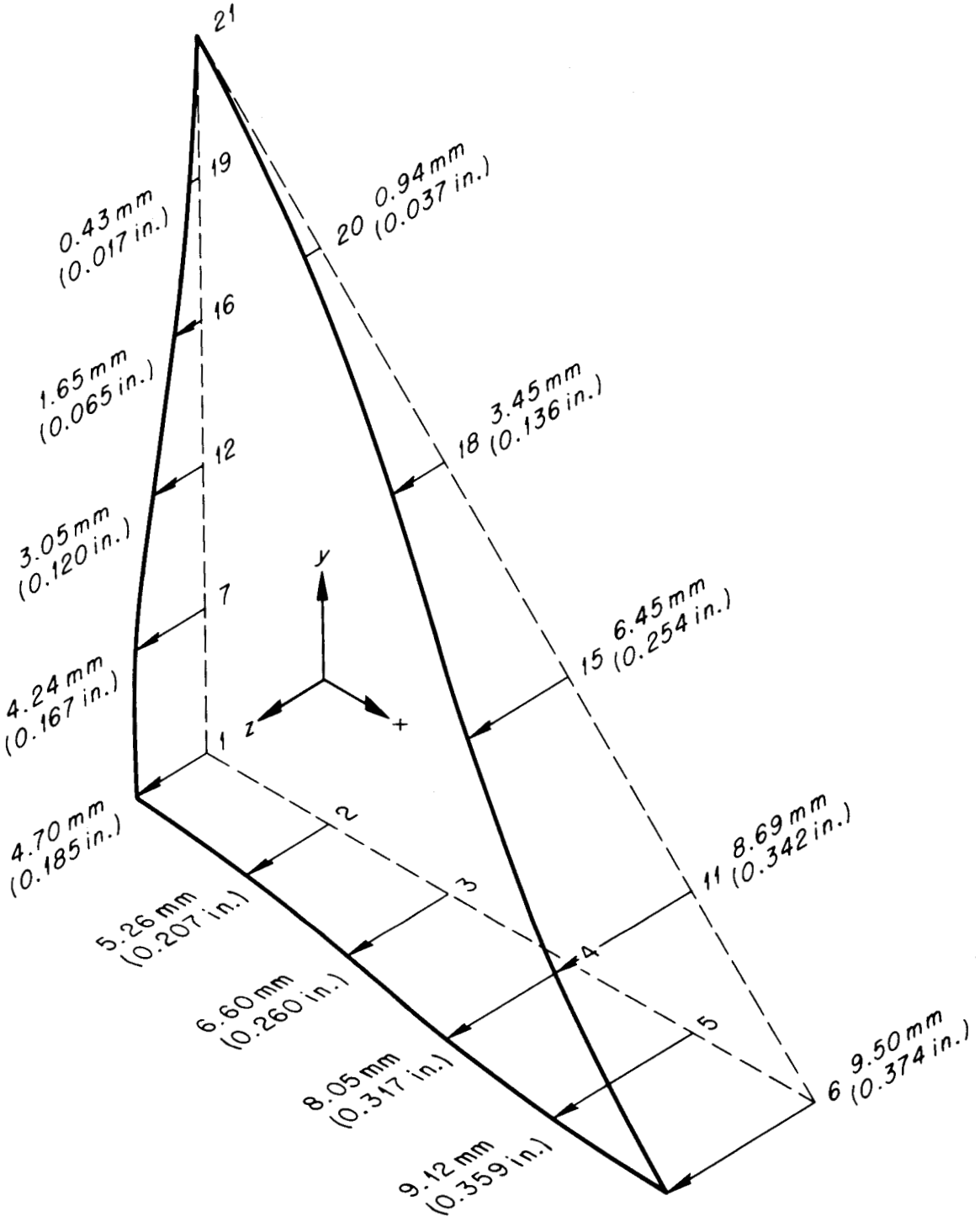


Fig. 4.9. Maximum calculated out-of-plane deformation of the steel liner plate at 537.8°C (1000°F) steady-state following 537.8°C (1000°F) sodium spill.

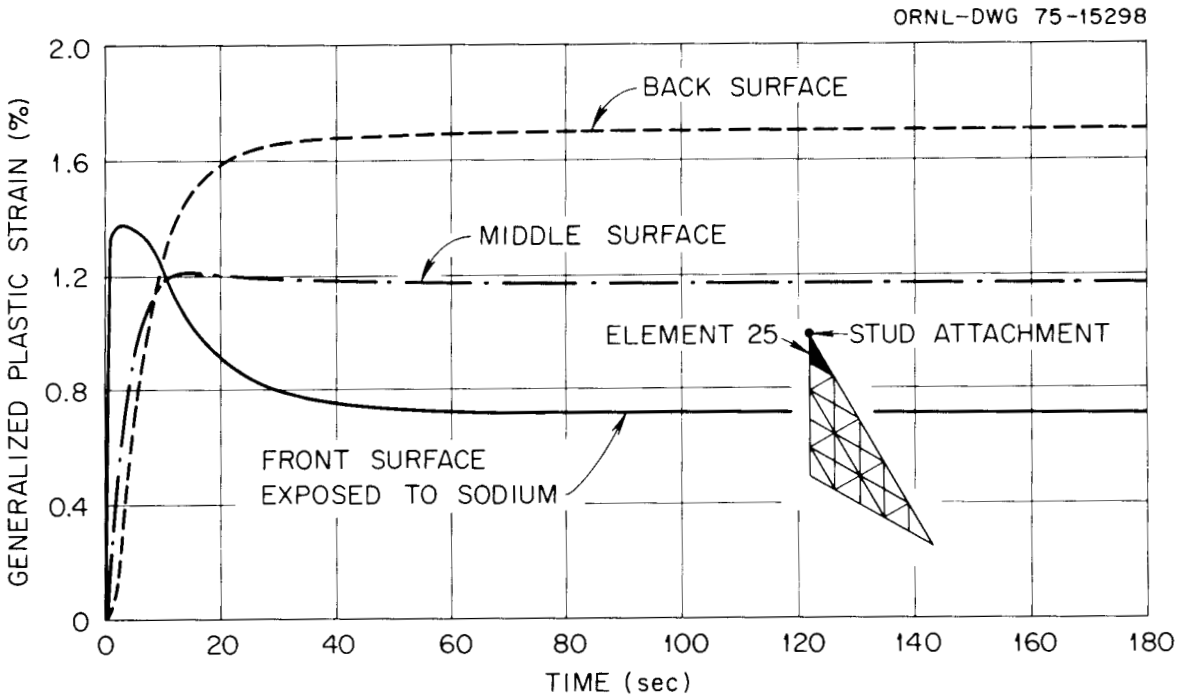


Fig. 4.10. Calculated transient generalized plastic strains of 3-dimensional shell element 25 – 537.8°C (1000°F) sodium spill accident.

It is emphasized that the discussion above is only a summary of the essential features of the thermal-inelastic analysis. Greater detail can be found in the report prepared by Swanson Engineering Associates (Appendix II).

## 5. CONCLUSIONS AND RECOMMENDATIONS

The results that have been presented in this report cover work that was intended for scoping purposes. Thus, in many cases they may seem incomplete or overly simple. However, such preliminary work is essential to laying the groundwork for a sound, reasonably oriented approach to the assessment of cell liner behavior during a sodium spill.

The bounding sodium-concrete reaction rate calculations indicated the potential for energy release sufficient to significantly deform the liner. However, the mechanism for such a sudden release does not seem to be present; that is, a somewhat slower energy release rate is expected. The calculations further indicated that for the conditions considered, sufficient pressure would not build up behind the liner to cause inelastic deformation of the liner. However, it was assumed that gases would vent through the defect at a maximum rate (sonic flow). If the defect were closed (e.g., by solid reaction products), the pressure would continue to rise until either the sodium in the cavity had all reacted or the pressure was relieved. Such relief could be through rupture of the liner.

Moisture between the liner and the concrete may dramatically affect the behavior of the sodium-concrete reaction. First, free moisture is a ready source of steam which, if unvented, could generate high pressures between the liner and concrete. Second, this moisture would be available to react immediately with sodium in case of liner failure. The presence of quantities of free moisture behind the liner should be considered through an extension of the calculations that have already been performed.

The calculations pointed up the need for more definitive data on the sodium-concrete reaction. The heat release will vary with type of concrete, moisture content, age, etc., and such data should be obtained, particularly on the influence of moisture content, in order to construct a reaction model that will provide greater prediction confidence.

The structural analysis indicated that for a thermal loading alone, the magnitude of stresses and strains in the base metal experienced by the unrestrained area of a liner should not be sufficient to cause gross failure. The discontinuities caused by anchor attachments, welds, corners, etc., were not modeled; thus no quantitative statements can be made. The

maximum strains calculated were 1.35% in the membrane (center) region and 1.7% in the anchor region. With good inspection and weld procedures, the magnitude of the strains would probably not cause fracture. However, the anchor region was not modeled in detail, and the maximum strains there should be greater than the 1.7% calculated. The interface between the concrete and the anchor stud was not modeled in sufficient detail to determine if the stresses generated would be great enough to cause localized failure in the concrete. These detailed studies should be pursued but were beyond the scope of this work. This study considered a single anchor arrangement, while in practice there is a wide range of anchor geometries or types used. An in-depth study should consider different prototypic anchor arrangements and identify structural problems related to each.

The sodium-concrete calculations indicated that the pressures generated would not add significantly to the load on the liner (based on the specific conditions considered), so that the thermal loading would be most important for assessing structural integrity and leak tightness. The structural calculations were based on an assumed maximum steady-state temperature of 537.8°C (1000°F). However, the reaction calculations indicated that, assuming a leak, there could be a large rise in temperature which would cause a further decrease in mechanical strength of both the steel and the concrete. Also, the thermal structural analyses indicated that an increase in the size of the air gap was beneficial. Based on the chemical calculations, an increase in air gap is detrimental because more sodium can accumulate in the cavity and react with the concrete.

The results of these preliminary studies indicate the need for additional work in a number of areas. A more comprehensive delineation of areas of research is included in the report by Chapman,[1] but the emphasis here is on those needs that became apparent during the course of these studies. These are briefly discussed as general problems rather than more detailed, specific test matrices.

There is a need for mechanical properties data over the range of temperatures of interest. The same, or a similar, concrete mix should be used for all investigations to remove variability from the interpretation of results. Emphasis should be put on relatively short-term behavior and

on the influence of moisture content on behavior. Data are required on the general aspects of moisture migration and, specifically, on the effect of high temperature and temperature differentials on moisture migration in thick sections. Sodium-concrete reaction rate data are needed over the temperature range 66°C (150.8°F) to 800°C (1472°F); once again moisture content is an important variable.

Studies of liner material behavior should emphasize failure behavior under multiaxial stress conditions. High-strain-rate data (up to 10%/min) are required to assess the capability of liner materials to withstand the shock loadings of the initial sodium spill. Short-term creep and creep rupture data, with emphasis on multiaxial loading, are also needed to evaluate the capability of the liner to function under sustained sodium spill conditions.

Analytical studies should concentrate on both the reaction aspects and the structural behavior aspects of the problem with a view toward coupling these two mechanisms to describe the dynamic behavior of a spill. Models of the sodium-concrete reaction should be developed that consider a greater range of parameters than was considered in this study. In particular, modeling of moisture migration in concrete under thermal-shock-type conditions would lead to an evaluation of free moisture available in a continuing sodium-concrete reaction.

Structural analyses of different liner configurations should be conducted. It is important to establish the general range of maximum stresses and strains developed in the liner material. To accomplish this, it will be necessary to perform detailed analyses of typical localized discontinuities caused by geometry or metallurgy variations.

Structural tests should be performed to investigate specific features of material behavior and to provide verification for the analytical studies as delineated above. Some of these tests should be thermal loadings of liner geometries in the absence of sodium, and others should use high-temperature sodium as the loading medium. Tests should be run with a model of a liner wall segment suddenly loaded and maintained at constant temperature. The results would be of value in assessing the basic structural analysis capability. Other tests should follow the initial shock by a ramp increase in temperature to simulate the probable performance in case

of a rupture in the liner. This series of tests should culminate in tests with sodium as the heat source and a precracked liner.

In conducting these tests, careful attention should be given to obtaining both temperature and structural response data (e.g., deformations). Also, at least one test should be run where the concrete is highly restrained as it would be in an actual mass concrete structure. Restraint is postulated as being one of the conditions leading to explosive thermal spalling.

The studies outlined above are not intended to be a complete program plan. Instead, these are areas that the present investigators found weak and that were a logical and necessary extension of the work reported herein. The results of these investigations should provide a sounder basis for assessment of liner behavior during and subsequent to a sodium spill.

REFERENCES


1. R. H. Chapman, A State-of-the-Art Review of Equipment Cell Liners for LMFBRs, ORNL-TM-4714 (February 1975).

2. R. K. Hilliard and J. M. Yatabe, FFTF Secondary Sodium Fire System Test F1, HEDL-TME-73-48 (April 1973).

3. R. K. Hilliard and L. D. Muhlestein, Sodium Fire Protection by Covered Trench – FFTF Proof Test F4, HEDL-TME-74-40 (July 1974).

4. R. K. Hilliard and L. D. Muhlestein, Sodium Fire Control by Space Isolation with Nitrogen Flooding – FFTF Proof Test F2, HEDL-TME-74-34 (June 1974).

5. J. A. Hassberger, R. K. Hilliard, and L. D. Muhlestein, Sodium-Concrete Reaction Tests, HEDL-TME-74-36 (June 1974).

6. Section 3, "Medium Carbon Steels," Nuclear Systems Materials Handbook, Vol. 1, TID-26666, Hanford Engineering Development Laboratory.

7. "Standard Specification for Pressure Vessel Plates, Carbon Steel, for Moderate- and Lower-Temperature Service," ASTM Standard A516-74, 1975 Annual Book of ASTM Standards, Part 4, American Society for Testing and Materials, April 1975.

8. Personal communication, W. J. Stelzman (ORNL) to W. J. McAfee (ORNL), June 1975.

9. ASM Materials Handbook, 8th ed., 1961, American Society for Metals, Metals Park, Ohio.

10. "Mechanical and Physical Properties of Steels for Nuclear Applications," Steels for Nuclear Applications, chap. 3, United States Steel, May 1967.

11. J. P. Callahan, J. M. Corum, and M. Richardson, "PCRV Thermal Cylinder Test," GCR-TU Programs Annu. Progr. Rep. Sept. 30, 1971, ORNL-4760, p. 88.

12. J. H. Hannah et al., "Basic Concrete Studies," GCR Program Semiannu. Progr. Rep. Sept. 30, 1968, ORNL-4353, p. 210.

13. I. A. Beryamin, "Fire Resistance of Reinforced Concrete," Symposium on Fire Resistance of Concrete, ACI Special Publication SP-5, 1962.

14. T. Harada et al., "Strength, Elasticity and Thermal Properties of Concrete Subjected to Elevated Temperatures," Paper SP-34-21, Concrete for Nuclear Reactors, Vol. I, ACI SP-34, 1972.

15. E. Crispino, "Studies on the Technology of Concrete Under Thermal Conditions," Paper SP 34-25 in Concrete for Nuclear Reactors, Vol. I, ACI SP-34, 1972.

16. R. D. Peak, "CACECO Code Modifications," HEDL Quarterly Technical Report, October, November, December 1974, HEDL-TME-74-4, Vol. 3, pp. 2-10.

17. S. Globe and D. Dropkin, "Natural-Convection Heat Transfer in Liquids Confined by Two Horizontal Plates and Heated from Below," Trans. ASME, J. Heat Transfer 81, 24 (1959).

18. C. E. Lapple, "Isothermal and Adiabatic Flow of Compressible Fluids," Trans. AIChE 39, 385 (1943).

19. G. B. Wallis, One-Dimensional Two-Phase Flow, p. 336, McGraw-Hill, New York, 1969.

20. Safety Research Bulletin, Spring 1971, Issue No. 8, United Kingdom Atomic Energy Authority, Authority Health and Safety Branch, Safeguards Division, Risley, Warrington, Lancashire.

21. J. H. Perry ed., Chemical Engineers' Handbook, 3d Ed., p. 800, McGraw-Hill, New York, 1950.

# APPENDIX I

## REVIEW OF LITERATURE ON HIGH-TEMPERATURE BEHAVIOR OF CONCRETE

# REVIEW OF LITERATURE ON HIGH-TEMPERATURE BEHAVIOR OF CONCRETE

Zdeněk P. Bažant
Professor of Civil Engineering
Northwestern University

CONTENTS

Page

PART I. PRESENT KNOWLEDGE OF VARIOUS PROPERTIES OF CONCRETE SUBJECTED TO HIGH TEMPERATURE ..... 75

1. Physical and Chemical Changes ..... 75

1.1 Loss of evaporable water from cement paste ..... 75
1.2 Dehydration of cement paste ..... 76
1.3 Porosity, density, and internal surface of cement paste ..... 76
1.4 Chemical changes in aggregates ..... 77
1.5 Moisture content and weight loss ..... 78

2. Thermal Expansion and Shrinkage ..... 81

2.1 Cement paste ..... 81
2.2 Concrete and aggregates ..... 81
2.3 Effect of moisture ..... 82
2.4 Drying shrinkage ..... 83

3. Pore Pressure ..... 86

3.1 Experimental facts ..... 86
3.2 Factors affecting pore pressures ..... 86

4. Strength, Ductility, Stress-Strain Diagrams ..... 89

4.1 Loss of strength ..... 89
4.2 Effect of drying and heating rate ..... 90
4.3 Ductility and stress-strain diagrams ..... 90
4.4 Moisture content and other factors ..... 91
4.5 Thermal cracking ..... 92

5. Modulus of Elasticity and Poisson Ratio ..... 96

5.1 Basic facts ..... 96
5.2 Effect of moisture, drying, and heating rate ..... 96
5.3 Other effects ..... 97
5.4 Shear modulus and Poisson ratio ..... 97
5.5 Deflections of beams ..... 98

6. Creep ..... 101

6.1 Physical nature of thermal effect ..... 101
6.2 Effect of moisture loss ..... 101
6.3 Basic facts on high-temperature creep ..... 102
6.4 Various factors affecting creep ..... 103

7. Heat Capacity ..... 108

7.1 Physical nature ..... 108
7.2 Observed temperature dependence ..... 108

Page

8. Thermal Conductivity and Diffusivity ..... 111

8.1 Basic facts on conductivity ..... 111
8.2 Experimental results and moisture effect ..... 111
8.3 Thermal diffusivity ..... 112

9. Moisture Conductivity and Diffusivity ..... 115

9.1 Moisture conductivity (due to moisture concentration gradient) ..... 115
9.2 Thermal moisture conductivity ..... 116

10. Explosive Thermal Spalling ..... 117

10.1 Physical nature ..... 117

11. Reinforcing and Prestressing Steels ..... 121

PART II. APPLICATION TO THE PROBLEM OF SODIUM SPILL ..... 122

1. Opinion Statement on the Effects of Sudden Exposure to Temperature of 538°C (1000°F)..... 122

1.1 Two possible effects of sodium spill on concrete wall ..... 122
1.2 Differences from cases tested in fire research ..... 123
1.3 The question of explosive spalling and damage ..... 124

1.3.1 Spalling ..... 124
1.3.2 Damage ..... 125

2. Research and Development Needs ..... 126

2.1 Material aspects ..... 126
2.2 Analytical prediction ..... 126
2.3 Model tests ..... 127

BIBLIOGRAPHY ..... 128

# PART I. PRESENT KNOWLEDGE OF VARIOUS PROPERTIES OF CONCRETE SUBJECTED TO HIGH TEMPERATURE

Mechanical behavior of concrete at high temperatures has been studied since the turn of the century, mainly for the purpose of evaluating fire resistance of concrete structures [Woolson (1905)]. Because of this objective, most of the investigations have been directed primarily to empirical determination of the behavior of whole structural parts, while comparatively less attention has been paid to the fundamental properties of cement paste and concrete. Nevertheless, a considerable body of knowledge has been assembled to date, and the intent of this work is to present a critical survey that is not exhaustive but selective.

Recently, knowledge of high-temperature behavior of concrete has acquired additional importance for the prediction of the response of nuclear concrete structures in various postulated accidents of very low probability. Here, the needs for the knowledge of fundamental properties of the material are considerably higher than those in prediction of fire response.

## 1. Physical and Chemical Changes

An increase of temperature causes profound changes in the chemical composition and microstructure of hardened Portland Cement paste which occur gradually and continuously over the entire range of 0 to 1000°C (320 to 1832°F).

At temperatures exceeding 1000°C (1832°F), ordinary Portland Cement concrete disintegrates. Special concretes, called refractory concretes (Petzold and Rohrs, 1967), made of refractory hydraulic cements (mainly aluminous cements, Briebach, 1972) and refractory aggregates (such as firebrick) can withstand temperatures up to 1600°C (2912°F). However, this subject is outside the scope of this study.

### 1.1 Loss of evaporable water from cement paste

At room temperature, about 50% by volume of saturated cement paste and between 2 to 10% by volume of saturated structural concrete is occupied by evaporable water (i.e., water that is not bound by chemical bonds). The loss of water (i.e., drying) depends on temperature and time. Increase of

temperature vastly accelerates drying, and when 100°C (212°F) is exceeded, the drying proceeds quite rapidly. No precise data on drying diffusivity seem to be available; however, at temperatures exceeding 100°C (212°F) all evaporable water is lost from 6-in.-diam cylinders in less than a day, while drying at room temperature takes years. The final loss of water depends on temperature, and at temperatures of about 105°C (221°F), all evaporable water is driven out of the specimens (after a sufficient period of exposure, of course).

## 1.2 Dehydration of cement paste

As temperature is raised beyond 120°C (248°F), the chemically bound water (water of constitution) is gradually lost from the hydrates in cement paste (Czernin, 1962). The most important of these is the gel of calcium silicate hydrates (CSH), also called tobermorite gel (abbreviations are C = CaO, S = $SiO_2$, H = $H_2O$), and calcium hydroxide crystals [CH = $Ca(OH)_2$]. The principal dehydration reactions are decomposition of CSH into β-dicalcium silicate (β-$C_2S$), β-wollastonite (CS), and water; and decomposition of CH into C (= CaO) and water.

The degree of final dehydration of CSH grows continuously from 105°C (221°F) up and becomes complete at 850°C (1562°F); at 500°C (932°F), about 70% of hydrate water is lost. The degree of dehydration of CH [$Ca(OH)_2$] is zero up to about 400°C (752°F), grows most rapidly around 535°C (995°F), and becomes complete at about 600°C (1112°F)(see Harmathy, 1970; Fischer, 1970; and Fig. 1.1).

## 1.3 Porosity, density, and internal surface of cement paste

The loss of evaporable water does not affect porosity, but dehydration creates additional pore space and thus porosity grows with temperature (Harmathy, 1970; Fischer, 1970). At 850°C (1562°F), porosity exceeds the porosity at 105°C (221°F) by about 40% (Harmathy, 1970; Fig. 1.2), and the increase is roughly parabolic (Fischer, 1970). The mass density of the constituents of cement paste increases from about 2.55 g/cm$^3$ (0.092 lb/in.$^3$) at 105°C (221°F) to about 3.2 g/cm$^3$ (0.116 lb/in.$^3$) at 850°C (1562°F); but, as a result of porosity increase, the bulk mass density of the cement paste decreases with temperature, from about 1.45 g/cm$^3$ (0.052

lb/in.$^3$) at 105°C (221°F) to about 1.3 g/cm$^3$ (0.047 lb/in.$^3$) at 850°C (1562°F) for a cement paste with a water/cement ratio of $\approx$0.5 (Harmathy, 1970, and Fig. 1.3).

The average pore size must increase with increasing temperature, because the ultrafine gel structure of calcium silicate hydrates is being destroyed by dehydration. Furthermore, as a consequence, the specific internal pore surface must also increase with temperature. However, it seems that no quantitative test data are available to this effect.

In concrete with quartz aggregate, no clear change of porosity is observed at $\alpha$-$\beta$ quartz transition temperature (Fischer, 1970).

Porosity increases with temperature less in loaded specimens than in unloaded ones (Fischer, 1970).

When concrete is cooled after temperature exposure, the fine gel microstructure is not immediately reestablished. This is evidenced by weight measurements of moisture content by Harmathy (1968) which show that on cooling the microstructure is essentially preserved and a further change occurs only when the previously reached temperature is exceeded on second heating (Fischer, 1970). After cooling, when the specimens are resaturated in water, porosity slowly returns almost to the original value at 20°C (68°F) (Fischer, 1970), which indicates rehydration. (In room atmosphere, return of porosity is only slight.)

## 1.4 Chemical changes in aggregates

Among these, the most important change below 850°C (1562°F) is that occurring in quartz ($SiO_2$) – the crystalline transformation from $\alpha$-quartz (trigonal) to $\beta$-quartz (hexagonal). This transformation occurs gradually between 500°C (932°F) and 650°C (1202°F), peaks (for 1 atm) at about 575°C (1067°F), and is accompanied by a substantial (5.7%) increase in volume (Harmathy, 1970, 1973; Waubke, 1973). Whether this transformation causes severe damage to concrete and produces spalling is debated (Harmathy, 1973). It is quite possible that the stiffness of concrete resists the volume expansion adequately without severe disruption. Moderate dehydration also occurs in some siliceous or calcareous aggregates holding some water of constitution. Such dehydration is accompanied by shrinkage

(Waubke, 1973) [about 13% by volume in opal, at 373°C (703°F)]; other aggregates are stable up to at least 600°C (1112°F). At higher temperatures, calcareous aggregates [calcite ($CaCO_3$), magnesite ($MgCO_3$), and dolomite] dissociate into an oxide and $CO_2$ (e.g., $CaO + CO_2$); calcium carbonate ($CaCO_3$) dissociates completely for 1 atm pressure at 898°C (1648°F) (CRC Handbook of Chemistry and Physics, 1974), but partial dissociation apparently proceeds at much lower temperature [at least as low as 700°C (1292°F); Harmathy and Allen, 1973].

## 1.5 Moisture content and weight loss

The main cause of the loss of weight of concrete above 105°C (221°F) is the dehydration of cement paste and, to a lesser extent, of aggregates. Dissociation of $CO_2$ also contributes to loss of weight of carbonate rocks. The curves of weight change (thermogravimetric curves) are exemplified in Fig. 1.4 (Harmathy and Allen, 1973; Philleo, 1958; Harmathy, 1968; Weigler and Fischer, 1972, 1968; Lankard, 1968). The curves in Fig. 1.4 indicate the equilibrium moisture content for various temperatures. The equilibrium is probably reached in less than a day of exposure to the given temperature and within one or more hours (in standard size cylinders) at higher temperatures. Tests of rate of moisture loss, time curves of weight, and precise data on the time needed to reach a moisture equilibrium state seem to be unavailable in the literature for temperatures exceeding 100°C (212°F). However, a note by Fischer (1970) indicates that at 100°C (212°F), a 6-cm-diam (2.36-in.) concrete cylinder takes two days to dry to equilibrium, and Bažant and Thonguthai's preliminary test results show that a 152-mm-diam (6-in.) concrete cylinder takes three days to dry at 100°C (212°F), 12 hr at 200°C (392°F), and 6 hr at 300°C (572°F). For moderate temperatures [<100°C (212°F)], abundant data are available; these include drying rate data and data on moisture and pore humidity distributions within the specimen (Hundt, 1972; England and Ross, 1972; Browne, 1967; McDonald; Yuan).

ORNL–DWG 75–17376

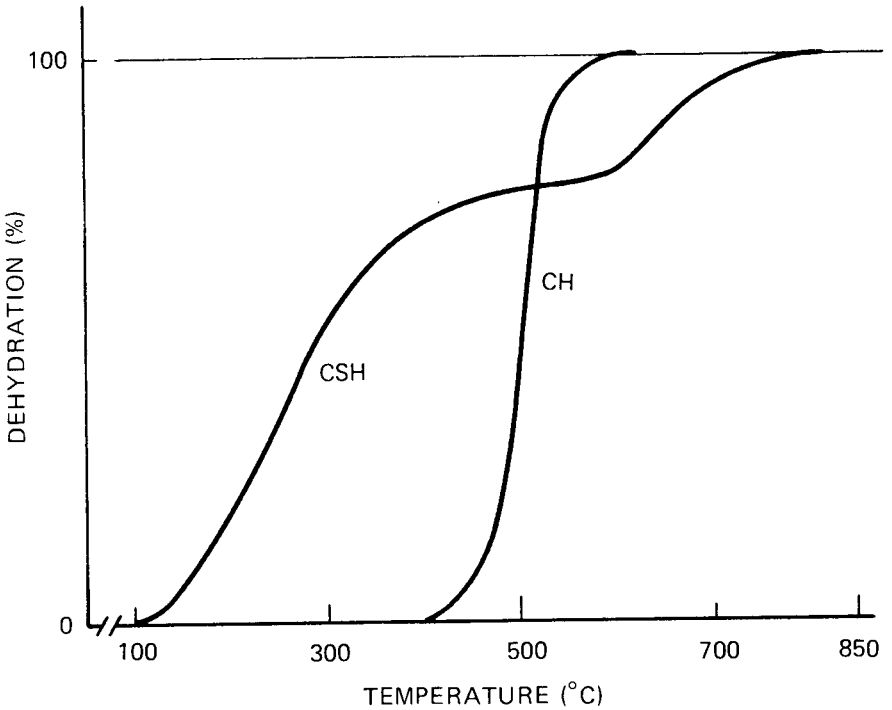


Fig. 1.1.

ORNL–DWG 75–17377

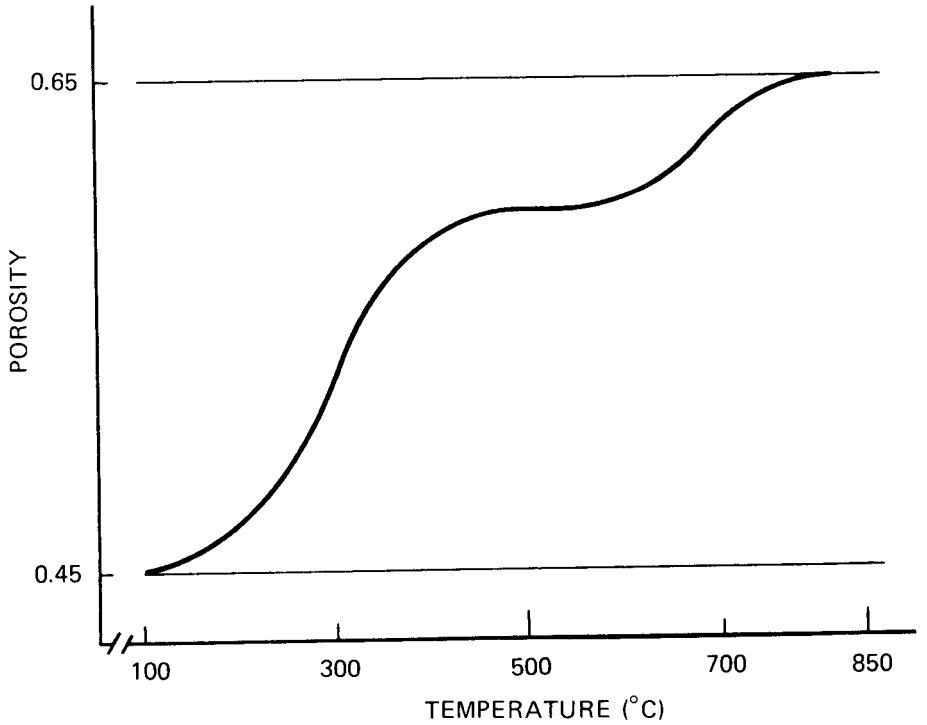


Fig. 1.2.

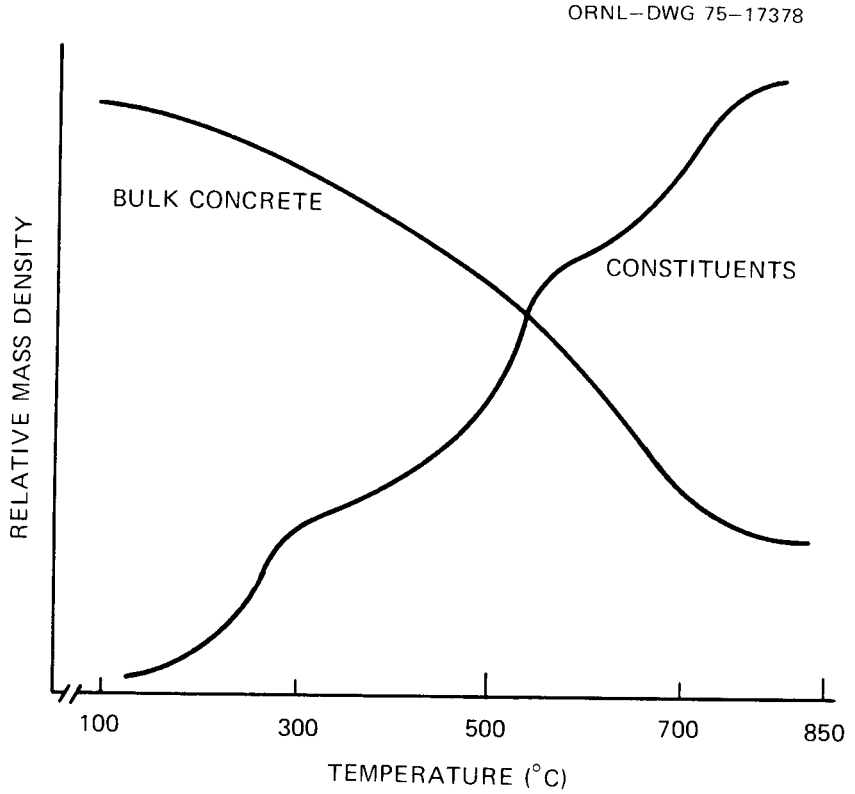
ORNL-DWG 75-17378
BULK CONCRETE
CONSTITUENTS
RELATIVE MASS DENSITY
100
300
500
700
850
TEMPERATURE (°C)

Fig. 1.3.

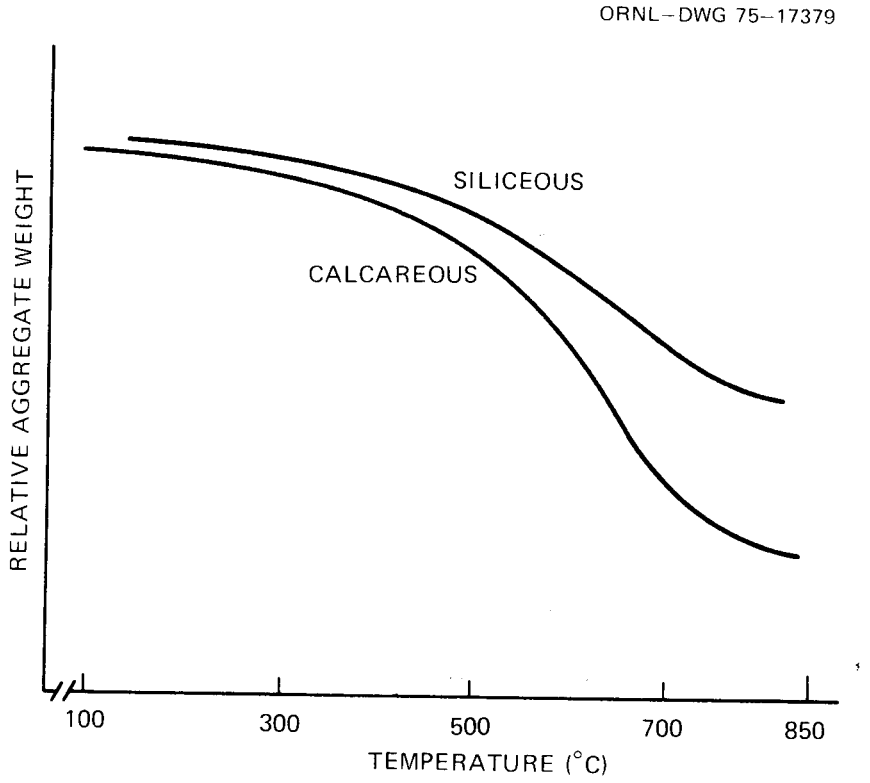
ORNL-DWG 75-17379
SILICEOUS
CALCAREOUS
RELATIVE AGGREGATE WEIGHT
100
300
500
700
850
TEMPERATURE (°C)

Fig. 1.4.

## 2. Thermal Expansion and Shrinkage

### 2.1 Cement paste

Pure hardened cement paste expands slightly on heating in the temperature range up to about 100°C (212°F), displays almost no further expansion from 100°C (212°F) to 300°C (592°F), and shrinks quite strongly when heated beyond 300°C (572°F) [and up to 850°C (1562°F)]. The thermal expansion of cement paste originates from the thermal expansion of the solid constituents of cement gel. Above 300°F (512°F), it is overpowered by thermal shrinkage which is caused by dehydration (i.e., withdrawal of water from the solid microstructure). Thermal shrinkage reaches about 1% (decrease of length) at 800°C (1472°F) (see Fig. 2.1; Harmathy and Allen, 1973; Philleo, 1958; Harada, 1972; Dougill, 1968). Because thermal shrinkage competes with thermal dilatation of the solid constituents, distress is created in the microstructure, and this is one reason for the drop of strength with temperature.

### 2.2 Concrete and aggregates

In concrete, the thermal strain and thermal shrinkage of aggregates succumb to the thermal strains of the aggregate framework, which is almost always positive (expansion on heating rather than shrinkage) (see Fig. 2.2; Harmathy, 1973). However, severe stresses are undoubtedly created in the microstructure by the differences in thermal expansions of cement paste and aggregate, and this again must be one culprit of the significant strength deterioration with temperature.

Typical aggregates for concrete always expand on heating, but considerable differences exist between various aggregates. The thermal dilatation is always less than that of steel (Harada, 1972). The largest volume expansion occurs in quartz ($SiO_2$) and siliceous rocks in general; this is due to $\alpha$-$\beta$ transformation of quartz at about 573°C (1063°F) [see Fig. 2.3, and Soles and Geller (1964), where data on quartz, gneiss, and various igneous and carbonate rocks can be found]. Carbonate aggregate concrete has a thermal expansion coefficient about one-half that of granite

gravel concrete [Browne; below 100°C (212°F)]. Mahmoudzadeh-Rahimi observed $12 \times 10^{-6}$ per °C ($6.7 \times 10^{-6}$ per °F) for quartz aggregate concrete and $6 \times 10^{-6}$ per °C ($3.3 \times 10^{-6}$ per °F) for limestone aggregate concrete.

Artificial aggregates, such as expanded clay, slag, and shale, and also firebrick, show (due to their previous heat treatment) the highest degree of stability with regard to high-temperature exposure; they have the lowest thermal expansion and the fewest chemical changes, change of weight, etc.

Thermal expansion of concrete is not fully reversible on subsequent cooling; the irreversible component, accounting for irreversible chemical changes and changes of microstructure, varies from 10 to 50% of total thermal expansion. The behavior of pure cement paste on second heating is substantially different – the paste expands up to the temperature of previous heating and begins to shrink only when this temperature is exceeded (Harmathy, 1966). When the total strain of specimens loaded during temperature changes was measured, the curves of strain on second heating and cooling were almost the same as those for unloaded companion specimens (Fischer, 1970).

Further test data on the thermal expansion of concrete are given by Philleo (1958); Crispino (1972) (reports on microcracks due to differences in thermal expansion of mortar and concrete); Aoyagi (1972) (reports on the effect of reinforcement on thermal expansion); Abe (1972) (reports on the effect of aggregate content for various aggregates and the reinforcement ratio); Maréchal (1972); Berwanger and Sarkar (1973); Sullivan and Poucher (1968) [who found an increase in the thermal expansion coefficient with temperature, $\alpha = (13.9T - 380) \times 10^{-6}$ for $100°C < T < 300°C$]; Weigler and Fischer (1972) [heating, 600°C (1112°F), and cooling].

## 2.3 Effect of moisture

Nearly all the test data mentioned above pertain to relatively small test specimens which are allowed to lose moisture freely. The loss of moisture takes time (depending on specimen size), and during the process of drying the strain varies. The test data refer usually to the final value of strain after an equilibrium water content for the particular temperature is attained. However, in many reported measurements it is not

certain whether a sufficient time period has been allowed for the attainment of the equilibrium state, and this makes the interpretation and generalization of test results very difficult.

In analyzing concrete structures for nuclear reactors, the thermal response without moisture exchange is of greatest interest because the concrete walls are so thick that no significant amount of moisture can be lost to the environment within a reasonable time. Therefore, specimens which cannot lose moisture are most relevant. It must be emphasized that sealing by a flexible jacket is not sufficient because moisture collects on the specimen surface under the jacket. Unfortunately, it seems that no test data on such truly sealed specimens above 100°C (212°F) have been reported in the literature.

Another poorly known phenomenon of considerable practical interest is the delayed thermal dilatation (Mitchell, 1966; Meyers, 1952; Bažant, 1971) (Fig. 2.4). It consists of a continuous change of thermal dilatation for some time after a time-constant temperature has been reached. The phenomenon has been explored under 100°C (212°F); here, thermal expansion partly recovers (at a decaying rate) after the temperature change ceases. Some test information on delayed thermal dilatation above 100°C (212°F) has been obtained by Gross (1973); it indicates a positive delayed thermal dilatation of about 20% of the instantaneous thermal dilatation.

## 2.4 Drying shrinkage

The loss of evaporable water, which is held in concrete below 105°C (221°F), causes drying shrinkage of concrete; the rate and magnitude of this shrinkage depend on temperature. Generally, both increase with temperature, as confirmed by test data of Seki and Kamasumi (1972) and by Becker and Bresler (1974). For concrete above 105°C (212°F), the drying shrinkage [after surpassing 105°C (221°F)] is completed, unless the temperature rise has been too rapid; if the temperature rise has been too rapid, the drying shrinkage rate is a constant (equal about 0.001; Becker and Bresler, 1974). However, for thick concrete walls from which water cannot escape rapidly, the time-development of drying shrinkage above 100°C (212°F) is of interest. However, no test data are available.

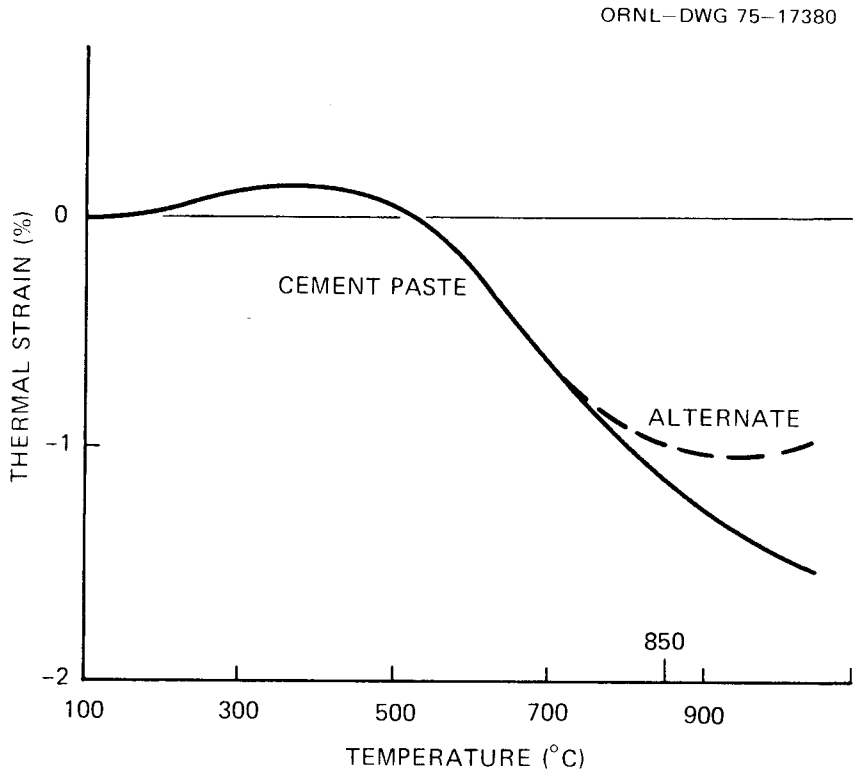
ORNL–DWG 75–17380
THERMAL STRAIN (%)
0
-1
-2
CEMENT PASTE
ALTERNATE
850
100
300
500
700
900
TEMPERATURE (°C)

Fig. 2.1.

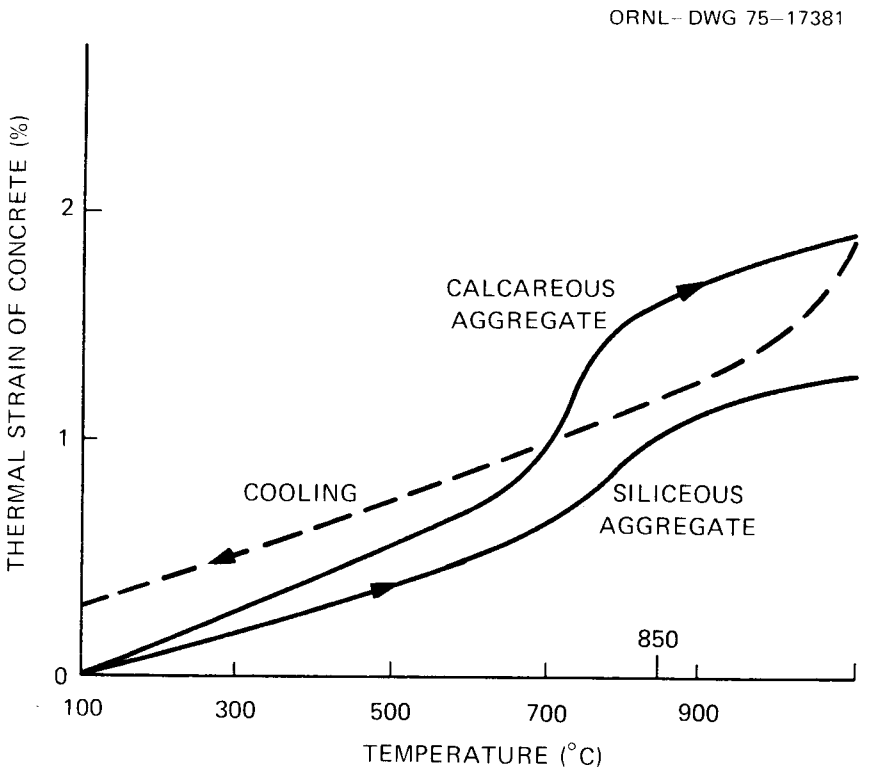
ORNL–DWG 75–17381
THERMAL STRAIN OF CONCRETE (%)
2
1
0
CALCAREOUS
AGGREGATE
COOLING
SILICEOUS
AGGREGATE
850
100
300
500
700
900
TEMPERATURE (°C)

Fig. 2.2.

ORNL–DWG 75–17382

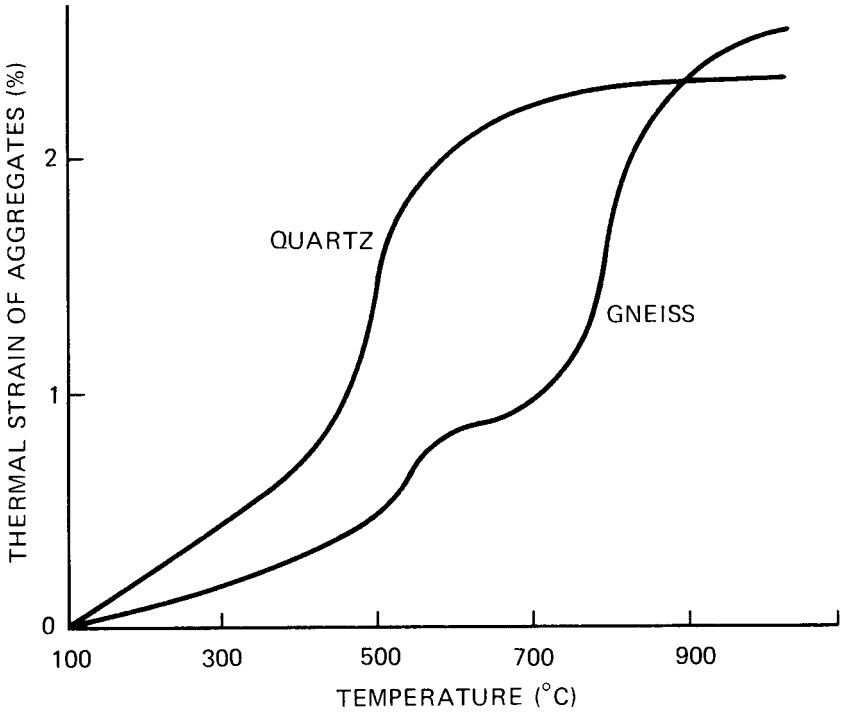


Fig. 2.3.

ORNL–DWG 75–17383

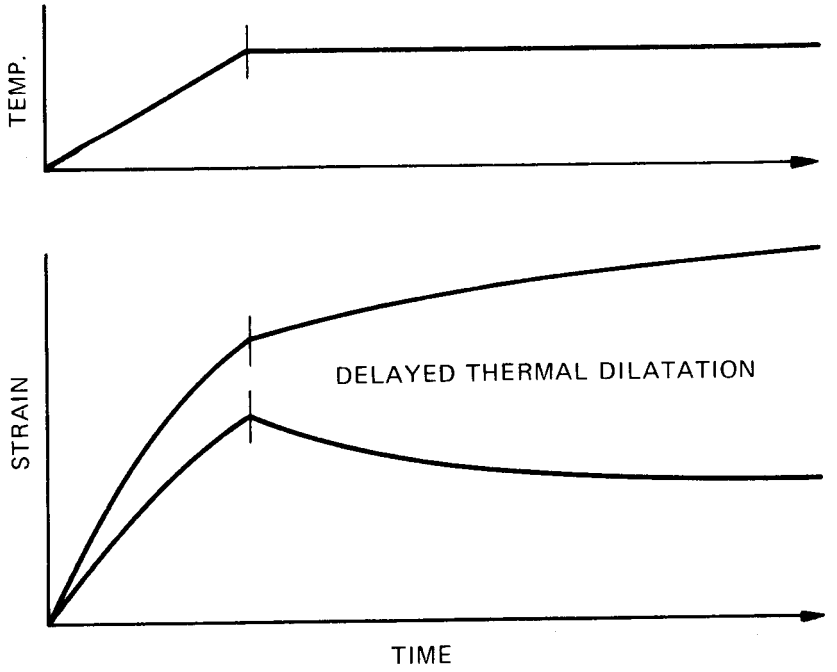


Fig. 2.4.

# 3. Pore Pressure

## 3.1 Experimental facts

Heating of concrete can produce very large pore pressures, which are functions of temperature, history of temperature, size of specimen or structure, and many other factors. Under 100°C (212°F), the phenomenon has been experimentally explored quite abundantly (England and Ross, 1970; England and Skipper, 1973; England, 1970; and Sullivan and Akhtaruzzaman). Beyond 100°C (212°F), very few measurements seem to exist, except for a few by England (1970) (Fig. 3.1). However, the existence of explosive spalling of specimens that are large enough and have not had enough time to dry during temperature rise (Sullivan) indicates that pore pressures above 100°C (212°F) in massive structures can be quite large.

## 3.2 Factors affecting pore pressures

No method of predicting pore pressures is available at present. The problem of equilibrium values of pore pressure is complicated by changes in the volume of pore space due to dehydration and volume changes of solids; by the changes in internal pore surface and the binding energies of water at solid surfaces, both of which affect the amount of water adsorbed on the walls; and by the changes in average pore size and in solute concentrations, which affect capillary tension and the amount of capillary water (Fig. 3.2). The calculation of transient pore pressures further requires knowledge of permeability and diffusivity of water in heated concrete; this is discussed in Section 8.

Hydration at moderate temperatures is known to produce a slight water deficiency in concrete, as manifested by self-desiccation (a decrease of pore relative humidity from 100% to about 97%) in sealed specimens. In the writer's opinion, it is thus possible that dehydration at high temperature produces the opposite (i.e., a surplus of water in the pores of cement paste). However, this could be altered by volume changes associated with other chemical reactions.

For calculations of pore vapor (steam) pressures, the sorption and desorption isotherms (i.e., equilibrium curves of pore relative vapor

pressure vs water content at constant temperatures) are very useful. However, these isotherms are available only for moderate temperatures (e.g., Powers and Brownyard, 1947). Theoretically, it should be possible to also determine them above 100°C (212°F), but this would require measurements at very high ambient steam pressures. No such data are available.

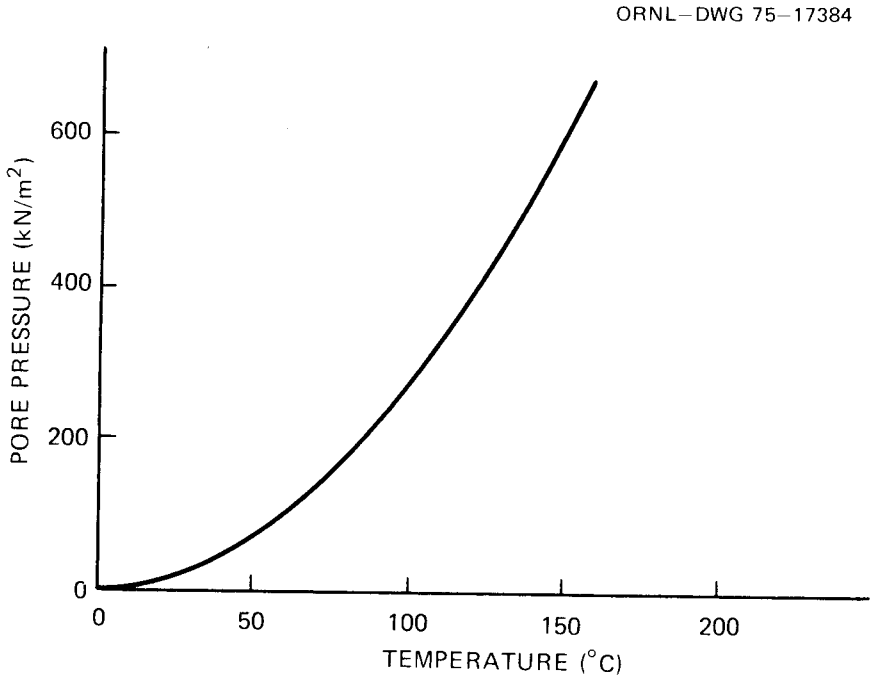
ORNL–DWG 75–17384
PORE PRESSURE (kN/m²)
600
400
200
0
0
50
100
150
200
TEMPERATURE (°C)

Fig. 3.1.

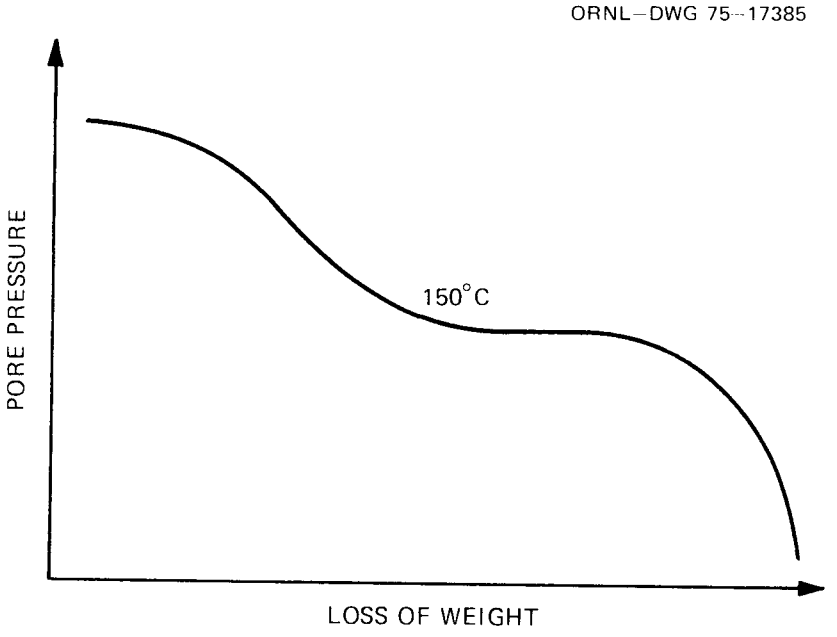
ORNL–DWG 75–17385
PORE PRESSURE
150°C
LOSS OF WEIGHT

Fig. 3.2.

## 4. Strength, Ductility, Stress-Strain Diagrams

Strength of concrete is the best explored material property at high temperature. However, similarly to other properties, all data refer to concrete which was allowed to reduce its moisture content to the equilibrium value for the given temperature at atmospheric pressure. Thus, the data are not very relevant for the study of accident situations in nuclear concrete structures, where the strength at high temperature before the loss of moisture is of main interest. It remains to be determined if this strength is substantially different.

### 4.1 Loss of strength

Cement paste is a material whose microstructure contains bonds of various strength and activation energy. On heating, some of the bonds are lost, especially those which are affected by dehydration, and consequently the strength (as well as elastic modulus) must decrease with increasing temperature. In concrete, further weakening is due to the incompatibility of thermal expansions of aggregate and cement paste. Also, strength of porous materials generally decreases when porosity increases, and thus the porosity increase with temperature also indicates a loss of strength. Experiments show that the basic effect of high temperature is a significant decrease in uniaxial compressive strength, $f'_c$, for both cement paste and concrete. It is marked above 450°C (842°F) and reaches about 10 to 20% of cold strength at 850°C (1562°F) (see Pihlajavaara, 1970; Abrams, 1968; Harada, 1959; Harmathy and Berndt, 1966; Browne, 1967; Desov, 1972; Weigler and Fischer, 1970; Gross, 1973; Lankard, 1968; Becker and Bresler, 1974; Zoldners and Wilson; and Fig. 4.1). In young concrete, the strength may slightly increase on moderate heating [<200°C (392°F)], undoubtedly due to vastly accelerated hydration (Waubke, 1973; Harada; Weigler and Fischer; Fischer, 1970).

The residual strength (i.e., the strength after cooling to room temperature from the previous high temperature) is normally lower than that at high temperature (Fischer, 1970; Malhotra, 1956; Waubke, 1973).* This

*Strength in pure torsion up to 800°C (1472°F) was reported by Thelandersson (1974) along with split cylinder and flexural strength.

is caused by cracking on cooling. The strength is partly recovered within months after high-temperature exposure (Harada, 1959; Fischer, 1970; Weigler and Fischer, 1972; Pihlajavaara, 1972; Zoldners and Wilson) (but not for tensile strength; Thelanderson, 1972).

## 4.2 Effect of drying and heating rate

The effect of drying on strength was investigated by Pihlajavaara, who found that the strength of dry heated concrete is substantially higher than that of wet heated concrete [up to 300°C (572°F)], provided that the drying can be accomplished without microcracking (for which the use of small specimens is probably necessary, in the writer's opinion).

The rate of heating, which affects the magnitude of (macroscopic as well as microscopic) thermal stresses in concrete specimens, also has a significant effect on strength; for faster heating the strength is less* (Harada, 1972; Weigler and Fischer, 1972) because at a higher heating rate the differences in temperature and moisture contents throughout the specimen are higher than the pore pressures and the reduction of thermal stress due to creep is less pronounced. Because heat conduction, moisture diffusion, and thermal stresses depend on the size, shape, and many other parameters, the effect of heating rate can be widely different in various situations and cannot be viewed as a material property.

## 4.3 Ductility and stress-strain diagrams

Ductility, as characterized by the strain at peak stress on the stress-strain diagram (Fig. 4.3), has been investigated by Harmathy and Berndt (1966). The ductility was found to increase from about 0.3 to 0.5% at 20°C (68°F) to about 2% at 750°C (382°F) for previous heating of 1 hr duration, and about 1.5% for a 24-hr duration.

The stress-strain diagrams up to failure were reported by Harmathy and Berndt (1966), Fischer (1970), Weigler and Fischer, and Harada (1959). The tangent moduli decrease with temperature (see Fig. 4.2). Fischer (1970) measured stress-strain diagrams up to 600°C (1112°F) and also after subsequent cooling and found that after cooling from temperatures over

*But tensile strength decreases more (Thelandersson, 1972).

400°C (752°F), the slope of the diagram was distinctly less for quartz aggregate and slightly less for baryte aggregate. (The duration of temperature exposure did not affect the stress-strain curves appreciably.) For concrete loaded during heating, Fischer found a smaller decrease of slope of the stress-strain diagram with temperature. [For torque-twist diagrams, see Thelandersson (1974).*]

## 4.4 Moisture content and other factors

A substantial difference in strength is to be expected before and after the loss of free moisture, because free moisture is known to decrease the surface energy (surface tension) of solids in cement paste and thereby the strength of bonds between the surfaces of solid particles. Fischer (1970) has confirmed this for 100°C (212°F), but apparently no data are available for higher temperatures.

The effect of aggregate type was studied by Fischer (1970), by Weigler and Fischer (1960) (quartz, baryte), by Abrams, by Zoldners and Wilson, and by Desov (1972) (heavy aggregate). Nasser (1973) found that air entrainment is beneficial in diminishing the strength loss up to 100°C (212°F).

Flexural strength, which is basically a measure of tensile strength, was reported by Gross (1972) and by Sullivan and Poucher (1970). They found that the flexural strength drops with temperature even more severely than does the compressive strength and the direct tensile strength (Thelandersson, 1972).

The loss of strength of loaded concrete is about the same as that of unloaded concrete (Fischer, 1970). (This holds for pulsating loads as well.) Cyclic temperature does not cause additional strength loss unless the previous peak temperature is exceeded (Fischer, 1970). The residual strength of concrete is not affected by the cooling rate (Fischer, 1970);

---

*Torsional ductility tremendously increases at high temperature (Thelandersson, 1974).

it decreases slightly in air storage after cooling* (Fischer, 1970). Duration of temperature exposure has no appreciable effect on strength (Fischer, 1970).

The age effect on concrete strength is also apparent at elevated temperatures (Seki and Kawasumi). At temperatures under 100°C (212°F), elevated temperature exposure accelerates hydration and thereby increases strength if concrete is young (Fischer, 1970).

Almost no data exist on multiaxial strength at elevated temperature, but a rational extrapolation of uniaxial strength is probably possible (Browne, 1967).

The loss of strength at high temperature appears to be much less when concrete is restrained, that is, when it cannot freely expand (Lankard, 1968), and also when concrete is loaded during heating (Fischer, 1970). This beneficial phenomenon (Fig. 4.4), which is of interest for nuclear concrete structures, is undoubtedly achieved by confining pressure (thermal stress) which is generated when thermal expansion is restrained. This pressure prevents the formation of microcracks in concrete and the ruptures of some of the bonds. Generally, whenever heating of a concrete wall is localized, there should be large confining stresses generated by thermal expansion.

Cyclic heating (Lankard, 1968; Fischer, 1970) generally gives less strength than a single heating, undoubtedly because of a higher degree of microcracking due to repeated thermal stresses (Fig. 4.4).**

## 4.5 Thermal cracking

The extent of visually observed cracking is also reported in the literature, and often it is noted that cracking becomes particularly severe above 500°C (932°F) (Waubke, 1973; Lankard, 1968; Harada). However, the observations are rather inconsistent; for example, in Fischer's tests (1970), specimens cooled rapidly from 600°C (1112°F) showed almost no

---

*But the effect of heating rate and of nonuniform thermal stress on direct tensile strength is negligible (Thelandersson, 1972).

**The times to failure under various values of constant load (i.e., the long-time strength) were measured in torsion by Thelandersson (1974).

visible cracks, whereas the slowly cooled specimens did. The inconsistency of results is not surprising because cracking should depend on the thermal stress, which is affected by size, shape, heating rate, initial shrinkage stresses, etc., and on the pore pressure, which also depends on pore size change, dehydration, specimen size, shape, etc.

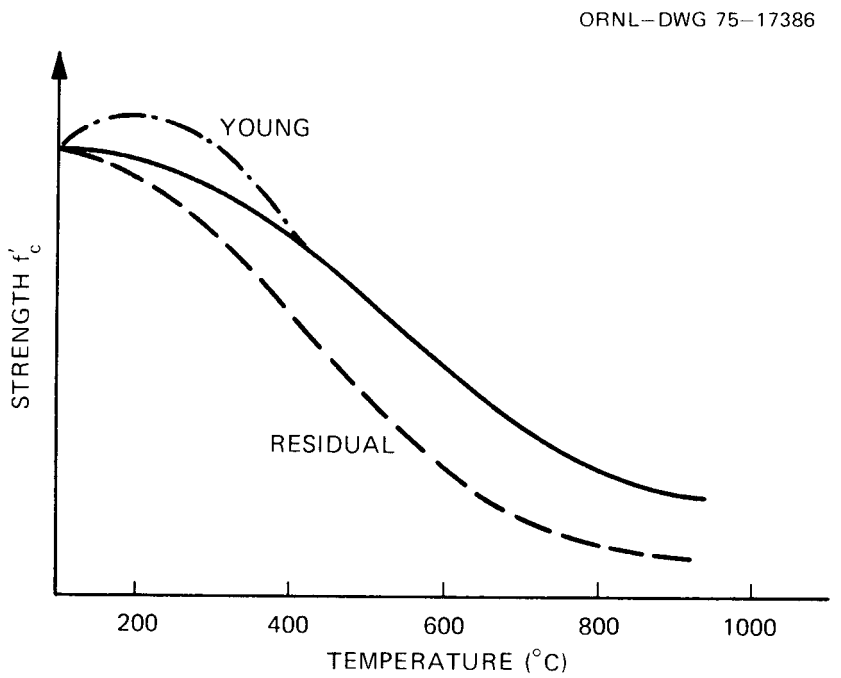
ORNL–DWG 75–17386
YOUNG
RESIDUAL
STRENGTH $f'_c$
200
400
600
800
1000
TEMPERATURE (°C)

Fig. 4.1.

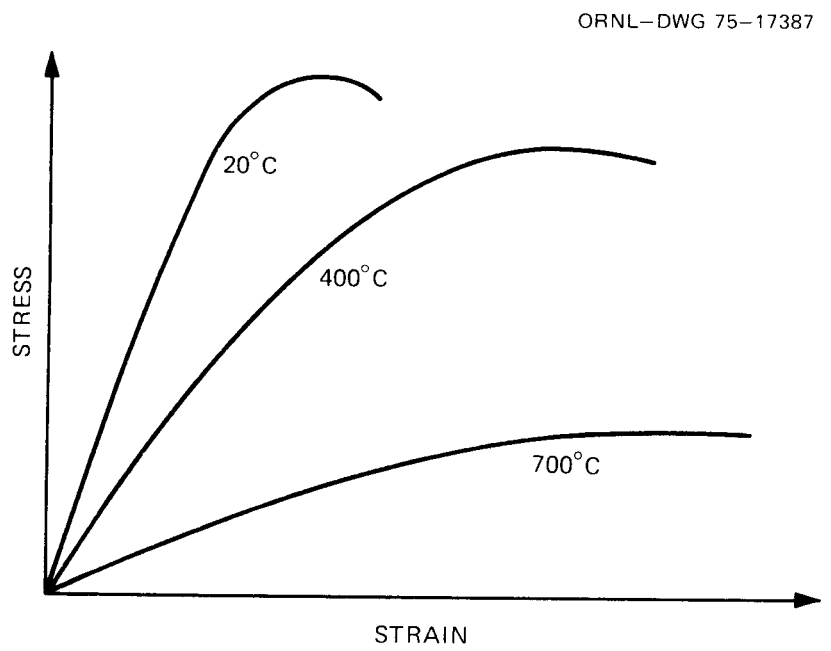
ORNL–DWG 75–17387
20°C
400°C
700°C
STRESS
STRAIN

Fig. 4.2.

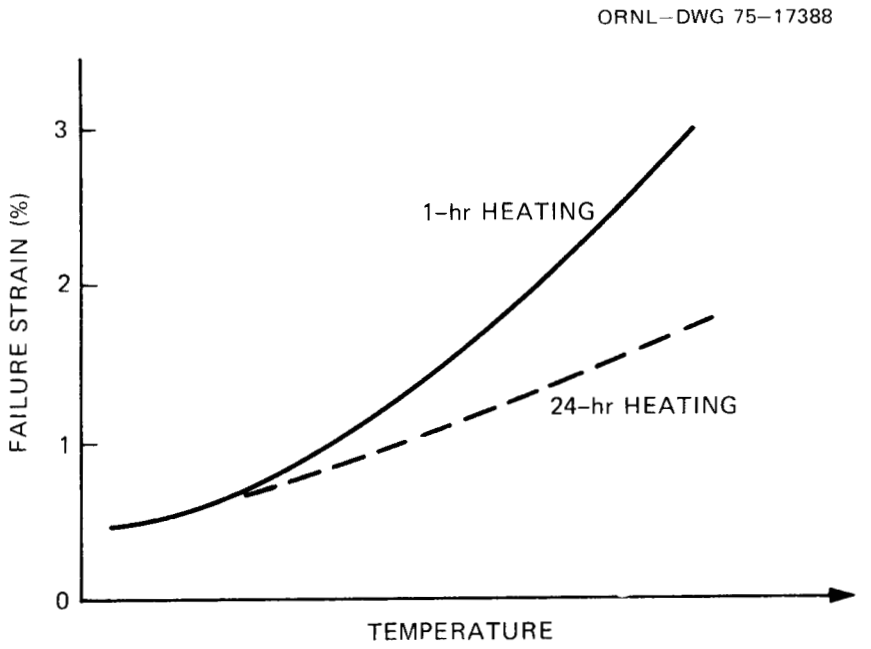
ORNL–DWG 75–17388
FAILURE STRAIN (%)
3
2
1
0
1-hr HEATING
24-hr HEATING
TEMPERATURE

Fig. 4.3.

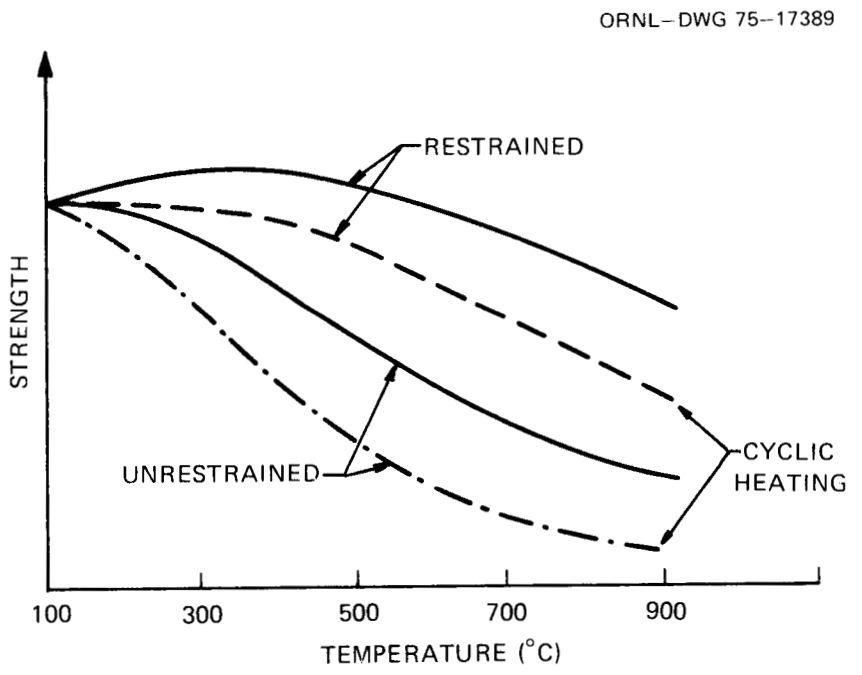
ORNL–DWG 75–17389
STRENGTH
RESTRAINED
UNRESTRAINED
CYCLIC
HEATING
100
300
500
700
900
TEMPERATURE (°C)

Fig. 4.4.

# 5. Modulus of Elasticity and Poisson Ratio

## 5.1 Basic facts

As mentioned previously, the breakage of bonds in the microstructure of cement paste due to a temperature increase results in a reduction of the elastic modulus. This has been observed in cement paste [Harmathy and Berndt (1966)]; in concrete or mortar (Maréchal, 1972; Harada et al., 1972; Aoyagi et al., 1972; Crispino, 1972; Philleo, 1958; Gross, 1972; Bertero and Polivka, 1972; Cruz, 1966; Sullivan and Poucher, 1971; Lankard, 1971; Ohgishi, 1966; Berwanger and Sarkar, 1973; Nasser, 1973); and indirectly in bending (Sullivan and Labani, 1974); see Fig. 5.1. However, in details, there is some quantitative disagreement between various types of tests, which is due partly to the ambiguity in the definition of elastic modulus E and partly to the effect of the simultaneously proceeding loss of moisture. The ambiguity of the value of E consists in the degree to which the time-dependent creep strain is separated from the instantaneous strain. Usually, the conventional value of E corresponds to a loading of several minutes duration, and this includes about 25% of creep strain at room temperature and still more creep strain (due to higher creep) at high temperatures.

The dynamic modulus, which is little affected by creep (measured by Philleo, 1958; Crispino, 1972; Berwanger and Sarkar, 1973), decreases with temperature similarly and is a more meaningful measure of the temperature effect on elastic response; but its value, also, includes a certain (though much smaller) percentage of creep strain, depending on temperatures.

## 5.2 Effect of moisture, drying, and heating rate

The drying which occurs simultaneously with temperature increase reduces the apparent E value because any movement of moisture results in rupture of some bonds. Thus, during the fast drying which accompanies heating, E drops more rapidly than it does at slow drying (exhibited by larger specimens, e.g.). This is corroborated by the tests of Gross (1972) and of Sullivan and Labani (1974). The effect of the moisture state is also manifested by a difference in the elastic modulus between sealed and unsealed specimens. According to Lankard (1968), sealed specimens exhibit

lower E than dried specimens [although Bertero and Polivka (1972) have not observed a strong effect]. This may be explained by smaller binding energy between wetted solid surfaces.

After drying is terminated, E is higher than before drying if drying occurs at the same temperature (which in turn is higher than the value during drying). This is explained again by binding energy and the dependence of surface tension of solid particles on moisture content.

The effect of the rate of heating on the elastic modulus is similar to that on strength. For faster heating, the elastic modulus is less (Harada), owing to higher thermal stresses, higher pore pressures, higher stresses due to thermal shrinkage, and greater damage to microstructure. Cyclic heating further reduces the elastic modulus (Lankard, 1968).

## 5.3 Other effects

The drop of E with temperature also depends on the type of aggregate used (Fig. 5.2). Aggregates that are more compatible and chemically more stable, such as limestone, give a smaller drop in E (Cruz, 1966). In high-strength concrete, the decrease of E with temperature seems to be somewhat stronger than it is in low-strength concrete (Aoyagi).

The value of elastic modulus after a previously heated concrete is cooled (residual modulus) shows a drop with temperature similar to that of concrete being heated for the first time. This indicates that the changes of microstructure and bonding are permanent (Harada).

## 5.4 Shear modulus and Poisson ratio

The dependence of the shear modulus of elasticity G is similar to that of E (Cruz, 1966; Anderberg, Thelandersson, 1974).

Poisson's ratio $\nu$ has been observed to drop with heating from about 0.2 at room temperature to about 0.1 at 400°C (752°F) (Fig. 5.3, Maréchal, 1974). This is undoubtedly a manifestation of weakening of the microstructure (rupture of bonds) due to heating. When the effect of transient moisture states and drying is included, still greater variations in the values of $\nu$ are observed. In general, $\nu$ is less after drying than before, as measured on sealed specimens. In these, the drop in $\nu$ with temperature

is small (from 0.2 to about 0.18) (Bertero and Polivka, 1972). Poisson's ratio for creep has also been measured (York et al., 1974; Bertero and Polivka, 1974).

The drop in Poisson ratio is undoubtedly a manifestation of a weakening of the microstructure by bond breakage due to heating as well as by microcracking. The latter effect should be much smaller when the heated concrete is restrained and/or subjected to confining pressure, which is typical of accident situations in nuclear reactor structures. Under high confining pressure, the Poisson ratio is likely to be almost the same as it is at room temperature (about 0.2), although apparently no data exist to confirm this hypothesis.

## 5.5 Deflection of beams

It is possible to make indirect inference on elastic modulus from test data on deflections of beams at various temperatures. Such data have been reported by Sullivan [up to 610°C (1130°F) for reinforced concrete and plain concrete, the reinforced one being more sensitive to temperature because of heat effect on steel]; Sullivan and Poucher (1968) [up to 360°C (680°F)]; and Lankard (1968). However, in addition to elastic modulus, deflection depends on many other factors (cracking, stress distribution, etc.).

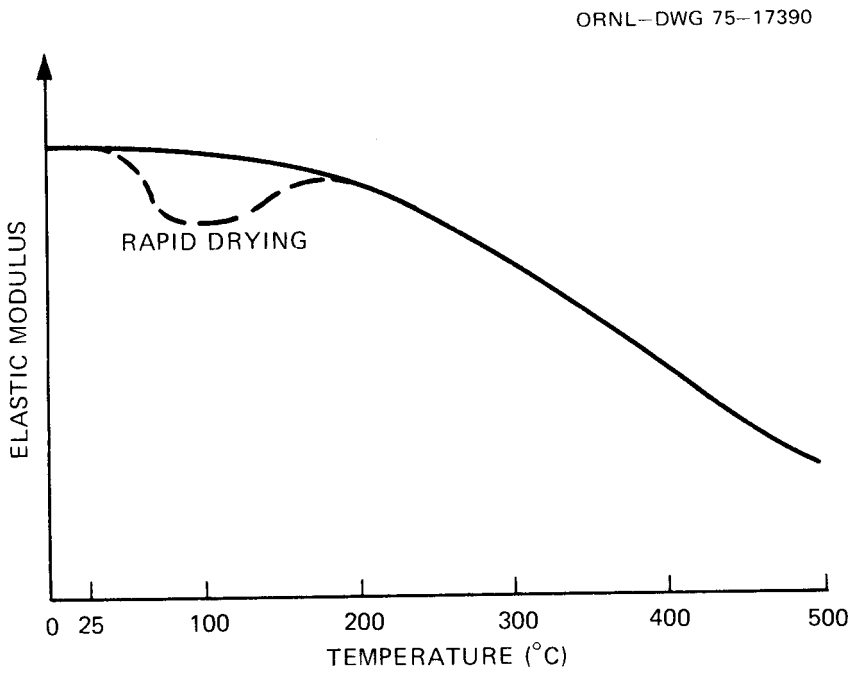
ORNL–DWG 75–17390
ELASTIC MODULUS
RAPID DRYING
0
25
100
200
300
400
500
TEMPERATURE (°C)

Fig. 5.1.

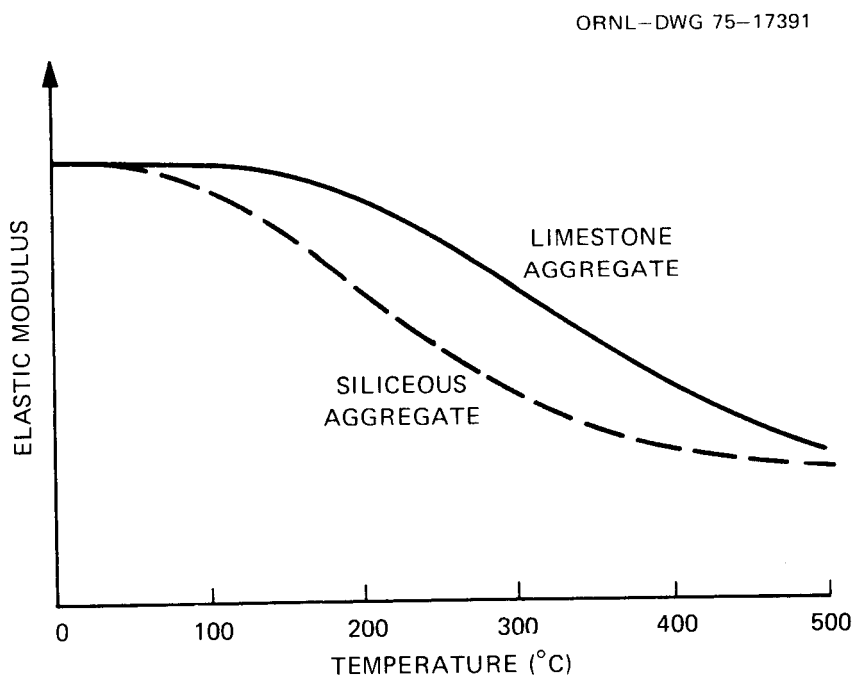
ORNL–DWG 75–17391
ELASTIC MODULUS
LIMESTONE
AGGREGATE
SILICEOUS
AGGREGATE
0
100
200
300
400
500
TEMPERATURE (°C)

Fig. 5.2.

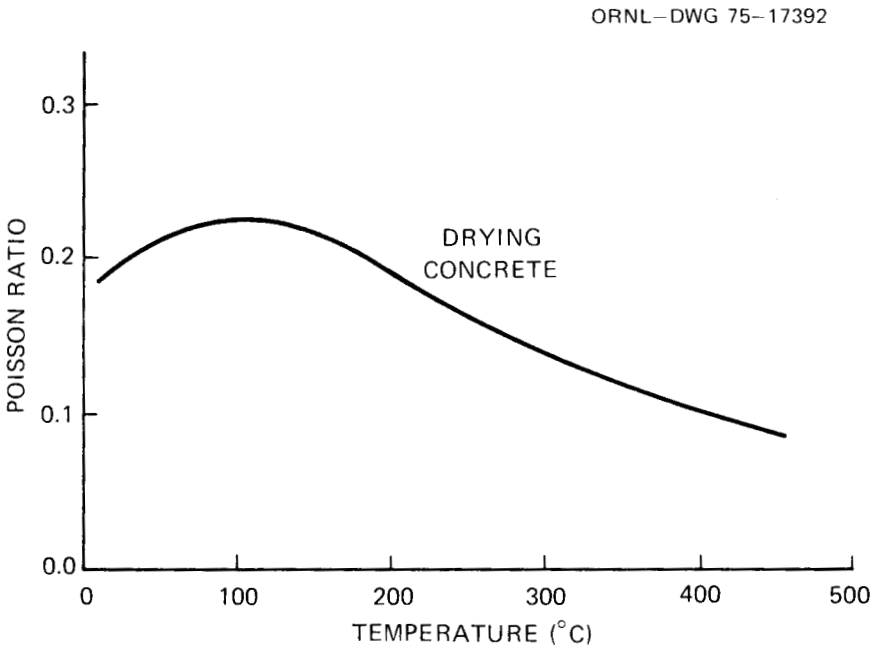
ORNL–DWG 75–17392
POISSON RATIO
0.3
0.2
0.1
0.0
DRYING
CONCRETE
0
100
200
300
400
500
TEMPERATURE (°C)

Fig. 5.3.

# 6. Creep

## 6.1 Physical nature of thermal effect

Increase of creep with an increase in temperature is the basic effect in all solids. Creep of concrete at moderate stress levels originates in the hardened cement paste and is probably due (for compression) to the mutual approach of adjacent laminar particles of cement gel. The approach of particles results from diffusion of some components of the solid particles (perhaps Ca ions) out of the thin gaps between the particles (of molecular-size thickness) out into larger (capillary) pores (Bažant, 1972, 1975). The diffusion is greatly facilitated by the presence of water in the gaps between particles and is further strongly accelerated when the water molecules move along the gaps, which happens when concrete is drying (or wetting).

The effect of temperature on creep (Figs. 6.1 to 6.3) is to accelerate the diffusion of the solid components, as well as water, along the gaps between particles, which is a process that should obey the activation energy model. Another effect of temperature consists in acceleration of hydration (aging) at moderate elevated temperatures. At high temperatures [above 105°C (221°F)], the reverse of this effect takes place; that is, dehydration occurring in a loaded concrete probably accelerates creep.

## 6.2 Effect of moisture loss

Further acceleration of creep is undoubtedly caused by movement of moisture (migration of water molecules), the same as that going on at room temperature. In unsealed specimens the drying has already become significant in the range 70 to 100°C (158 to 212°F). After exceeding 100°C (212°F), drying is very rapid, and indeed in this region (i.e., during drying) there is a marked increase of creep rate until a stable moisture content is reached (Maréchal, 1968; see Fig. 5.1).* After the moisture is lost and a stable moisture content for the given temperature is attained,

---

*See also Thelandersson (1974) and Anderberg and Thelandersson (1973).

the creep rate becomes less than that before the loss of moisture (which in turn is less than that during the loss of moisture). This is evidenced in the moderate temperature range [(70–100°C) (158–212°F)] by the decrease of creep rate of unsealed specimens when 70 to 90°C (158 to 194°F) is exceeded [see Geymeyer (1970), Nasser and Neville (1965), Browne (1967), Hannant (1967), Maréchal (1968), Browne and Blundell (1969)].

Movements of moisture are also induced by temperature changes, and creep is greatly accelerated by any temperature change (Fig. 6.4; Nishizawa, 1972; Illston, Sanders, 1973; Arthanari and Yu, 1967; Fahmi, Polivka, Bresler, 1972; Johansen, Best, 1962; Serafim, Guerreiro, 1960; Wallo, 1965; York, Kennedy, Perry, 1972).*

Creep tests of specimens enclosed in rather flexible metallic jackets that prevent escape of moisture to the environment but do not prevent diffusion of water out of the specimen into the gap between the specimen and the jacket have been carried out by Bertero, Polivka, and Bresler (1972).

## 6.3 Basic facts on high-temperature creep

Nearly all the testing of creep at high temperature [well surpassing 100°C (212°F)] has been confined to specimens which were freely losing their moisture; see Maréchal (1968), Crispino (1972), Cruz (1968), Bertero, Polivka, and Bresler (1968) [and up to 140°C (284°F); Hickey (1967), England and Ross (1962)]. From these tests it appears that in predried specimens (i.e., those which have lost their evaporable water), the creep rate $\epsilon$ increases with temperature [up to 400°C (752°F)] according to the rate process theory (Arrhenius equation):

$$\epsilon = \epsilon_0 \exp\left(\frac{Q}{RT_0} - \frac{Q}{RT}\right),$$

where $T_0$ is chosen reference temperature, $\epsilon_0$ is corresponding creep rate, Q is activation energy of creep** (Maréchal, 1968; Bažant, 1975, 1972). This dependence has been verified up to 400°C (752°F) (Maréchal, 1968).

---

*See also Thelandersson (1974) for creep in torsion up to 480°C (896°F).

**Approximately, Q/R = 1600 to 2000°F above 100°C (212°F) (see also Thelandersson, 1974).

Very little information beyond 400°C (752°F) is available at present. Fischer (1970) observed creep up to 600°C (1112°F) for 30-hr load and temperature durations and found that creep at 600°C (1112°F) was less than that at 450°C (842°F); this indicates that the activation energy formulation loses validity before reaching 600°C (1112°F) and must be due to the strong dehydration between 450 and 600°C (842 and 1112°F). At one-half the failure load and a 30-hr load duration, Fischer indicates a creep strain of ~0.1% for both quartz and baryte aggregates at 300°C (572°F) and, in the range 300 to 600°C (572 to 1112°F) ~0.25% for quartz aggregate and ~0.65 to 0.80% for baryte aggregate. Also, he found a linear dependence of creep on stress at high temperatures.

The shape of the creep curves in time (Figs. 6.2 and 6.3) may be described by power curves, $\epsilon \sim t^n$ (t = creep duration) with a small exponent, $0 \leq n \leq 1/3$. Curves of the type $\epsilon \sim \log t$ have also been used, but they seem to underestimate creep toward end of life.

Creep in torsion up to 480°C (896°F) was measured by Thelandersson (1974).

For moderate climate temperatures, the effect of variable stress history with simultaneous aging and of multiaxial stress states has been explored in depth. For the working stress range, the linear viscoelasticity of aging materials appears to be the appropriate formulation, but there seem to be no data to indicate whether this formulation can be extended to high temperature. However, the effect of aging (hydration) is certain to be negligible above 100°C (212°F), while possibly the reverse process (dehydration) may be of importance for creep. Also, the range of memory (history dependence) at high temperature is likely to be short, and possibly the total strain rate under generally variable stress would be just a function of current stress rate and current stress (as in a simple Maxwell solid).

## 6.4 Various factors affecting creep

Connected with the moisture content and drying effect already discussed is the effect of the size and shape of the structural member on the time rate of moisture loss. As a limiting case, massive concrete walls such as those in nuclear structures cannot lose their moisture on

rapid heating, because the diffusion of moisture out of a very thick solid takes many days even at very high temperatures. Therefore, creep occurs essentially at constant total water content, although the subdivision of water content into steam, free liquid (capillary) pore water, physically adsorbed water, and chemically bound water varies with temperature. Creep at such conditions undoubtedly occurs in the presence of a high pore pressure and, in case of local heating of a massive wall, a high confining thermal stress in the solid microstructure.

At present, there seem to be no test data on creep in such mass concrete conditions [beyond 100°C (212°F)]. To be sure, the need for testing creep without moisture loss has been realized before, but the tests which were carried out included only specimens sealed in metallic jackets which were flexible and allowed moisture to diffuse out of specimen and collect, at high pressure, under the jacket. (Note, however, that a very stiff and tight jacket cannot be used because the jacket stiffness would affect the deformation of the specimen.) On the other hand, at moderately elevated temperatures [below 100°C (212°F)], there is no problem in achieving mass concrete conditions by using metallic jackets. Several tests of such specimens have been made (Nishizawa, 1972; England and Ross, 1962; Hickey, 1967; Nasser and Neville, 1967; Hannant, 1967; Serafim and Guerreiro, 1960; Arthanari and Yu, 1967; Browne, 1967; McDonald, 1972; Wallo, Yuan, Kesler, 1965; York, Kennedy, Perry, 1972; Ruetz, 1965; Hansen, 1960). Specimens in water have been also tested in this range (Neville and Liszka, 1973).

Creep in bending was tested by Sullivan (1971) and by Sullivan and Labani (1974). The effect of temperature cycles on creep was investigated by Nishizawa (1972) and by Fahmi, Polivka, Bresler (1972). The activation energy of creep at moderate elevated temperatures was determined by Bažant and Wu (1974) and at high temperatures by Sullivan (1971). Creep of high-strength and low-strength concrete was compared by McDonald (1972) and Aoyagi (1972). Creep of young and 50-year-old concretes under 100°C (212°F) was compared by Nasser and Neville, and creep for ages at loading from 7 to 400 days and temperatures up to 95°C (203°F) was measured by Browne and Blundell (1967). Torsional creep at variable temperatures under 100°C (212°F) was investigated by Fahmi, Polivka, and Bresler (1972) (Fig. 6.4).

Creep of concretes with various aggregates up to 95°C (203°F) (limestone and dolerite) was studied by Browne and Blundell (1967). The Poisson ratio in creep below 100°C (212°F) was determined by Hannant (1967) and by Arthanari and Yu (1967). Creep recovery under 100°C (212°F) was observed by Nasser and Neville (1966) and Arthanari and Yu (1967). Relaxation of beams up to 600°C (1112°F) was tested by Sullivan and Labani (1974).

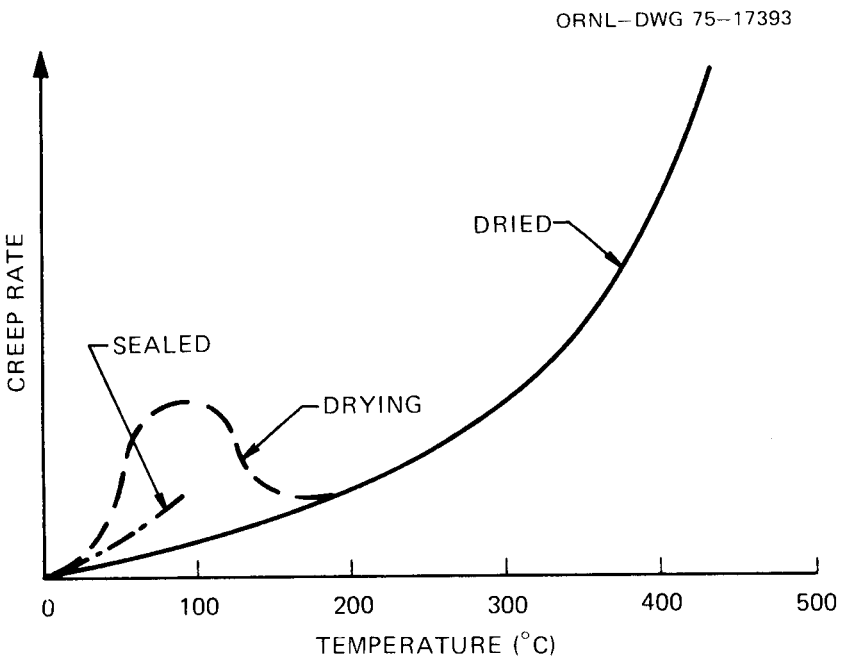
ORNL-DWG 75-17393
CREEP RATE
DRIED
SEALED
DRYING
0
100
200
300
400
500
TEMPERATURE (°C)

Fig. 6.1.

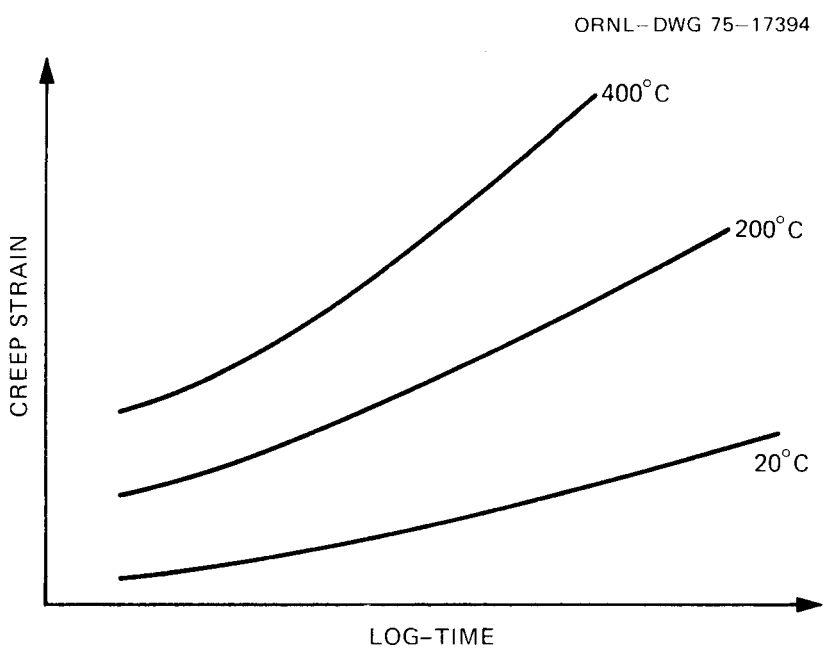
ORNL-DWG 75-17394
CREEP STRAIN
400°C
200°C
20°C
LOG-TIME

Fig. 6.2.

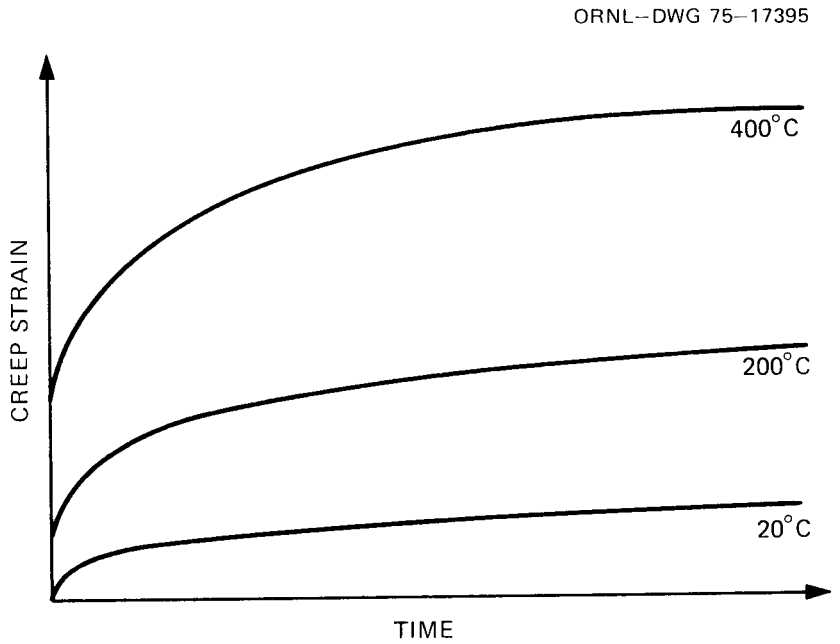
ORNL–DWG 75–17395
400°C
200°C
20°C
CREEP STRAIN
TIME

Fig. 6.3.

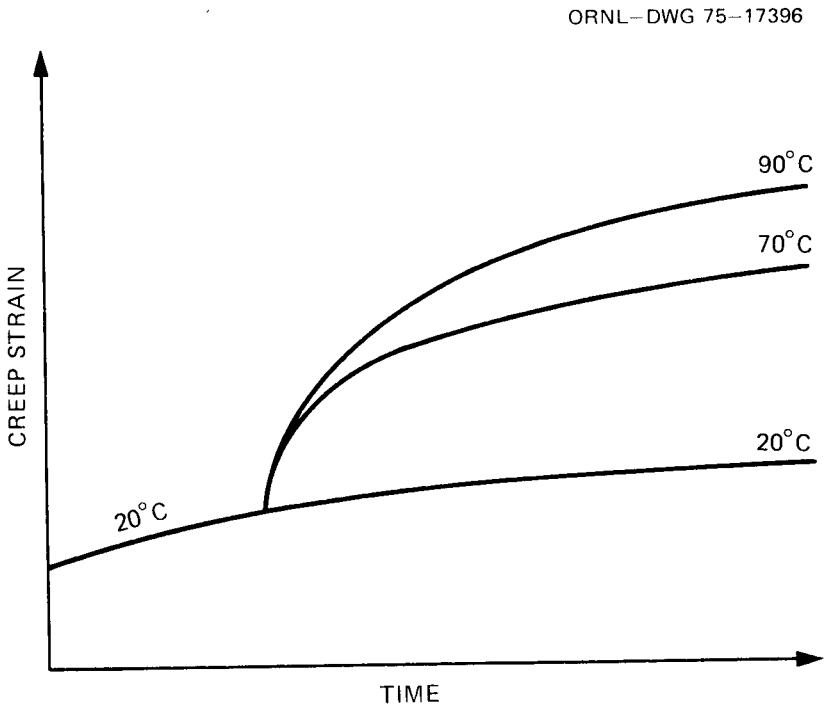
ORNL–DWG 75–17396
90°C
70°C
20°C
20°C
CREEP STRAIN
TIME

Fig. 6.4.

# 7. Heat Capacity

## 7.1 Physical nature

As with other properties, the evaluation of heat capacity (specific heat) of concrete is substantially complicated by the chemical and structural changes in the material, by changes in the binding energy of water, by phase changes of water, and by changes in moisture content. These changes, such as dehydration or vaporization of water, the escape of water molecules from the adsorption layers, dissociation of calcium hydroxide, etc., either require heat to be supplied or evolve heat (latent heat); and in observing bulk cement paste or concrete they appear as apparent, hidden components of heat capacity $C_p$. Likewise, changes in the aggregate, such as $\alpha$-$\beta$ transformation of quartz or dissociation of carbonates, also consume or evolve heat. In general, the apparent bulk heat capacity at constant pressure p may be expressed as (Harmathy and Allen, 1973; Harmathy, 1970):

$$C_p = \left(\frac{\partial H}{\partial T}\right)_p = \left(\frac{\partial H}{\partial T}\right)_{p,\xi} + \left(\frac{\partial H}{\partial \xi}\right)_{p,T} \frac{\partial \xi}{\partial T} ,$$

where H is enthalpy per unit mass of bulk cement paste or concrete, T is temperature, and $\xi$ is degree of chemical reaction or phase transition taking place at the given temperature. The last term in this expression is the apparent, hidden contribution to heat capacity $C_p$.

## 7.2 Observed temperature dependence

The total apparent heat capacity $C_p$ of cement paste rises with temperature up to about 500°C (932°F) and then declines up to 1000°C (1832°F); the true heat capacity, the first term in the above equation, rises uniformly and moderately up to 1000°C (1832°F) (Harmathy and Allen, 1973; Harmathy, 1970). The heat capacity of most aggregates generally increases smoothly up to 900°C (1652°F) (e.g., anorthosite – Harmathy), about doubling the value at 25°C (77°F), but siliceous aggregates show a peak (apparent $C_p$) around 575°C (1067°F), the temperature of $\alpha$-$\beta$ quartz transformation (Harmathy and Allen). The heat capacity of concrete [generally of

the order of $0.84 \times 10^6$ to $1.26 \times 10^6$ J/kg°C (200 to 300 Btu/lb°F)] is dominated by that of the aggregate and shows a similar trend with temperature (Fig. 7.2). A similar rise of the $C_p$ of concrete was found by the U.S. Bureau of Reclamation and by Browne (1967). The effect of various aggregates (granite, serpentine, limonite, magnetite) on heat capacity was reported by Desov and Jankelev (1972).

Plots of the temperature dependence of enthalpy of the constituents of cement paste have been given by Harmathy (1970).

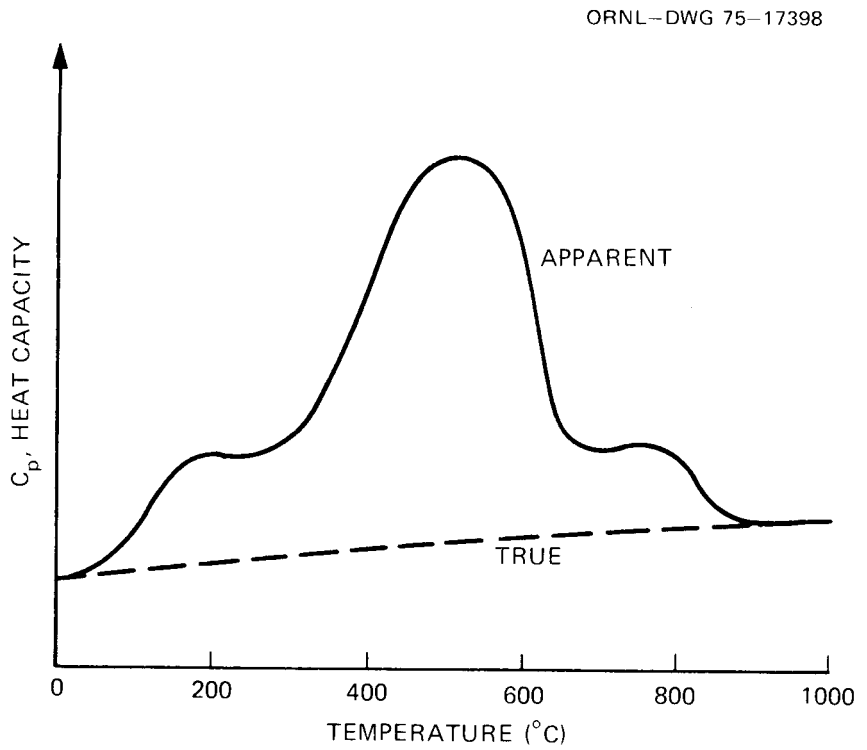
ORNL–DWG 75–17398
$C_p$, HEAT CAPACITY
APPARENT
TRUE
0
200
400
600
800
1000
TEMPERATURE (°C)

Fig. 7.1

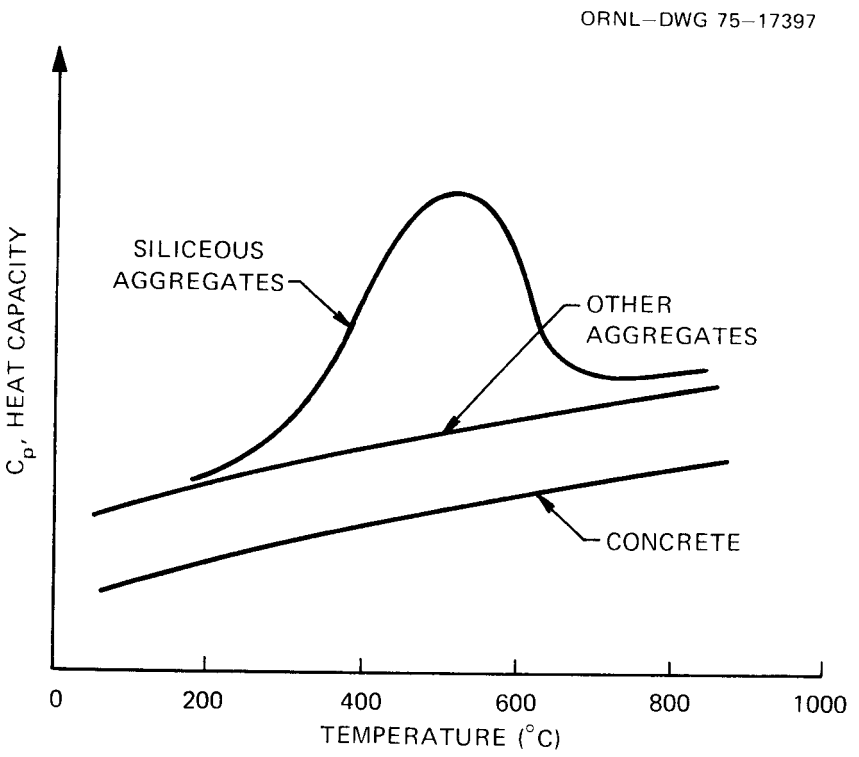
ORNL–DWG 75–17397
$C_p$, HEAT CAPACITY
SILICEOUS AGGREGATES
OTHER AGGREGATES
CONCRETE
0
200
400
600
800
1000
TEMPERATURE (°C)

Fig. 7.2.

# 8. Thermal Conductivity and Diffusivity

## 8.1 Basic facts on conductivity

Thermal conductivity and diffusivity must be known for prediction of temperature changes. Thermal conductivity of concrete is a certain, rather complex combination of thermal conductivities of its constituents, including air in the pore. Thermal conductivities of aggregates vary by orders of magnitude. The highest is displayed by crystalline rocks (of which that of quartz is highest), while that of amorphous rocks is much lower. Thermal conductivities of crystalline rocks decrease with temperature up to 1000°C (1832°F), while those of amorphous rocks are essentially constant (Fig. 8.1). Thermal conductivity of cement paste (Fig. 8.2) generally decreases with temperature, and the same is true of concrete as a whole (Fig. 8.2) although a spurious upward trend between 0 and 400°C (32 and 752°F) may be observed due to heat convection in moisture. Heat in solids (i.e., the kinetic energy of molecules) is mainly transmitted by bonds, and, noting that heating reduces the number of bonds in cement paste as well as many aggregates, the decrease of thermal conductivity with temperature is explained. Loss of water decreases the amount of heat conducting matter, and thus the conductivity must decrease after drying (Fig. 8.3).

## 8.2 Experimental results and moisture effect

Experimental data on thermal conductivity have been presented by Harmathy and Allen (1973), Harmathy (1970), the U.S. Bureau of Reclamation, Browne (1967), Harada (1972), Crispino (1972), Aoyagi (1972), Abe (1972), Maréchal (1972), Desov and Jankelev (1972), Ödeen (1965), and Neville (1973). The dependence on moisture content and water-cement ratio of the mix was given by the U.S. Bureau of Reclamation. Wet and dry samples were compared by Abe (1972), who found higher conductivity for the wet samples at moderately elevated temperatures. Various types of concrete were studied by Crispino (1972) and Harada (1954), and various aggregate types were compared by Desov and Jankelev (1972), Abe (1972),

and Harmathy and Allen (1973). Thermal conductivities of various aggregates (quartz, igneous and carbonate rocks, gneiss) were reported by Zoldners and Geller (1968) and also by Harmathy (1970). Most experiments pertain to small thermal gradients. In case of high thermal gradient, the convective heat flux due to the migration of moisture becomes significant and can substantially increase the apparent (not true) value of thermal conductivity (so that even an increase with temperature may be observed). Such conditions apparently occurred in tests by Crispino (1972), Abe (1972), and Maréchal (1972).

## 8.3 Thermal diffusivity

Thermal diffusivity can be determined as the product of thermal conductivity and heat capacity; however, because of the experimental error in each of these, it is more advantageous to observe thermal diffusivity directly. Because heat capacity changes only modestly with temperature, the temperature dependence of diffusivity shows a trend similar to that of conductivity. A typical value is 0.3 $mm^2/sec$ ($4.65 \times 10^{-4}$ $in.^2/sec$). Experimental data were given by Harmathy and Allen (1973) for various aggregates and concretes, the U.S. Bureau of Reclamation [up to 100°C (212°F)], and Harada (1954) for various water-cement ratios [up to 800°C (1472°F)], Desov and Jankelev (1972) (various types of aggregate), Yuan et al. (1972) [for various moisture contents up to 160°C (320°F)].

Measured and approximately calculated temperature distributions in test cylinders have been reported by Thelandersson (1974).

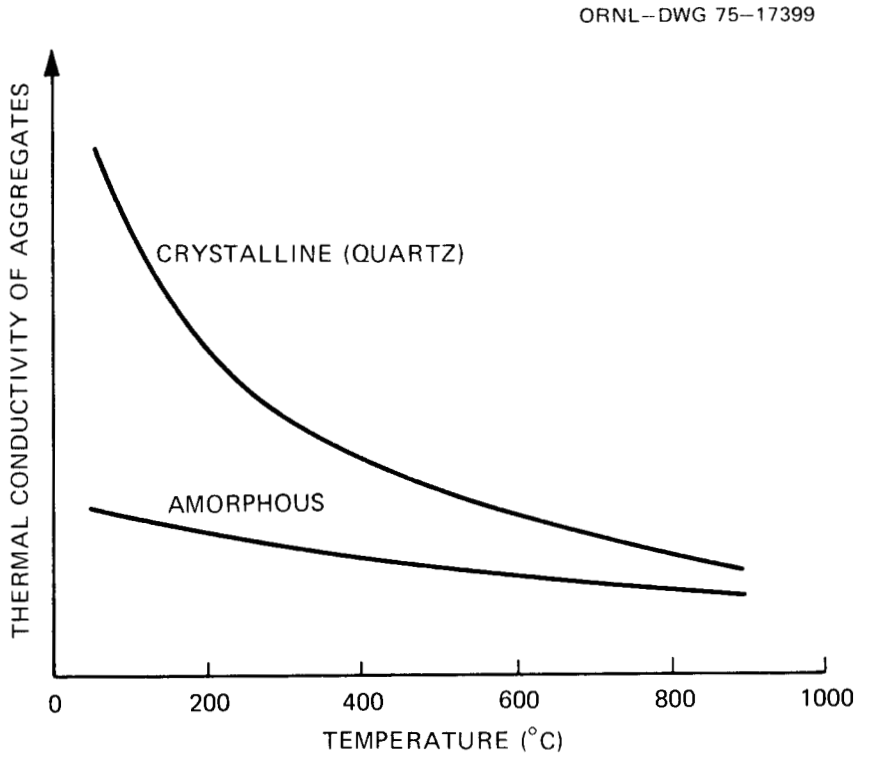
ORNL–DWG 75–17399
THERMAL CONDUCTIVITY OF AGGREGATES
CRYSTALLINE (QUARTZ)
AMORPHOUS
0
200
400
600
800
1000
TEMPERATURE (°C)

Fig. 8.1.

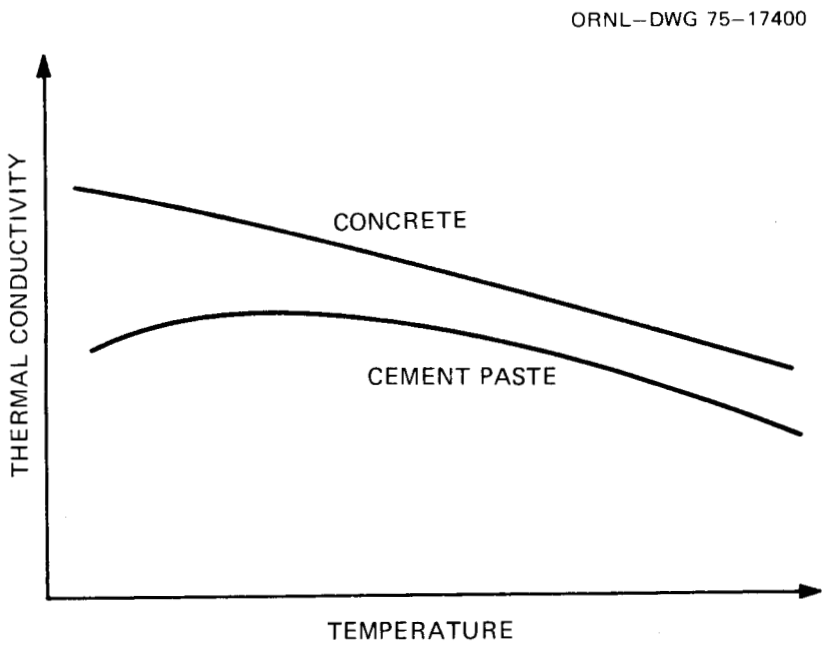
ORNL–DWG 75–17400
THERMAL CONDUCTIVITY
CONCRETE
CEMENT PASTE
TEMPERATURE

Fig. 8.2.

ORNL-DWG 75-17401

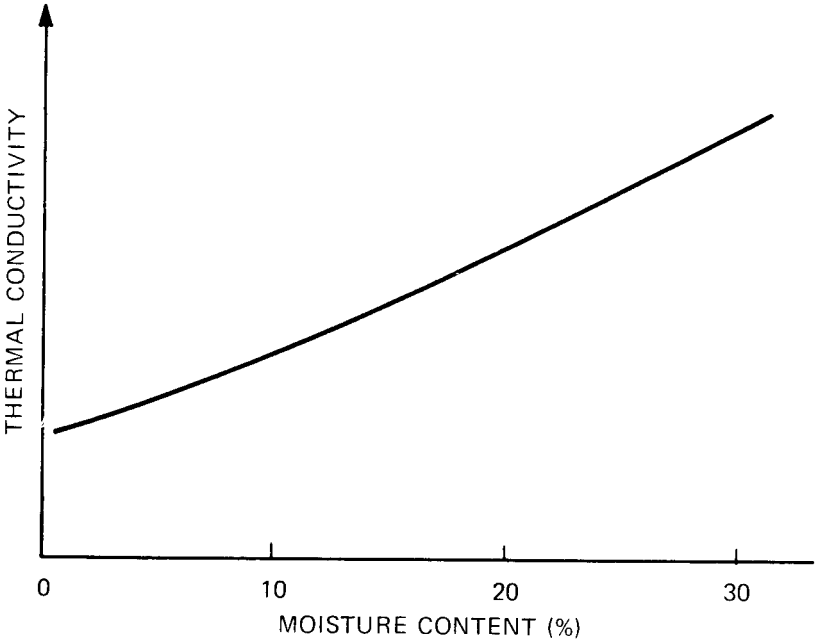


Fig. 8.3.

# 9. Moisture Conductivity and Diffusivity

## 9.1 Moisture conductivity (due to moisture concentration gradient)

Moisture conductivity (and permeability) below 100°C (212°F) has been studied intensely (see Bažant and Najjar, 1972), but it is amazing that above 100°C (212°F) no solid facts exist in the literature except for vague remarks on drying times used in conditioning test specimens.

At moderate temperatures, the transfer of moisture in cement paste as well as in uncracked concrete is extremely slow [diffusivity being of the order of 10 $mm^2$/day ($1.55 \times 10^{-2}$ in.$^2$/day)]. As temperature increases, the permeability and diffusivity grow and approximately obey the activation energy concept up to 100°C (212°F). The transfer of moisture probably takes place mainly in the adsorbed state, which is inferred from the fact that diffusivity drops by an order of magnitude with decreasing water content.

However, above 100°C (212°F), the drying times become orders of magnitude shorter [probably several hours for a 152.4-mm (6-in.) cylinder, as compared with 10 years at 20°C (68°F)], as determined from drying concrete in ovens and from fire testing. However, no precise data are available [except that Fischer (1970) reports that at 100°C (212°F) a 6-cm-diam (2.36-in.) concrete cylinder takes two days to dry to equilibrium]. Preliminary tests of Bažant and Thonguthai (1975) indicated that a 15.2-cm-diam (6-in.) concrete cylinder takes three days to dry at 100°C (212°F), 12 hr at 200°C (392°F), and 6 hr at 300°C (572°F). Thus, there must be a quantum jump upward in diffusivity as 100°C (212°F) is exceeded. This may be explained only by a change in the mode of moisture transfer; instead of flow in adsorption layers, the flow of water probably takes place mainly in a vaporized state (steam). This, in turn, is possible only if the average pore size increases above 100°C (212°F) quite drastically and the large pores become continuous passages (rather than enclaves). However, this picture is a logical hypothesis of the writer and is so far unconfirmed. With further increase of temperature, the diffusivity undoubtedly further increases, perhaps again according to a certain activation energy or steam viscosity. Permeability of concrete to gases (air) up to

600°C (1112°F) was measured by Fischer (1970) and was found to increase many times from the value at 20°C (68°F); the main increase occurred from 450 to 600°C (842 to 1112°F).

## 9.2 Thermal moisture conductivity

Moisture transfer in cement paste and concrete is also generated by temperature gradients at zero gradient of moisture concentration. This phenomenon has received little attention. The only test data pertain to temperatures below 100°C (212°F) (Pihlajavaara and Tiusanen, 1970). A general theory for thermal moisture transfer in capillary solids, without particular reference to concrete, has been given by Luikov (1966).

In the writer's opinion, the effect of a temperature gradient above 100°C (212°F) need not be considered separately if the moisture flux is considered to be driven by pore pressure gradient rather than by moisture concentration gradient.

# 10. Explosive Thermal Spalling

## 10.1 Physical nature

In nuclear accidents, the effect of very rapid and localized heating upon a concrete wall is of interest. This problem has been, and is being, studied in fire research, although on walls of much smaller thickness than those in nuclear structures. In considering the structural effects of sudden heating, the crucial question is that whether the explosive thermal spalling known from fire testing (Harmathy, 1965; Shorter and Harmathy, 1961; Saito, 1965; Kordina, 1966; Meyer-Ottens, 1965; Dougill, 1972 and 1974; Waubke, 1966, Akhtaruzzaman and Sullivan, 1970) would or would not occur. Most of the information on spalling is a by-product of fire testing, with the exception of the tests by Meyer-Ottens (1965) in Braunschweig, whose experiments were intended to study spalling exclusively.

Two different explanations of explosive spalling have been advanced in the past:

1. Thermal expansion due to localized sudden heating of a wall is opposed by the stiffness of the remaining portion of the wall which remains cool and surrounds the heated spot. Thus, a large compressive thermal stress parallel to the surface is generated in the heated concrete and may cause a crushing failure (Saito, 1965) (see also Dougill, 1972 and 1974).

2. Heating produces very high steam pressures in the pores which, in turn, cause large tension in the solid microstructure. In the transverse direction of the wall, there is no thermal compressive stress to oppose this tension, and so spalling of concrete in the transverse direction is possible (Harmathy, 1965) (see also Dougill, 1972 and 1974).

Frequent discussions have been conducted recently as to which of these two mechanisms is correct. In favor of mechanism 1 is the experimental fact that high restraint (giving rise to high thermal stress) promotes spalling, and in favor of mechanism 2 is the fact that higher moisture content promotes spalling (although this could also act indirectly, through higher thermal expansion of concrete containing more moisture).

The fact that higher heating rate promotes spalling is explicable by both mechanisms, because reduction of thermal stress by creep and reduction of pore pressure by moisture escape are less. In the writer's opinion, both mechanisms contribute to thermal spalling, and the first one does not merely consist of crushing of concrete but further causes a bulging instability (or buckling) of the slab, leading to a deformation mode shown in Fig. 10.1. (However, no attempt to formulate and check this last hypothesis mathematically has yet been made.)

Harmathy (1965) proposed a hypothesis stating that effect No. 2 (pore steam pressure) is further intensified by the so-called moisture clog, which may be described as follows. Assuming that heating reaches no deeper into the slab than to midthickness, the moisture, in order to escape the heated wall, diffuses toward the surface which is closest. But this is the heated surface, and a small layer under the heated surface is already dried by heating. The degree of saturation of water must be the highest right under the dry layer of concrete, and temperature there is higher than deeper in the wall. Hence, the highest pore pressure should occur right under the dried layer and should be less at greater depth. Thus, the effect of the pressure gradient is opposite to that of the temperature gradient; namely, the pressure gradient tends to drive moisture back into the wall, while further moisture is arriving from the deeper layers of the wall. This causes a concentration of pore water of high pressure right beneath the dried layer, opposes the escape of moisture toward the heated surface, and thus creates a moisture "clog," in which very high pore pressures can build up and produce spalling. However, accurate mathematical analysis of this phenomenon has not yet been carried out, and it is uncertain whether substantially higher pore pressures can indeed develop as compared to those in concrete without moisture movement.

Explosive spalling has been found to be a very random phenomenon. Some empirical rules to avoid, or at least minimize, explosive spalling in walls of relatively small thickness have already been developed in fire research. These include requirements of low moisture content (less than 5% weight, and preferably less than 3%) and low porosity (which necessitates a small water-cement ratio), and of low thermal expansion coefficient of the aggregate (Harmathy, 1965; Harmathy and Lie, 1971).

Yet, these rules are not reliable and their transplantation to nuclear structures is not necessarily warranted. However, from experiments it seems that spalling is less likely to occur in walls of thick cross section [Kordina, 1966; and also Dougill, 1974, referring to Ashton and Bate (1961) and Hill (1965)] which speaks in favor of a better resistance of nuclear structures against spalling. On the other hand, these facts are based on tests of concrete with small restraint, while it has been found from tests that high longitudinal restraint promotes spalling. Likewise, prestressed concrete is more likely to spall than reinforced concrete. Faster heating rates also invite spalling, and, in the case of a sodium spill acting on concrete, the heating rate would undoubtedly be higher than that in a fire. By contrast, these facts seem to indicate a poorer resistance of nuclear structures, because in them the restraint of a hot spot is very high.

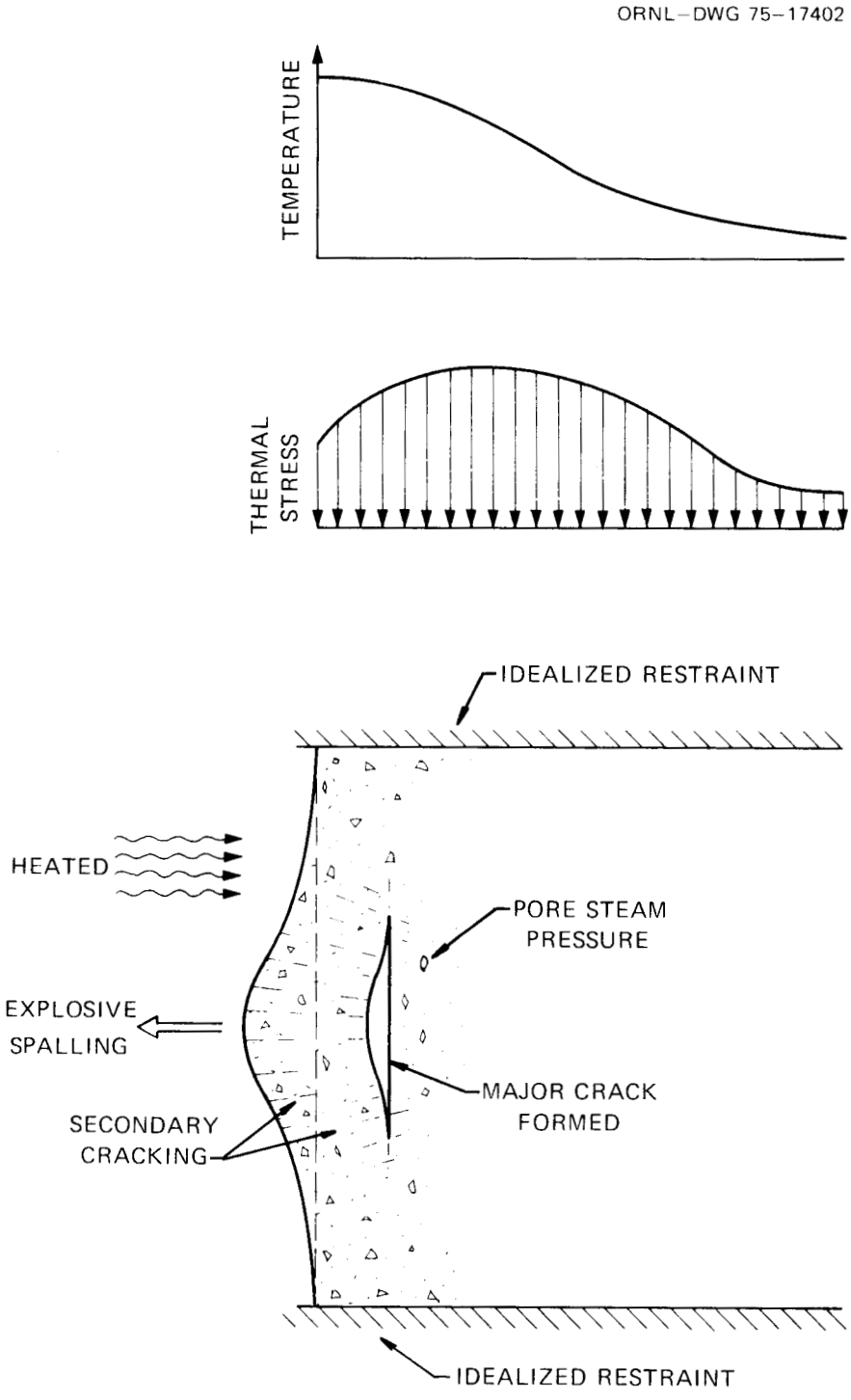
ORNL-DWG 75-17402
TEMPERATURE
THERMAL STRESS
IDEALIZED RESTRAINT
HEATED
PORE STEAM PRESSURE
EXPLOSIVE SPALLING
MAJOR CRACK FORMED
SECONDARY CRACKING
IDEALIZED RESTRAINT

Fig. 10.1.

## 11. Reinforcing and Prestressing Steels

Although the purpose of this work was not to survey the literature on high-temperature effects on reinforcing and prestressing steel, a brief mention is in order. Increase of temperature reduces the yield limit of steels and increases creep significantly. This dependence may be adequately described by rate process theory (i.e., in terms of activation energy), except near the melting point. A consequence of creep and the drop of the yield limit is that, in a constant rate tensile test, the observed strength decreases with temperature. This decrease is more dramatic than that in concrete. A survey of the high-temperature (fire) effect on reinforcing and prestressing steels has been given by Harmathy and Stanzak (1969) (see also Danneberg et al., 1957).

# PART II. APPLICATION TO THE PROBLEM OF A SODIUM SPILL

## 1. Opinion Statement on the Effects of Sudden Exposure to Temperature of 538°C (1000°F)

### 1.1 Two possible effects of sodium spill on concrete wall

A sodium spill reaching a concrete wall would act on concrete in two ways: (1) heating of the concrete surface to about 538°C (1000°F), and (2) chemical reaction of sodium with water escaping from concrete, in case that the integrity of the liner is lost.

Sodium has a very high chemical affinity to water. The chemical reaction of sodium with water is rapid and highly exothermic, producing sodium hydroxide [(NaOH), which has a heat of fusion of 209 J/g ($1.984 \times 10^3$ Btu/lb) or $8.37 \times 10^3$ J/mole]. However, it is not quite clear to what extent, and at what rate, the evaporable water and the chemically bound water in cement paste would react with sodium. Possibly, the reaction would be rather slow because (1) much of the evaporable water (except capillary water), and even more the chemically bound water, is firmly held within the microstructure of cement paste, and (2) only the water in a narrow surface layer of concrete can come in direct contact with sodium. If this layer does not crack and disintegrate, sodium would not be able to come in contact with water in concrete beneath its surface, and then the reaction could possibly be quite mild. On the other hand, if cement paste and concrete crack on contact with sodium, concrete could disintegrate layer by layer and the reaction with sodium could proceed quite rapidly. One might also expect quite different behavior of concretes having different water contents and different porosities and of concretes which are water saturated at the time of sodium spill and those which are predried (i.e., contain only chemically bound water but no evaporable water). For conditions of concrete under the steel liner, the case of water-saturated concrete is typical (and so tests of a sodium spill in a trench of concrete which has previously been exposed to the atmosphere rather than being sealed, need not necessarily be relevant because such a concrete has already lost part of its evaporable water, namely, the capillary water). However, it is not the intent of this work to address itself to the problem of chemical action of sodium on concrete.

## 1.2 Differences from cases tested in fire research

1. The heating of a concrete surface to 538°C (1000°F) is in the range explored in fire testing, but the rise of temperature due to the spill is much more rapid, almost sudden, as compared with the much slower temperature rise in a fire. This is the main difference with regard to the conditions in fire tests and undoubtedly results in a steeper temperature gradient beneath the surface, a smaller reduction of thermal stress by creep, and a higher pore steam pressure because insufficient time is available for the diffusion of moisture away from the heated layer.

2. Another important difference from fire tests is the presence of the liner, which, if it retains its integrity, prevents escape of the moisture from the heated side of the wall. However, escape of moisture in the opposite direction is hardly possible, because the wall is too thick and too cool at the opposite face; thus times of migration through the wall are too long to allow any appreciable loss of moisture to the environment in that direction. Therefore, moisture would tend to be forced into the cooler layer of concrete beneath the heated surface layer. This cooler layer can probably accommodate some additional moisture because it has previously developed some vapor bubbles due to self-desiccation (pore humidity drop to about 97% due to the deficiency of moisture created by hydration). Nevertheless, the amount of water that this cooler layer can accommodate before reaching 100% saturation is probably quite limited, and soon this layer may be subjected to very high pore pressures that may burst the concrete.

Remark. A similar problem of a liner that blocks the escape of moisture, although at a considerably smaller temperature, occurs in service conditions in a prestressed concrete reactor vessel with a hot liner and a layer of sacrificial concrete underneath (the Austrian design). The designers must have examined the problem, but no reports appear in the literature.

3. Another difference from fire tests is the thickness of the concrete wall, which is much greater than that in typical building structures tested for fire, and the high degree of restraint provided by the surrounding wall that remains cool.

## 1.3 The question of explosive spalling and damage

A sodium spill can either result in explosive spalling, which is a catastrophic consequence, or merely in serious damage to the concrete wall but (partial or total) preservation of its integrity and containment capability during the accident.

1.3.1 Spalling. With regard to the containment after an accident with a sodium spill, the crucial question is whether or not explosive spalling of the concrete wall would occur. In the writer's opinion, it might be possible to design the concrete wall so as to withstand the effects of a sodium spill for a limited time. This necessitates quantitative analysis of stresses, strains, and temperatures in the concrete wall. The available data on fundamental properties of concrete (Part I) would allow a rough analytical estimate to be made, but further experiments would be also necessary for a more reliable prediction.

Various measures that may be considered to eliminate (or at least reduce the chance of) explosive spalling include the following.

1. Use of concrete having a minimum moisture content by proper gradation of aggregate, additives, method of placement, etc.

2. Use of aggregates that have the lowest thermal expansion coefficient and best thermal stability, perhaps a heated-treated aggregate such as crushed firebrick, which has a very small thermal expansion and is perfectly stable for the temperatures of interest. Limestone might be the next possibility. Any aggregate containing quartz would be undesirable [although 538°C (1000°F) is below the quartz transition temperature]. The selected aggregate might be used only in a layer of concrete near the inner face rather than throughout the concrete wall as a whole.

3. Reinforcement of the wall. The chances of explosive spalling might be severely limited by strong, densely spaced steel ties across the wall, in conjunction with a steel reinforcing mesh parallel to the liner located close to the liner. A question to be considered here would be the creep of the steel ties (loaded as a reaction to pore steam pressure) at temperatures up to 538°C (1000°F). Note that most slabs in which explosive spalling has been observed in fire exposure did not have transverse ties.

1.3.2 Damage. The minimum effect of a sodium spill would be serious damage to a layer of concrete beneath the liner at least several inches thick. The damage would include at least a several-fold drop of strength and elastic modulus and severe microcracking. The structure could remain serviceable after such an accident only if this layer were considered in the design as sacrificial.

A more severe damage would be local (nonexplosive) spalling and extensive cracking of the concrete. Repair of the wall would probably require removal of the damaged layer.

The factors inhibiting explosive spalling (listed above) would also tend to inhibit the damage of the wall. In addition, a dense reinforcing mesh parallel to the liner would be beneficial.

## 2. Research and Development Needs

### 2.1 Material Aspects

As has been mentioned, nearly all tests of basic properties of concrete at elevated temperature have been made on small specimens that allow a rapid escape of moisture and a quick attainment of the equilibrium moisture content for the given temperature. On the contrary, the massive wall cannot lose its moisture during the accident, and therefore tests of concrete which is forced to keep its moisture are needed to predict the effects of a sodium spill. Inferences from presently known material data are possible, but unreliable.

In particular, it is highly desirable to test initial elastic modulus, stress-strain curves, short-time creep, and thermal expansion of specimens forced to retain moisture.

Another important gap in the present knowledge is the moisture permeability and diffusivity of concrete at high temperature. This calls for measuring the time progress of drying in an oven.

Further it would be desirable to measure pore steam pressures in concrete heated to high temperature.

Finally, with a view toward possible contact between sodium and concrete, observations of small water-saturated specimens suddenly submerged in a hot liquid sodium bath should be made.

In addition to the above experiments, mathematical formulation of the corresponding constitutive relation would be an important task.

### 2.2 Analytical prediction

The consequences of a sodium spill could be predicted by developing a finite-element program for coupled heat conduction and convection, moisture diffusion, and thermal stress and strain of the concrete wall. Even a one-dimensional axisymmetric program (in the dimension across the wall) would be very useful. This program could also receive as input the proper history of pressure on the liner. A two-dimensional program would allow inclusion of possible deformation instability in explosive spalling.

Present experimental knowledge would allow only crude estimates to be made with this program. Having further data from the tests outlined

before (Section 2.1), more accurate material properties could be fed into the program, thus gaining an improvement in the reliability of prediction.

## 2.3 Model tests

For better reliability of prediction, model tests are required, which may be of two types:

1. A reduced-scale model of a section of the wall would mainly be useful for testing the accuracy of the program mentioned in Section 2.2 and for adjusting the parameters of the program to fit the results of model tests. The concrete of the reduced-scale model would have to be prevented from losing its moisture on both sides.

2. A full-scale model can be limited to a portion of the wall having actual full thickness and provided with the actual liner. A difficult aspect, however, would be the attainment of sufficient longitudinal restraint.

Two types of thermal exposure may be considered:

1. Rapid heating of the liner surface in a furnace, with a correct history of temperature. This precludes, of course, the study of chemical action of sodium if the liner breaks.

2. Dumping hot liquid sodium into a pool, one wall of which is a model of the cell wall.

# BIBLIOGRAPHY


1. Abe, H., et al., "Influence Factors of Elevated Temperatures on Thermal Properties and Inelastic Behavior of Concrete," Concrete for Nuclear Reactors, American Concrete Inst., Special Publication 34, Vol. II, pp. 847–70, 1972.

2. Abrams, M. S., "Compressive Strength of Concrete at Temperatures up to 1600°F," Temperature and Concrete, American Concrete Inst., Special Publication 25 (PCA Bull. RD 016), pp. 33–58, 1971.

3. Abrams, M. S., and A. H. Gustaffero, "Fire Endurance of Concrete Slabs as Influenced by Thickness, Aggregate Type and Moisture," J. PCA Res. and Dev. Lab. 10, 9–24 (1968) (PCA Bull. RD 223).

4. Abrams, M. S., and D. L. Orals, "Concrete Drying Methods and Their Effect on Fire Resistance; Moisture of Materials in Relation to Fire Tests," STP No. 385 (PCA Bulletin 181), pp. 52–73, 1965.

5. Anderberg, Y., and J. Thelandersson, "Stress and Deformation Characteristics of Concrete at High Temperatures," Bulletin 36, Div. of Structural Mech. and Concrete Constr., Lund Institute of Technology, Lund, Sweden, 1973.

6. Aoyagi, Y., H. Ohnuma, and M. Kawasaki, "Behavior of Flexurally Restrained Prestressed Concrete Beams under Temperature Gradient," Concrete for Nuclear Reactors, American Concrete Inst., Special Publication 34, Vol. II, pp. 799–821, 1972.

7. Arthanari, S., and C. W. Yu, "Creep of Concrete under Uniaxial and Biaxial Stresses at Elevated Temperatures," Mag. Concr. Res. 19, 149–56 (1967).

8. Barrett, N. T., and J. T. Murray, "Creep in Pressure Vessels at Elevated Temperatures," Conference on Prestressed Concrete Pressure Vessels, Institution of Civil Engineers, London, England, 1967, Paper C14, pp. 33–46.

9. Bažant, Z. P., "A Correlation Study of Formulations of Incremental Deformation and Stability of Continuous Bodies," J. Appl. Mech., Trans. ASME 38, 919–28, 39, 371 (1971).

10. Bažant, Z. P., "Delayed Thermal Dilatations of Cement Paste and Concrete Due to Mass Transport," Nucl. Eng. Des. 14, 308–18 (1970).

11. Bažant, Z. P., Numerical Analysis of Long-Time Deformations of a Thick-Walled Concrete Cylinder, Report 69-12 (Report to Oak Ridge National Laboratory), Div. of Struct. Engng. and Struct. Mech., Univ. of California, Berkeley, 52 pp. (1969).

12. Bažant, Z. P., "Theory of Creep and Shrinkage in Concrete Structures: A Précis of Recent Developments," Mechanics Today, Vol. 2, S. Nemat-Nasser, Ed. (Am. Acad. Mech.), Pergamon, pp. 1–93 (1975).

13. Bažant, Z. P., Thermodynamic Theory of Concrete Deformation at Variable Temperature and Humidity, Report 69-11 (Report to Oak Ridge National Laboratory), Div. of Struct. Engng. and Struct. Mech., Univ. of California, Berkeley, 100 pp. (1969).

14. Bažant, Z. P., "Thermodynamics of Interacting Continua with Surfaces and Creep Analysis of Concrete Structures," Nucl. Eng. Des. 20, 477–505 (1972).

15. Bažant, Z. P., and L. J. Najjar, "Nonlinear Water Diffusion in Nonsaturated Concrete," Materials and Structures (RILEM) 5, 3–20 (1972).

16. Bažant, Z. P., and S. T. Wu, "Creep and Shrinkage Law of Concrete at Variable Humidity," J. Eng. Mech. Div., Proc. ASCE 100, 1183–1209 (1974).

17. Bažant, Z. P., and S. T. Wu, "Thermoviscoelasticity of Aging Concrete," J. Eng. Mech. Div., Proc. ASCE 100(EM3), 575–97 (1974) (also as ASCE Meeting Preprint No. 2110, October 1973).

18. Becker, J., and B. Bresler, A Computer Program for the FIre REsponse of Structures – Reinforced Concrete Frames, Report UCB FRG 74-3, Struc. Engng. and Struct. Mech. Dept. of Civil Engineering, Univ. of California, Berkeley (August 1974).

19. Becker, W., and J. Stanke, "Feuerwiderstandsdauer von Stahlbetonstützen," Deutscher Ausschuss für Stahlbeton, Heft 214, W. Ernst and Sohn, Berlin, 1970 (Fire Resistance of Concrete Columns).

20. Becker, W., and J. Stanke, "Fire Tests on Precast Concrete Columns" (in German), Deutscher Ausschuss für Stahlbeton, Heft 215, W. Ernst and Sohn, Berlin, 1970.

21. Bertero, V. V., and M. Polivka, "Influence of Thermal Exposures on Mechanical Characteristics of Concrete," Concrete for Nuclear Reactors, American Concrete Inst., Special Publication 34, Vol. I, pp. 505–34, 1972.

22. Berwanger, C., and A. F. Sarkar, "Effect of Temperature and Age on Thermal Expansion and Modulus of Elasticity of Concrete," Behavior of Concrete under Temperature Extremes, American Concrete Inst., Special Publication 39, pp. 1–22, 1973.

23. Briebach, A. V., "A Review of Refractory Hydraulic Cements," Trans. Brit. Ceram. Soc. 153–58 (July 1972).

24. Browne, R. D., "Properties of Concrete in Reactor Vessels," Conf. on Reactor Concrete Pressure Vessels, Institution of Civil Engineering, London, 1967.

25. Browne, R. D., and R. Blundell, "The Influence of Loading Age and Temperature on the Long Term Creep Behavior of Concrete in a Sealed, Moisture Stable State," Materials and Structures (RILEM) 2, 133–44 (1969).

26. Campbell-Allen, D., and C. P. Thorne, "Thermal Conductivity of Concrete," Mag. Concr. Res. 15(43), 39–48 (1963).

27. Chuang, J. W., et al., "Prediction of Multiaxial Creep from Uniaxial Tests," Concrete for Nuclear Reactors, American Concrete Inst., Special Publication 34, Vol. II, 701–34, 1972.

28. Copeland, L. E., and J. C. Hayes, "Determination of Non-Evaporable Water in Hardened Portland Cement Paste," ASTM Bulletin No. 194, ASTM, Philadelphia, pp. 70–74, December 1953.

29. Crispino, E., "Studies on the Technology of Concrete under Thermal Conditions," Concrete for Nuclear Reactors, American Concrete Inst., Special Publication 34, Vol. I, pp. 443–80, 1972.

30. Cruz, C. R., "Apparatus for Measuring Creep of Concrete at High Temperatures," J. Portland Cement Association 10(3), 36–42 (September 1968).

31. Cruz, C. R., "Elastic Properties of Concrete at High Temperature," J. PCA Res. and Dev. Lab (PCA Bull. 191) 8(1), 37–45 (January 1966).

32. Czernin, W., Cement Chemistry and Physics for Engineers, Chemical Publishing Co., New York, 1962 (Translation of "Zementchemie für Bauingenieure," Bauverlag, Wiesbaden, 1960).

33. Danneberg, J., H. Deutschmann, and P. Melchor, "Heat Rupture Tests of Prestressing Steels and PC Members" (in German), Deutscher Ausschuss für Stahlbeton, Heft 122, W. Ernst and Sohn, Berlin, 1957.

34. Da Silveira, A. F., and C. A. Florentino, "Influence of Temperature on the Creep of Mass Concrete," Temperature and Concrete, American Concrete Inst., Special Publication 25, pp. 173–90, 1971.

35. Desov, A. E., and L. F. Jankelev, "Some Peculiarities and Results of Investigations of Thermal Conductivity and Diffusivity of Heavy Concrete," Research Institute of Concrete and Reinforced Concrete (NIIZhB), Gosstroy, USSR, American Concrete Inst., Special Publication 34, pp. 1059–67, 1972.

36. Desov, A. E., K. D. Nekrasov, and A. F. Milovanov, "Cube and Prism Strength of Concretes at Elevated Temperatures," Concrete for Nuclear Reactors, American Concrete Inst., Special Publication 34, Vol. I, pp. 423–33, 1972.

37. Dettling, H., Thermal Dilatation of Hardened Cement Paste, Aggregates and Concrete, Ottar Graf Institut, Techn. Hochschule, Stuttgart, 1965.

38. Dettling, H., "Thermal Expansion of Cement Paste, Aggregates and Concretes" (in German), Deutscher Ausschuss für Stahlbeton, Heft 64, W. Ernst and Sohn, Berlin, 1964.

39. Dougill, J. W., "A Note on the Mechanics of Spalling in Concrete," presented at the meeting of C.I.B. Commission, 1972.

40. Dougill, J. W., "Conditions for Instability in Restrained Concrete Panels Exposed to Fire," Mag. Concr. Res. 24, 139–48 (1972).

41. Dougill, J. W., "Fire Resistance and Spalling," Chap. I of a work in preparation, private communication, September 1974.

42. Dougill, J. W., "Modes of Failure of Concrete Panels Exposed to High Temperatures," Mag. Concr. Res. 24, 71–76 (1972).

43. Dougill, J. W., "Some Effects of Thermal Volume Changes on the Properties and Behavior of Concrete," The Structure of Concrete, pp. 499–513, Cement and Concrete Association, London, 1968.

44. Dougill, J. W., "The Effect of Thermal Incompatibility and Shrinkage on the Strength of Concrete," Mag. Concr. Res. 13(39), 119–26 (1961).

45. Drysdale, R. G., and E. F. Vickers, "Effect of Fire on the Capacity of Reinforced Concrete Columns," Int. Assoc. Bridge and Struct. Eng. Symp., "Design and Safety of Reinforced Concrete Compression Members," Reports of Working Commissions, Vol. 16, pp. 227–34, 1974 (held in Quebec 1974).

46. England, G. L., "Migration of Moisture and Pore Pressures in Heated Concrete," Paper H2/4, 1st Int. Conf. Struct. Mech. Reactor Technol., Berlin, 1971.

47. England, G. L., and A. D. Ross, "Reinforced Concrete under Thermal Gradients," Mag. Concr. Res. 14(40), 5–12 (March 1962).

48. England, G. L., and A. D. Ross, "Shrinkage, Moisture and Pore Pressures in Heated Concrete," Concrete for Nuclear Reactors, American Concrete Inst., Special Publication 34, Vol. 2, pp. 883–907, 1972.

49. England, G. L., and M. E. Skipper, "On the Prediction of Moisture Movement in Heated Concrete up to 550°C," Paper H6/2, 2d Int. Conf. Struct. Mech. Reactor Technol., Berlin, 1973.

50. Fahmi, H. M., M. Polivka, and B. Bresler, "Effect of Sustained and Cyclic Elevated Temperature on Creep of Concrete," Cement Concr. Res. 2, 591–606 (1972).

51. Fahmi, H. M., B. Bresler, and M. Polivka, "Prediction of Creep of Concrete at Variable Temperatures," Am. Concr. Inst. J., 70, 709–13 (1973).

52. Fischer, R., "On the Behavior of Cement Mortar and Concrete at High Temperatures" (in German), Deutscher Ausschuss für Stahlbeton, Heft 214, W. Ernst and Sohn, Berlin, 1970.

53. Fisher, R., "Über das Verhalten von Zementmörtel u. Beton bei Höheren Temperaturen," Deutscher Ausschuss für Stahlbeton, Heft 214, W. Ernst and Sohn, Berlin, 1970.

54. Freyssinet, E., "Action de la Température. Coefficient de Dilatation Vraie d'un Béton en Equilibre de Retrait," Travaux, No. 376, Tome 2, p. 904, 1966.

55. Geymayer, H. G., "The Effect of Temperature on Creep of Concrete: A Literature Review," U.S. Army Engineer Waterways Experiment Station, Corps of Engineers, Vicksburg, Miss., Misc. Paper C-70-1, January 1970.

56. Gross, H., "On High Temperature Creep of Concrete," Paper H6/5, 2nd Int. Conf. Struct. Mech. Reactor Technol., Vol. 3, Berlin, 1973.

57. Gustaferro, A. H., and S. L. Selvaggio, "Fire Endurance of Simply Supported Prestressed Concrete Slabs," J. Prestressed Concr. Inst. 12 (PCA Bull. RD 212), 37–52 (February 1967).

58. Hannant, D. J., "Strain Behavior of Concrete up to 95°C under Compressive Stresses," Proceedings, Conference on Prestressed Concrete Pressure Vessels, Institution of Civil Engineers, London, England, Group C, Paper 17, pp. 57–71, 1967.

59. Hannant, D. J., "Strain Behavior of Concrete up to 95°C under Compressive Stresses," Conference on Prestressed Concrete Pressure Vessels, Institution of Civil Engrs., pp. 57–71, London, 1967.

60. Hannant, D. J., and P. S. Pell, "Thermal Stresses in Reinforced Concrete Slabs," Mag. Concr. Res. 14(41), 91–98 (July 1962).

61. Hansen, T. C., "Creep and Stress Relaxation of Concrete," Proceedings NR 31, Swedish Cement and Concrete Research Institute of Royal Institute of Technology, Stockholm, Sweden, 1960.

62. Hansen, T. C., and L. Eriksson, "Temperature Change Effect on Behavior of Cement Paste, Mortar and Concrete," ACI J. 37, 489–503 (1966).

63. Hansen, T. C., and L. Ericksson, "Temperature Change Effect on Behavior of Cement Paste, Mortar and Concrete under Load," J. Amer. Concr. Inst. 36, 489–504 (1966).

64. Hansson, V., and G. Schnellenbach, "Spezielle Probleme bei der Berechnung von Spannbeton-Reaktordruckbehältern," Paper H1/3, 2d Int. Conf. Struct. Mech. Reactor Technol., Vol. 3, Berlin, 1973.

65. Harada, T., "Strength and Elasticity of Concrete Subjected to Elevated Temperature," Trans. of Architectural Institute of Japan, No. 47, October 1953; No. 48, March 1954; No. 56, June 1957; and No. 63, October 1959 (in Japanese).

66. Harada, T., "Variation of Thermal Conductivity of Cement Mortar and Concrete under High Temperatures," Trans. of Architectural Institute of Japan, No. 49, September 1954.

67. Harada, T., et al., "Strength, Elasticity and Thermal Properties of Concrete Subjected to Elevated Temperatures," Concrete for Nuclear Reactors, American Concrete Inst., Special Publication 34, Vol. 1, pp. 377–406, 1972.

68. Harmathy, T. Z., "Determining the Temperature History of Concrete Constructions Following Fire Exposure," J. Amer. Concr. Inst. 65, 959–64 (1968).

69. Harmathy, T. Z., "Effect of Moisture on the Fire Endurance of Building Materials," Moisture in Materials in Relation to Fire Tests, ASTM Techn. Publ. No. 385, pp. 74–95, 1965.

70. Harmathy, T. Z., "Simultaneous Moisture and Heat Transfer in Porous Systems with Particular Reference to Drying," Ind. Eng. Chem. Fundam. 8(1), 92–102 (February 1969).

71. Harmathy, T. Z., "Thermal Properties of Concrete at Elevated Temperatures," ASTM J. Mater. 5, 47–74 (1970).

72. Harmathy, T. Z., and L. W. Allen, "Thermal Properties of Selected Masonary Unit Concretes," J. Amer. Concr. Inst. 70, 132–42 (1973).

73. Harmathy, T. Z., and J. E. Berndt, "Hydrated Portland Cement and Light-weight Concrete at Elevated Temperatures," J. Amer. Concr. Inst. 63, 93–112 (1966).

74. Harmathy, T. Z., and T. T. Lie, "Experimental Verification of the Rule of Moisture Content," Fire Technol. 7, 17–24 (1971).

75. Harmathy, T. Z., and W. Stanzak, "Elevated Temperature Tensile and Creep Properties of Some Structural and Prestressing Steels," Symp. on Fire Test Performance, ASTM Spec. Techn. Publ. 464, February 1969.

76. Helmuth, R. A., "Dimensional Changes of Hardened Portland Cement Pastes Caused by Temperature Changes," Proc., Highway Research Board, Vol. 40 (PCA Bull. 129), pp. 315–36, 1967.

77. Hickey, K. B., Creep Strength and Elasticity of Concrete at Elevated Temperatures, Concrete and Structural Branch, Division of Research, U.S. Department of Interior, Bureau of Reclamation, Report No. C-1257 (December 1967).

78. Hundt, J., "On the Non-Stationary and Distribution of Temperature and Moisture in Concrete under the Effect of a Temperature Gradient," Beitrag für Sitzung des Ausschusses, CIB W40: Heat and Moisture Transfer in Porous Building Materials and Structures, Tegernsee, 1972.

79. Illston, J. M., and P. D. Sanders, "The Effect of Temperature Change upon the Creep of Mortar under Torsional Loading," Mag. Concr. Res. 25(84), 136–44 (1973).

80. Irving, J., and G.D.T. Carmichael, "The Influence of Creep on the Behavior of Concrete Structures Subjected to Cyclic Heating," Proc., Southhampton 1969 Civil Engng. Materials Conference, pp. 1299–1311, Wiley, 1971.

81. Irving, J., G.D.T. Carmichael, and I. W. Hornby, "A Full-Scale Model Test of Hot Spots in the Prestressed Concrete Pressure Vessels of Oldbury Nuclear Power Station," Proc. Inst. Civil Eng. 57, 331–51 (1974).

82. Jet-Piercing Research Project, Mines Branch Investigation Report IR 62-27, Department of Mines and Technical Surveys, 621 pp., Ottawa, Canada, 1962.

83. Johansen, R., and C. H. Best, "Creep of Concrete With and Without Ice in the System," Bulletin, Reunion Internationale des Laboratoires d'Essais et de Recherches sur les Matériaux et les Constructions, No. 16, pp. 47–57, 1962.

84. Jordaan, I. O., "A Note on Concrete Creep Analysis under Static Temperature Fields," Materials and Structures (RILEM), 7, 329–33 (1974).

85. Karasuda, S., and I. Hoshino, "Dry Density of Concrete at Elevated Temperature," Concrete for Nuclear Reactors, American Concrete Inst., Special Publication 34, Vol. II, pp. 931–56, 1972.

86. Klug, P., and F. Wittmann, "Activation Energy of Creep of Hardened Cement Paste," Materials and Structures (RILEM) 2, 11–16 (1969).

87. Kordina, K., "Der Einfluss von Abplatzungen, Schutzschichten und des Spann-systems auf die Feuerwiderstandsdauer," Proc. Symp. Fire Resistance of Concrete Structures, Braunschweig, Germany, 1965, Bauverlag GmbH, pp. 51–56, Berlin, 1966.

88. Kordina, K., and W. Klingsch, "Fire Resistance of Reinforced Concrete Columns," Int. Assoc. Bridge Struct. Eng. Symp., pp. 235–43, 1974.

89. Kordina, K., and C. Meyer-Ottens, "Fire Resistance of Reinforced and Prestressed Members under Bending," Betonstein-Zeitung 20(8), 9, 10 (1963). (In German.)

90. Kordina, K., "Behavior of Reinforced and Prestressed Concrete Members in Fire" (in German), Deutscher Ausschuss für Stahlbeton, Heft 162, W. Ernst and Sohn, Berlin, 1966.

91. Kordina, K., and C. Meyer-Ottens, "Fire Resistance of Reinforced and Prestressed Concrete Members in Flexure," Betonstein-Zeitung, Heft 1, 1963. (In German.)

92. Kordina, K., "Fundamentals of the Design of Reinforced and Prestressed Concrete Members of Specified Fire Resistance Time" (in German), Stahlbetonbau, Berichte aus Forschung und Praxis (Festschrift Professor Rüsch), W. Ernst and Sohn, Berlin-Munich, 1969.

93. Krampf, L., "Some Recent Experiments on the Behavior of Concrete Structures Subjected to Fire," 7th Congress FIP, New York, 1974.

94. Kristen, Th., and H. J. Wierig, "Effect of High Temperatures on Prestressed Concrete Members" (in German), Bauingenieur 35(1)(1960).

95. Lankard, D. R., et al., "Effects of Moisture Content on the Structural Properties of Portland Cement Concrete Exposed to Temperatures up to 500°F," American Concr. Inst., Special Publication 25, pp. 59–102, 1971.

96. Lea, F. M., The Chemistry of Cement and Concrete, pp. 526–27, Chemical Publ. Co., New York, 1971.

97. Lehmann, H., and G. Mülzig, "On the Compression Strength of Heated Concrete" (in German), Tonind.-Ztg. 84(17), 414–17 (1960).

98. Lie, T. T., and D. E. Allen, "Fire Resistance of Reinforced Concrete Columns," Inst. Assoc. Bridge Struct. Eng. Symp., pp. 245–54, 1974.

99. Luikov, A. V., Heat and Mass Transfer in Capillary-Porous Bodies, Pergamon, Oxford, 1966.

100. Mahmoudzadeh-Rahimi, M., Contribution à l'étude de la dilatation thermique des bétons (Contribution to thermal dilatation of concretes), Rapport de recherche, No. 18, Laboratoire Central des Ponts et Chaussées, Paris, 1972.

101. Malhotra, M. L., "The Effect of Temperature on the Compressive Strength of Concrete," Mag. Concr. Res. 8, 23 (1956).

102. Malhotra, M. L., and F. R. Stevens, "Fire Resistance of Encased Steel Stanchions," Proc. Inst. Civil Eng. 27, 77–98 (1974), with Disc. 29, 1964.

103. Maréchal, J. C., "Creep of Concrete as a Function of Temperature," Concrete for Nuclear Reactors, American Concrete Inst., Special Publication 34, Vol. I, pp. 547–64, 1972.

104. Maréchal, J. C., "Fluage du béton en fonction de la température," Mater. Struct. 2, 111–15 (1969); 3, 395–406 (1970).

105. Maréchal, J. C., "Le fluage du béton en fonction de la température," RILEM Colloquium, Munich, 1968.

106. Maréchal, J. C., "Thermal Conductivity and Thermal Expansion Coefficients of Concrete as a Function of Temperature and Humidity," Concrete for Nuclear Reactors, American Concrete Inst., Special Publication 34, Vol. 2, pp. 1047–57, 1972.

107. Maréchal, J. C., "Variations in the Modulus of Elasticity and Poisson's Ratio with Temperature," Concrete for Nuclear Reactors, American Concrete Inst., Special Publication 34, Vol. 1, pp. 495–503, 1972.

108. McDonald, J. E., "An Experimental Study of Moisture Migration in Concrete," Concrete for Nuclear Reactors, American Concrete Inst., Special Publication 34, Vol. 2, pp. 957–89, 1972.

109. McDonald, J. E., "An Experimental Study of Multiaxial Creep in Concrete," Concrete for Nuclear Reactors, American Concrete Inst., Special Publication 34, Vol. 2, pp. 735–97, 1972.

110. McDonald, J. E., Moisture Migration in Concrete, Technical Report C-75-1, Concrete Laboratory, U.S. Army Engineer Waterways Experiment Station, Vicksburg, Miss. (1975).

111. Meyer-Ottens, C., "Verhalten von Betonbauteilen im Brandfall," Beton 24, 133–36, 175–78 (1974).

112. Meyers, S. L., "Thermal Expansion Characteristics of Hardened Cement Paste and Concrete," Proc., Highway Research Board, Vol. 30, pp. 193–203, 1950.

113. Mitchell, L. J., "Thermal Expansion Test on Aggregates, Neat Cements and Concrete," Proc. ASTM 53, 963 (1953).

114. Mitchell, L. J., "Thermal Properties of Hardened Concrete," ASTM Special Techn. Publ. No. 169A, April 1966.

115. Mukaddam, M. A., and B. Bresler, "Behavior of Concrete Under Variable Temperature and Loading," Concrete for Nuclear Reactors, American Concrete Inst., Special Publication 34, Vol. II, pp. 771–97, 1972.

116. Nasser, K. W., "Creep of Concrete at Low Stress-Strength Ratio and Elevated Temperatures," American Concrete Inst., Special Publication 25, pp. 137–47, 1968.

117. Nasser, K. W., "Elevated Temperature Effect on the Structural Properties of Air-Entrained Concrete," Behavior of Concrete under Temperature Extremes, American Concrete Inst., Special Publication 39, pp. 139–48, 1973.

118. Nasser, K. W., and A. M. Neville, "Creep of Concrete at Elevated Temperatures," J. Amer. Concr. Inst. 62, 1567–79 (1965).

119. Nasser, K. W., and A. M. Neville, "Creep of Concrete at Temperature above Normal," Nucl. Eng. Des. 4, 90–96 (1966).

120. Nasser, K. W., and A. M. Neville, "Creep of Old Concrete at Normal and Elevated Temperature," ACI J., 97–103 (February 1967).

121. Nekrassow, K. D., "Hitzebeständiger Beton," Bauverlag Wiesbaden-Berlin, 1961 (translation from Russian).

122. Neville, A. M., and W. Dilger, Creep of Concrete: Plain, Reinforced, Prestressed, American Elsevier, New York, 1970.

123. Neville, A. M., and W. Z. Liszka, "Accelerated Determination of Creep of Lightweight Aggregate Concrete," Civil Engineering and Public Works Review, pp. 515–19 (June 1973).

124. Nishizawa, Noriaki, and Hajime Okamura, "Strength and Inelastic Properties of Concrete at Elevated Temperature," Concrete for Nuclear Reactors, American Concrete Inst., Special Publication 34, Vol. 1, pp. 407–21, 1972.

125. Ödeen, K., "Fire Resistance of Reinforced Concrete Beams," Fire Resistance of Prestressed Concrete, Proceedings of a Symposium, Braunschweig, Germany, June 1965.

126. Ödeen, K., and Å. Nordström, "Thermal Properties of Concrete at High Temperature" (in Swedish), Cement Och Betong, No. 1, 1972.

127. Ohgishi, S., "Experiments on Strength and Elasticity at High Temperature of Radiation Shield Concrete," Trans. ALJ, No. 103, 1964.

128. Petersson, O., "The Possibilities of Predicting the Fire Behavior of Structures on the Basis of Data from Standard Fire-Resistance Tests," Bulletin 20, Div. of Str. Mech. and Concrete Constr., Lund Institute of Technology, Lund, Sweden, 1971.

129. Petzold, A., and M. Rohrs, Beton für hohe Temperaturen, 2d Ed., VEB Verlag für Bauwesen, Berlin, 1967 (also Engl. transl., by Pergamon Press).

130. Philleo, R., "Some Physical Properties of Concrete at High Temperature," J. ACI 54, 857–66 (1958).

131. Pihlajavaara, S. E., and K. Tiusanen, "A Preliminary Study of Thermal Moisture Transfer in Concrete," Concrete for Nuclear Reactors, American Concrete Inst., Special Publication 34, Vol. 2, pp. 1019–32, 1972.

132. Pihlajavaara, S. E., "An Analysis of the Factors Exerting Effect on Strength and Other Properties of Concrete at Elevated Temperatures," American Concrete Inst., Special Publication 34, Vol. 1, pp. 347–54, 1972.

133. Poitevin, P., "Water Migration in Concrete Under a Sustained Temperature Gradient," Concrete for Nuclear Reactors, American Concrete Inst., Special Publication 34, Vol. 2, pp. 909–29, 1972.

134. Polivka, M., and C. H. Best, Investigation of the Problem of Creep in Concrete by Dorn's Method, Department of Civil Engineering Report, University of California, Berkeley, Calif., January 1960; 39th Annual Meeting, Highway Research Board, Washington, D.C.

135. Powers, T. C., and T. L. Brownyard, "Studies of the Physical Properties of Portland Hardened Cement Paste," J. ACI 101–249 (1946); pp. 549, 669, 856, 933, 1974 (PCA Bull. No. 22).

136. Rashid, Y. R., "Nonlinear Analysis of Two-Dimensional Problems in Concrete Creep," Trans. ASME, J. Appl. Mech. 39, 475–82 (1972).

137. Rickenstorf, G., "Spalling of Heated Concrete, Reinforced and Prestressed," Proc. 6th Congress FIP, Prague, 1970.

138. Rickenstorf, G., and R. Liscovius, "Kriechen and Relaxation des Betons bei hohen Temperaturen," Wiss. Z. Techn. Univ. Dresden 17, 1563–65 (1968).

139. Robson, T. C., Symposium on Chem. of Cements (Refractory Concretes Survey), Tokyo, 1968.

140. Ruetz, W., "A Hypothesis for the Creep of Hardened Cement Paste and the Influence of Simultaneous Shrinkage," Proceedings, International Conference on the Structure of Concrete, London, England, 1965, Cement and Concrete Association, pp. 111–15, 1969; Deutscher Ausschuss für Stahlbeton, Heft 183, Berlin, Germany, 1966.

141. Saito, H., "Explosive Spalling of Prestressed Concrete in Fire," Building Research Institute, Shinijuku, Tokyo, Japan, 1965.

142. Saito, H., "Explosive Spalling of Prestressed Concrete in Fire," Proc. of a Symp. held at Braunschweig, Germany, 1965, Fire Resistance of Concrete Structures, Bauverlag GmBH, Berlin, pp. 80–91, 1966.

143. Schimmelwitz, P., and J. Hundt, "A Note on the Moisture Condition of Concrete," Concrete for Nuclear Reactors, American Concrete Inst., Special Publication 34, Vol. 2, pp. 873–82, 1972.

144. Schneider, U., "Physical Properties of Concrete Under Non-Steady State Conditions," Proc. 7th Congress FIP, New York, 1974.

145. Sechamp, H., et al., "Behavior of Reinforced and Restressed Concrete in Fire" (in German), Deutscher Ausschuss für Stahlbeton, Heft 162, W. Ernst and Sohn, Berlin, 1964.

146. Sefarim, J. L., and M. Q. Guerreiro, "Influence of Temperature on the Creep of Mass Concrete," Bulletin RILEM, No. 6, pp. 23–32, March 1960.

147. Seki, S., and M. Kawasumi, "Creep of Concrete at Elevated Temperatures," Concrete for Nuclear Reactors, American Concrete Inst., Special Publication 34, Vol. I, pp. 591–638, 1972.

148. Selvaggio, S. L., and C. C. Carlson, "Fire Resistance of Prestressed Concrete Beams – Study B: Influence of Aggregate and Load Intensity," J. PCA Res. and Dev. Lab., 6(1/2)(1964).

149. Shorter, G. W., and T. Z. Harmathy, "Contribution to the Disc. of a Paper by L. A. Ashton and S.C.C. Bate," Proc. Inst. Civil Eng. 20, 313–15 (1961).

150. Silveira, A.F.D., and C. A. Florentino, "Influence of Temperature on the Creep of Mass Concrete," American Concrete Inst., Special Publication 25, pp. 173–85, 1968.

151. Soles, J. A., and L. B. Geller, "Experimental Studies Relating Mineralogical and Petrographic Features to the Thermal Piercing of Rocks," Mines Branch Technical Bulletin TB 53, Dept. of Mines and Technical Surveys, Ottawa, Canada, 13 pp., 1964.

152. Sullivan, P.J.E., "Time-Temperature Extrapolations Techniques as Applied to Concrete Creep Strains," 1st Int. Conf. Struct. Mech. Reactor Technol., Vol. 3, Reactor Pressure Vessels, September 1971.

153. Sullivan, P.J.E., and A. A. Akhtaruzzaman, "Explosive Spalling of Concrete Exposed to High Temperatures," Imperial College of Science and Technology, London.

154. Sullivan, P.J.E., and A.A.A. Zaman, "Explosive Spalling of Concrete Exposed to High Temperatures," Paper H2/2, 1st Int. Conf. Struct. Mech. Reactor Technol., Berlin, 1971.

155. Sullivan, P.J.E., and M. P. Poucher, "The Influence of Temperature on the Physical Properties of Concrete and Mortar in the Range 20°C to 400°C," American Concrete Inst., Special Publication 25, pp. 103–36, 1971.

156. Sullivan, P.J.E., and J. M. Labani, The Performance of Light Weight Aggregate Concrete at Elevated Temperature, Imperial Colleges, Concrete Str. and Technology Reports CSTR No. 73/2, London, Preprint of a paper for FIP Congress, New York, 1974; also "Flexural Behavior of Plain and Reinforced Lightweight Aggregate Concrete Beams up to 600°C," Cement Concr. Res. 4, 231–37 (1974).

157. Takuda, H., and T. Ho, "Some Experimental Results on Thermal Properties of Concrete," Proc., 7th Japan Congress on Testing Materials, Kyoto, October 10–11, 1963.

158. Thelandersson, S., "Effect of High Temperature Exposure on Tensile Strength of Concrete," Nordisk Betong, 1972, No. 2, pp. 1–28.

159. Thelandersson, S., "Mechanical Behavior of Concrete Under Torsional Loading at Transient, High-Temperature Conditions," Bulletin 46, Div. of Str. Mech. and Concrete Constr., Lund Institute of Technology, Lund, Sweden, 1973.

160. Theuer, A. V., "Effect of Temperature on the Stress Deformation of Concrete," J. Res. Nat. Bur. Stand. 18, 195–204 (1937).

161. Torroja, E., and C. de la Peña, discussion of "Volume Changes of Concrete," by R. L'Hermite, 4th International Symposium on Chemistry of Cement, Washington, D.C., 1960, United States National Bureau of Standards Monograph 43, Vol. II, pp. 695–99; also de la Peña, Bulletin Reunion Internationale des Laboratoires d'Essais et de Recherches sur les Materiaux et les Constructions No. 3, pp. 60–70, 1959.

162. U.S. Bureau of Reclamation, "The Thermal Properties of Cement," Bulletin No. 1 of Final Report, Pt. 7, Boulder Canyon Project, Denver, Colo.

163. Wallo, E. M., et al., Sixth Progress Report, Theoretical and Applied Mechanics Report No. 658, University of Illinois, Urbana, Ill., "Prediction of Creep in Structural Concrete from Short Time Tests," 1965.

164. Waubke, N. V., "On One Physical Aspect of Strength Loss of Portland Cement Concretes at Temperatures up to 1000°C" (in German), in Brandverhalten von Bauteilen, Schriftenreibe der Deutchen Furschungsgemeinschaft, Heft 2, Techn. Univ. Braunschweig, November 1973.

165. Waubke, N. V., "Transportphänomene in Betonporen," Heft 6, Institut für Baustoffkunde und Stahlebetonbau, T.H. Braunschweig, 1966.

166. Waubke, N. V., and U. Schneider, "On Tensile Stresses in Structural Concretes Due to Fast Steam Flows" (in German), in Brandverhalten von Bauteilen, Schriftenreihe der Deutchen Furschungsgemeinschaft, Heft 2, Techn. Univ. Braunschweig, November 1973.

167. Weigler, H., and R. Fischer, "Beton bei Temperaturen von 100°C bis 750°C," Beton Herstellung-Verwendung 18, 33–46 (February 1968).

168. Weigler, H., and R. Fischer, "Effect of Temperatures above 100°C on the Compressive Strength of Cement Mortar, Behavior of Concrete at High Temperatures," Deutscher Ausschuss für Stahlbeton, Heft 164, pp. 1–18, W. Ernst and Sohn, Berlin, 1964.

169. Weigler, H., and R. Fischer, "Influence of High Temperatures on Strength and Deformations of Concrete," Concrete for Nuclear Reactors, American Concrete Inst., Special Publication 34, Vol. I, pp. 481–93, 1972.

170. Whitman, G. D., J. P. Callahan, and J. M. Corum, "An Investigation of the Time-Dependent Behavior of Prestressed Concrete Pressure Vessels," Concrete for Nuclear Reactors, American Concrete Inst., Special Publication 34, Vol. II, pp. 823–43, 1972.

171. Wischers, G., "Effect of Temperature Change of the Strength of Cement Paste and Mortar with Additives of Various Thermal Expansion," Schriftenreihe der Zement Industrie, Heft 28, Verein Deutcher Zement-werke, Düsseldorf, 1961, Forschungs institut der Zement-Industrie (dissertation, T. H. Aachen).

172. Woolson, I. H., "Investigation of the Effect of Heat upon the Crushing Strength and Elastic Properties of Concrete," Proc. ASTM, Vol. 5, 1905.

173. York, G. P., T. W. Kennedy, and E. S. Perry, Experimental Investigation of Creep in Concrete Subjected to Multiaxial Compressive Stresses and Elevated Temperatures, Research Report 2864-2, University of Texas, Austin, June 1970; Concrete for Nuclear Reactors, American Concrete Inst., Special Publication 34, pp. 647–700, 1972.

174. York, G. P., et al., "Effects of Temperature and Moisture on Triaxial Creep," Concrete for Nuclear Reactors, American Concrete Inst., Special Publication 34, Vol. 2, pp. 659–99, 1972.

175. York, G. P., et al., "Experimental Determination of Poisson's Ratio for Creep," Concrete for Nuclear Reactors, American Concrete Inst., Special Publication 34, Vol. I, pp. 535–46, 1972.

176. Yuan, R. L., H. K. Hilsdorf, and C. E. Kesler, "The Effect of Temperature on the Drying of Concrete," Concrete for Nuclear Reactors, American Concrete Inst., Special Publication 34, Vol. II, pp. 991–1017, 1972.

177. Zoldners, N. G., "Thermal Properties of Concretes under Sustained Elevated Temperatures," Temperature and Concrete, pp. 1–31, 1968.

178. Zoldners, N. G., and H. S. Wilson, "Effect of Sustained and Cyclic Temperature Exposures on Light-Weight Concrete," Behavior of Concrete under Temperature Extremes, American Concrete Inst., Special Publication 39, pp. 149–78, 1973.

179. Zielinski, J. L., and A. Sadowski, "The Influence of Moisture Content on the Creep of Concrete at Elevated Temperatures," 2d Int. Conf. Struct. Mech. Reactor Technol., Berlin, Germany, Vol. 3, Reactor Vessels, September 1973.

# APPENDIX II

## THERMAL-STRUCTURAL ANALYSIS OF A REPRESENTATIVE LMFBR EQUIPMENT CELL LINER

# THERMAL-STRUCTURAL ANALYSIS OF A REPRESENTATIVE LMFBR EQUIPMENT CELL LINER

by

P. A. Stancampiano

August 1975

FOR

OAK RIDGE NATIONAL LABORATORY
Oak Ridge, Tennessee 37830
operated by
UNION CARBIDE CORPORATION

SWANSON ENGINEERING ASSOCIATES
CORPORATION

CONTENTS

Page

1. INTRODUCTION ..... 149
2. SUMMARY AND CONCLUSIONS ..... 151
3. ONE-DIMENSIONAL TRANSIENT THERMAL ANALYSIS ..... 153
   3.1 One-Dimensional Finite-Element Thermal Model ..... 153
   3.2 One-Dimensional Analysis Results ..... 155
4. THREE-DIMENSIONAL THERMAL ANALYSIS ..... 165
   4.1 Three-Dimensional Finite-Element Thermal Model ... 165
   4.2 Three-Dimensional Thermal Analysis Results ..... 167
5. THREE-DIMENSIONAL PLASTIC STRUCTURAL ANALYSIS ..... 185
   5.1 Three-Dimensional Finite-Element Structural Model ..... 185
   5.2 Three-Dimensional Structural Model Results ..... 187
6. REFERENCES ..... 202
   6.1 Computer References ..... 202

# 1. INTRODUCTION

Liquid-metal-cooled fast breeder reactor (LMFBR) loop-type systems employ steel-lined concrete equipment cell structures. One of the design functions of the steel liner is to prevent contact of hot sodium with the concrete structure under faulted conditions. A comprehensive state-of-the-art review of LMFBR cell liners by Chapman[1] indicates that LMFBR cell liners are generally firmly anchored to the backup concrete structure with the notable exception of the "free-floating" Fast Flux Test Facility (FFTF) concept. The anchored liners naturally would experience larger thermal strains during a massive sodium spill accident. However, anchored liners are significantly less costly to construct than the floating liners. This report discusses a thermal-structural analysis of a representative anchored cell liner subjected to a sodium spill.

The representative cell liner arrangement shown in Fig. 1.1 was selected by ORNL[2] for analysis. This arrangement shows a 3/8-in.-thick steel liner anchored to a 36-in.-thick concrete wall by 1/2-in.-diam steel anchor studs embedded to a depth of 8 in. in the wall. For analysis purposes, ORNL selected ASTM A516 carbon steel for the liner material, since it is representative of the material proposed for use in LMFBR cell liners.[3] The anchors are assumed to be spaced on a 15-in.-square pattern as shown. The analysis assumes the cell structure is initially at 150°F and is then suddenly flooded with liquid sodium at 1000°F.

Section 2 of this report summarizes the thermal-structural analysis results and conclusions. Details of the analysis are presented in Sections 3, 4, and 5. Section 3 discusses a simplified one-dimensional transient thermal analysis employed to identify significant heat transfer parameters, such as the heat flow resistance of the air gap between the steel liner and concrete wall. Section 4 contains the details of the three-dimensional transient thermal analysis using the results of the one-dimensional analysis as a guide. The three-dimensional elastic-plastic large deflection structural analysis of the steel liner's response to the sodium spill is presented in Section 5. These sections contain detail discussions of the assumptions, analytical models, and material properties used and also present the results of each analysis in detail.

ORNL-DWG 75-4856R1

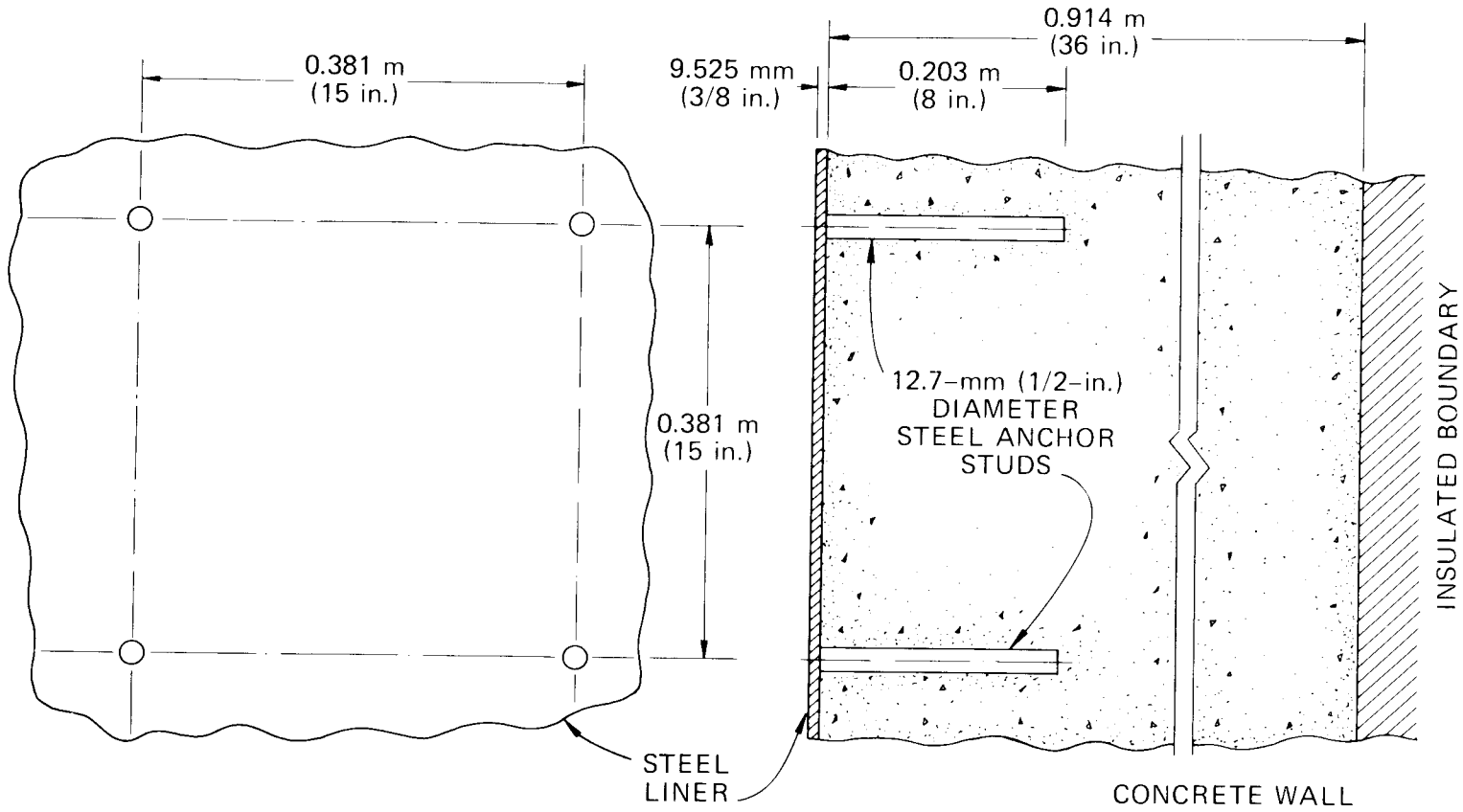


Fig. 1.1. Schematic of representative anchored LMFBR cell liner arrangement selected for thermal-structural analysis.

## 2. SUMMARY AND CONCLUSIONS

Thermal-structural analyses of a representative anchored LMFBR cell liner arrangement have been completed. The liner arrangement selected for analysis is shown in Fig. 1.1. The problem under investigation was a postulated sudden massive sodium spill accident in which the outer surface of the steel cell liner plate heats from 150 to 1000°F in 1 sec. All analyses were conducted using the transient thermal and structural options of the ANSYS general-purpose finite-element computer program. Nonlinear effects (such as radiation between the liner and concrete wall in the thermal analysis, plasticity, and large displacements in the structural analysis) were considered.

A simplified one-dimensional transient thermal model of the cell liner was used to parametrically study the effects of the stagnant air gap size between the liner and concrete wall. The one-dimensional thermal analysis results indicated little difference in any of the temperature responses for air gaps greater than 0.25 in. The one-dimensional thermal model was also used to demonstrate the convergence of the transient thermal solution.

A three-dimensional transient heat transfer analysis, guided by the results of the one-dimensional analysis, was then conducted. A 0.25-in. initial stagnant air gap was assumed; therefore the transient thermal analysis was essentially decoupled from the liner plate structural deformations. Since the one-dimensional model indicated most of the concrete had not responded to the transient by the time the steel liner reached quasi-steady-state, the concrete wall was modeled to a depth of 10 in. only. The three-dimensional transient thermal analysis was carried out for the first 3 min of the transient following the 1000°F massive sodium spill. During the first 30 sec, the steel liner heats rapidly to about 975°F. The concrete and embedded steel anchor stud heat much more slowly. The stud has only begun to heat slightly to about one-third of its length in the first 3 min. The maximum temperature of the front face of the concrete wall near the stud was less than 500°F after 3 min. The temperature difference (interaction) between the anchor stud and adjacent concrete appears to be long term over the total length of the stud (8 in.),

with the peak interaction occurring at the front face very early in the transient and moving slowly along the stud with decaying amplitude.

The steel liner plate structure was modeled with elastic-plastic three-dimensional shell elements. Transient temperatures calculated from the three-dimensional thermal model were used in the structural plate model. In addition, an isothermal steady state at 1000°F followed by an isothermal cooldown to 150°F to unload the plate were considered. Nonlinear effects such as plasticity and large deformations were treated incrementally. Reversed loading was simulated assuming classical bilinear kinematic hardening. The elevated-temperature carbon steel stress-strain curves measured by ORNL were used in the structural model. Seventy-one total increments were employed in the structural solution.

The maximum out-of-plane bulge of the steel liner was approximately 3/8 in. at 1000°F, and the plate was nearly straight after the cooldown, having yielded in tension. The maximum calculated generalized membrane plus bending strain in the plate was 1.7% near the stud attachment. The maximum local membrane strain was about 1.35%.

# 3. ONE-DIMENSIONAL TRANSIENT THERMAL ANALYSIS

Transient heat transfer will occur between the steel cell liner and concrete wall as a result of an accidental hot sodium spill. In the cell liner arrangement selected for analysis (Fig. 1.1), the heat transfer mechanisms between the liner and concrete are (1) radiation between the back face of the steel liner and front face of the concrete, (2) conduction through the air gap between the liner and concrete assuming stagnant air, and (3) conduction along the steel anchor studs which act like fins.

Radiation is important early in the transient, when the temperature differences between the liner back face and concrete front face are greatest. Heat conduction in the air gap is dependent primarily on the gap size neglecting any circulation. The gap size, in turn, is dependent on the thermal-structural deformation of the liner relative to the concrete. Since the liner heats from the outer surface, it naturally tends to bulge outward at the center of each square formed by the anchor pattern. Since the stud is a relatively good conductor, heat will flow in the plane of the plate toward the stud and away from the stud in the concrete. Therefore, the transient heat transfer in the cell liner arrangement shown in Fig. 1.1 is three dimensional.

Even though the transient temperature distributions in the cell liner and concrete are actually three dimensional, the net flow of heat is essentially one dimensional from the steel liner to the concrete wall. Therefore, prior to performing a three-dimensional transient thermal analysis of the cell liner arrangement, a one-dimensional simplified analysis was performed to assess the importance of the stagnant air gap size and other parameters. This section discusses this simplified one-dimensional analysis in detail.

## 3.1 One-Dimensional Finite-Element Thermal Model

The one-dimensional finite-element transient thermal analysis was performed using the ANSYS general-purpose finite-element computer program.[4] Figure 3.1 shows a schematic of the model used in the transient thermal analysis of a sodium spill accident. The model contains 36 finite elements that simulate a prism with square bases (15 × 15 in.) that

straddle the center line of a typical anchor stud. Elements 1, 2, and 3 model the steel liner plate with ANSYS STIF 32 conducting bar elements each with 225-in.$^2$ cross-sectional areas. Elements 4 through 14 model the 1/2-in.-diam steel anchor stud again using ANSYS STIF 32, each element having a 0.196-in.$^2$ cross-sectional area. Elements 15 and 16 both span node 3 on the back face of the steel liner plate and node 4 on the front face of the concrete wall. Element 15 simulates the stagnant air gap, also using the STIF 32 element with a 225-in.$^2$ cross section. Element 16 simulates the radiation between the liner and concrete using ANSYS STIF 31 radiation link elements of 225 in.$^2$ surface area with a form factor of 1.0 and an effective emissivity of 0.54 (see below). The concrete wall is modeled with elements 17 through 36 using the STIF 2 conducting bar element, again with a 225-in.$^2$ cross section.

The length of the air gap between nodes 3 and 4 was studied parametrically. Analyses were conducted assuming 0.01-, 0.26-, and 0.51-in. stagnant air gaps between the liner and concrete. In all cases, the temperature of node 14 on the hot end of the steel stud was coupled to node 3 on the steel plate. This forces node 14 to have the same temperature as node 3 and essentially connects the stud to the plate without increasing the stud length since node 3 may be moved independently of node 14 to vary the air gap size.

Nodes 4 through 13 are common to the anchor stud elements and concrete wall elements. Node 4 is also common to the cold end of the radiation link element. The temperatures calculated for these nodes, therefore, represent weighed averages. For example, the temperature of node 4 is a weighed average temperature of the front face of the concrete and anchor stud temperatures. In all cases, node 113, at the back end of the concrete wall, was assumed to be perfectly insulated (adiabatic).

The material properties assumed in the one-dimensional model are listed in Table 3.1. The thermal properties for steel and concrete were taken from data specified by ORNL[3] for a temperature of 500°F. The properties for air were taken from Ref. 5 for a temperature of 530°F. Since the one-dimensional analysis was a first approximation, the temperature dependence of the material properties was neglected.

Table 3.1. Material properties assumed in the one-dimensional finite-element transient thermal model of the LMFBR cell liner[a]

| Material | Thermal conductivity (Btu/hr-in.-°F) | Density ($lb_m/in.^3$) | Specific heat (Btu/$lb_m$-°F) |
|---|---|---|---|
| Concrete[3] | 0.072 | 0.097 | 0.256 |
| Steel[3] | 1.99 | 0.281 | 0.115 |
| Air[5] | 0.0021 | 0.000023 | 0.25 |

[a]Property values are tabulated for a temperature of about 500°F.

The effective emissivity, or interchange factor for radiant heat exchange between two parallel surfaces, is given on pp. 403–404 of Ref. 5 to be

$$\bar{\epsilon} = \left(\frac{1}{\epsilon_1} + \frac{1}{\epsilon_2} - 1\right)^{-1} , \qquad (1)$$

where $\epsilon_1$ is emissivity of back face of steel liner and $\epsilon_2$ is emissivity of front face of concrete. Emissivity values used in this study were taken from Ref. 6. Again, in this approximate one-dimensional analysis, no attempt was made to include the temperature dependence of these emissivities. Taking $\epsilon_1 = 0.79$ for oxidized steel and $\epsilon_2 = 0.63$ for concrete yields an effective emissivity of $\bar{\epsilon} = 0.54$. The radiant absorptivity of the air gap was neglected, and a form factor of 1 for infinite parallel surfaces was assumed.

## 3.2 One-Dimensional Analysis Results

Four analysis cases were run with the one-dimensional model of the cell liner discussed in Section 3.1. In three of these cases, the air gap was varied to study this effect, and in the fourth case, the times between integration points were doubled to check for convergence of the

solution. The air gaps and number of integration points used are given below:

| Case | Size of air gap (in.) | Number of time integration points |
|---|---|---|
| 1 | 0.26 | 113 |
| 2 | 0.51 | 113 |
| 3 | 0.01 | 113 |
| 4 | 0.26 | 57 |

The 0.01-in. air gap was taken to be a nominal "zero" gap or "contact" resistance case. It was assumed that a gap of 1/4 to 1/2 in. is probably more likely at assembly. Therefore, stagnant air gaps of 0.01, 0.26, and 0.51 in. were selected for parametric study.

In cases 1, 2, and 3, 113 time points were used in the sodium spill thermal transient incremental solution, as follows:

1. The first load step was a steady-state solution at 150°F to initialize all node temperatures at 150°F.

2. In the second load step, the outer surface of the steel liner plate, node 1, was ramped from 150 to 1000°F in 1 sec with 10 substeps; i.e., $\Delta t = 0.1$ sec between solutions.

3. In the third load step, the outer surface of the liner, node 1, was held at 1000°F for 19 sec, from $t = 1$ sec to $t = 20$ sec, with 38 integration points or substeps of 0.5 sec each.

4. The fourth load step consisted of 64 integration points or substeps of 2.5 sec each and extended the solution to $t = 180$ sec. Again node 1, the outer surface of the steel liner, was held at 1000°F.

In addition to the uncertainty associated with the air gap size, the radiation link element (ANSYS STIF 31) used to model the radiation from the liner to the concrete is nonlinear and requires small time steps for accuracy. Therefore, case 4 was run assuming a 0.26-in. air gap and doubling the times between integration points to check the accuracy and convergence of the transient solution. In case 4, the second load step had 5 substeps, the third had 19 substeps, and the fourth had 32 substeps, giving a total of 57 integration points compared to 113 points for cases 1 through 3.

Solutions for all four cases were conducted using the ANSYS type 1 heat transfer analysis option.[4] For this option, the fundamental system equilibrium equation solved by ANSYS is

$$[C]\{\dot{T}\} + [K]\{T\} = \{Q\} , \qquad (2)$$

where

$[K]$ = the thermal conductivity matrix,

$\{Q\}$ = the heat flow vector,

$\{T\}$ = the nodal point temperature vector,

$[C]$ = the specific heat matrix.

Equation (2) was solved at each time point in the heat transfer transient for the load steps and boundary conditions discussed above. Second-order integration was assumed; i.e., the nodal temperatures were assumed to be quadratic functions of time in the integration.

The results for each one-dimensional case are plotted in Figs. 3.2 through 3.5 for cases 1 through 4 respectively. Each of these figures shows the calculated temperature-time responses for nodes 1, 2, 3, 4, 9, and 63 of the cell liner one-dimensional model shown in Fig. 3.1. Nodes 1, 2, and 3 are the front, middle, and back surfaces of the steel liner plate respectively. The sodium exposed face (node 1) was actually specified to ramp from 150 to 1000°F in 1 sec as discussed above and as shown in each plot. Node 4 represents the average temperature of the concrete front face exposed to the liner plate. Node 9 represents the average temperature of the concrete and steel stud 4 in. from the concrete front surface, halfway along the embedded stud length. Node 63 is 14 in. from the back face of the concrete wall.

In each case, the steel liner comes to a "quasi-steady-state" in about 20 sec, after which the entire plate is above 950°F and continues to heat up very slowly.

Case 1 (0.26-in. air gap) and case 2 (0.51-in. air gap), Figs. 3.2 and 3.3 respectively, indicate little difference in any of the responses (particularly node 4, the concrete front face) to the large change in air gap. However, in case 3 (0.01-in. air gap), shown in Fig. 3.4, the concrete front face responds much more rapidly. Case 4 (Fig. 3.5) shows

Table 3.2. Comparison of calculated temperatures of back face of steel liner from one-dimensional model

| Time (sec) | Node 3 temperatures (°F) | | | |
|---|---|---|---|---|
| | Case 1, gap = 0.26 in. | Case 2, gap = 0.51 in. | Case 3, gap = 0.01 in. | Case 4,[a] gap = 0.26 in. |
| 0 | 150.0 | 150.0 | 150.0 | 150.0 |
| 3 | 471.1 | 471.2 | 467.8 | 449.6 |
| 5 | 713.7 | 713.9 | 705.1 | 713.9 |
| 10 | 921.9 | 922.2 | 907.5 | 925.1 |
| 15 | 963.3 | 963.6 | 948.7 | 964.5 |
| 20 | 972.0 | 972.4 | 958.3 | 972.4 |
| 40 | 976.5 | 976.8 | 966.5 | 976.6 |
| 60 | 978.5 | 978.8 | 971.2 | 978.5 |
| 80 | 980.2 | 980.4 | 974.7 | 980.2 |
| 100 | 981.6 | 981.8 | 977.4 | 981.6 |
| 120 | 982.8 | 982.9 | 979.6 | 982.8 |
| 140 | 983.8 | 983.9 | 981.2 | 983.8 |
| 160 | 984.6 | 984.7 | 982.6 | 984.6 |
| 180 | 985.4 | 985.4 | 983.6 | 985.4 |

[a]Case 4 used one-half as many integration points as cases 1, 2, and 3.

essentially the same temperature-time responses as case 2 for a 0.26-in. air gap. The results of case 4 were calculated with half the integration points used in case 2, indicating that the solutions are in fact converged. Tables 3.2 and 3.3 provide a comparison of node 3 and node 4 temperatures at selected times in the transient calculated for each case. Finally, it can be seen in all cases that, except for near the front surface, the concrete wall temperatures respond very slowly as would be expected.

Table 3.3. Comparison of calculated temperatures of front face of concrete wall from one-dimensional model

| Time (sec) | Node 4 temperatures (°F) | | | |
|---|---|---|---|---|
| | Case 1, gap = 0.26 in. | Case 2, gap = 0.51 in. | Case 3, gap = 0.01 in. | Case 4,[a] gap = 0.26 in. |
| 0 | 150.0 | 150.0 | 150.0 | 150.0 |
| 3 | 164.8 | 164.5 | 179.1 | 164.3 |
| 5 | 203.8 | 202.7 | 249.6 | 201.9 |
| 10 | 288.4 | 286.2 | 382.9 | 288.7 |
| 15 | 332.0 | 329.3 | 442.2 | 332.6 |
| 20 | 357.5 | 354.6 | 475.1 | 357.8 |
| 40 | 427.1 | 423.6 | 561.7 | 427.2 |
| 60 | 481.8 | 477.9 | 624.8 | 481.9 |
| 80 | 526.4 | 522.3 | 672.4 | 526.5 |
| 100 | 563.0 | 558.8 | 708.6 | 563.1 |
| 120 | 593.4 | 589.1 | 736.6 | 593.5 |
| 140 | 618.7 | 614.5 | 758.5 | 618.8 |
| 160 | 640.2 | 636.0 | 775.9 | 640.3 |
| 180 | 658.5 | 654.3 | 790.0 | 658.5 |

[a]Case 4 used one-half as many integration points as cases 1, 2, and 3.

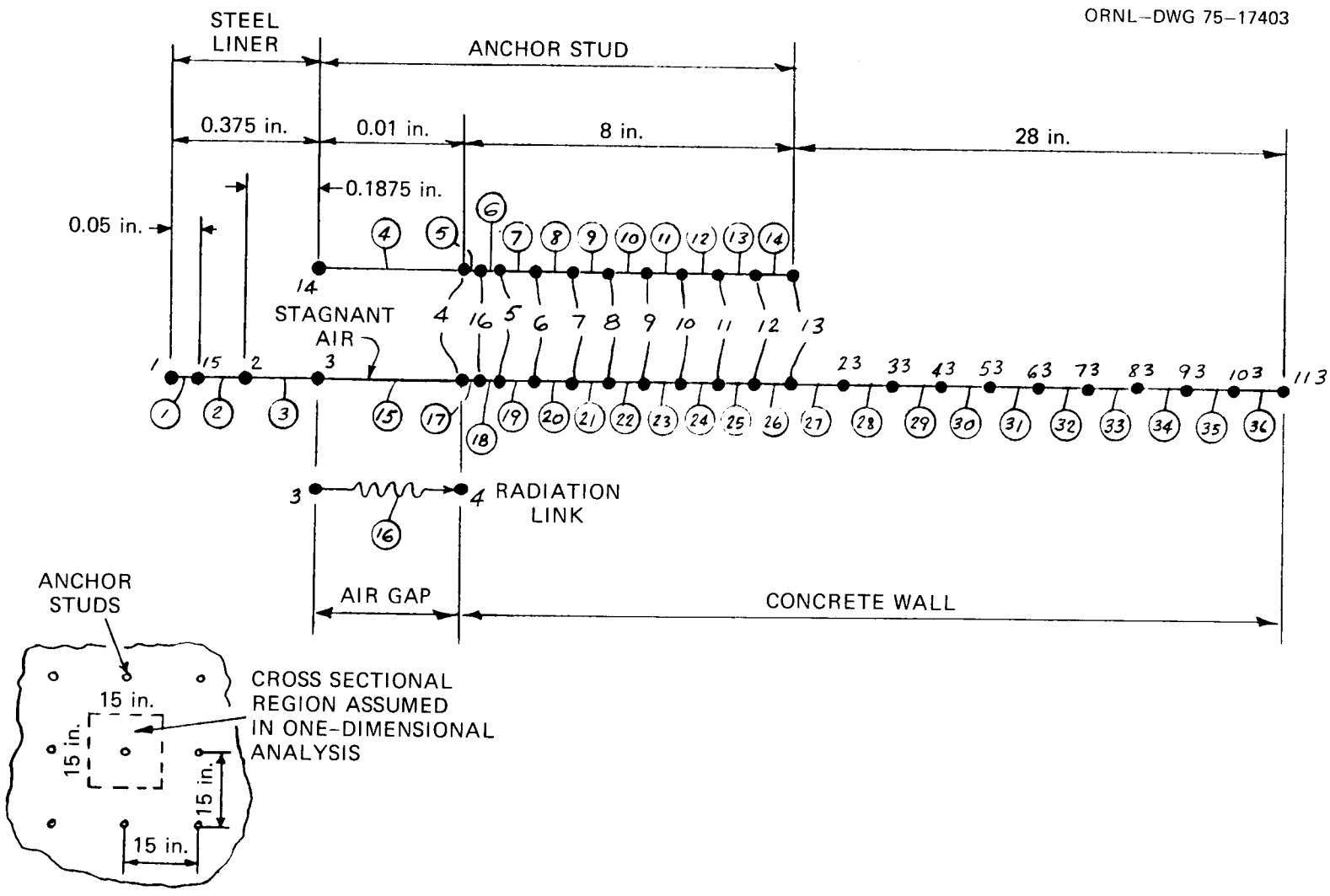


Fig. 3.1. Schematic of one-dimensional finite-element model of LMFBR cell liner arrangement used in transient thermal analysis of a sodium spill accident.

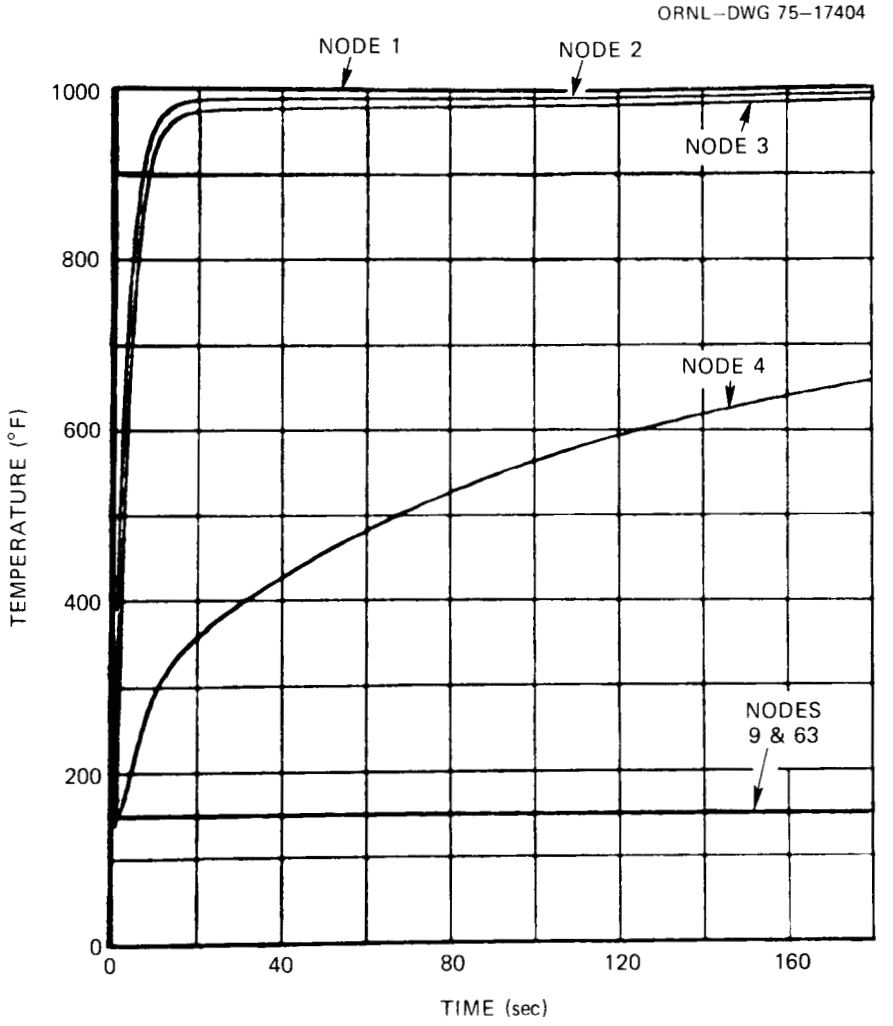


Fig. 3.2. Temperature vs time for nodes 1, 2, 3, 4, 9, and 63 of one-dimensional finite-element model, Case 1, 0.26 in. stagnant air gap.

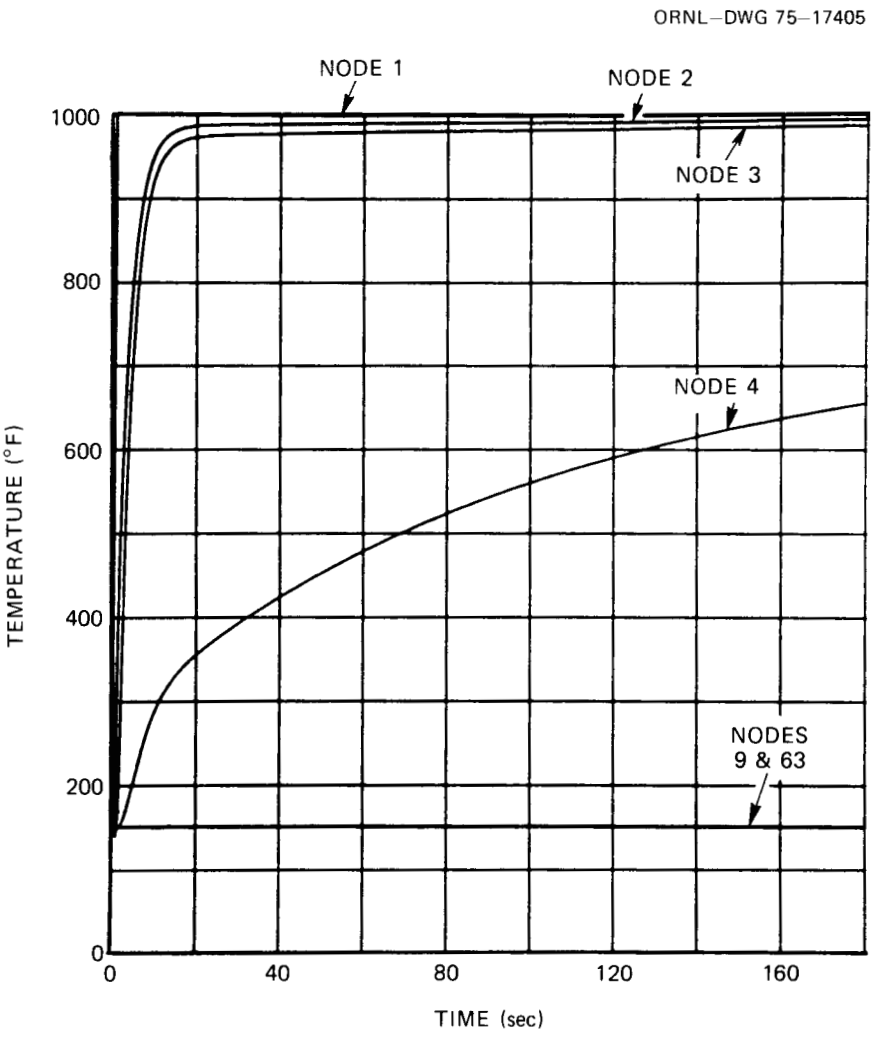


Fig. 3.3. Temperature vs time for nodes 1, 2, 3, 4, 9, and 63 of one-dimensional finite-element model, Case 2, 0.51 in. stagnant air gap.

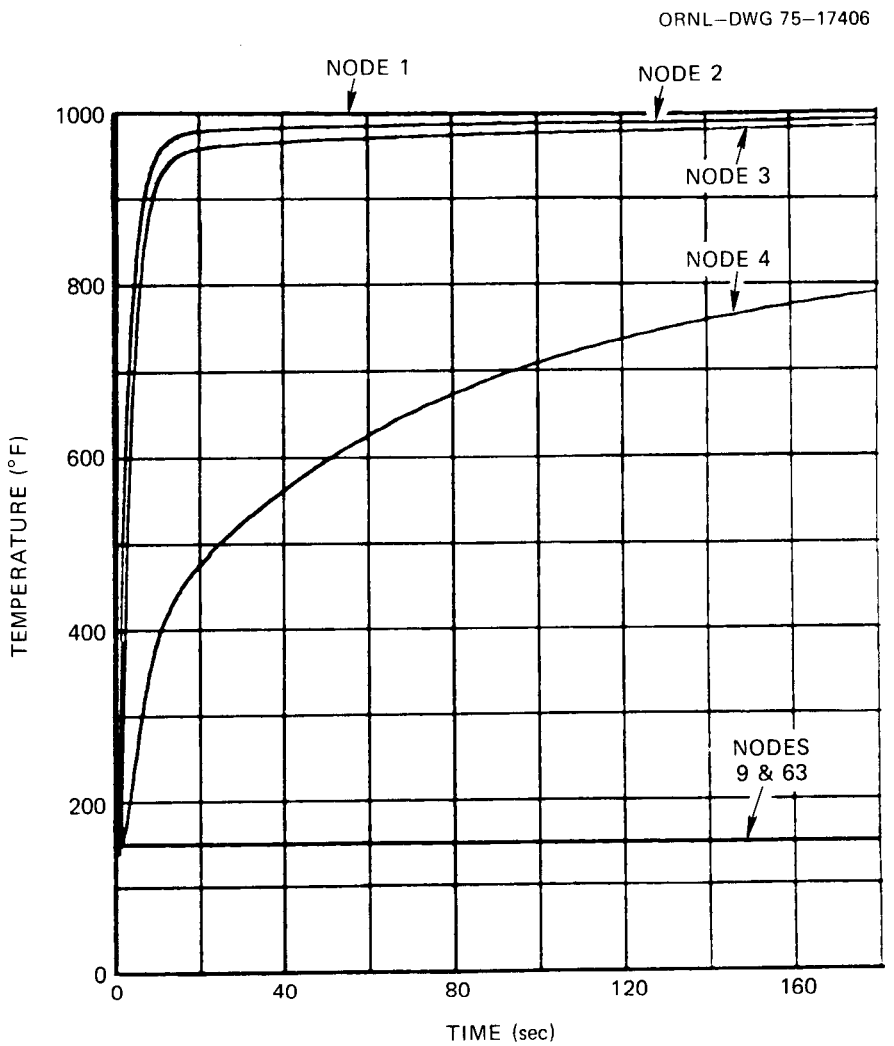


Fig. 3.4. Temperature vs time for nodes 1, 2, 3, 4, 9, and 63 of one-dimensional finite-element model, Case 3, 0.01 in. stagnant air gap.

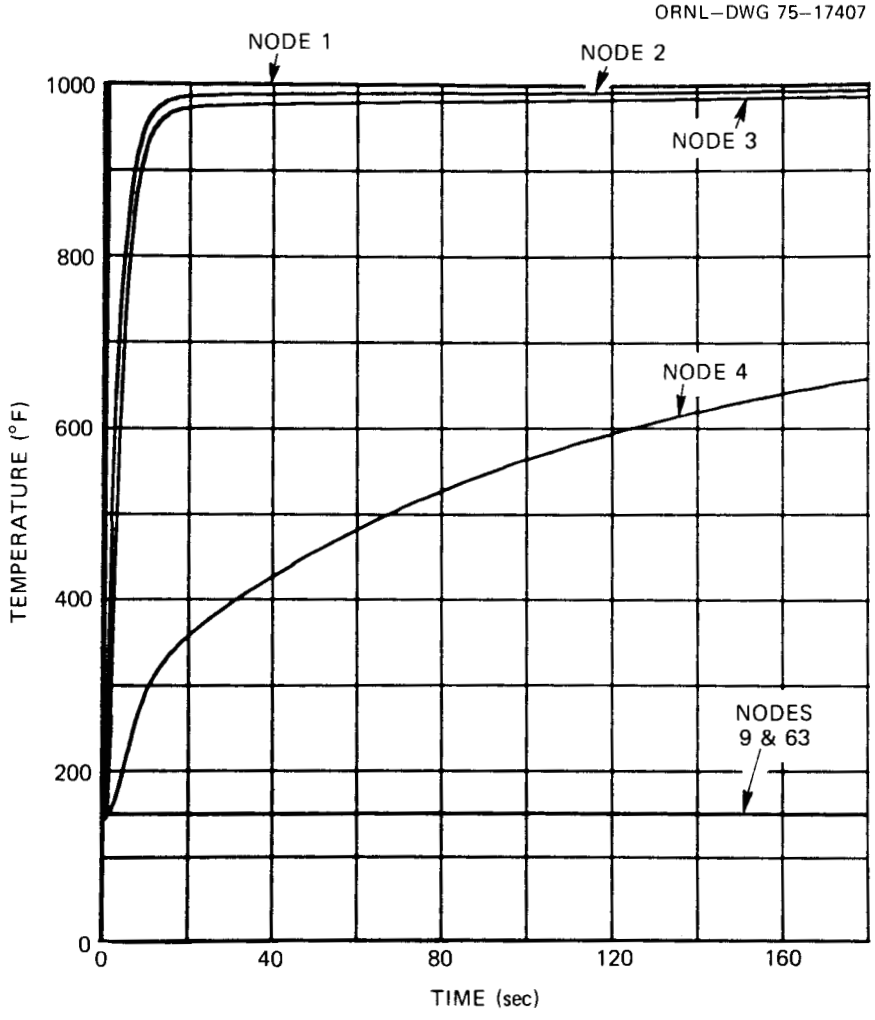


Fig. 3.5. Temperature vs time for nodes 1, 2, 3, 4, 9, and 63 of one-dimensional finite-element model, Case 4, 0.26 in. stagnant air gap and twice the time between integration points.

# 4. THREE-DIMENSIONAL THERMAL ANALYSIS

A three-dimensional transient heat transfer analysis of the representative anchored LMFBR cell liner arrangement shown in Fig. 1.1 was performed using the results of the simplified one-dimensional analysis discussed in Section 3. Again, an accidental hot sodium spill was considered. The three-dimensional transient analysis included radiation between the liner and concrete, conduction through the stagnant air gap, and conduction along the steel anchor studs. This section discusses the three-dimensional transient thermal analysis in detail.

## 4.1 Three-Dimensional Finite-Element Thermal Model

The three-dimensional finite-element transient thermal analysis of the LMFBR cell liner was also performed using the ANSYS general-purpose finite-element computer program.[4] Figure 4.1 shows a schematic of the model used. The air gap size and concrete depth shown were essentially selected using the results of the one-dimensional analysis.

A 0.25-in. initial stagnant air gap was assumed. Such an initial gap could be reasonably expected at assembly. Also the liner plate out-of-plane deformations were expected to be away from the concrete, tending to increase the air gap. The one-dimensional analysis showed the liner plate reaching 950°F in about 20 sec for a 1000°F spill with the concrete essentially remaining at 150°F. Figure 4.2 shows a very approximate estimate of the resulting liner plate deformation which is about 0.9 in. Therefore, most of the transient occurs with a substantial air gap between the liner and concrete regardless of the initial gap size. The one-dimensional analysis showed that the transient heat transfer is essentially unaffected by gaps between 0.26 and 0.51 in. Therefore, it was reasonably assumed that the three-dimensional transient thermal analysis conducted using a constant 0.25-in. stagnant air gap was decoupled from the liner plate structural deformations.

The one-dimensional analysis indicated that the bulk of the concrete wall had not yet responded to the transient in the first 180 sec. This was true even in the vicinity of the steel anchor stud 4 in. from the front face of the concrete (see node 9 in Figs. 3.2 through 3.5). The

liner plate, however, had essentially reached a quasi-steady-state in the first 30 sec. Therefore, the concrete wall was modeled to a depth of 10 in., 2 in. deeper than the stud, and the remaining concrete was neglected in the three-dimensional model.

The three-dimensional transient thermal model shown in Fig. 4.1 contains 270 elements and 357 nodes, starting with node 190 through node 546. This model makes use of the 1/8 symmetry shown schematically in Fig. 4.3. The planes associated with the 1/8 symmetry were assumed adiabatic, as was the back face of the concrete.

The 0.375-in.-thick steel liner plate is modeled with 75 ANSYS STIF 70 three-dimensional isoparametric thermal conducting solid elements. There are five equally spaced layers of these elements through the thickness of the plate. Six nodal points through the plate thickness were used to define the large through-the-thickness temperature gradients expected early in the sodium spill transient. Figure 4.4 is a computer-drawn geometry plot of the steel plate elements.

The 1/2-in.-diam steel anchor stud was modeled with nine ANSYS STIF 33 three-dimensional solid heat conducting bar elements that span nodes 252, 273, 294, 315, 336, 357, 378, 399, 420, and 441 in Fig. 4.1. Note that only one-eighth of the stud's cross-sectional area (0.0245 in.$^2$) was modeled due to the existing symmetry.

The 0.25-in.-stagnant air gap was modeled with one layer containing 15 ANSYS STIF 70 three-dimensional isoparametric thermal conducting solid elements. Again any circulation in the air gap was neglected. Radiant exchange across the air gap was modeled using 21 ANSYS STIF 31 radiation link elements. These radiation elements were assumed to link directly opposite nodes across the air gap, e.g., nodes 426 and 405, nodes 431 and 410, etc., as shown in Fig. 4.5. Cross radiation paths, such as 426 and 410, 426 and 414, etc., were neglected since the air gap was small compared to the surface areas. Typical areas used with the radiation links are shown in Fig. 4.5. As in the one-dimensional case, a form factor of 1.0 for parallel planes was assumed. The effective emissivities were again computed assuming Eq. (1) applies. The temperature dependence of the emissivities given in Table 4.1 was used in the three-dimensional model. The absorptivity of the air was neglected.

Table 4.1. Emissivities assumed in the three-dimensional thermal model of the LMFBR cell liner[a]

| Temperature (°F) | Steel $\epsilon_1$ | Concrete $\epsilon_2$ | Effective[b] $\bar{\epsilon}$ |
|---|---|---|---|
| 70 | 0.939 | 0.93 | 0.877 |
| 200 | 0.945 | 0.907 | 0.862 |
| 400 | 0.955 | 0.874 | 0.839 |
| 600 | 0.965 | 0.839 | 0.814 |
| 800 | 0.97 | 0.806 | 0.786 |
| 1000 | 0.97 | 0.772 | 0.754 |

[a]Emissivities were taken from Table 12.1 of Ref. 6. The steel plate surface was assumed rough and oxidized. The concrete emissivity was assumed to vary linearly between 0.93 at 70°F to 0.63 at 1832°F.

[b]Calculated using Eq. (1).

The material properties assumed in the three-dimensional model for steel, concrete, and air are listed in Tables 4.2, 4.3, and 4.4 respectively. The temperature dependence shown for steel and concrete thermal properties was taken from data specified by ORNL,[3] and the thermal properties for air were taken from Ref. 5.

## 4.2 Three-Dimensional Thermal Analysis Results

The one-dimensional thermal analysis results indicated that about 50 integration points would be sufficient to accurately define the sodium spill transient, assuming these points were spaced as in the one-dimensional analysis. Therefore, the 1000°F accidental sodium spill transient three-dimensional analysis was conducted for the following load steps:

1. The first load step was a steady-state solution at 150°F to initialize all node temperatures at 150°F.

Table 4.2. Thermal properties assumed in the three-dimensional thermal model for the steel liner plate[3]

| Temperature (°F) | Density ($lb_m/in.^3$) | Thermal conductivity (Btu/sec-in.-°F) | Specific heat (Btu/$lb_m$-°F) |
|---|---|---|---|
| 70 | 0.284 | 0.000625 | 0.103 |
| 200 | 0.283 | 0.000602 | 0.112 |
| 400 | 0.282 | 0.000569 | 0.123 |
| 600 | 0.280 | 0.000535 | 0.133 |
| 800 | 0.279 | 0.000502 | 0.149 |
| 1000 | 0.2775 | 0.000468 | 0.170 |

Table 4.3. Thermal properties assumed in the three-dimensional thermal model for the concrete cell wall[3]

| Temperature (°F) | Density ($lb_m/in.^3$) | Thermal conductivity (Btu/sec-in.-°F) | Specific heat (Btu/$lb_m$-°F) |
|---|---|---|---|
| 70 | 0.0973 | 0.0000232 | 0.175 |
| 200 | 0.0971 | 0.0000228 | 0.197 |
| 400 | 0.0967 | 0.0000209 | 0.230 |
| 600 | 0.0963 | 0.0000190 | 0.282 |
| 800 | 0.0958 | 0.0000170 | 0.302 |
| 1000 | 0.0952 | 0.0000150 | 0.282 |

Table 4.4. Thermal properties assumed in the three-dimensional thermal model for stagnant air[5]

| Temperature (°F) | Density ($lb_m/in.^3$) | Thermal conductivity (Btu/sec-in.-°F) | Specific heat (Btu/$lb_m$-°F) |
|---|---|---|---|
| 70 | 0.0000434 | 0.00000034 | 0.240 |
| 200 | 0.0000349 | 0.00000042 | 0.241 |
| 400 | 0.0000268 | 0.00000052 | 0.245 |
| 600 | 0.0000208 | 0.00000062 | 0.252 |
| 800 | 0.0000182 | 0.00000070 | 0.257 |
| 1000 | 0.0000108 | 0.00000078 | 0.263 |

2. In the second load step, the outer surface of the steel liner plate, nodes 526 through 546, was ramped from 150 to 1000°F in 1 sec with 5 substeps, i.e., $\Delta T = 0.2$ sec between solutions.

3. In the third load step, the outer surface of the liner, nodes 526 through 546, was held at 1000°F for 19 sec, from t = 1 sec to t = 20 sec with 19 integration points or substeps of 1.0 sec each.

4. The fourth load step consisted of 32 integration points or substeps of 5.0 sec each and extended the solution to t = 180 sec. Again nodes 526 to 546, the outer surface of the steel liner, were held at 1000°F.

The transient solution was conducted using the ANSYS type 1 heat transfer analysis option,[4] which solved Eq. (2) for the three-dimensional model of the cell liner at each of the above time points. The results of the three-dimensional transient thermal analysis of the 1000°F sodium spill accident are shown in Figs. 4.6 through 4.14.

Typical transient responses of the steel cell liner plate are shown in Figs. 4.6 through 4.9. The liner plate transient temperatures at the six nodes through the plate thickness at the center and at the stud attachment are shown in Figs. 4.6 and 4.7 respectively. It can be seen that the plate responds rapidly as expected. Since more heat flows into the stud, the gradient through the plate at the stud attachment is much larger than at the center of the plate. Figure 4.8 shows the temperature difference across the plate thickness at its center which peaks at the end of the specified 1-sec outer surface temperature ramp. Figure 4.8 again shows the rapid heating of the plate. A measure of the in-plane temperature difference of the steel liner is shown in Fig. 4.9. While the maximum in-plane difference peaks early at about 15 sec, there will be a long-term in-plane gradient to supply heat to the stud while the concrete wall is heating. The calculated transient temperature drops across the air gap between the steel liner and concrete at several locations are plotted in Fig. 4.10. Figure 4.11 shows the calculated transient temperatures of the front face of the concrete wall at these same locations. The slight drops in temperature which occur very early in the transient are not real;

they are numerical errors introduced by the relatively large element spacings employed in the three-dimensional model. This error is not serious, and temperature trends appear to be reasonable after a few more time points. Figure 4.12 shows the transient temperatures into the concrete at the model center line. It can be seen that the concrete has begun to heat only to a depth of about 1 in. in the first 3 min of the transient.

Figure 4.13 shows transient plots of the steel anchor stud nodal temperatures. The stud has only begun to heat to about one-third of its length in the first 3 min of the transient. The maximum transient temperature differences between the steel stud and concrete are shown in Fig. 4.14. These curves indicate that the temperature difference has peaked at the concrete wall front face and is about to peak 0.25 in. in from the face. Thus the thermal structural interaction between the stud and concrete appears to be long term over the total length of the stud, with the peak interaction occurring at the front (heated) end very early in the transient and moving slowly along the stud with decaying amplitude.

The calculated transient thermal behavior of the LMFBR representative anchored cell liner subjected to a sudden 1000°F sodium flood spill appears to be reasonable. The calculated transient temperatures of the steel liner plate, concrete, and anchor stud are responding as expected. The resolution of the three-dimensional finite-element thermal model appears to be good for the plate and the anchor stud. However, more elements would probably be required to better define the early transient three-dimensional gradients in the concrete wall.

The three-dimensional transient temperature distributions of the cell liner model were stored on tape and used in the structural analysis discussed in Section 5.

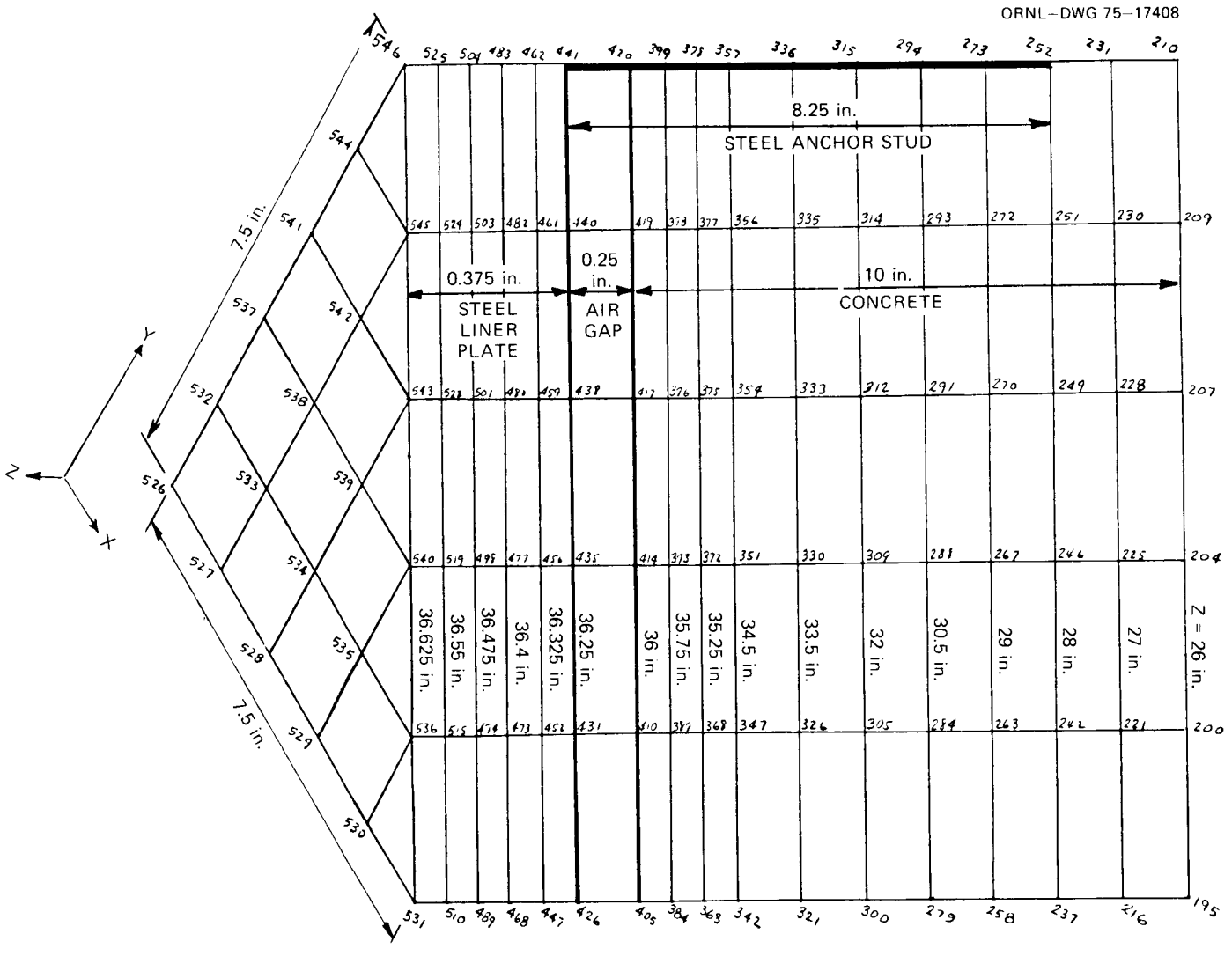


Fig. 4.1. Schematic of three-dimensional finite-element model of LMFBR cell liner.

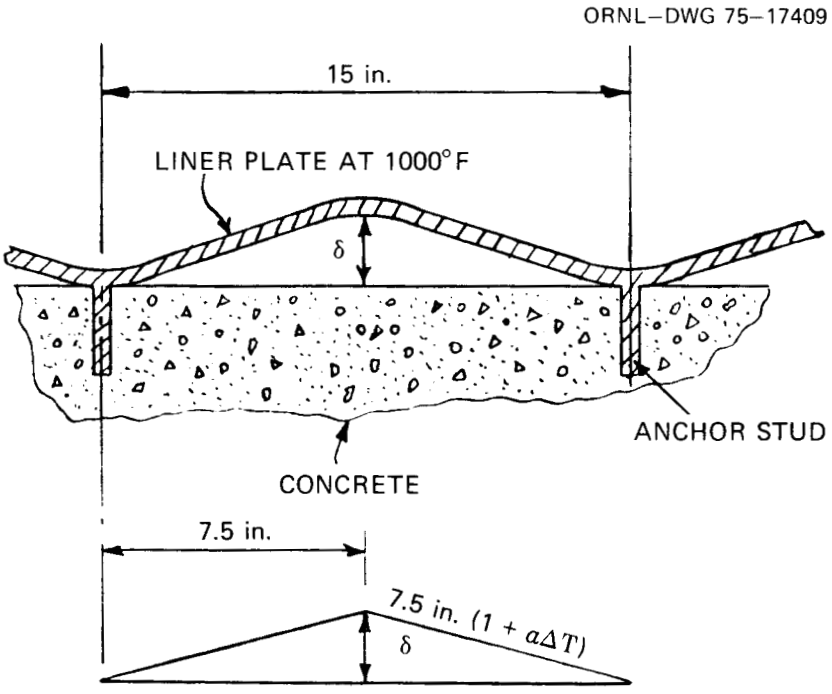


Assume plate temperature is 1000°F and concrete temperature is 150°F, then an approximate value for δ is given by

$$\delta^2 + (7.5)^2 \cong [(7.5)(1 + \alpha\Delta T)]^2$$

$$\Delta T = 1000 - 150 = 850°F$$

$$\alpha = 8.4 \times 10^{-6}\ °F^{-1}$$

Therefore,

$$\delta \cong 0.9 \text{ in.}$$

Fig. 4.2. Schematic of deformed cell liner plate assumed to roughly estimate the hot bulge dimension.

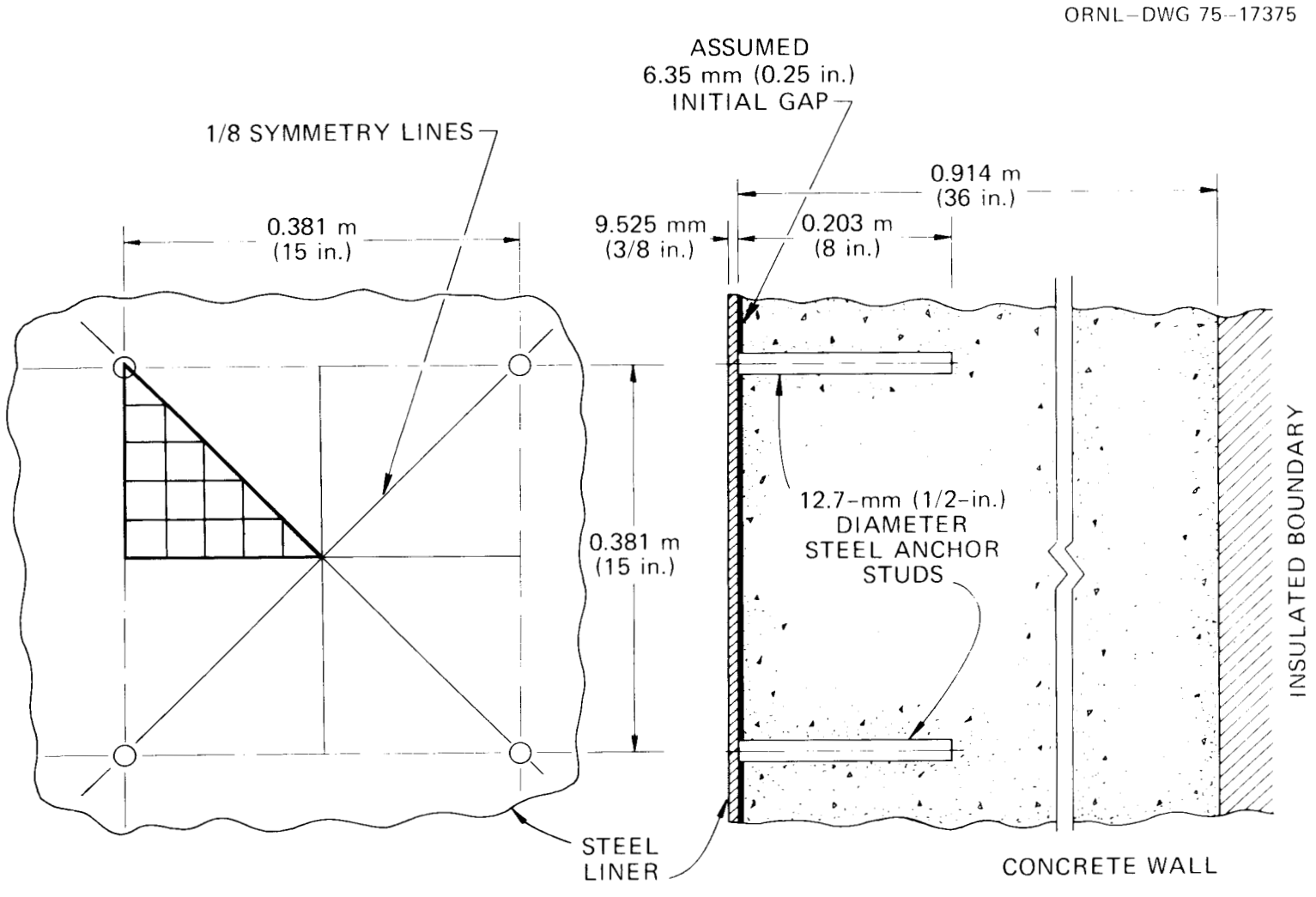


Fig. 4.3. Schematic of representative anchored LMFBR cell liner arrangement showing 1/8 symmetry lines and assumed 0.25-in. initial air gap.

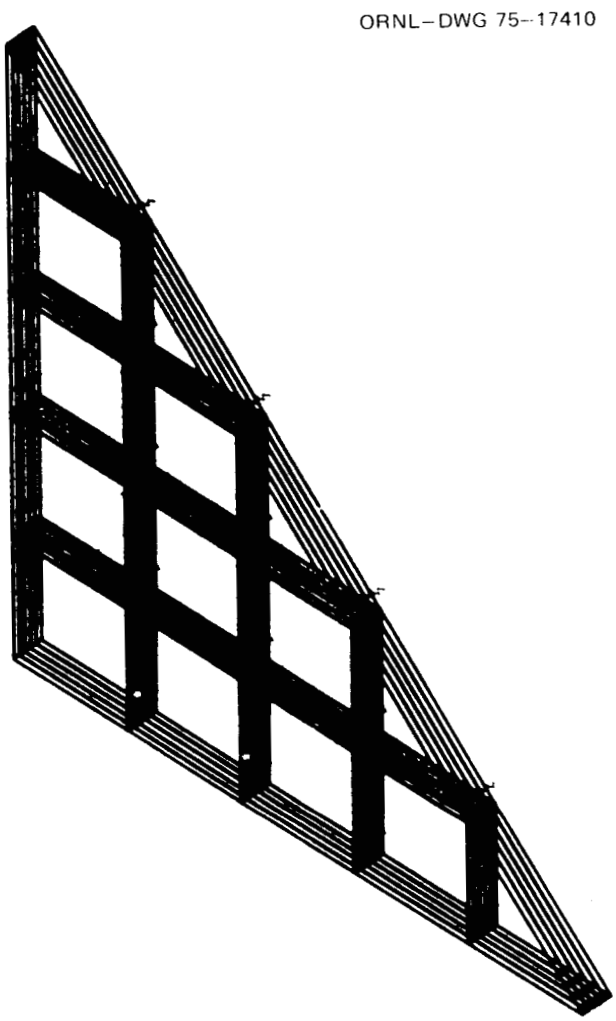


Fig. 4.4. Computer drawn geometry plot of the steel liner three-dimensional transient thermal analysis finite-element model.

ORNL-DWG 75-17411

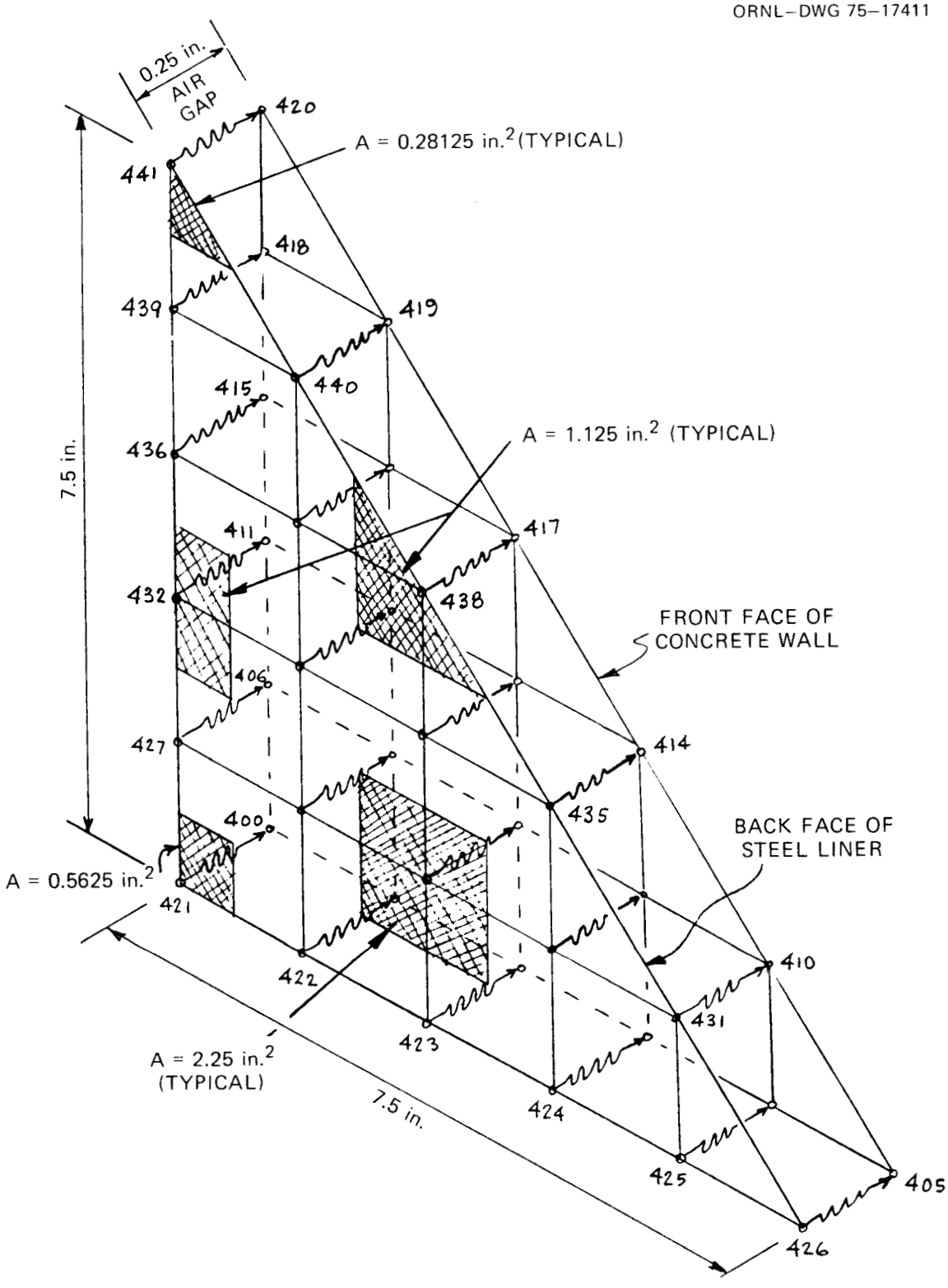


Fig. 4.5. Details of radiation links between back face of steel liner and front face of concrete used in three-dimensional thermal model.

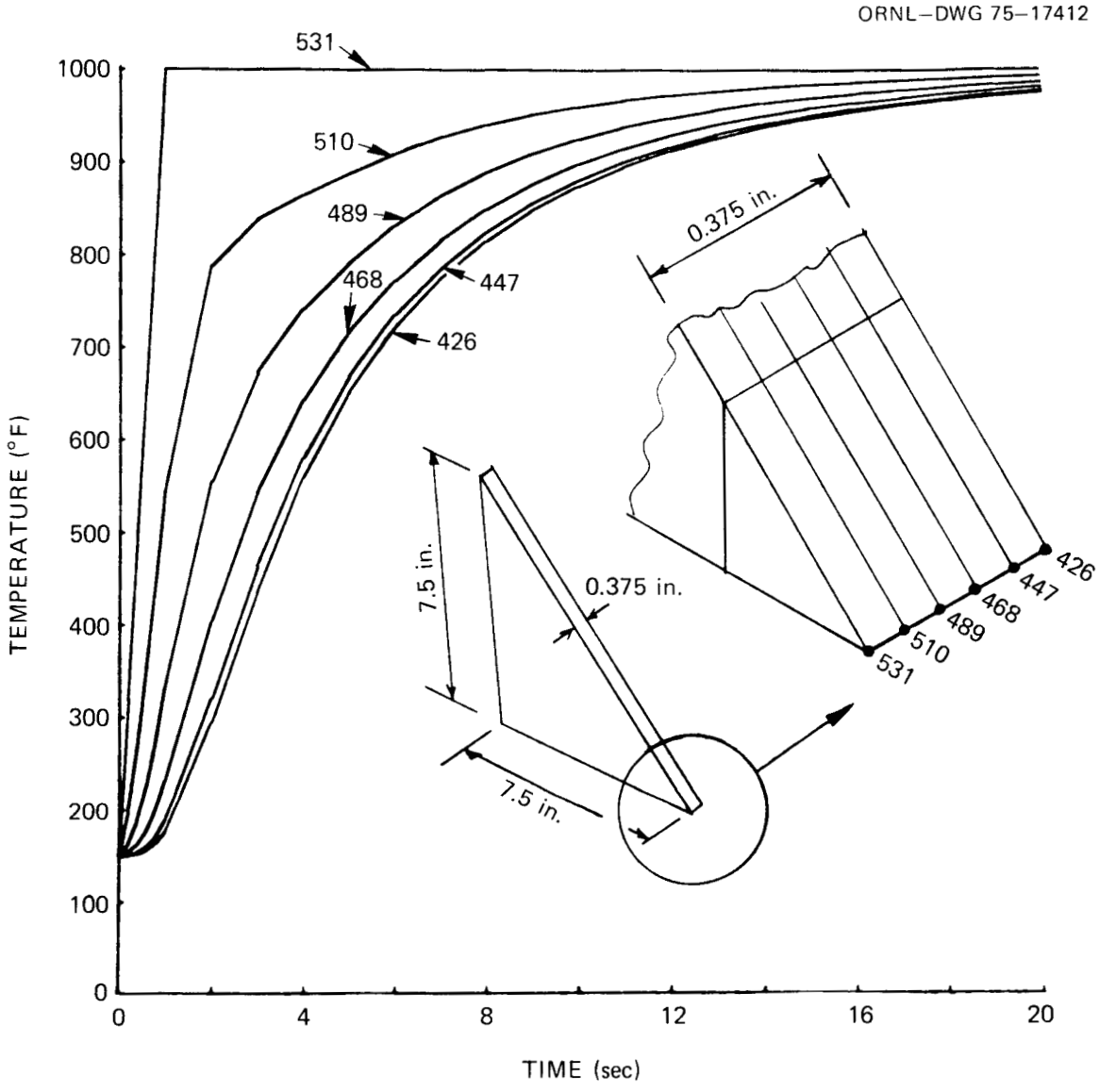


Fig. 4.6. Calculated liner plate transient temperatures at nodes through the thickness at center of model – 1000°F sodium spill accident.

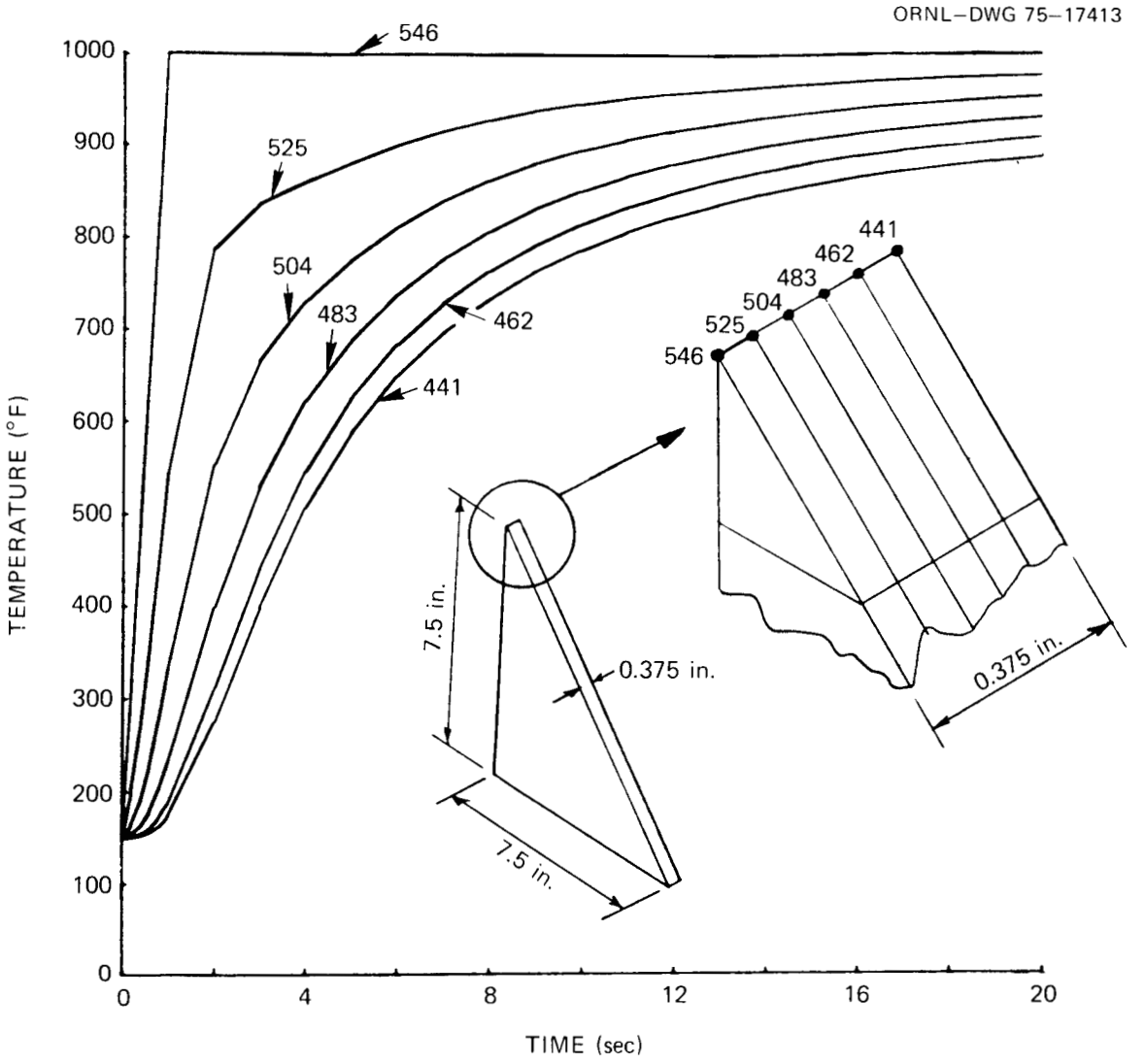


Fig. 4.7. Calculated liner plate transient temperatures at nodes through the thickness at the stud attachment – 1000°F sodium spill accident.

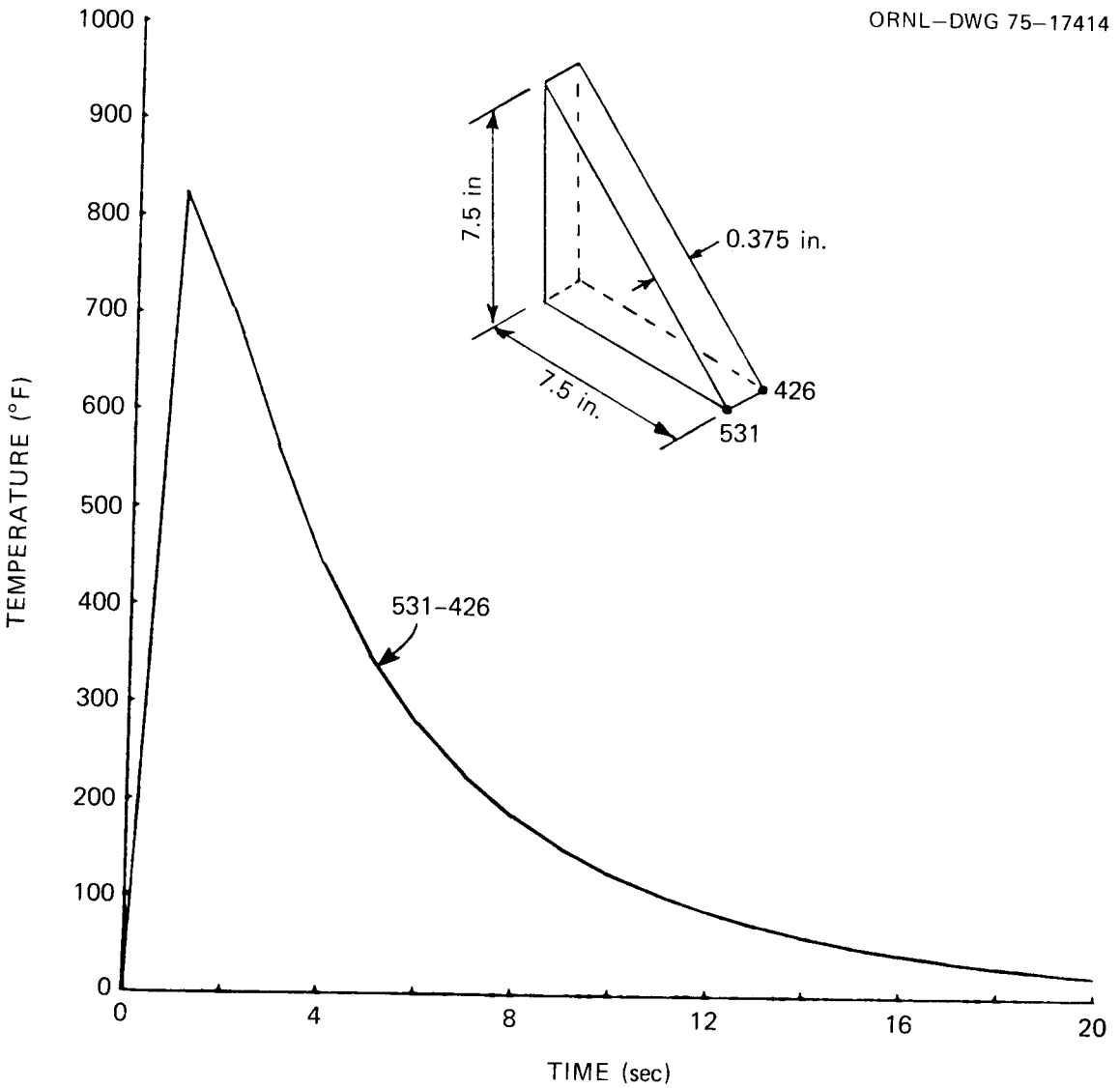


Fig. 4.8. Calculated transient through-thickness temperature difference of steel liner plate center – 1000°F sodium spill accident.

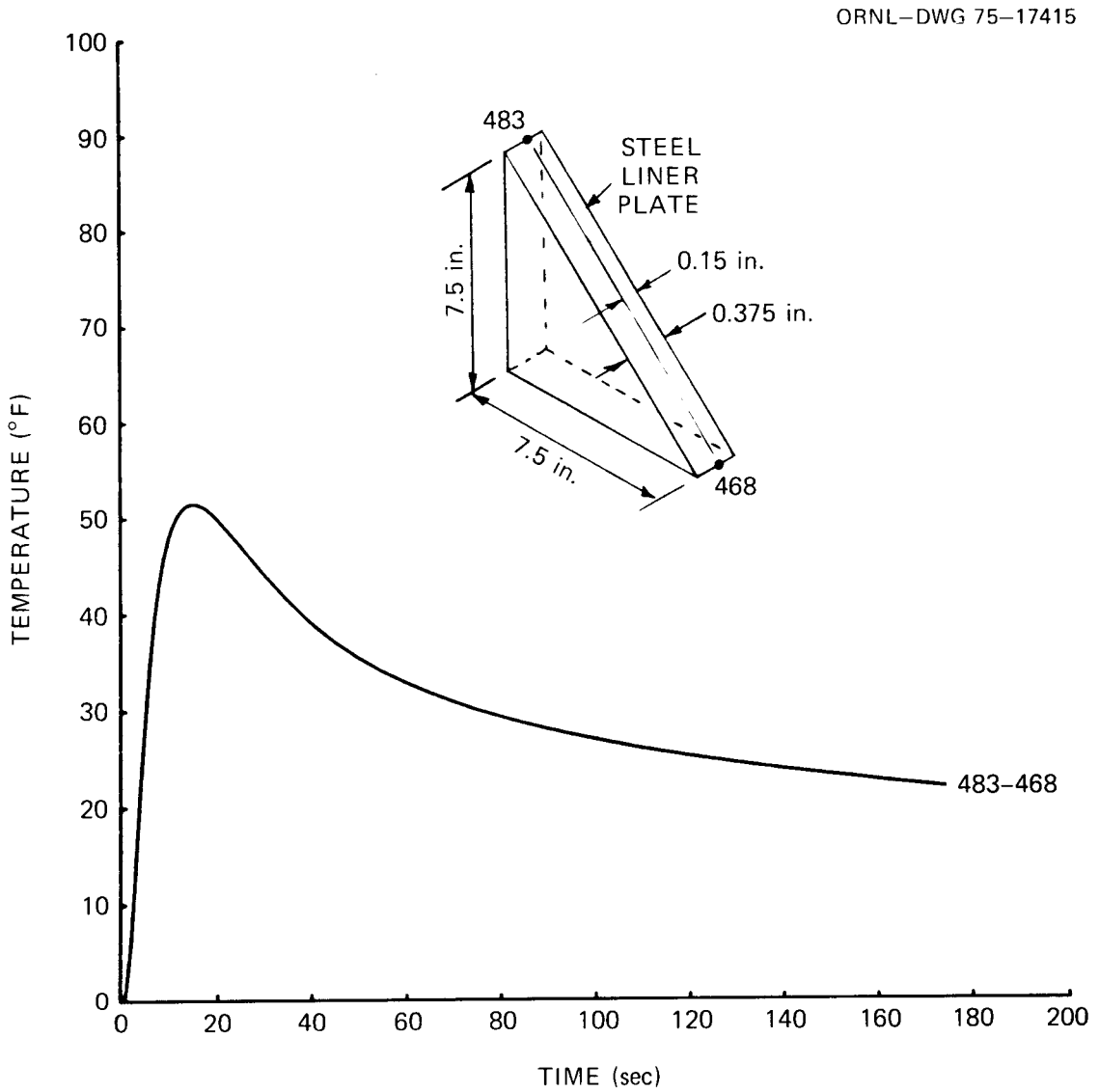


Fig. 4.9. Calculated transient in-plane temperature difference of steel cell liner plate – 1000°F sodium spill accident.

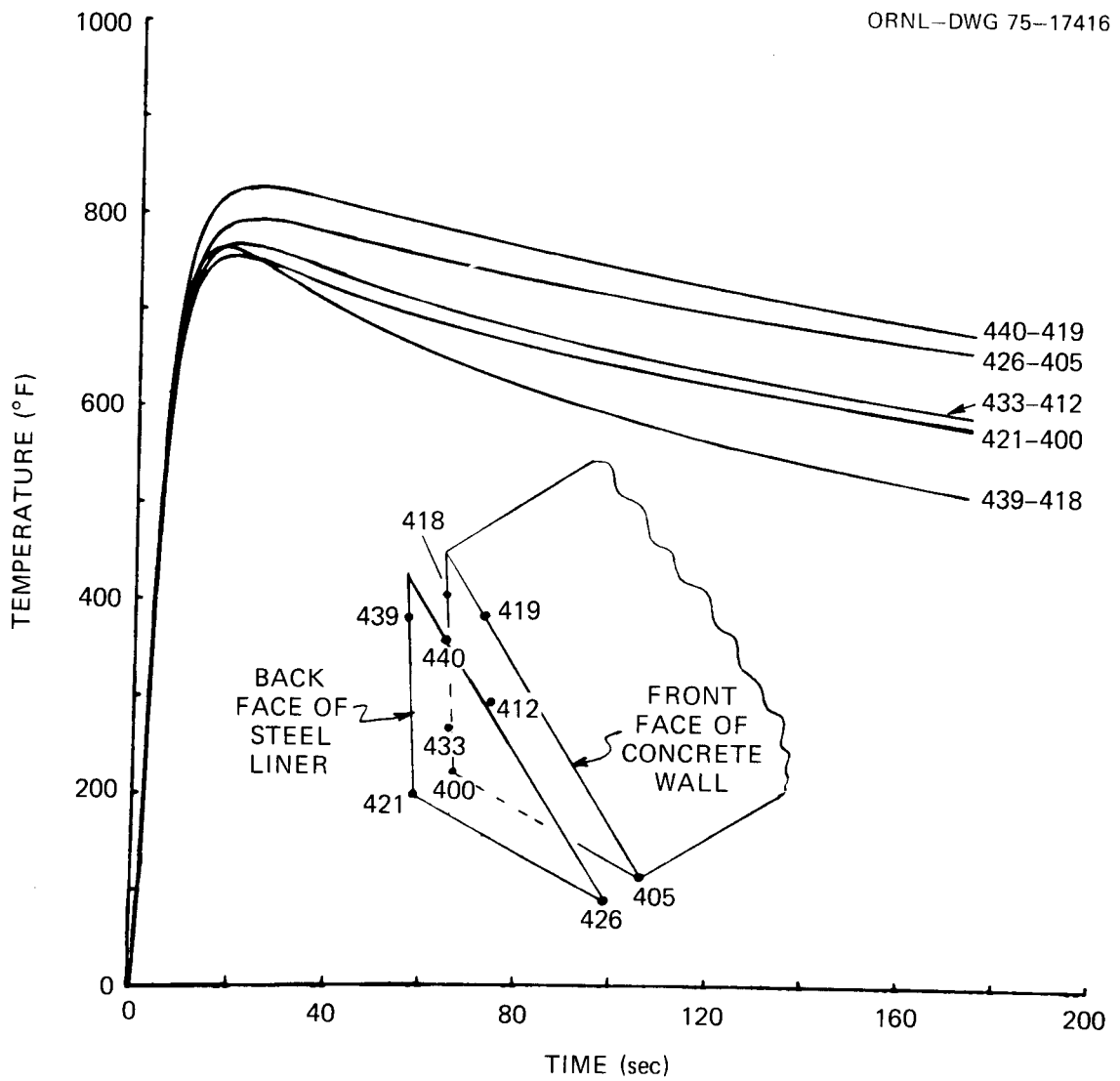


Fig. 4.10. Calculated transient temperature drops across the air gap between the steel liner and concrete wall – 1000°F sodium spill accident.

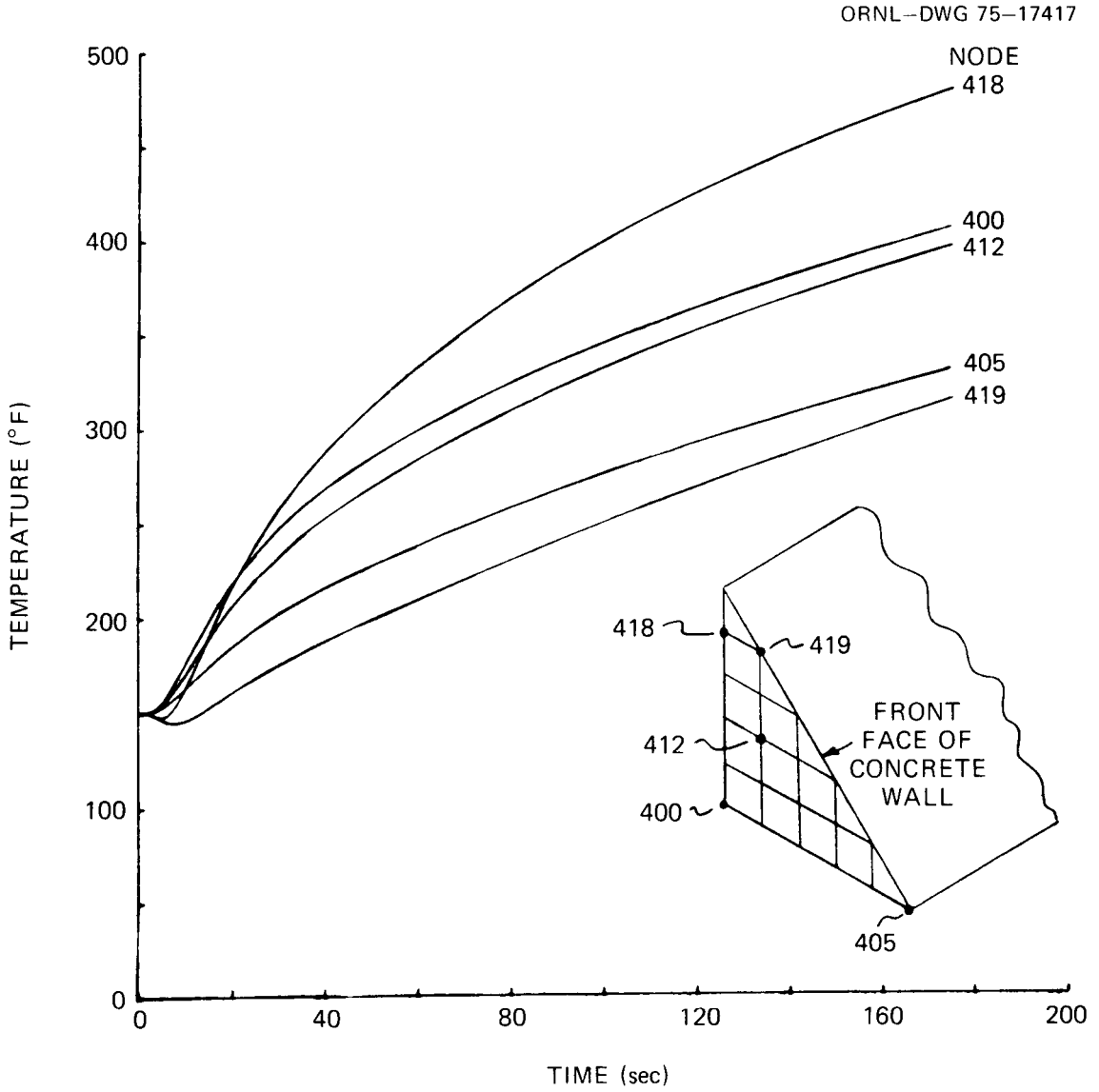


Fig. 4.11. Calculated transient temperatures of front face of concrete wall – 1000°F sodium spill accident.

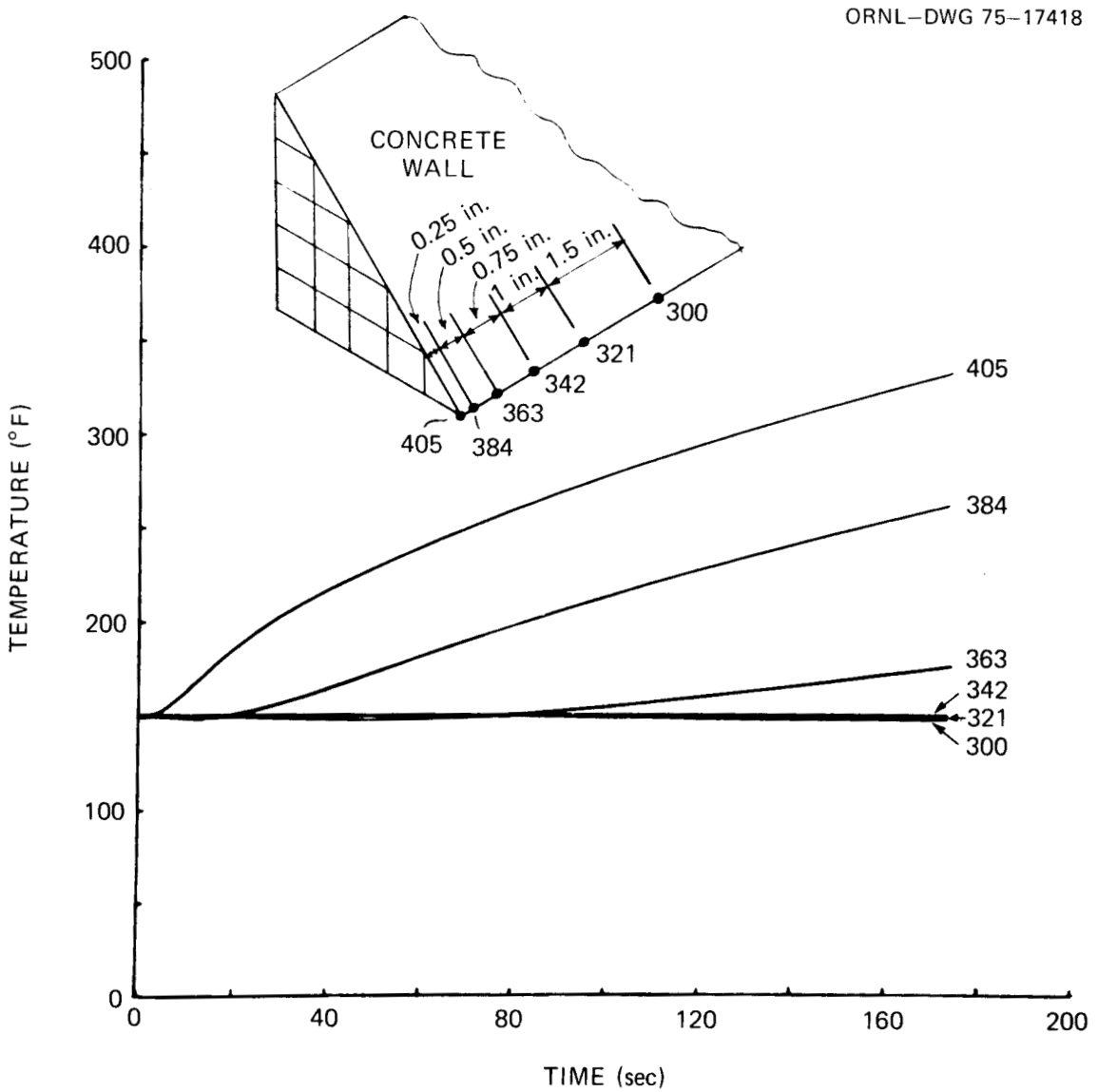


Fig. 4.12. Calculated transient temperatures in the concrete wall at model centerline – 1000°F sodium spill accident.

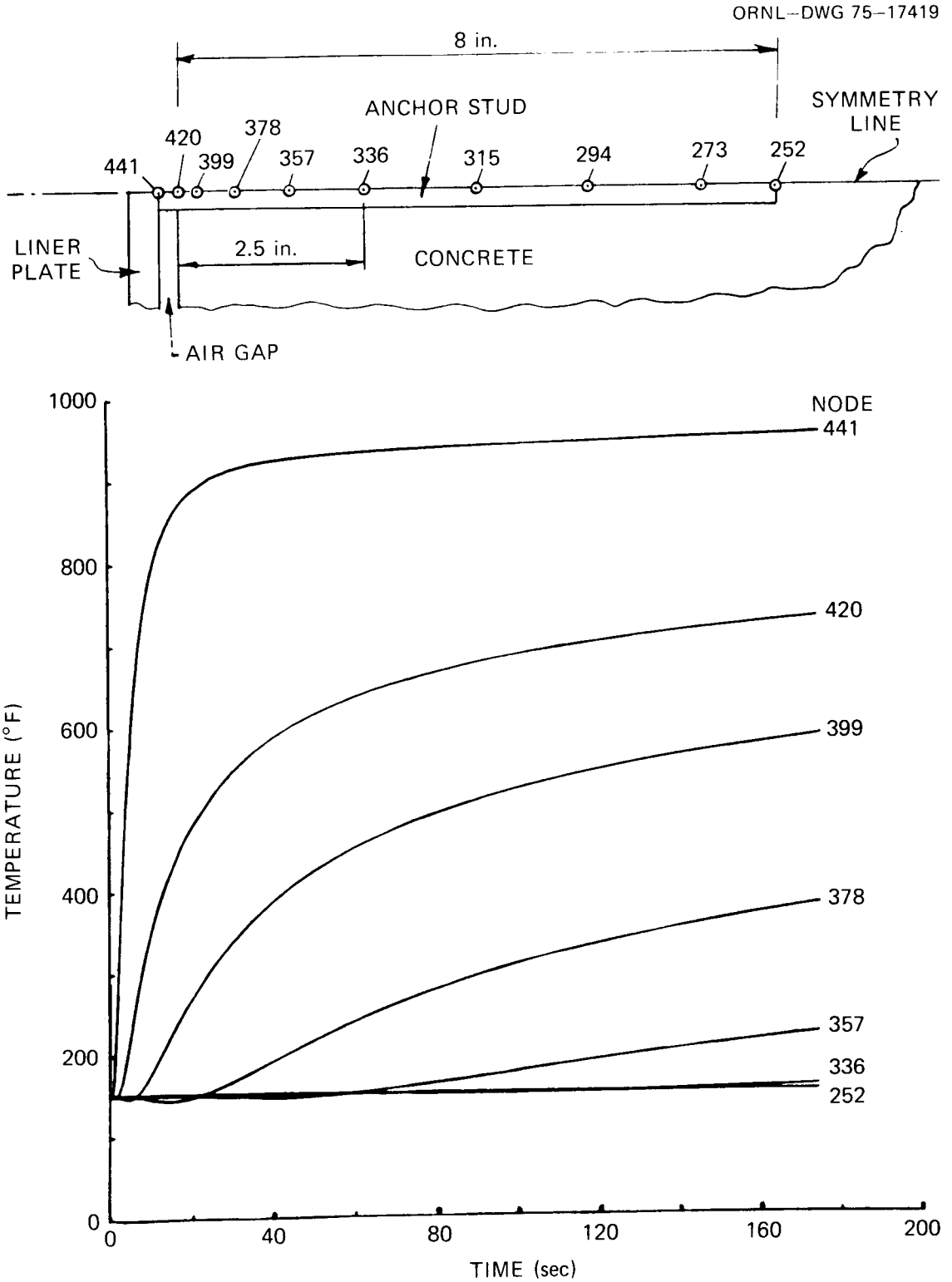


Fig. 4.13. Calculated transient temperature distribution along the length of the embedded steel anchor stud – 1000°F sodium spill accident.

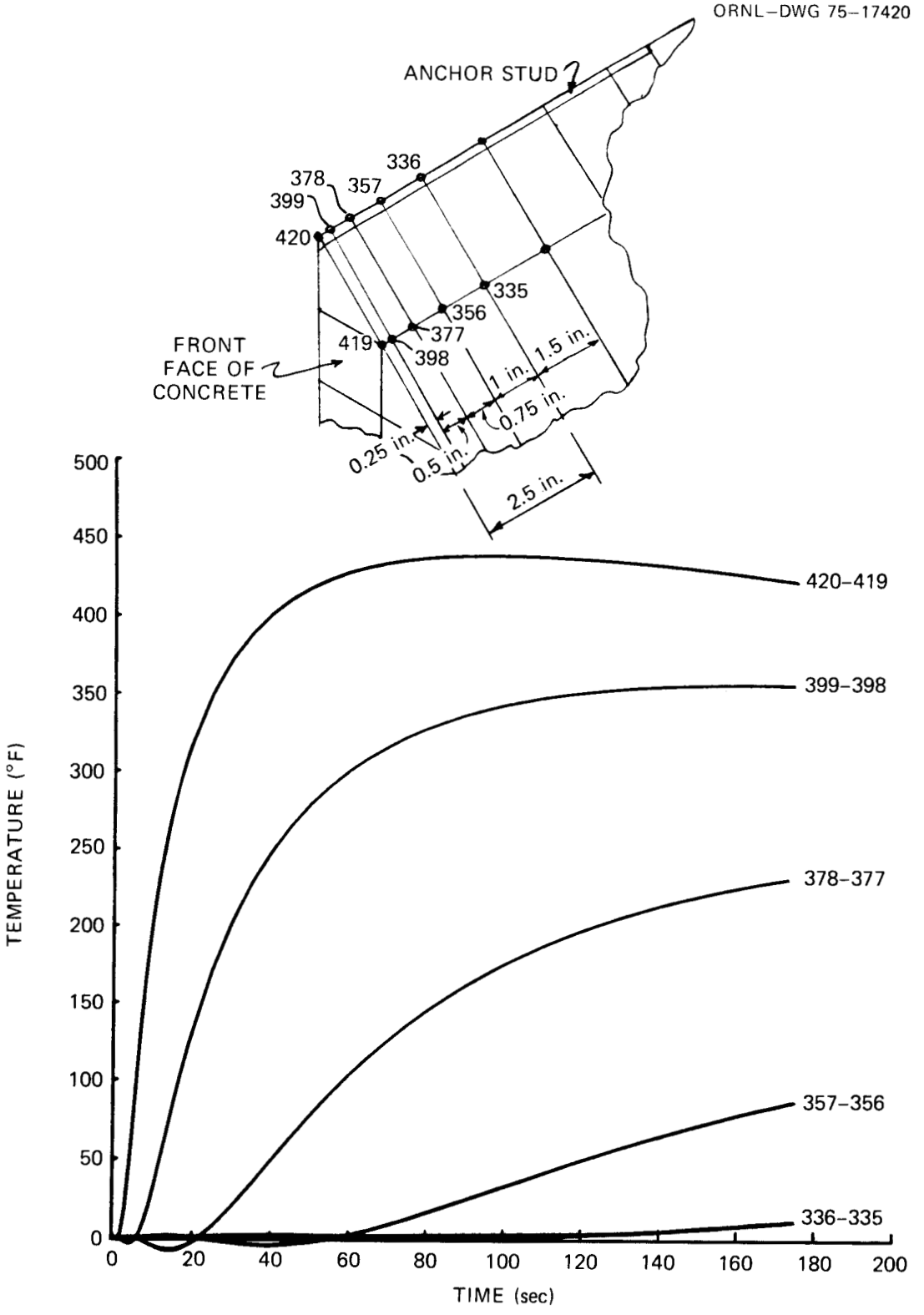


Fig. 4.14. Calculated temperature difference between steel anchor stud and adjacent concrete nodes – 1000°F sodium spill accident.

# 5. THREE-DIMENSIONAL PLASTIC STRUCTURAL ANALYSIS

A three-dimensional elastic-plastic finite-element structural analysis of the steel liner plate in the representative anchored LMFBR cell liner arrangement shown in Fig. 1.1 was performed using the transient material temperatures calculated for the postulated 1000°F sodium spill. The structural analysis also considered an isothermal cooldown back to 150°F, the initial temperature. This section discusses the three-dimensional structural analysis in detail.

## 5.1 Three-Dimensional Finite-Element Structural Model

The three-dimensional elastic-plastic structural analysis was also performed using the ANSYS general-purpose finite-element computer program.[4] The structural problem also exhibits the symmetry shown in Fig. 4.3; therefore, only one-eighth of the structure need be modeled. In addition, the three-dimensional thermal analysis results reported in Section 4 indicated that while the steel plate heats rapidly to a kind of quasi-steady-state, the concrete wall has hardly felt the transient. Therefore, it is reasonable to neglect the concrete wall by assuming it to remain rigidly at the initial 150°F temperature. The intent of this structural analysis is to estimate the plate performance; therefore, it is conservative and not too unrealistic to make this assumption.

The stud was not explicitly treated in the structural analysis for the following reasons. Due to the assumed symmetry, there is little or no structural interaction with the stud; i.e., the studs (ideally) are fixed in all six degrees of freedom at the plate attachment. Also the three-dimensional mesh (Fig. 4.1) was not fine enough to pick up the stud-concrete interaction in detail. The stud-concrete temperature difference plotted in Fig. 4.14 indicates that the interaction is greatest at the edges and moves into the wall (wavelike) very slowly with time. Such edge effects require an extremely fine mesh to pick up the abrupt shear gradient, and the long-term effects require consideration of creep strains (relaxation) in the steel stud. These considerations were beyond the scope of this study.

The steel liner plate was modeled with ANSYS STIF 48 plastic flat three-dimensional triangular shell elements as shown in Fig. 5.1. The structural model also utilized 21 in-plane nodes at the same x-y coordinates as the three-dimensional thermal model. The triangular pattern results in 25 shell elements in the structural model. The ANSYS STIF 48 plastic shell element requires specification of five temperatures through its thickness at the following surfaces: bottom; 1/4 thickness; 1/2 thickness, or middle surface; 3/4 thickness; and top surface. The top surface in this model is the exposed or heated outer surface of the steel liner.

Temperatures calculated from the three-dimensional thermal model were used in the structural plate model. The thermal model had six nodes through the plate thickness, as shown in Fig. 4.1, which were used to define the five temperatures through the thickness required at each node in the plate model. For example, the five temperatures required at node 6 of the structural plate model (Fig. 5.1) were defined using the six calculated temperatures at nodes 426, 447, 468, 489, 510, and 531 of Fig. 4.1. A fifth-degree general polynomial of the form

$$T = a_0 + a_1 z + a_2 z^2 + a_3 z^3 + a_4 z^4 + a_5 z^5 \qquad (3)$$

was fitted through the six temperatures, where z is the local through-the-thickness coordinate. The five required structural temperatures at each node were then evaluated directly using Eq. (3). The element temperature used was the average of the three nodes defining the shell element.

Figure 5.2 shows the displacement boundary conditions employed in the structural model. The steel liner plate was assumed to be fixed at the stud attachment (node 21) in all six degrees of freedom. The symmetry shown in Fig. 4.3 imposes normal displacement and rotation constraints along the model boundaries as shown in Fig. 5.2. Under these conditions the liner plate can essentially only move out of its plane.

Nonlinear effects such as large displacements and plasticity were included. The ANSYS program incremental plasticity option was employed. The large displacement effect was included by geometry modification after

each incremental solution. The plasticity solution in the ANSYS STIF 48 shell element makes use of nine integration points through the thickness. Reversed loading behavior was simulated using the ANSYS classical bilinear kinematic hardening option. The stress-strain curves for the steel liner material were measured by ORNL, since low-carbon-steel elevated-temperature stress-strain data were not readily available.[3] The material used in the measurements was ASTM A212B, which should be similar to the material proposed for use in LMFBR cell liners. These measured curves were simulated with bilinear fits out to approximately 1% strain. The work-hardening portion was fitted by least squares, and the elastic portion was assumed to follow the elastic slope (modulus) given in Ref. 3. The "yield" point in the bilinear model was assumed to be the intersection of the elastic and work-hardening lines. Table 5.1 lists the stress-strain parameters as a function of temperature assumed in the structural model.

## 5.2 Three-Dimensional Structural Model Results

The three-dimensional thermal analysis results reported in Section 4 indicated that the liner plate will experience large through-thickness thermal gradients (Fig. 4.8) and gross interactions due to the stud and symmetry constraints. The through-thickness gradients peak very early in the transient, and the gross interaction peaks a little later when the majority of the plate has heated up. Incremental elastic-plastic structural analyses were conducted for the same time span as the thermal analysis, approximately the first 3 min of the transient. In addition, an isothermal steady state at 1000°F followed by an isothermal cooldown to 150°F to unload the plate were considered.

Sixteen major load steps were used to define the temperature transient out to 175 sec. Each major load step consisted of three substeps, between which the material temperatures were linearly interpolated. The 1000°F steady state and cooldown to 150°F required 23 additional iterations. Therefore, a total of 71 incremental solutions or cumulative iterations were employed in the structural analysis. Table 5.2 lists the major load steps employed in the liner plate structural analysis.

Table 5.1. Stress-strain data vs temperature assumed in structural model of LMFBR steel cell liner[3]

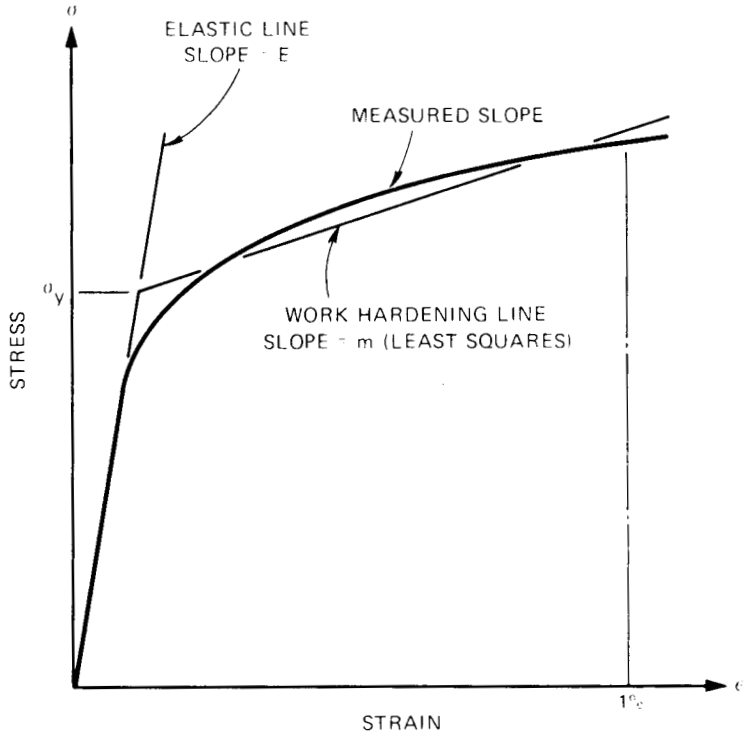


| Temperature (°F) | Elastic modulus E ($10^6$ psi) | Poisson's ratio $\nu$ | Coefficient of thermal expansion $\alpha$ ($10^{-6}$°$F^{-1}$) | Yield stress $\sigma_y$ (ksi) | Work hardening m/E |
|---|---|---|---|---|---|
| 150 | 27.8 | 0.3 | 8.4 | 39.0 | 0.004[a] |
| 500 | 26.4 | 0.3 | 8.4 | 28.3 | 0.0436 |
| 650 | 25.3 | 0.3 | 8.4 | 25.5 | 0.0613 |
| 800 | 23.4 | 0.3 | 8.4 | 25.3 | 0.0543 |
| 900 | 21.2 | 0.3 | 8.4 | 26.6 | 0.0467 |
| 1000 | 18.5 | 0.3 | 8.4 | 21.4 | 0.0503 |

[a]Measured curve at 150°F was flat to 1% strain; therefore, a value of 0.004 was assumed.

Table 5.2. Major load steps used in the incremental plasticity structural analysis of the LMFBR liner plate – 1000°F sodium spill accident

| Load step | Thermal transient time at end of step (sec) | Number of cumulative structural solutions at end of step |
|---|---|---|
| 1 | 0.2 | 3 |
| 2 | 0.4 | 6 |
| 3 | 0.6 | 9 |
| 4 | 0.8 | 12 |
| 5 | 1.0 | 15 |
| 6 | 2.0 | 18 |
| 7 | 4.0 | 21 |
| 8 | 6.0 | 24 |
| 9 | 8.0 | 27 |
| 10 | 10.0 | 30 |
| 11 | 15.0 | 33 |
| 12 | 25.0 | 36 |
| 13 | 40.0 | 39 |
| 14 | 60.0 | 42 |
| 15 | 80.0 | 45 |
| 16 | 175.0 | 48 |
| 17[a] | 1000°F | 61 |
| 18[a] | 575°F | 66 |
| 19[a] | 150°F | 71 |

[a]Isothermal solutions at the temperature indicated.

The calculated transient out-of-plane displacements of node 1 (midway between adjacent anchor studs) and node 6 (center of the square anchor pattern) are plotted in Fig. 5.3. It can be seen that the plate bulged out very rapidly as it heated, reaching maximum displacements in about 30 sec. Figure 5.4 shows the maximum possible calculated out-of-plane deformation of the steel liner plate at the 1000°F steady state following the spill. The maximum bulge was approximately 3/8 in., and the plate deformations were as expected for the imposed boundary and symmetry conditions assumed in this analysis. Figure 5.5 shows the calculated residual out-of-plane liner deformations at 150°F after the assumed

isothermal cooldown. Note that the deformation scales used to plot Figs. 5.4 and 5.5 are different. The liner is essentially straight again at 150°F.

Figures 5.6 through 5.9 contain transient plots of the calculated generalized plastic strains of shell elements 1, 9, 12, and 25 respectively. The generalized plastic strain is given by

$$\bar{\epsilon}_p = \frac{\sqrt{2}}{3} \left[(\epsilon_x - \epsilon_y)^2 + (\epsilon_y - \epsilon_z)^2 + (\epsilon_z - \epsilon_x)^2 + 6\epsilon_{xy}^2 + 6\epsilon_{yz}^2 + 6\epsilon_{zx}^2\right]_p , \qquad (4)$$

where the subscript p denotes that the plastic strain component is used. Generalized plastic strains are plotted for the front (top) face exposed to sodium, the middle surface, and back face for each element. These plots indicate that elements 1 and 12 were subjected to mostly membrane or direct straining. Element 9 (at the center) and element 25 (at the stud) appear to experience bending strains of opposite curvature. This behavior would be expected for the boundary conditions imposed and is consistent with the deformed shape shown in Fig. 5.4. The maximum generalized membrane plus bending plastic strain of 1.7% occurred at the back face of element 25 (stud attachment). The maximum local generalized membrane strain of 1.35% occurred at element 1, Fig. 5.6.

Typical calculated loading-unloading responses are shown in Figs. 5.10 and 5.11. These curves are plots of the local x stress component vs the local x total (elastic plus plastic) strain component from the start of the sodium spill accident through steady state and back to the initial temperature. The x and y components are nearly equal (the plate is essentially uniformly loaded biaxially). The small fluctuations in the curves are due primarily to the thermal stress-strain softening effects and plastic load redistributions. The residual biaxial membrane tension in the plate is about 42,500 psi at 150°F after the assumed isothermal cooldown. The plate yielded in tension due to the reversed loading as the cooldown continued to 150°F.

ORNL-DWG 75-15296

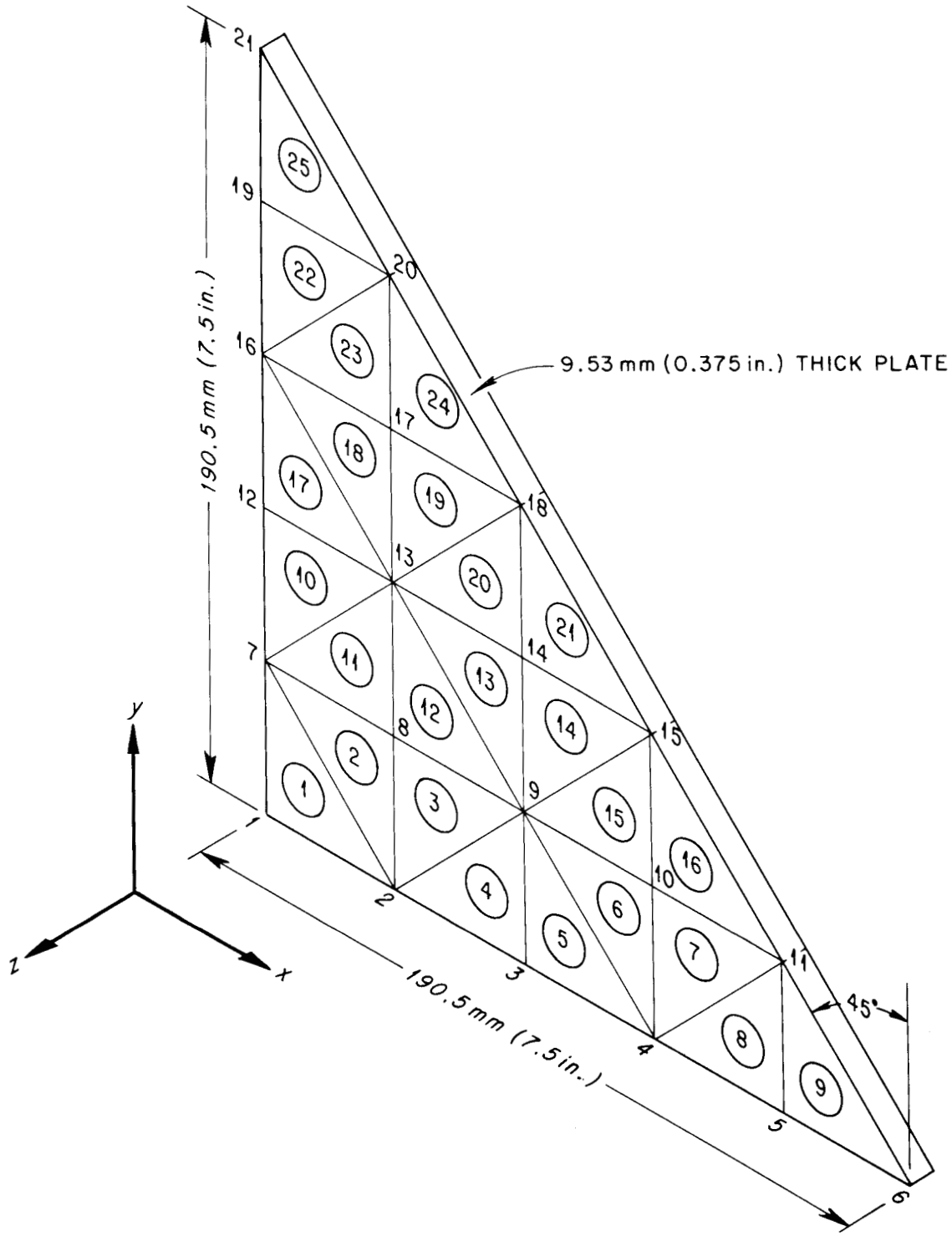


Fig. 5.1. Schematic of the 1/8 symmetry three-dimensional elastic-plastic finite-element shell model of the LMFBR cell liner plate.

ORNL–DWG 75–17421

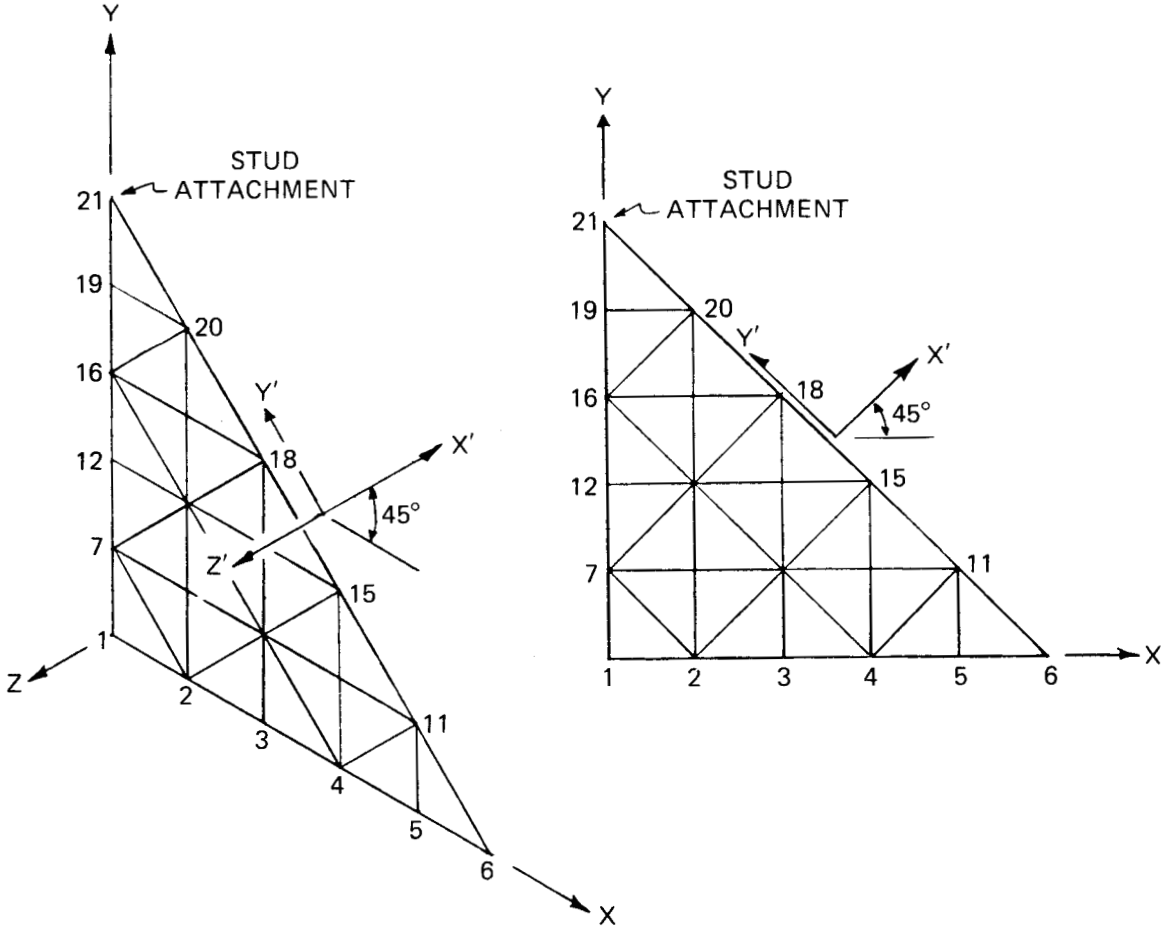


Node 21:

$$U_x = U_y = U_z = \theta_x = \theta_y = \theta_z = 0 \text{ (fixed)}$$

Nodes 1, 2, 3, 4, 5, 6:

$$U_y = \theta_x = \theta_z = 0$$

Nodes 1, 7, 12, 16, 19:

$$U_x = \theta_y = \theta_z = 0$$

Nodes 11, 15, 18, 20:

$$U_{x'} = \theta_{y'} = \theta_{z'} = 0$$

Fig. 5.2. Displacement boundary conditions assumed in the 1/8 symmetry three-dimensional shell model of the liner plate.

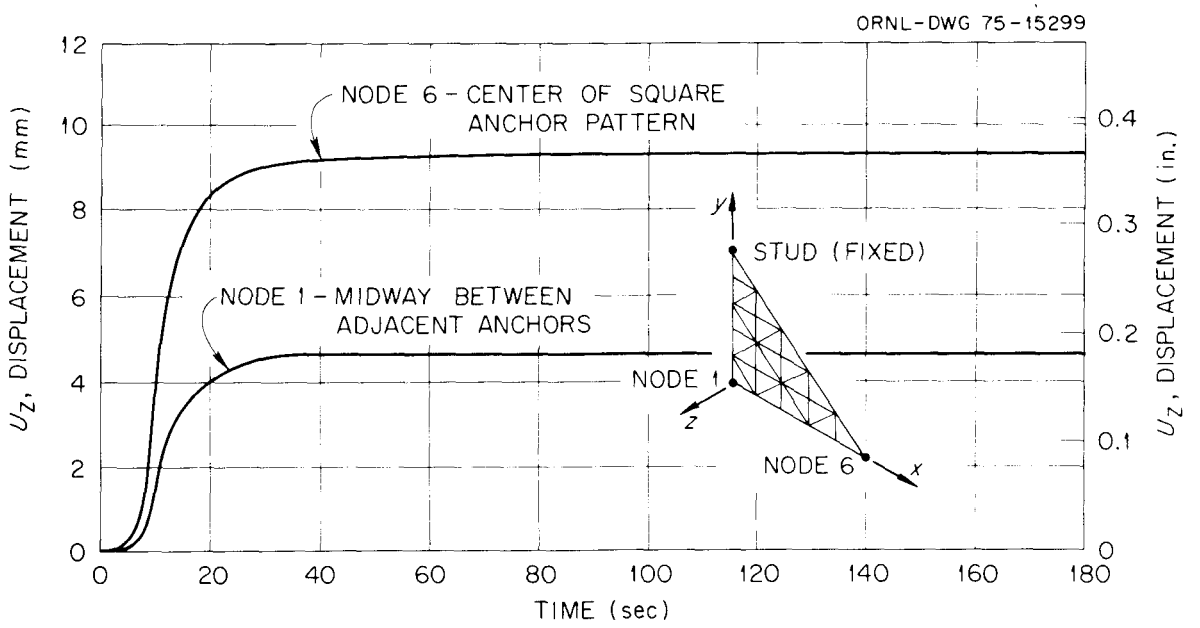


Fig. 5.3. Calculated transient out-of-plane displacements ($U_z$) of nodes 1 and 6 – 1000°F sodium spill accident.

ORNL-DWG 75-15297

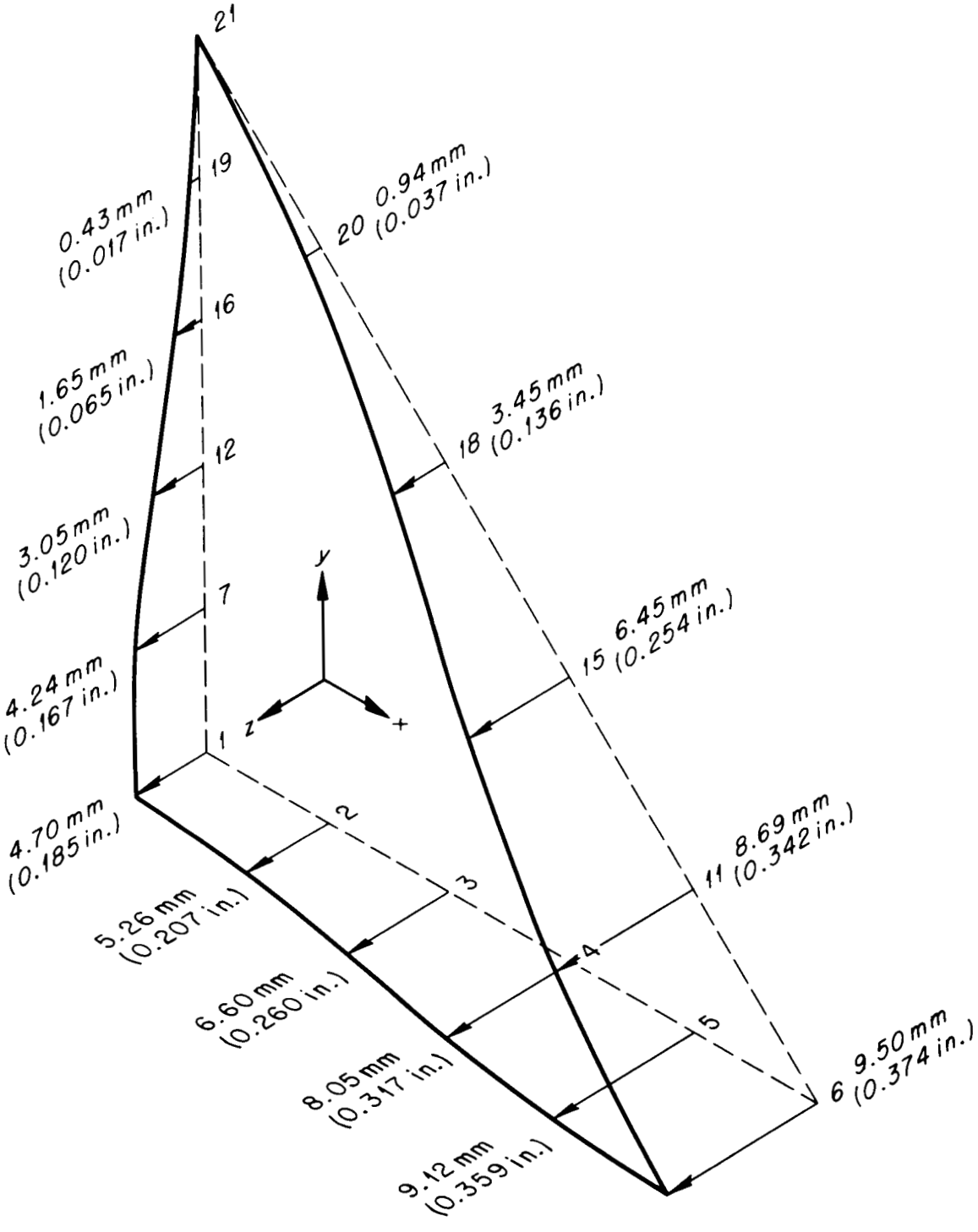


Fig. 5.4. Maximum calculated out-of-plane deformation of the steel liner plate at 1000°F steady state following 1000°F sodium spill.

ORNL–DWG 75–17422

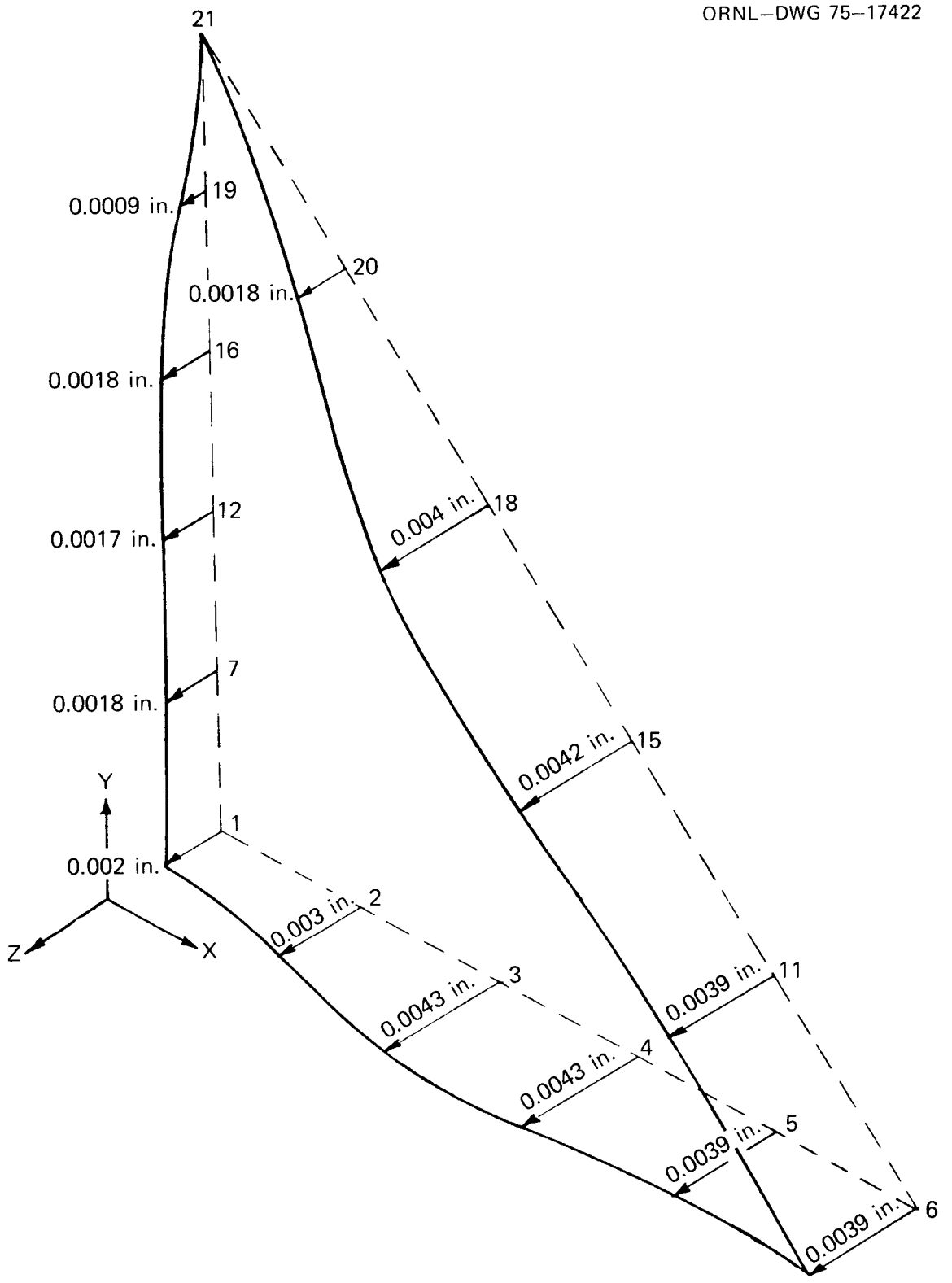


Fig. 5.5. Calculated residual out-of-plane deformation of the steel liner plate at 150°F following 1000°F sodium spill.

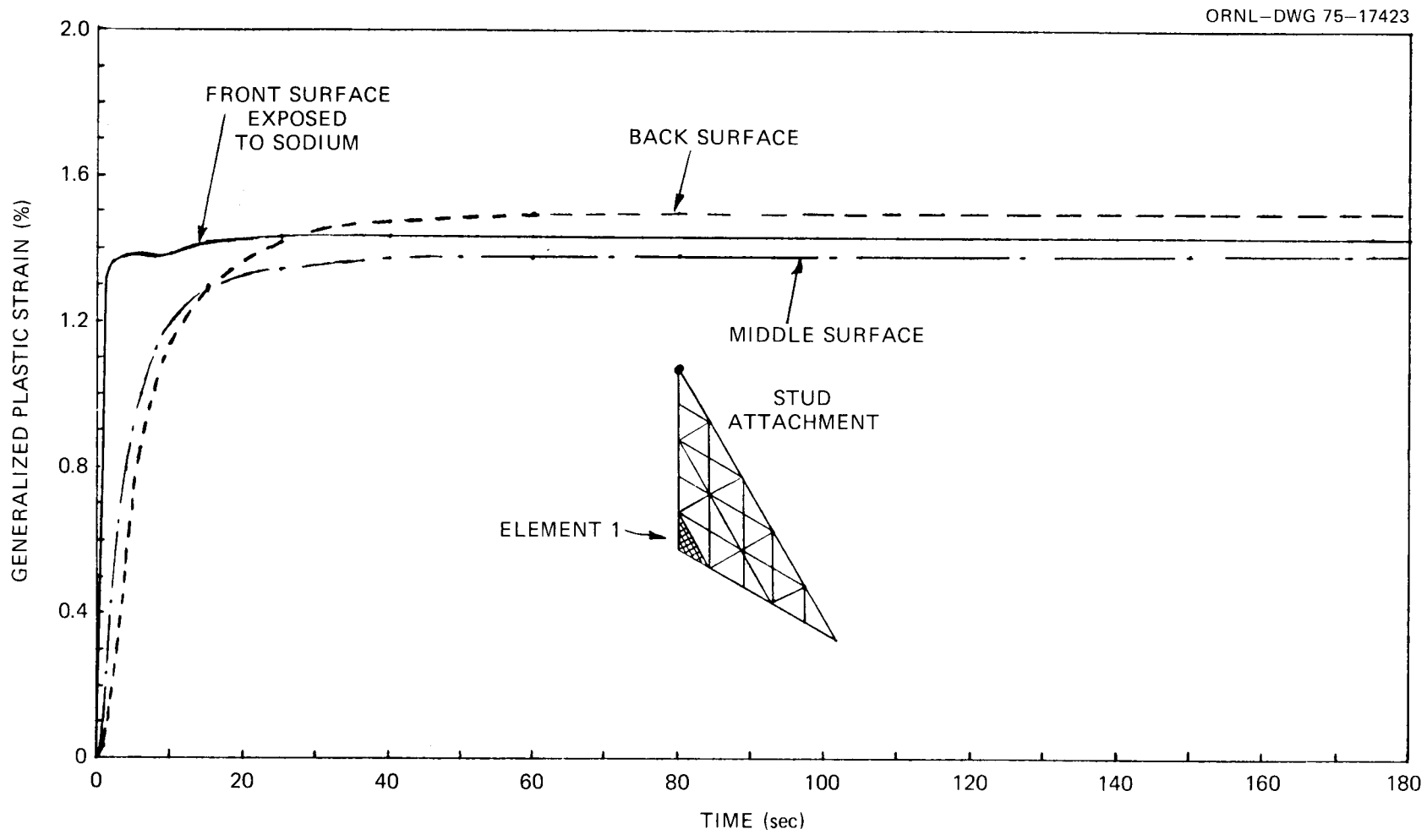


Fig. 5.6. Calculated transient generalized plastic strains of 3-D shell element 1 – 1000°F sodium spill accident.

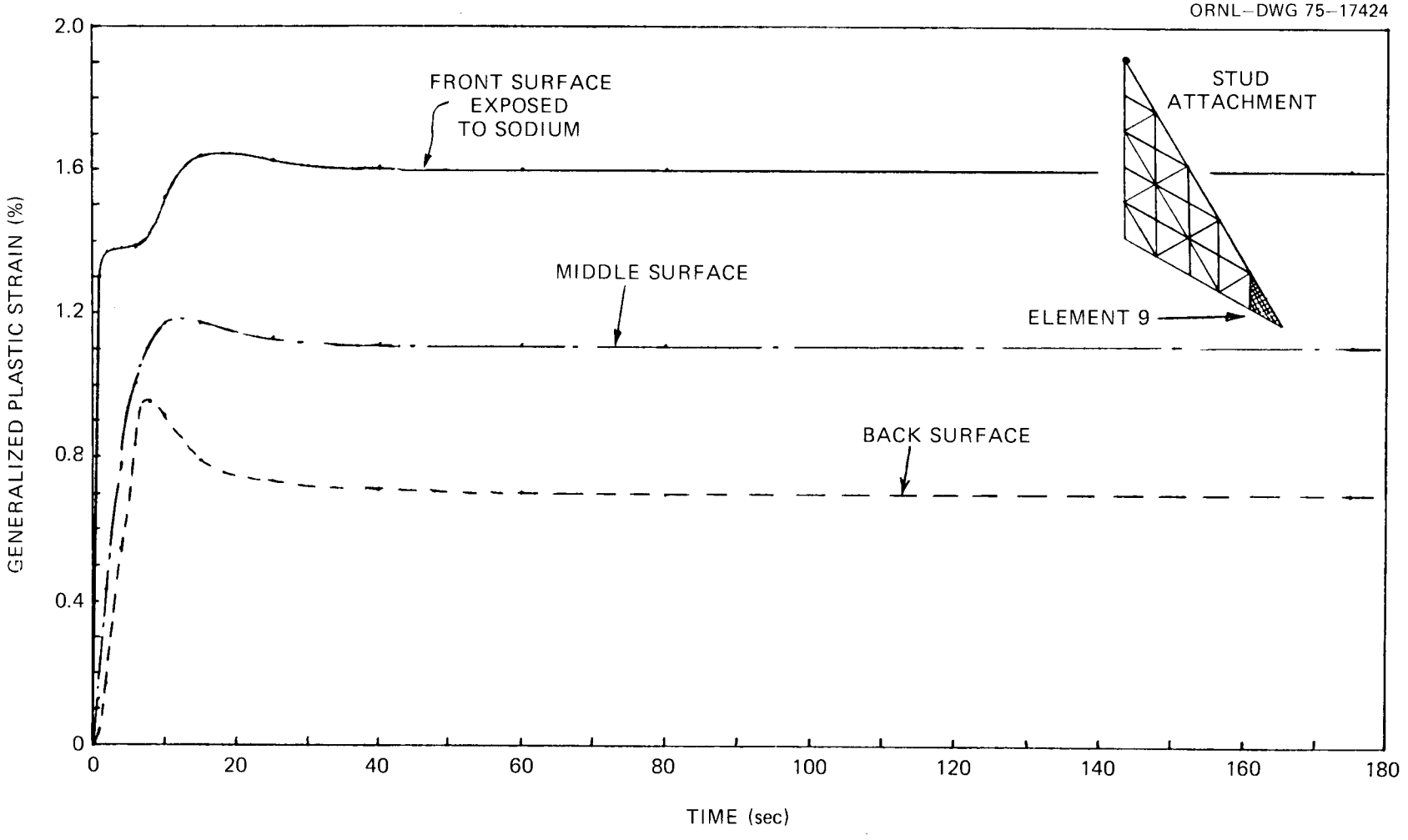


Fig. 5.7. Calculated transient generalized plastic strains of 3-D shell element 9 – 1000°F sodium spill accident.

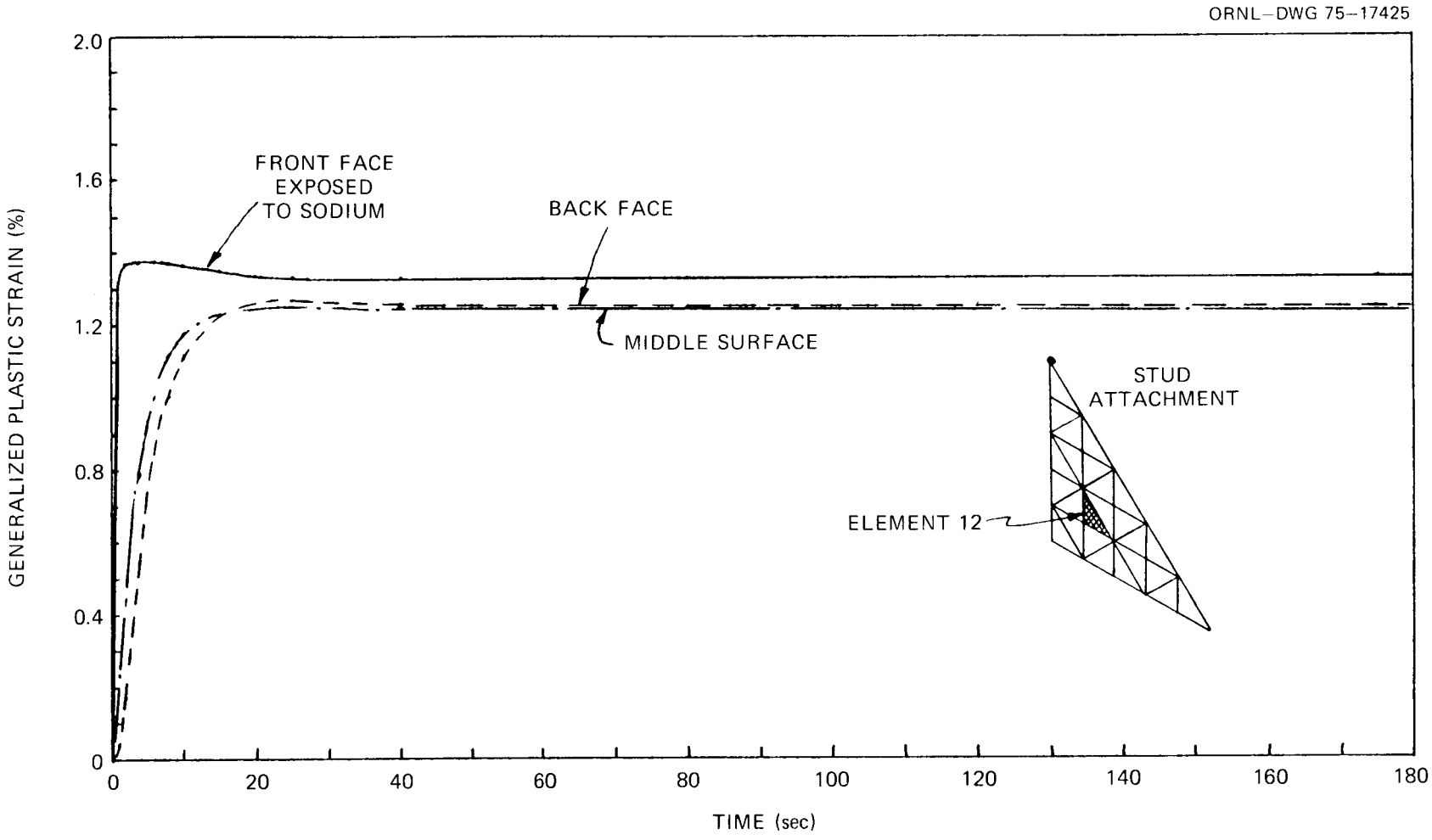


Fig. 5.8. Calculated transient generalized plastic strains of 3-D shell element 12 – 1000°F sodium spill accident.

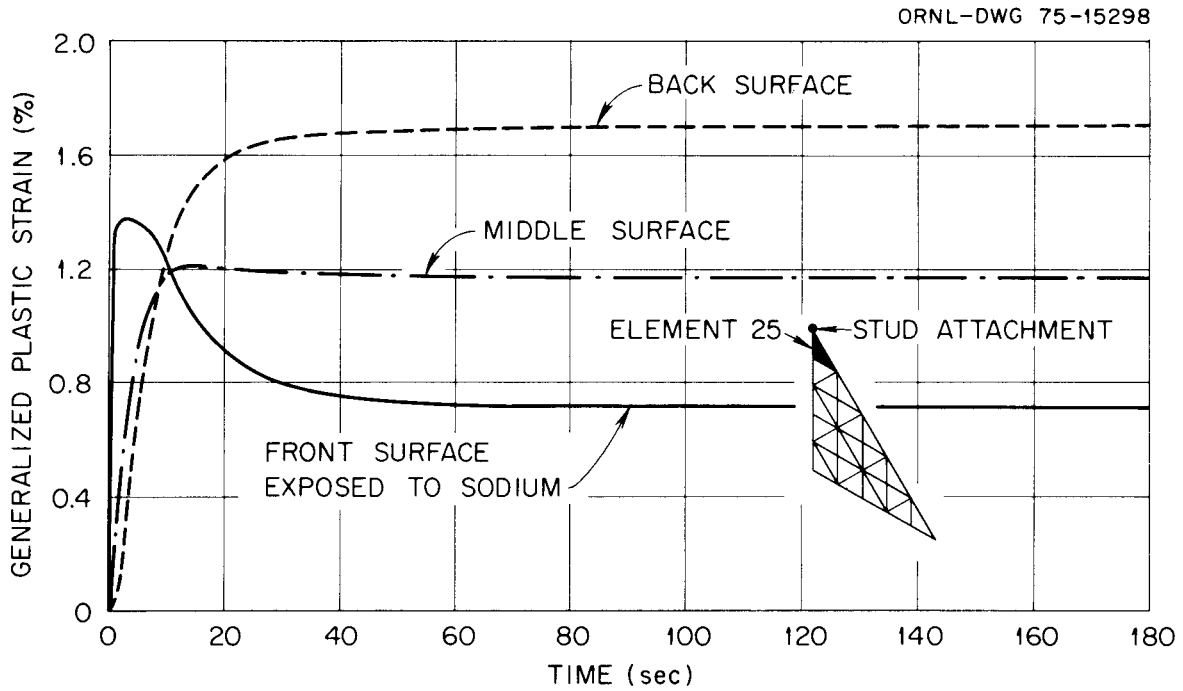


Fig. 5.9. Calculated transient generalized plastic strains of 3-D shell element 25 – 1000°F sodium spill accident.

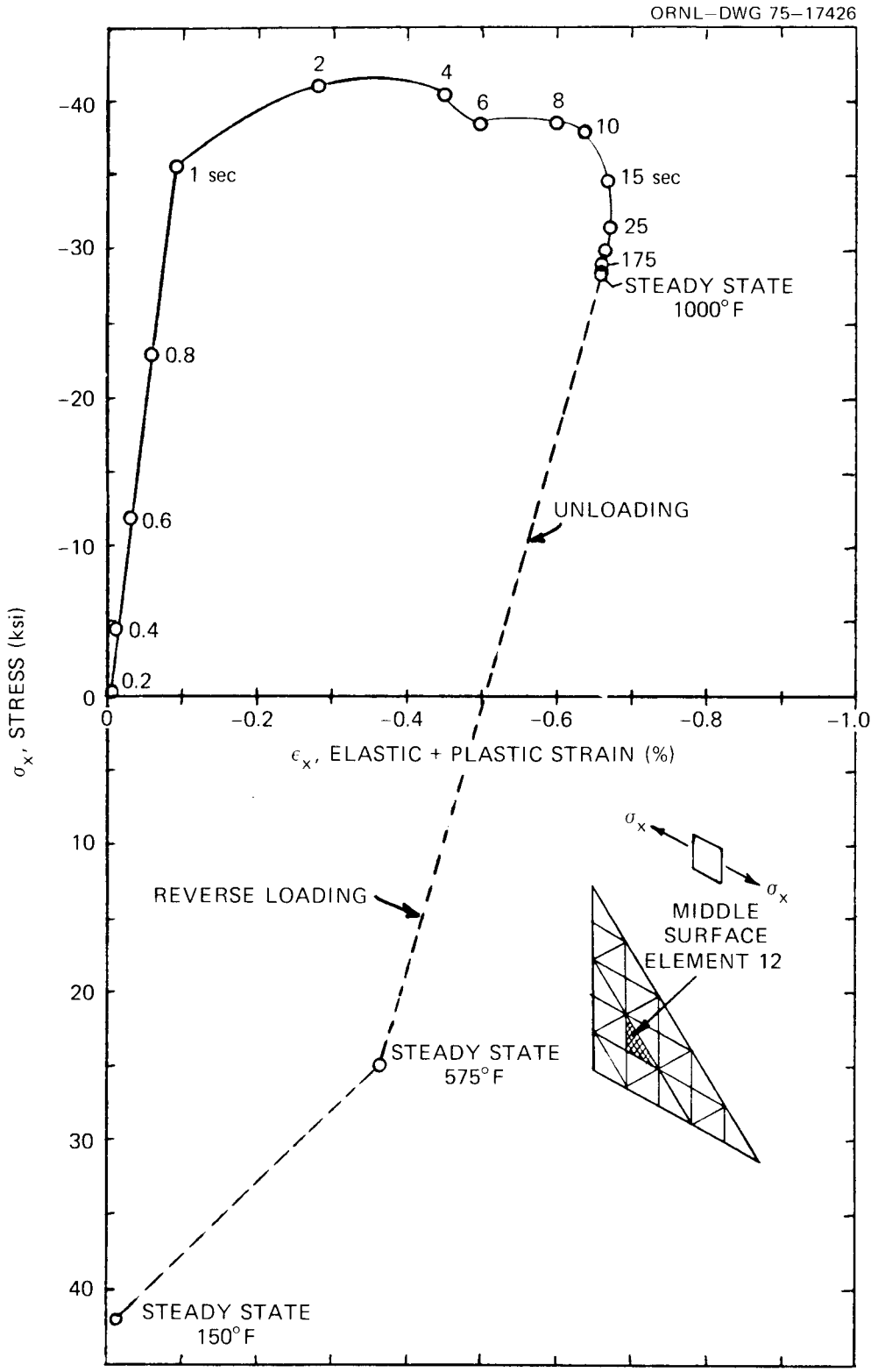


Fig. 5.10. Calculated stress vs elastic-plus-plastic strain in middle surface of element 12 – 1000°F sodium transient and cooldown.

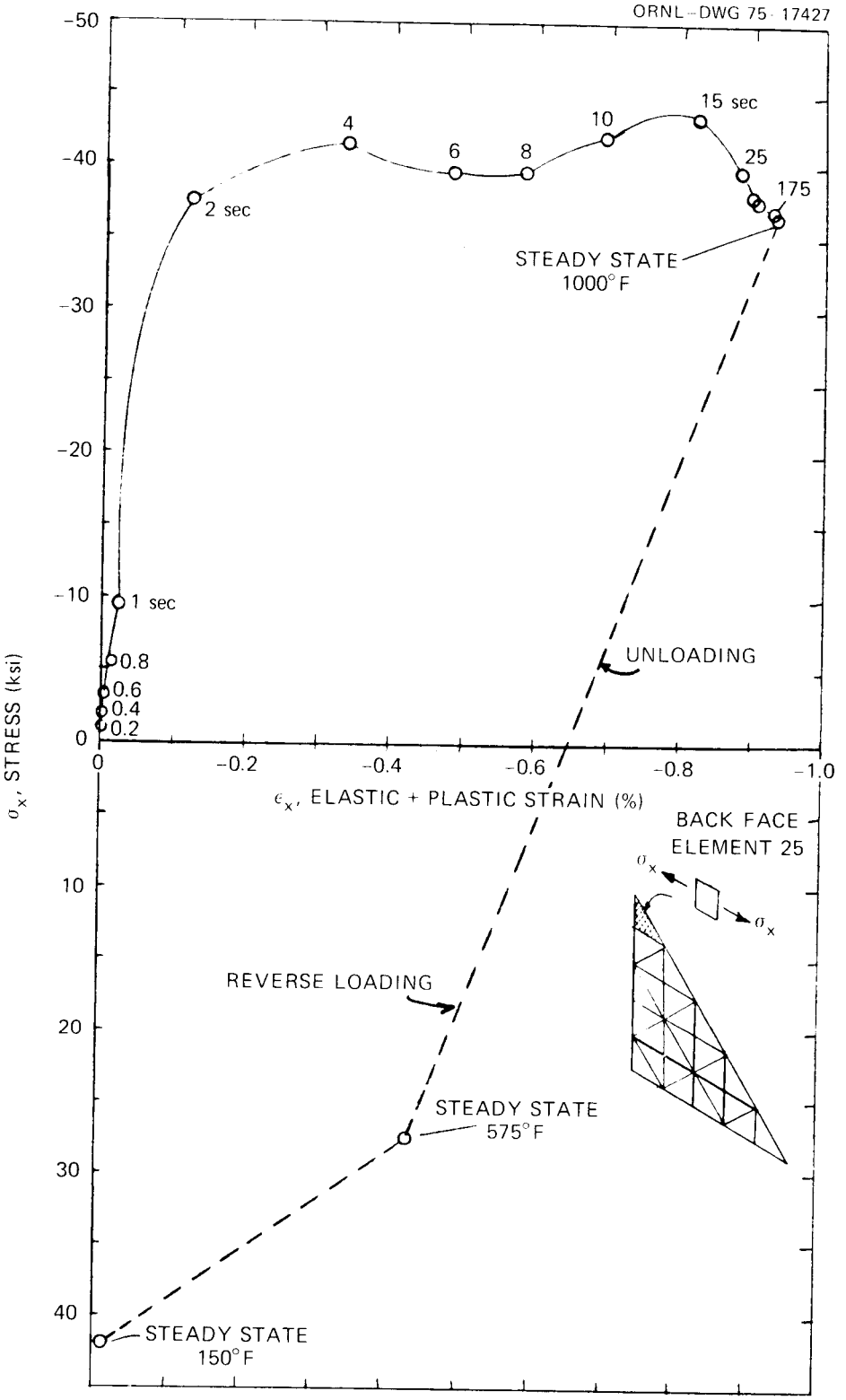


Fig. 5.11. Calculated stress vs elastic-plus-plastic strain at back face of element 25 – 1000°F sodium transient and cooldown.

# 6. REFERENCES


1. R. H. Chapman, A State-of-the-Art Review of Equipment Cell Liners for LMFBRs, ORNL-TM-4714 (February 1975).

2. Letter, W. J. McAfee (ORNL Reactor Division) to P. A. Stancampiano (SEAC), Apr. 29, 1975.

3. Letter, W. J. McAfee (ORNL Reactor Division) to P. A. Stancampiano (SEAC), May 16, 1975.

4. G. J. DeSalvo and J. A. Swanson, "ANSYS Engineering Analysis System User's Manual," Swanson Analysis Systems, Inc., Elizabeth, Pa., Mar. 1, 1975.

5. R. M. Drake, Jr., Heat and Mass Transfer, McGraw-Hill, New York, 1959.

6. W. H. Giedt, Principles of Engineering Heat Transfer, p. 249, D. Van Nostrand, New York, 1957.


## 6.1 Computer References

All the finite-element analyses discussed in this report were performed on the Westinghouse CDC 7600 high-speed digital computer using the ANSYS program.[4] The following runs were used as indicated. The alphanumeric and graphic output are stored on 105-mm Microfiche at 48 to 1 reduction. Copies of these Microfiche output have been transmitted to ORNL under separate cover.

| Date | Sequence No. | |
|---|---|---|
| 6/13/75 | YN62242 | 1-D model, air gap = 0.26 in. |
| 6/16/75 | YN622VT | 1-D model, air gap = 0.51 in. |
| 6/17/75 | YN62264 | 1-D model, air gap = 0.01 in. |
| 6/20/75 | YN622AT | 1-D model, air gap = 0.26 in. $2 \times \Delta T$ between integration points |
| 6/25/75 | YN622CQ | 3-D thermal model, 0–175 sec |
| 7/8/75 | YN6221S | 3-D thermal model plots, 0–20 sec, 0–50 sec |
| 7/10/75 | YN622AC | 3-D thermal model plots, 0–175 sec |
| 8/12/75 | YN622X3 | Structural model, 0–175 sec + 1000°F stainless steel |
| 8/14/75 | YN62225 | Structural model, cooldown 1000°F to 150°F |

ORNL-TM-5145
NRC-7

INTERNAL DISTRIBUTION

1. R. G. Alsmiller, Jr.
2. R. L. Battiste
3. M. Bender
4. H. W. Bertini
5. J. J. Blass
6. S. E. Bolt
7. C. R. Brinkman
8. J. W. Bryson
9. J. R. Buchanan
10. J. H. Butler
11. J. P. Callahan
12. D. A. Canonico
13. R. H. Chapman
14. J. A. Clinard
15-17. J. M. Corum
18. W. B. Cottrell
19. G. E. Creek
20. F. L. Culler
21. W. G. Dodge
22. G. G. Fee
23. D. E. Ferguson
24. G. F. Flanagan
25-29. M. H. Fontana
30. P. A. Gnadt
31. M. J. Goglia
32. W. L. Greenstreet
33. A. G. Grindell
34. R. C. Gwaltney
35. J. T. Han
36. N. Hanus
37. W. O. Harms
38. H. W. Hoffman
39. P. R. Kasten
40. M. J. Kelly
41. T. S. Kress
42. R. A. Lorenz
43. R. E. MacPherson
44. F. C. Maienschein
45. A. P. Malinauskas
46. W. R. Martin
47-66. W. J. McAfee
67. W. J. McCarthy
68. H. D. McNary
69. L. E. McNeese
70. J. G. Merkle
71. H. J. Metz
72. S. E. Moore
73. F. H. Neill
74. L. C. Oakes
75. G. W. Parker
76. L. F. Parsly
77. P. Patriarca
78. H. Postma
79. C. E. Pugh
80. M. Richardson
81. D. N. Robinson
82. G. C. Robinson
83. J. M. Rochelle
84. J. P. Sanders
85-89. W. K. Sartory
90. Myrtleen Sheldon
91. G. M. Slaughter
92. A. M. Smith
93. Cyrus Smith
94. J. E. Smith
95. I. Spiewak
96. J. A. Stevens
97. R. W. Swindeman
98. J. J. Taylor
99. D. G. Thomas
100. D. B. Trauger
101. W. E. Unger
102. J. L. Wantland
103. J. R. Weir
104. G. D. Whitman
105. W. J. Wilcox
106. G. T. Yahr
107. H. C. Young
108. Patent Office
109-110. Central Research Library
111. Y-12 Document Reference Section
112-124. Laboratory Records Department
125. Laboratory Records (RC)

Subcontractors

126. Z. P. Bažant, Northwestern University, Evanston, IL 60201
127. J. A. Swanson, Swanson Engineering Associates Corp., McMurray, PA 15317

EXTERNAL DISTRIBUTION

128-135. Director, Office of Nuclear Regulatory Research, Nuclear Regulatory Commission, Washington, D.C. 20555
136. Director, Reactor Division, ERDA, ORO
137. Director, Research and Technical Support Division, ERDA, ORO
138-399. Given distribution as shown in category NRC-7 (25 copies — NTIS)

☆ U.S. GOVERNMENT PRINTING OFFICE: 1976-748-189/200